Durham E-Theses

Cold Gas in Galaxy Cluster Cores

HAMER, STEPHEN,LESLIE

How to cite:

HAMER, STEPHEN,LESLIE (2012) *Cold Gas in Galaxy Cluster Cores* , Durham theses, Durham University. Available at Durham E-Theses Online: http://etheses.dur.ac.uk/5888/

Use policy

Cold Gas in Galaxy Cluster Cores

Stephen L. Hamer

Supervised by Dr. Alastair Edge

[False colour image of Hydra-A,
the blue shows the X-ray gas,
the green shows the radio emission
and the red shows the stellar continuum.]

A Thesis presented for the degree of
Doctor of Philosophy

Extragalactic & Cosmology Group
Department of Physics
Durham University
England

September 2012

Durham
University

Dedicated to

My fiancée, Liz, for putting up with me all this time.

Cold Gas in Galaxy Cluster cores

Stephen L. Hamer

Submitted for the degree of Doctor of Philosophy
September 2012

Abstract

We present a survey of 73 galaxy groups and clusters aimed at determining the role played by the cold gas in the feedback process. We use optical Integral Field Spectroscopy from the *VIsible Multi Object Spectrograph* in conjunction with high spatial resolution X-ray observations from the *Chandra X-ray Observatory* and extensive multi-wavelength observations to study the interactions of the cold gas with the Intra Cluster Medium and the Brightest Cluster Galaxy. The wealth of information provided by these observations has allowed us to study the kinematic structure of the cold gas in the largest sample of cluster cores to date. We use this information to shed new light three key questions i) *Are all line emitting systems highly disturbed?* ii) *What role does the Brightest Cluster Galaxy play in the cooling of gas from the ICM?* iii) *What role does the cold gas play in the feedback process and what is its relationship to the fuelling of the AGN?*.

The analysis of the full survey immediately suggests that the line emitting gas in the majority of cluster cores isn't highly disturbed. While several clusters do show a disturbed Hα morphology (13/73) the majority appeared uniform and quiescent (45/73). Similarly the velocity structure of the ionised gas within most systems also appears to be very ordered and interestingly appears decoupled from the stellar kinematics of the brightest cluster galaxy. Several of the more disturbed systems do show evidence of an interaction with another cluster member, however, this is not common to all disturbed systems.

One of the most interesting discoveries to come out of the sample analysis is the identification of a small sub–sample of objects which show an offset between the brightest cluster galaxy and the bulk of the ionised gas. Comparison to X-ray observations indicates that the cluster core is spatially coincident with the ionised

gas emission and not the galaxy. These objects provided an opportunity to study the role played by the BCG in the cooling of gas from the ICM. The kinematics of these objects suggests that these offsets should be transient and short lived. Despite this we identify a substantial mass of cold molecular gas ($\sim 10^9$ M$_\odot$) associated with the offset emission, and not the BCG, for one object. This mass is consistent with the upper limit of the cooling during the lifetime of the offset suggesting that the cooling continues to occur in the core despite being offset from the BCG. This result clearly indicates that while the BCG may typically reside at the centre of most clusters it is not required for cooling gas to condense from the ICM.

Finally, we address the ordered velocity structure of the ionised gas in BCG in much greater detail. As a pilot project we study the kinematics of Hydra-A using detailed multi-wavelength observations and identify the presence of a disk of cold gas which has an axis of rotation parallel to the axis along which the AGN is inflating cavities into the ICM. Comparison to the energetics of the cavities suggests that the mass of cold gas in the disk is sufficient to fuel a future outburst of comparable magnitude. Noting the similar velocity structure in many of the clusters in our sample we apply a similar analysis to the full sample. We use kinemetry and determine that $\approx 62\%$ of the sample have ionised gas kinematics which are consistent with a rotating disk. A linear trend is identified between the peak rotational amplitude of these disks and the linewidth of CO observations which suggests that the large mass of cold molecular gas present in the cores of clusters shares the kinematic structure of the ionised gas. Finally, we compare the axis of rotation of all disks with radio and X-ray observations and identify a clear alignment between the jets/cavities and the disks axis of rotation. The prevalence of these disks and their alignment with the axis along which the AGN is injecting mechanical energy into the ICM clearly suggests that they play an important role in the feedback process and provides a link between the gas cooling on kpc scales and the fuelling of the black hole at the centre of the BCG.

Declaration

The work in this thesis is based on research carried out at the Extragalactic & Cosmology Group, the Department of Physics, Durham University, England. No part of this thesis has been submitted elsewhere for any other degree or qualification and it is all my own work unless referenced to the contrary in the text.

Two Chapters from this thesis are, or will be, published in the Monthly Notices of the Royal Astronomical Society. The titles of these articles, their publication date, and the location of the published results in this thesis are as follows:

Paper Title	Pub. Date (Journal)	Thesis Chapter
The Relation Between Line Emission and Brightest Cluster Galaxies in Three Exceptional Clusters: Evidence for Gas Cooling from the ICM	04/2012 (MNRAS)	§ 4
Cold gas dynamics in Hydra-A: evidence for a rotating disk	*10/2012 (MNRAS)	§ 5

* — Planned submission date

Acknowledgements

I would like to take this opportunity to thank all the people without whose help and support I would not be writing this. There are far too many people for me to list individually but I would like to give special mention to a few.

First and foremost I would like to thank my Ph.D. supervisor, Alastair Edge, for all the help he has provided me over the past four years. More importantly, I would like to thank him for providing me with the opportunity to to become involved in an interesting and active area of research that I have found truly enjoyable to be a part of. His enthusiastic attitude and attention to detail while allowing me considerable flexibility created a relaxed but focused working environment that has helped me to grow as a scientist and as a person. I look forward to many more years of continued collaboration and more of his insights on the parts of the world that I have yet had a chance to visit.

I also owe a great deal to Mark Swinbank for his considerable contributions to this work. Mark introduced me to IFU spectroscopy and taught me everything I know about its reduction and analysis and has remained a friendly and willing source of information and assistance throughout my time in Durham. It is largely due to his efforts and assistance that I was able to complete the analysis of this sample in a timely fashion. He also taught me two of the most important lessons I have learned about research, that details are key to making your point clearly and concisely and the importance of working efficiently and not becoming too bogged down in a single piece of work.

There are several other people from Durham and elsewhere who stand out as worthy of mention. Floyd Jackson, Andy Sutton and Helen Russell all deserve considerable thanks for sharing with me their expertise in X-ray astronomy. Brian McNamara, Richard Wilman, Philippe Salomé, Francoise Combes and Andy Fabian

for their useful discussion and extensive constructive feedback on this work over the years. I would also like to thank my office mates of the last few years, Rachael Livermore, Alice Danielson and Chris Harrison, for small, but perhaps collectively immeasurable, assistance during my time in Durham. Their friendship and willingness to provide their expertise and technical skills in both astronomy and other areas at a moments notice has helped to make my time here both productive and enjoyable.

My family are deserving of a great deal of thanks for their assistance and support throughout the years. To my parents who instilled in me the determination to overcome any difficulties and achieve everything I could, thank you. For teaching me the value of hard work and the importance of remaining relaxed and focused. None of this would have been possible without your support, encouragement and determination. Finally, to my fiancée, Liz, thank you for being so amazing. My appreciation for everything that you have done, do and will do for me cannot be easily expressed. You are both my friend and partner in the truest sense of the word and I am forever grateful to have you in my life.

Contents

List of Figures

List of Tables

Chapter 1

Introduction

Galaxy clusters and groups are the largest gravitationally bound objects known to have been formed thus far in the evolution of the Universe. Clusters form in the densest regions of the Universe where the dark matter distribution forms massive halos at the intersection of filaments which channel gas and dark matter into the cluster. Clusters are rich environments each containing in excess of 1,000 densely packed galaxies with a large mass of hot gas filling the space between them. The total masses in these systems can range from 10^{13} M$\odot$ for groups as high as 10^{14} or 10^{15} M$\odot$ for clusters. This environment makes groups and clusters the ideal laboratories in the local universe to study the interaction of galaxies with each other and with a hot diffuse medium, allowing the effects of this environment on galaxy formation to be studied in detail in the local universe.

One of the key issues for our understanding of galaxy formation and evolution is the mechanism through which feedback from a galaxy affects the cooling of gas surrounding it. Simulations of galaxy formation which ignore non-gravitational heating (e.g. Katz & White, 1993) produce a galaxy population with an excess of massive galaxies when compared to the observed Universe. This occurs as a result of gas cooling being constrained only by its density, which results in rapid cooling and an over production of stars in the dense clumps where galaxies form. To address this problem the injection of energy into the gas from non-gravitational processes within the galaxies is invoked, a process dubbed 'feedback'. By including feedback in the simulations the over production of massive galaxies is stopped resulting in a galaxy population in closer agreement to that which is observed (Bower et al., 2006).

While feedback is widely accepted as the means to slow the cooling of gas, the form that it takes is a highly debated topic within the field of extragalactic astronomy and galaxy formation. Directly studying the nature of this feedback is difficult as the majority of gas cooling occurs when galaxies are forming at high redshift, which limits the detail of these observations. However the environment within galaxy

clusters is believed to be similar to that in the high redshift universe. Indeed naive X-ray observations of clusters suggest that gas is cooling rapidly and should condense into cold gas clouds and/or form stars. However the cold gas mass and star formation rates observed are too low to be consistent with the mass of gas that should be cooling from the ICM. For this to be the case some process must be occurring in clusters which is preventing most of the gas from cooling sufficiently to form stars. Thus by studying the processes which inhibit cooling in galaxy clusters we can gain an understanding of the feedback mechanisms which affect galaxy formation and evolution.

1.1   Clusters Of Galaxies

The study of extragalactic sources has been a key issue in astronomy ever since the first "spiral nebulae" were discovered to be galaxies external to our own (Hubble, 1926). This realisation presented astronomers the opportunity to study the physics of galaxies from an external vantage point, eliminating the biasing effects present in studies of our own Milky Way. This was the dawn of extragalactic astronomy and since this time increasingly sophisticated and deeper surveys (National Geographic Society - Palomar observatory Sky Survey (NGS-POSS), Minkowski & Abell (1963); 2-micron All-Sky Survey (2MASS), Skrutskie et al. (2006); Sloan Digital Sky Survey (SDSS), Abazajian et al. (2009)) have mapped out the universe and drastically increased the number of extragalactic sources known.

One of the earliest discoveries of extragalactic astronomy was the fact that galaxies were not uniformly distributed across the sky but tended to bunch together (Zwicky, 1938). Over the next few decades many thousands of galaxy groupings were identified (Herzog et al., 1957; Abell, 1958; Zwicky et al., 1961, 1963, 1965, 1966; Zwicky & Kowal, 1968; Zwicky et al., 1968; Abell et al., 1989), in fact it was found that the majority of galaxies (Zwicky, 1938; Abell, 1965) reside within these associated environments of groups and clusters. Clusters contain a substantial fraction of galaxies and as such are key to our understanding of how environment affects galaxy formation and evolution.

1.2   X-ray Emission from Clusters

The mass in clusters can be divided into three major components: stars, gas and dust which make up the galaxies observed in early surveys; the dark matter which is the main contributor to the gravity binding the cluster; and an extended atmosphere of hot gas (at near the virial temperature of the cluster, typically at 10–100 million K (Mushotzky et al., 1978)) which makes up the intracluster medium (ICM). The ICM is formed when baryons are caught up in the collapse of dark matter during the clusters formation and evolution. As the baryons fall inward they are shocked and adiabatically compressed which heats the gas to the virial temperature of the halo. For most clusters the gas contained in the ICM constitutes the great majority (~ 90 %) of the baryonic mass of the cluster (Lin et al., 2003). Galaxy clusters had been studied for many years before the first X-ray detectors were flown into space which identified the bright (clusters typically have X-ray luminosities in the range of 10^{44} to 10^{45} ergs s^{-1}) and extended X-ray emission coming from the ICM. The discovery of this hot atmosphere revolutionised the study of galaxy clusters with the focus shifting from the stars and galaxies to the physical processes governing the ICM.

The ICM is made up primarily of ionised hydrogen and helium with a mix of heavier elements at $\sim 1/3$ solar abundance (Loewenstein, 2004). The electrons and ions of this ionised gas interact through Coulomb collisions which results in copious bremsstrahlung emission at X-ray wavelengths (Sarazin, 1988). Since the ICM is only directly observable through this X-ray emission, the ROSAT All-Sky Survey (RASS) (Voges et al., 1999) provided a major advancement in the study of the ICM by providing X-ray observations of many known galaxy clusters as well as detecting a large sample of potential new clusters identified by their X-ray properties alone (e.g. RXCJ1257.1-1339, RXCJ1558.3-1410, RXJ0352.9+1941 and many other objects in the RXJ and RXCJ catalogues, Böhringer et al. (2004)).

X-ray emission from thermal bremsstrahlung is the means through which the ICM radiates away the energy in the gas with the cooling time (t_{cool}) being proportional to the temperature (T) and the gas density (n) such that

$$t_{cool} \propto T^{\alpha}/n \qquad\qquad (1.2.1)$$

where $-1/2 \gtrsim \alpha \lesssim 1/2$ (see Fabian, 1994a, for a review). As such in the densest regions the time in which the ICM can radiate away all its energy can become very short compared to the Hubble time.

The temperature and density of the ICM can be parametrised as the Intracluster Entropy (K) defined as

$$K = P\rho^{-5/3} \propto T n_e^{-2/3} (KeV cm^2) \tag{1.2.2}$$

where P is the pressure, ρ is the density and n_e is the electron number density. Since entropy incorporates both the gas temperature and density it is a good measure of the ICMs thermodynamic state. Low entropy gas is cool and dense meaning it is much more likely to cool and condense from the hot phase than hotter, more diffuse, high entropy gas.

Observations of the central regions of massive galaxy clusters show intense X-ray emission suggesting that the ICM is undergoing significant radiative cooling (Fabian et al., 1981). The central regions of clusters show a dichotomy in the X-ray surface brightness profiles with many showing highly peaked cuspy (Fabian, 1994a) profiles while others are smoother and flatter (Figure 1.1).

The highly peaked profiles of some clusters suggest that the gas within their cores is extremely dense, on the order of 10^{-2} cm^{-3} or higher. From eq. 1.2.1 it can be seen that with the core temperature in most clusters on the order of 10^7 K such objects can have typical cooling times which are frequently less than the age of the system. It is also apparent from eq. 1.2.2 that the cores of such clusters will have very low entropy values when compared to the cores of clusters with shallower profiles. By considering just the entropy of the ICM Sanderson et al. (2009a) were able to show that the thermodynamics of the cluster population is bimodal with a separation between cluster with low entropy cores (cooling flow clusters) and those with higher entropy cores (non-cooling flow clusters).

In cluster cores with a high cooling rate and low entropy the hot gas from the ICM should quickly and easily condense and fall out of the hot phase resulting in a phenomenon known as a cooling flow. A cooling flow occurs due to the pressure in the cluster core being determined by the mass of the gas in the ICM pushing down on it under the clusters gravity. Thus as the core radiates energy and cools the
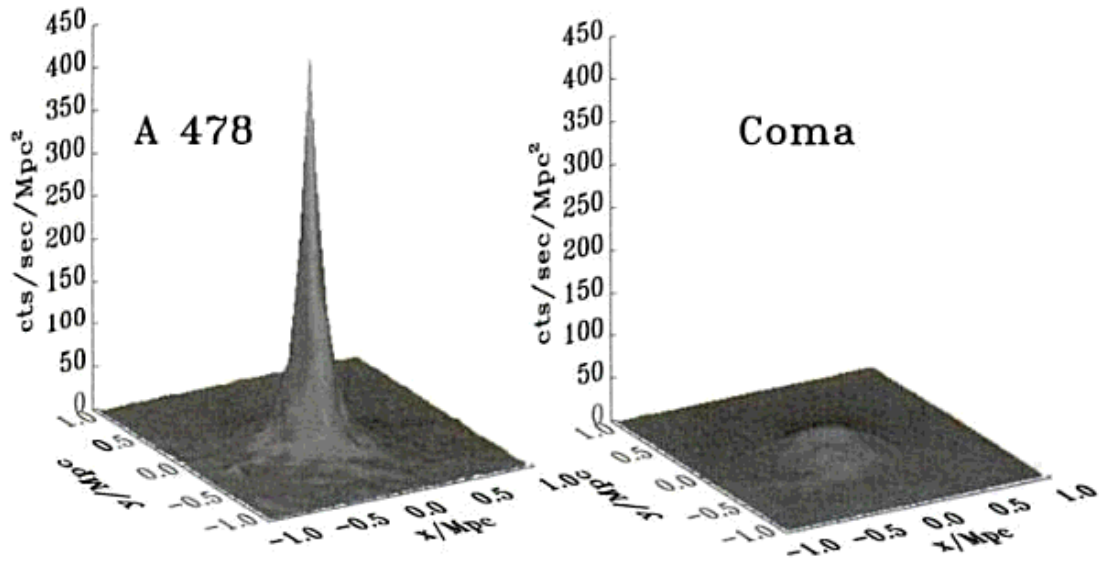
Figure 1.1: Comparison of the X-ray surface brightness of a cluster with a strong cooling flow (Abell 478) and a cluster which has no cooling flow (Coma) taken from Fabian (1994b). It can clearly be seen that in clusters with cooling flows the surface brightness profiles show a clear cusp which is not present in clusters without cooling flows.
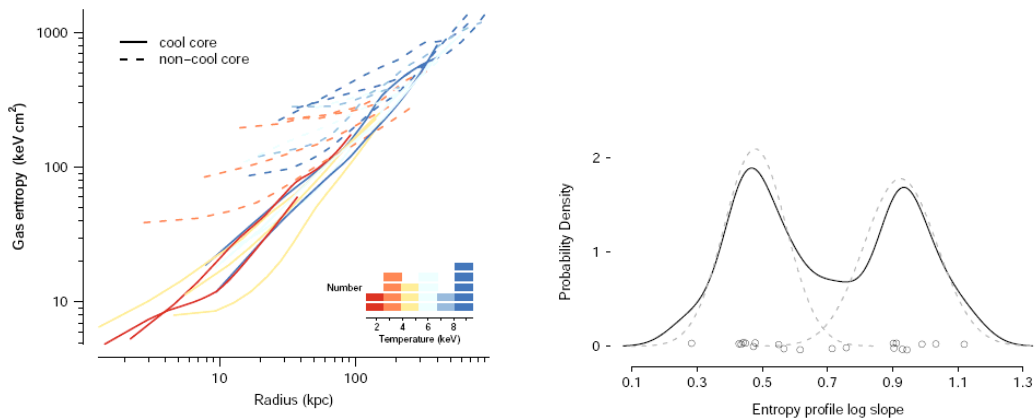
Figure 1.2: Figures taken from Sanderson et al. (2009a). *Left* - The entropy profiles of the clusters in their sample. The profiles are grouped by cool core status and colour coded by temperature. *Right* - Probability density of a cluster having an entropy profile with a given log slope. The jittered points show the positions of the individual clusters. Gaussian best fits were produced for the sample as a whole and separated by cool–core status and are shown as a solid line and dashed lines respectively. A clear bimodality can be seen in the cluster population from this plot.

gas must increase in density to maintain the pressure balance, for this to occur the gas in the core must flow inward. The surrounding gas will then fall into the core regions as it fills the space left by the contracting gas. This process will continue as long as the dense core remains resulting in a sub-sonic (on the order of a few cm s^{-1}) flow of the ICM towards the centre of the cluster.

This process would suggest that a substantial mass ($\sim 10^{12}$ M$_\odot$) of cool gas should be deposited into the central regions of the cluster. As the gas in the core continues to cool and increase in density it should fall out of the hot phase and eventually form molecular gas clouds and ultimately stars (for a review see Fabian, 1994a). From a simple analysis of the X-ray data the cooling rate of a typical cluster is expected to be 10–100 M$_\odot$yr^{-1} rising as high as >500 M$_\odot$yr^{-1} in the most extreme systems.

1.3 Cold Molecular Gas in Galaxy Clusters

In the idealised cooling flow as described above a large mass of material is predicted to cool from the ICM and should be observable within the cores of clusters. The ultimate fate of cooling gas should be to end up as cold molecular clouds (Fabian & Nulsen, 1977; Fabian et al., 1981) in which stars can form. Cold molecular Hydrogen is itself difficult to detect directly (O'Dea et al., 1994), however as we know the cooling gas is not primordial (having $\sim 1/3$ solar metallicity) we expect that the molecular clouds which form from it will have a similar abundance. Molecular emission from cold CO (carbon monoxide) gas emits several bright lines in the sub-mm wavelength range and can be used as a tracer of molecular gas clouds at $\sim$ 10–200 K (O'Dea et al., 1994).

The large mass of cool material predicted to form from a cooling flow should be observable in the cores of clusters as CO emission. Early searches for this CO failed to make a significant detection of molecular gas in the cores of most clusters (Braine & Dupraz, 1994; McNamara & Jaffe, 1994; O'Dea et al., 1994). X-ray observations of clusters suggest that a substantial mass of cold gas ($\sim 10^{12}$ M$_\odot$) with a high column density ($N_H \sim 10^{21}$ cm^{-2}) should be present in cluster cores (White et al., 1991). However for this to be consistent with the observations of O'Dea et al. (1994) the molecular gas would have to be very cold, on the order of a few Kelvin. This violates the minimum temperature set by cosmic microwave background (CMB)

and is inconsistent with the derived equilibrium temperature of molecular clouds in clusters which falls in the range of $\sim$ 20–30 K. Therefore the gas cooling from the ICM is not condensing into clouds of molecular gas at a sufficient level to explain the predicted rate of cooling.

Star formation is another possible fate of the gas deposited by the cooling flow, however searches for star formation in cluster cores have yielded similar results. McNamara & O'Connell (1989) study a sample of 13 cD galaxies in cooling flow clusters and find that eight show spectral anomalies in the form of abnormally strong [OII] emission or an excess in the Ultra Violet (UV) flux. The UV excess in these galaxies is shown to be caused by the presence of massive and young OB stars implying that star formation is active within these systems. McNamara & O'Connell (1989) suggest the possibility that this star formation is occurring as a direct result of gas being deposited by the cooling flow. However, assuming a standard Initial Mass Function (IMF), the star formation rate implied by the UV excess cannot account for the full mass of gas that X-ray observations suggest should be deposited by the cooling flow. At best the star formation can account for $\sim$20% of the cooling gas (in two of the objects), with a more likely estimate being the mean of the whole sample of 7%.

The lack of a detection of substantial masses of cold molecular gas or a high rate of star formation within the cores of clusters poses a problem for the cooling flow model. The X-ray emission clearly shows the rate of cooling which should be expected within cluster cores, however if this gas is not forming cold molecular gas or stars then where is it going? This problem was partially addressed by later more systematic surveys for CO in clusters (for example see Edge, 2001; Salomé & Combes, 2003) which were able to detect gas masses of $10^{9-11} M_\odot$ within the cores of some clusters. This does reduce the large discrepancy between the predictions from X-ray observations and the mass of cooled gas detected. However it only accounts for $\sim$ 10% of the gas which the classic cooling flow model predicts should have cooled the ICM.

1.4   Feedback, solving the cooling flow problem

With the launch of the most sensitive X-ray satellites (*Chandra* and *XMM-Newton*) new X-ray observations began to make this picture much clearer. Early observations with XMM-Newtons highly sensitive Reflection Grating Spectrometer (RGS) failed to detect the X-ray spectral features of gas cooling at ∼1 keV (Peterson et al., 2001; Tamura et al., 2001). Predominantly the FeXVII line, which is emitted by gas at 0.5–1×10^6 K, is weak or absent in many cooling flow clusters (Peterson et al., 2003), though it is still consistent with a high rate of cooling (~ 100 M$\odot$ yr^{-1}) in some systems (Morris & Fabian, 2005; Sanders et al., 2010).

These findings suggest that the cooling rates of typical clusters are much lower than were suggested by the X-ray luminosity found by earlier observations at only ∼1–10 M$_\odot$ yr^{-1}. Indeed the apparent lack of gas at X-ray temperatures of < 1 keV suggests that some process is truncating the cooling to lower temperatures and preventing much of the gas from cooling further. In principle this solves the cooling flow problem as the upper limit of the detected gas mass and lower estimate of the cooling are now consistent (see the review by Peterson & Fabian, 2006).

However, this presents a new problem as the core ICM is still radiating away most of its energy through X-ray emission at a high rate. This suggests that there must be some process acting in the cores of cooling flow clusters which is continually reheating the gas. Thus "feedback" from non-gravitational processes needs to be invoked in order to inject energy into the ICM and balance the effects of X-ray cooling. Many possible contributors to ICM heating have been suggested such as starbursts (Veilleux et al., 2005), shocks from mergers (Markevitch & Vikhlinin, 2007), sloshing of gas (ZuHone et al., 2010), conduction from the surrounding ICM (Voigt & Fabian, 2004) and mechanical or radiative feedback from an AGN (McNamara et al., 2005; McNamara & Nulsen, 2007).

While all of these processes are likely to affect the cores of clusters, their relative importance in terms of the ICM energetics is unclear and has a strong dependence on environment. By considering each process individually we can infer something about their relative importance. Shocks from cluster mergers for example can provide more than enough energy to quench the cooling of the ICM (Randall et al., 2002). However

mergers are likely to be too stochastic to be a reliable means of reheating the ICM. Starbursts are another option as gas cooling should imply more star formation, but the energy they can inject into the ICM is not sufficient to balance cooling in the most extreme systems ($\sim$ few percent of that required, McNamara et al. 2006). Sanderson et al. (2009b) were able to show that non-cooling flow clusters can be conductivity stable at all radii, however thermal conduction was not sufficient to oppose radiative cooling in the inner regions ($< 0.1r_{500}$) of cooling flow clusters (Voigt & Fabian, 2004). "Sloshing" occurs in clusters after a major event, such as a merger with a sub halo, has displaced the cooling flow from the clusters centre of mass. The momentum given to the core then causes it to oscillate about the centre of mass, a process which can last a few Gyr if the disturbance is large enough (ZuHone et al., 2010). ZuHone et al. (2010) show that such "sloshing" can facilitate heat transfer into the cluster core by mixing the low entropy gas in the cooling flow and the higher entropy gas from the surrounding ICM. However, in order for this to prevent a cooling flow the process would have to be continuous, requiring repeated encounters with merging subclusters in order to maintain the sloshing effect.

Towards the centre of each cluster core there is typically a bright dominant galaxy, with a mass of the order of 10^{11} M$\odot$, which hosts a massive central black hole. The AGN outbursts from these brightest cluster galaxies (BCGs) are some of the most energetic events in the Universe (Nulsen et al., 2005). However the radiative energy from these outbursts is very localised and it is difficult to see how this can reheat the larger scale ICM at a wide range of densities. While the radiative energy from AGN outbursts may not be able to counteract cooling it has been discovered that AGN outbursts from the BCG can create "bubbles" of non-thermal plasma in the ICM (for example see figure 1.3 which shows X-ray cavities in Abell 2052). This provides a means by which the AGN can inject mechanical energy into the large scale ICM which has been shown to be sufficient to counteract the cooling (Fabian et al., 2003, 2006; McNamara et al., 2005). Bîrzan et al. (2004) found a trend between the central X-ray luminosity of a cluster and the mechanical luminosity of the AGN outburst. Such a trend suggests that the amount of feedback from an AGN outburst scales proportionally with the cooling rate, resulting in a self regulated feedback loop ideally suited to maintaining gas at a given temperature.
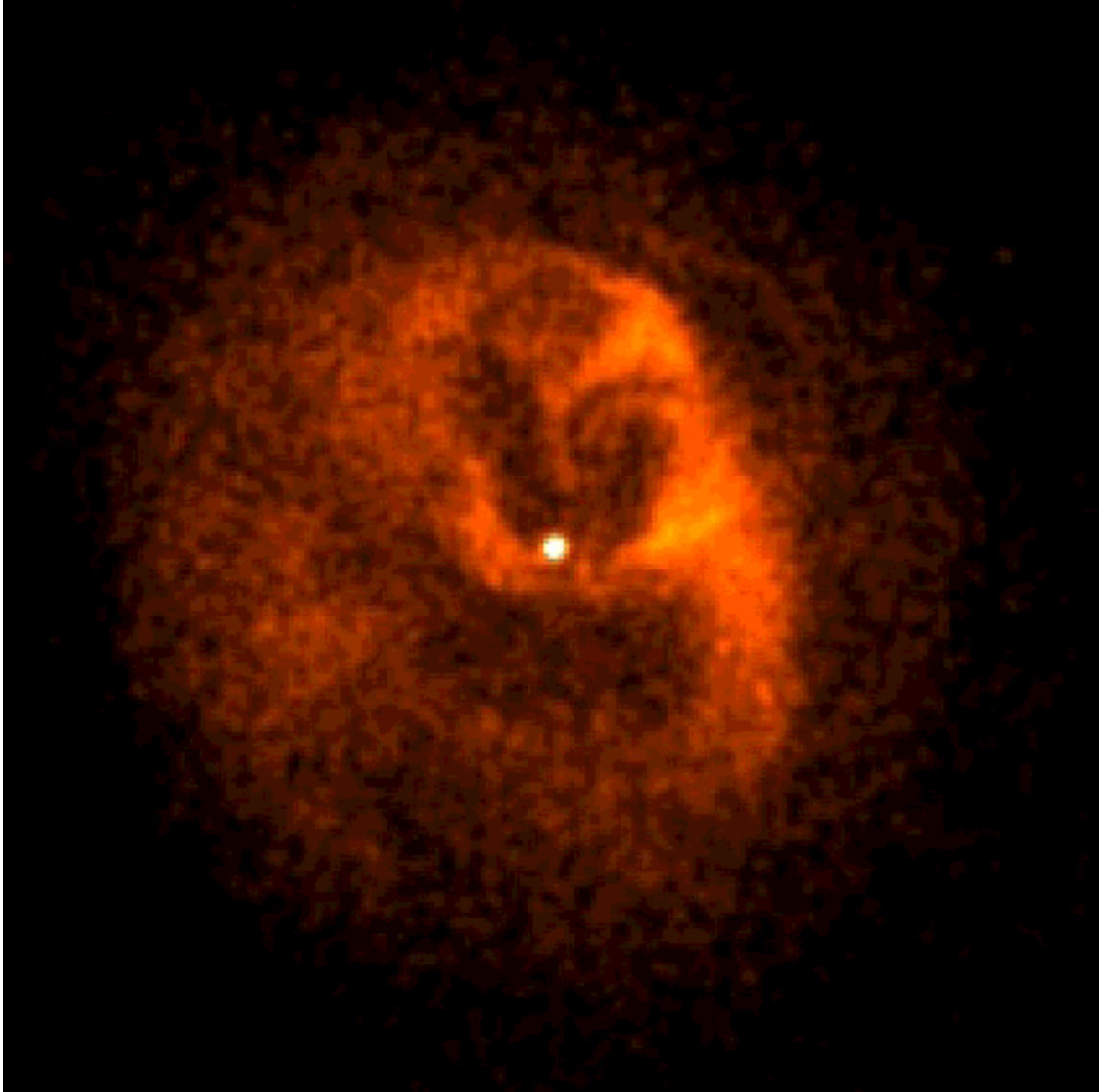
Figure 1.3: This is an X-ray image of Abell 2052 which is one of the most striking examples of a cluster with large bubbles in the ICM (Blanton et al., 2011). To the north and south of the central bright peak clear depressions in the X-ray surface brightness can be seen. Comparison to radio observations show that these cavities are filled with radio emission.

1.5   Modeling Feedback

The problem of over-cooling is one which is also seen in simulations of galaxy formation which ignore the effects of non-gravitational heating (Katz & White, 1993). Such simulations produce a galaxy population with a substantially higher fraction of massive galaxies than that observed in galaxy surveys (Bell et al., 2003). This over production of massive galaxies occurs as gas cools too rapidly and forms stars much more efficiently than observations suggest is the case (Lewis et al., 2000). This "cooling crisis" is in many ways similar to the cooling flow problem in that the amount of cooling predicted vastly exceeds that which is seen.

More recent simulations include a "feedback" effect into the models which represents the heat injected into the gas by non-gravitational processes such as Active Galactic Nuclei (AGN) outbursts, star formation and supernovae. By including such feedback in the models, the simulations are able to produce a galaxy population in closer agreement to the observed one (Bower et al., 2006). While including these processes produces a more realistic model of galaxy formation, the mechanism through which these processes can inject energy into a large volume from just a single galaxy is the subject of some debate (Fabian, 2012; McNamara & Nulsen, 2012).

There is a growing consensus in the community that AGN outbursts, fed by the cooling gas, are responsible for reheating the ICM in a self regulated feedback mechanism. This interaction of gas cooling, fuelling of an AGN, subsequent disruption of the cooling and hence the black hole fuel supply are key issues in the wider debate about galaxy formation (Bower et al., 2006). One of the main drawbacks of this mechanism however is that it requires the fine tuning of the AGN power which is heating the X-ray gas in order for the mechanism to be self regulating. Too much AGN power could quench cooling entirely, while too little would not offset the cooling. For this to be true the activity from the localised region of the AGN must be coupled to the larger kpc scale cooling of the cluster. As such the conversion efficiency of AGN mechanical power into gas heating is uncertain.

There has been extensive work to attempt to model the AGN output and couple it to heating of the ICM gas. Churazov et al. (2002) consider a simple model in which the AGN is powered through Bondi accretion (Bondi, 1952) which assumes

spherical accretion and does not account for angular momentum. This accretion then powers an outflow which inflates cavities in the ICM which rise buoyantly injecting mechanical energy into the hot gas. This model suggests that the efficiency of AGN feedback must be high with a few percent of the rest mass of the accreted material needing to be transferred into the outflow. For this model jet power depends directly on the accretion rate which in turn depends on the cooling rate of the ICM which presents a natural coupling. Churazov et al. (2002) find that less than a quarter of the internal energy of the bubble can escape the cooling flow region as sound waves suggesting a substantial fraction of the AGNs mechanical power remains and heats the cooling flow region.

Croton et al. (2006) studied the relation between galaxy evolution and AGN activity. Their semi-analytic model allows for three modes of AGN growth, "quasar mode" accretion, black hole mergers and "radio mode" accretion. They show that "radio mode" accretion, continual and quiescent accretion of gas from a hot halo surrounding the black hole, grows in importance towards z=0 and is the main contributor to the feedback responsible for shutting off cooling flows. In "radio mode" the accretion rate is low but can still provide enough power to suppress the cooling flow leading to the models producing luminosity functions with a cut off at the bright end, similar to that which is observed. Although Croton et al. (2006) consider two physical models for "radio mode" accretion their main results are insensitive to the actual model used.

1.6 The evolution of the cluster core and the role of the BCG

The clusters X-ray luminosity and temperature relate closely to the intrinsic luminosity of the BCG (Schombert, 1987, 1988; Edge & Stewart, 1991a,b). This connection between the BCG and cluster properties makes BCGs an important tool for studying clusters. Since the dense environment at the centre of a cluster means that BCG experiences a much higher ICM pressure than any other cluster member galaxy. Also radiative cooling is at its strongest in the cluster core and gas cooling from the hot phase can be accreted onto the BCG, fueling its evolution. However,

these regions are also densely populated by other galaxies making the likelihood of interactions and mergers much higher. Both mergers and gas accretion are therefore likely to play important roles in the growth and evolution of the BCG and cluster core (Tremaine, 1990; Wilman et al., 2006).

For the most rapidly cooling cluster cores, the BCGs ubiquitously exhibit optical line emission (Heckman et al., 1989; Cavagnolo et al., 2008). Crawford et al. (1999) found significant line emission in 32 per cent of a sample of 201 BCGs selected from the Brightest Cluster Survey (BCS) X-ray selected sample (Ebeling et al., 1998). This line emitting gas at 10^4 K traces filamentary structures (for example see Figure 1.4) around the BCG (Hatch et al., 2005, 2006; McDonald et al., 2011) and direct comparison has shown qualitatively similar structures in the 10^7 K X-ray (Fabian et al., 2008) (Figure 1.5) and 30 K molecular (Salomé et al., 2011) gas. This structural similarity suggests that the gas phases are linked with gas from the ICM cooling through the warm phase before quickly condensing out into cold molecular gas clouds. However, the masses of the gas at these temperatures isn't consistent with that predicted from cooling (Johnstone et al., 1987). Once the gas is in these molecular clouds, ionising radiation from within the cluster core can easily re-ionise and excite the surface of the gas clouds. The recombination of these ions with electrons gives rise to line emission from the surface of the molecular clouds. As such studying the easily observable ionised gas through its line emission can give an insight into the physical mechanisms operating within the cluster cores.

Early studies of the brightest handful of BCGs showed a variety of complex spatial and velocity structures present in the ionised gas (Crawford et al., 2002; Hatch et al., 2006; Wilman et al., 2006; Edwards et al., 2009). These early studies are highly suggestive, with some objects showing rotation, offset emission and most having largely uniform [NII]/Hα ratios. They also show that the most kinetically disturbed objects tend to be those which show evidence of a recent interaction. The presence of strong radio sources from the BCG at the centre of clusters further complicates the situation. In several clusters the intricate filamentary structures formed by the optical line emission appear to be spatially and dynamically linked to the expanding radio lobes (Conselice et al., 2001; Hatch et al., 2006), the most clear example of this is NGC 1275 in the core of the Perseus cluster (Figure 1.4).
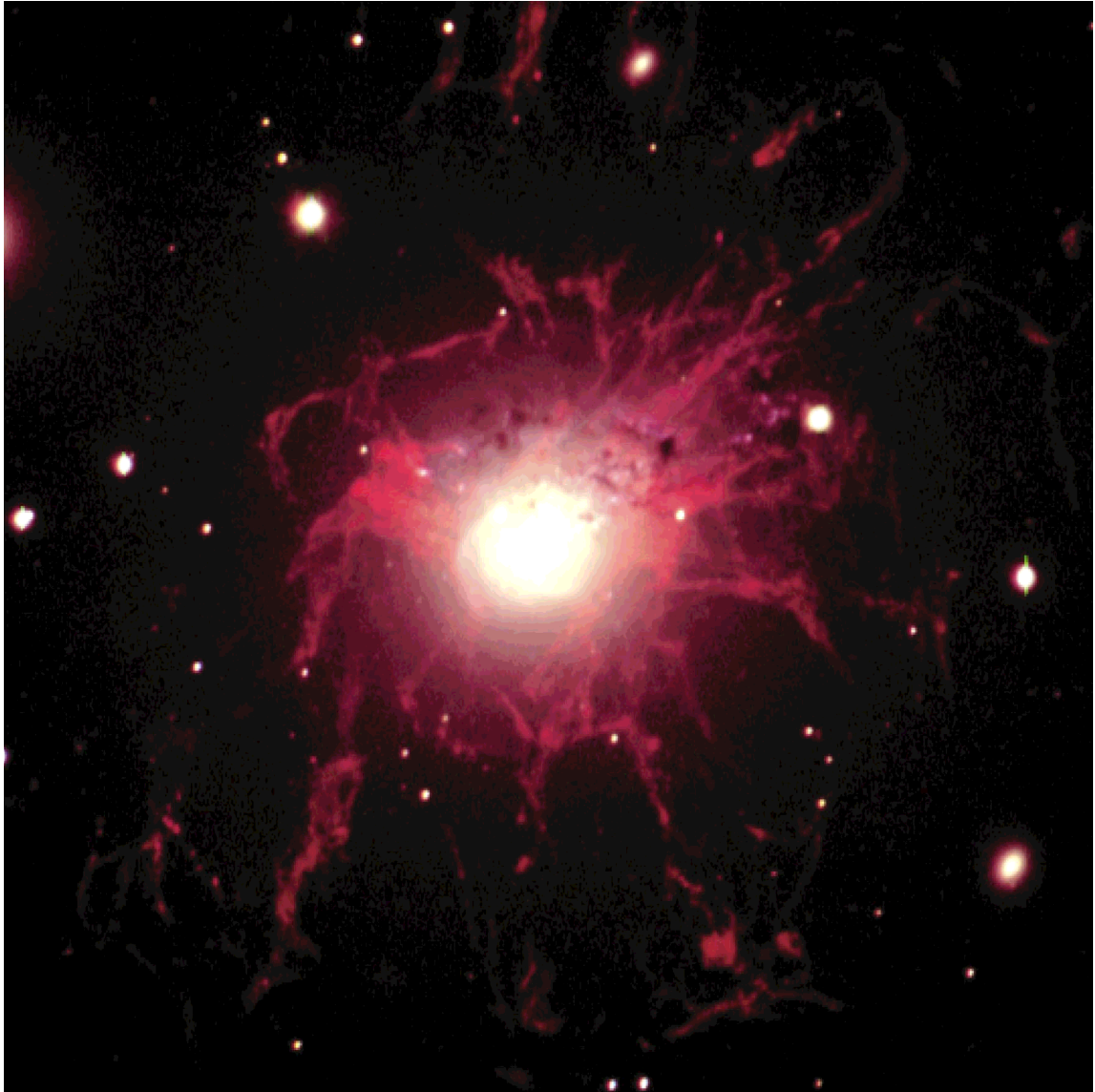
Figure 1.4: This is a narrow band Hα image of the BCG in the Perseus cluster of galaxies taken from (Conselice et al., 2001). The Hα emission is shown in pink overlaid on a white continuum image. It can clearly be seen that the line emitting gas forms filamentary structures which extend out from the BCG and into the ICM.
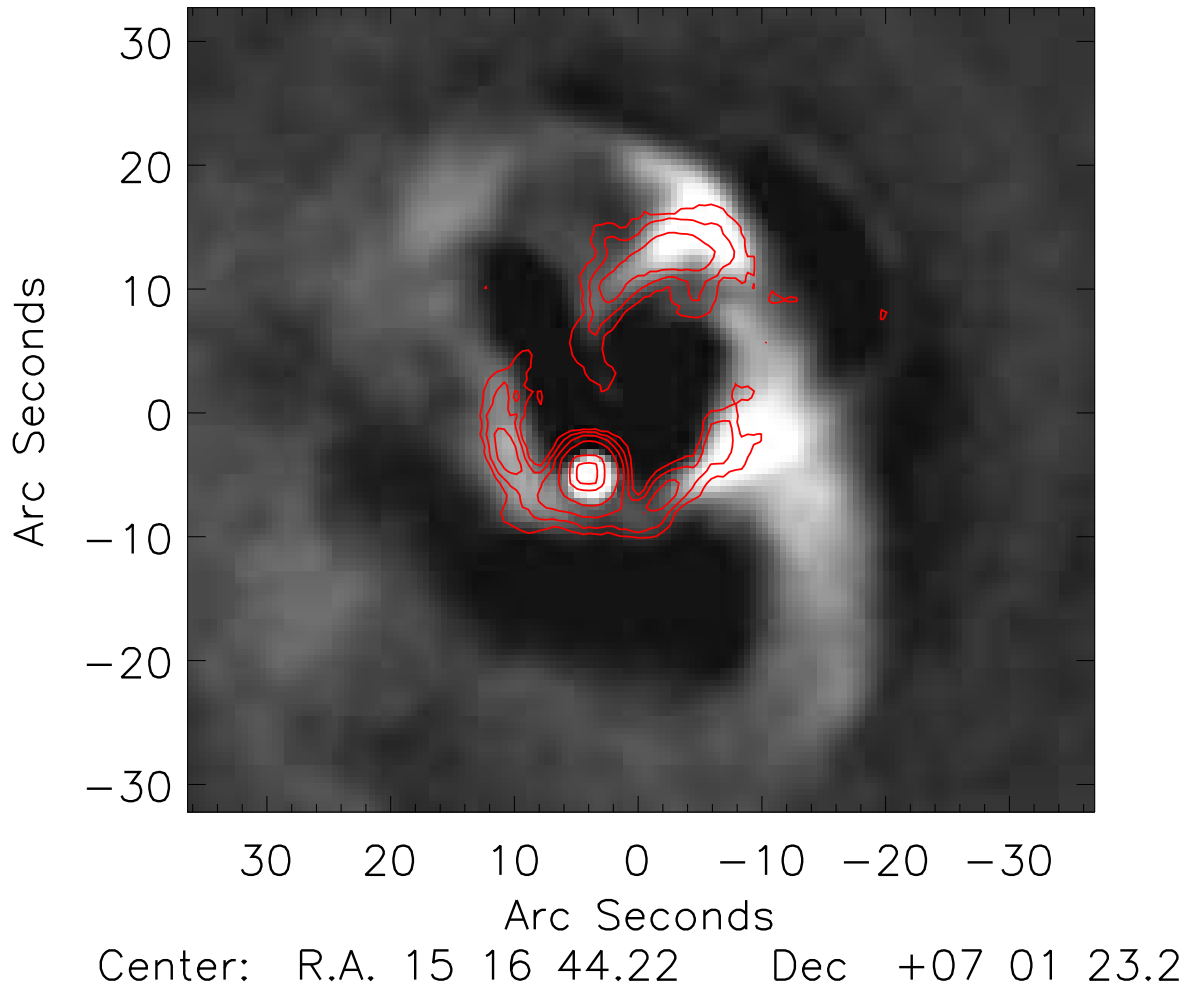
Figure 1.5: The greyscale shows an X-ray image of Abell 2052 which shows clear depressions in the X-ray surface brightness. Contoured in red is the narrow band Hα image of (McDonald et al., 2011) which can clearly be seen to match the bright structures seen in the X-ray image.

However, the small number of objects studied mean that any conclusions drawn can only be applied to the specific case being studied as the statistics are not sufficient to apply the findings to the cluster population as a whole. In order to place constraints on the BCG population in general a larger, more systematic survey of the emission lines structures in BCGs is needed which spans a range in radio power. To that end we have used the VIsible Multi Object Spectrograph (VIMOS) on the Very Large Telescope (VLT) to obtain spatially resolved spectroscopy around the redshifted Hα emission of 73 BCGs selected to show evidence of extended line emission structures. These observations will allow the kinematics of a significant population of BCGs to be studied, representing a factor of five increase in the number of cluster cores studied with an IFU.

The analysis and interpretation of that data set will make up the majority of this thesis. By using this representative sample we will attempt to address three key questions pertinent to our understanding of cluster cores:

i *Are all line emitting systems highly disturbed?* Previous IFU observations of just a handful of objects indicated the presence of gas at high velocity with structures and kinematics suggesting possible interactions with other cluster members (Wilman et al., 2006).

ii *What role does the Brightest Cluster Galaxy play in the cooling of gas from the ICM?* Most clusters of galaxies have Brightest Cluster Galaxies whose positions are strongly correlated with the cluster core (Peres et al., 1998; Sanderson et al., 2009a; Hudson et al., 2010) which makes disentangling their respective roles in the cooling of gas difficult.

iii *What role does the cold gas play in the feedback process and what is its relationship to the fuelling of the AGN?* If radio jets are responsible for injecting energy into the ICM then the degree of fine tuning required suggests a link between the black hole in the Brightest Cluster Galaxy and the gas cooling from the ICM.

1.7 Outline of Thesis

The primary aim of this thesis has been to study kinematic and spectroscopic properties of a statistically significant sample of BCGs which exhibit optical line emission,

and determine the relationship between the cooling flow of the clusters, the line emission and the feedback from the BCG required to truncate the cooling of the ICM. From this sample several objects which exhibited unique or interesting kinematic or structural properties were identified and studied in detail. The studies and findings from these objects are presented in individual chapters towards the end of this thesis.

In Chapter 2 we present details of the observations, data reduction and analysis techniques used throughout this thesis. This chapter describes how the initial integral field unit (IFU) sample was selected and observed, the spectral fitting routine used to extract kinematic and spectroscopic information from the data cubes and the instruments used to provide supplementary observations of other gas phases which are used to construct a complete picture of the processes affecting the cluster core.

Chapter 3 then presents the analysis of the sample beginning by showing the maps of continuum, line flux, [NII]/Hα ratio, mean velocity and velocity dispersion produced by the spectral fitting routine for every object. The statistics of the sample are discussed and the objects are classified based upon their Hα (or [NII] where Hα is very weak) morphology. We identify a rare class of objects which show an offset between the BCG and the peak of their line emission. Evidence is also presented which suggests that the gas kinematics for most of the objects are highly ordered.

In Chapter 4 we discuss a study of three exceptional clusters which show a physical and kinematic offset between the BCG and the peak of X-ray cooling which is presented in Hamer et al. (2012). In this study we use a multi-wavelength analysis to show that the cooling of gas from the ICM into the molecular phase can occur independently of any influence from the BCG. This has previously been difficult to ascertain due to the high spatial coincidence between the BCG and cooling peak observed in most clusters.

We present an analysis of Hydra-A (a very well studied object with a wealth of supplementry data available) in Chapter 5. We identify the presence of a rotating disk of cold gas and dust running across the BCG. Comparison to the energetics of the cavities in this system suggests that the mass of gas in the disk is sufficient to fuel a future outburst of comparable magnitude to the one which created them. We

discuss the implications of this in the light of the fact that we identify the axis of rotation of the disk to align with the axis of the jets created by the AGN.

An expansion of this analysis is presented in Chapter 6 in which we consider the full VIMOS sample in the context of what we learned from Hydra-A. We first use the kinemetry analysis technique (Krajnović et al., 2006; Shapiro et al., 2008) to compare the kinematics of each object in the sample to that of an ideal disk in order to determine if any others are disks. Having identified a substantial population of disks ($\approx 62\%$ of the sample) we determine their axes of rotation and compare this to known jets and X-ray cavities to determine if the alignment seen in Hydra-A is common to all systems. We see a clear alignment in the majority of systems and we note that this configuration is similar the the unified model of an AGN, however the scales are much greater in these objects.

Finally we present a summary of our findings in Chapter 7 before discussing these findings with regard to the questions posed earlier in this Chapter. We briefly consider several projects which are currently underway or beginning which will aim to build upon or expand the work presented in this thesis. We end with a short discussion of our conclusions and their implications for our understanding of AGN feedback and cluster cores in general.

Chapter 2

Sample selection,

Instrumentation and

Data Reduction.

2.1 Overview

This Chapter will outline the methodology used in the collection and analysis of the datasets used throughout this thesis. First the selection criteria of the 73 objects that make up the sample of extended optical line emitting BCGs will be explained. Next a brief outline of the instruments and observatories used to obtain the data sets used throughout this thesis will be given. The Chaper will conclude with a description of the observations of the sample along with the data reduction and analysis techniques used in studying the IFU data.

2.2 Sample Selection

Spectroscopic studies of line emission in BCGs has found roughly a third of clusters (e.g. 64 of 201 clusters or 32%, Crawford et al., 1999) show evidence of optical line emission in their cores. This sample was drawn from the ROSAT selected Brightest Cluster Survey (BCS Ebeling et al. (1998)) and as such was restricted to the Northern hemisphere. To extend this work to the Southern hemisphere the ESO X-ray Cluster Elliptical Spectral Survey (EXCESS) was conducted which obtained long slit spectra for 446 BCGs from the ROSAT-ESO Flux Limited X-ray (REFLEX) Galaxy cluster survey (Böhringer et al., 2004). The EXCESS survey used the FORS instrument on ESOs Very Large Telescope (VLT) to obtain optical long slit spectra for clusters in the southern sky up to declination $\delta = +2.5^o$. The EXCESS spectra

were then used to identify clusters with optical line emission, the Hα emission line was identified in 30% of the sample which is consistent with the findings of Crawford et al. (1999). The sample for this work was drawn from these two surveys, with a total sample size of 647 objects of which ≈ 184 show evidence of optical line emission. The observations were performed using the ESO VLT as a poor weather back up project, as such the sample was limited to a maximum declination of $\delta = +20^o$ to ensure the objects were sufficiently high in the sky to be visible throughout the year.

Two further selection criteria were then applied to the sample, first only objects with an integrated Hα emission of greater than 10^{-15} erg cm^{-2} s^{-1} were selected to ensure a significant detection ($> 7 \; \sigma$) of the Hα at 10^{-16} erg cm^{-2} s^{-1} in a 30 min observations. The second selection criteria for the sample was that the Hα emission showed an extent of greater then two arcsec in the long slit observations of Crawford et al. (1999) or the EXCESS survey. This ensured that only objects with line emission extended on scales of greater than the expected seeing were observed. 78 objects matched the selection criteria of which five already had optical IFU observations. The final X-ray selected sample includes all extended Hα bright BCGs out to a redshift z $= 0.25$ and represents an increase in the number of systems studied with IFUs of more than an order of magnitude. The presence of extended line emission suggests that all objects in the sample have low central entropy values (Cavagnolo et al., 2008) and are thus consistent with classical cooling flows. Figure 2.1 shows the locations of all objects from the parent samples and identifies those which were selected to be observed with VIMOS.

2.3   Observatories and Instrumentation

The cores of galaxy clusters and BCGs are complex environments in which a multitude of gas phases are all present and interacting with each other. As such it is vital to use multiwavelength observations when studying this wide range of temperatures to ensure that all gas phases are accounted for. This thesis predominantly focuses on the use of optical and infra-red IFU spectroscopy to study the kinematic and spectral properties of ionised gas but also uses supplementary data ranging from radio observations to X-ray data. The seven instruments used throughout this work are briefly described below.
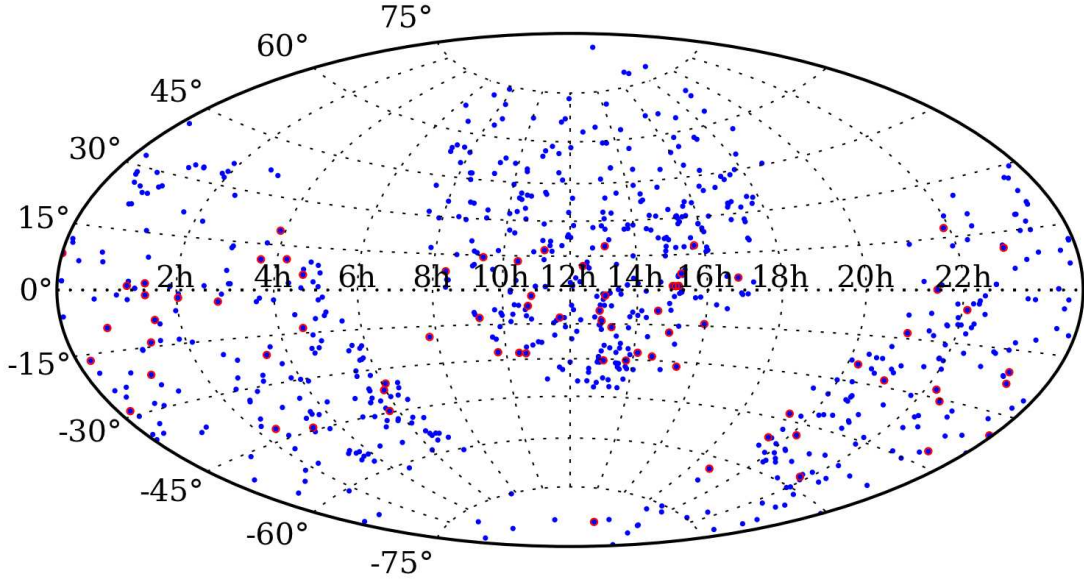
Figure 2.1: Here we show a plot of the sky identifying the locations of the sample. The blue points show the objects in both the BCS and EXCESS samples, the objects selected and observed with VIMOS are circled in red.

2.3.1   VLT – VIMOS

The Visible Multiobject Spectrograph (VIMOS) instrument on the 8.2–m Very Large Telescope (VLT) was the primary optical IFU used throughout this work. The VIMOS IFU is made up of 6400 fibres with a scale on the sky which can vary from 0.33" to 0.67" per fibre which corresponds to a field of view ranging from 13"×13" to 54"×54" on the sky. The VIMOS instrument consists of four arms which split the VIMOS field of view into four identically sized quadrants. Each quadrant feeds to a separate grism which disperses the incident light onto its own CCD. There are six grisms equipped on each arm which provide overlapping coverage from 360 to 1000 nm with a spectral resolution ranging from R∼200–2500. The higher spectral resolutions require the light from each pseudo-slit to be dispersed over the full length of the CCD which limits the field of view to one quarter of the maximum possible at a given spatial resolution (∼27"×27" at 0.67" per pixel).

These capabilities make VIMOS the most well suited instrument for the purposes of studying the kinematic and spectral properties of the extended ionised gas within cluster cores. The wavelength coverage allows easy access to the bright Hα line in BCGs out to a redshift of z=0.25 while the field of view is more than sufficient to

contain the emission in all but the most local clusters. At high spectral resolution the kinematics of the gas can be mapped to a high degree of accuracy with each spectral resolution element (0.6 Å) corresponding to ~ 30 km s^{-1} (at the wavelengths observed) with broad resolved lines allowing accurate centroiding to a fraction of this. The spectral resolution also allows for the independent fitting of the Hα and [NII] lines meaning a measure of the ionisation state of the gas can be obtained from the line ratios. Finally the wavelength coverage will provide a detection of other important spectral features should they be present including the [SII] doublet (allowing for a measure of the electron density), the sodium D absorption feature (which can be used to study the stars from the BCG) and the Hβ and [OIII] lines in some objects. The bulk of this thesis is based on observations of the ionised gas at $\sim 10^4$ K that were observed using the VIMOS IFU.

2.3.2   VLT – SINFONI

The spectrograph for integral field observations in the near infrared (SINFONI) is a near-infrared ($1.1 - 2.45$ μm) integral field spectrograph on the VLT. It was used to provide supporting observations of a subset of the BCGs observed as part of the larger VIMOS sample. SINFONI can used with an Adaptive Optics (AO) module using either natural or laser guide stars to provide high resolution observations regardless of seeing conditions, or can be used without the AO in seeing limited mode. It can provide resolutions of 0.25", 0.1" or 0.025" per image slice which correspond to a field of view of 8"×8", 3"×3" or 0.8"×0.8" respectively. In typical seeing conditions however only the first of these modes is suitable for use without the AO module. The spectral coverage of the instrument is divided into the three infrared bands J (1.1–1.4 μm), H(1.45–1.85 μm) and K(1.95–2.45 μm) with a spectral resolution of R~ 2000, 3000 and 4000 respectively. The instrument can also provide a single observations covering the H + K band (1.45–2.45 μm) with R$\sim$1500.

The K band coverage of SINFONI in particular provides good overlap with the VIMOS observations providing access to the ionised Paschen-alpha (Pα) line as well as several transitions of warm molecular hydrogen (1-0 S(0) to S(3)) for most BCGs above a redshift of z=0.05. Its resolving capabilities are also comparable with each spectral resolution element corresponding to ~ 40 km s^{-1} (which again

can be improved by centroiding spectrally resolved lines). While the field of view of SINFONI is substantially smaller than that of VIMOS the coverage of the K-band limits observations to objects with a redshift of z>0.05, of which most of the most extended objects fall below. The fact that SINFONI is also a VLT instrument means that potential sky coverage is identical to that of VIMOS ensuring a good overlap of potential targets. For these reasons SINFONI was selected to provide supporting near-infrared (NIR) IFU spectroscopy of gas at a few 100–1000 K.

2.3.3 Gemini – GMOS

The Gemini Multi-Object Spectrographs (GMOS) are two optical IFU capable instruments on the twin 8.1–m Gemini North and South telescopes. GMOS can cover a spectral range of 460nm – 933nm in IFU mode with a resolving power comparable to that of VIMOS. The location of Gemini South allows for similar sky coverage to VIMOS however the GMOS instrument on Gemini North provides the same capabilities with access to northern objects. However, the GMOS field of view is more limited than that of VIMOS, being made up of 1500 fibres of which 500 are used to observe a sky offset region $\sim$ 1 arcminute away from the target field. The remaining 1000 fibres observe the target field at a spatial sampling of 0.2" limiting observations to a 5"$\times$7" field of view. The GMOS instrument was only used to provide archival observations of a single object which was compared to similar objects observed with VIMOS. The description of these data and their analysis can be found in Chapter 4.

2.3.4 Chandra X-ray observatory – ACIS

The hot gas ($\sim 10^7$ K) of the ICM which makes up the majority of the baryonic mass of clusters can only be observed at X-ray wavelengths. As such to study the interaction of cooling gas in the ICM with the cold gas associated with the BCG and/or cluster core X-ray observations at comparable spatial sampling are required. The Advanced CCD Imaging Spectrometer (ACIS) on the *Chandra X-ray observatory* is the ideal instrument to study the ICM due to its large field of view and excellent spatial resolution. The ACIS instrument can provide accurate spatial sampling of $\sim$0.7", comparable to the resolution of the VIMOS IFU. This

allows structures within the ICM and ionised gas to be identified and compared on similar spatial scales, of particular interest to this thesis are the location and shape of cavities in the ICM and the centre of ICM cooling. The ACIS instrument also provides spectral information from $\sim$ 0.5–8.0 keV at each pixel position. This allows the soft X-ray emission of the ICM to be disentangled from the harder emission of the AGN within the BCG which is required to accurately identify the centre of the ICM cooling.

2.3.5 IRAM 30m – Sub-mm CO observations

The IRAM 30m telescope is one of the largest and most sensitive millimetre telescopes operating today. Millimetre observations provide access to a number of carbon monoxide (CO) transitions which are ideally suited to studying cold ($\sim$ 20-40 K) molecular gas which should form at the centre of most clusters as gas cools from the ICM. The new EMIR receiver provides a minimum bandwidth of 4 GHz in each of the 3mm, 2mm, 1.3mm and 0.9mm atmospheric windows allowing it to cover a frequency range of 83-358 GHz with some gaps between the bands (Carter et al., 2012). The EMIR bandwidth is a substantial improvement over previous IRAM instruments which only provided a 400 MHz bandwidth which resulted in broad CO lines being indistinguishable from the background. However these observations were able to detect CO lines in the cores of many clusters provided the lines were narrow ($<$ 500 km s^{-1} Edge, 2001). CO observations from IRAM with both the EMIR and its predecessors are used throughout this thesis to compare the kinematics of the cold molecular gas to the other gas phases.

2.3.6 Herschel – PACS

The Herschel Space Observatory is a 3.5m Far–Infrared telescope capable of performing photometry and spectroscopy in the 55-671 μm range. The PACS instrument provides both imaging and spectroscopic capabilities in the range of $\sim$ 60–210 μm. This spectral coverage allows it to observe the 'cool universe' ($\sim$ 30K) and provide observations of several previously unobtainable atomic cooling lines including [OI] and [CII].

2.3.7 Radio observations

Radio observations of cluster cores trace the synchrotron emission from non thermal plasma ejected from the AGN in the BCG. As such radio observations can trace the injection of mechanical energy into the cluster core through the interaction of the jets with the ICM. Observations from several radio telescopes have been used in this thesis to trace the AGN activity within the clusters that are part of the VIMOS sample. Data from the Very Large Array(VLA), Very Long Baseline Array (VLBA) and the Australian Telescope Compact Array (ATCA) have been used to map the radio emission in a sample of cluster cores which has some overlap with the VIMOS sample. These observations cover a range of frequencies from 1.4 GHz to 15 GHz and have varying spatial resolutions, some as low as a few milliarcsec while others are several arcsec. Within this thesis the primary use of this data is to determine the alignment of the radio axis and as such the spatial sampling is not important so long as the radio source is resolved.

2.4 Data Reduction

2.4.1 VIMOS

VIMOS was used to obtain the Optical IFU spectroscopy of the 73 BCGs in the sample between October 2007 and September 2008. For each object a set of three 600s exposures were performed with a pointing dither included between each to account for bad pixels. The *HR_Orange Grism* and *GG435* filter (spectral resolution of $\sim \Delta\lambda/\lambda \sim 2650$ over a wavelength range 5250–7400 Å) were used to observe Hα(λ_{rest}6562.8 Å) in clusters with a redshift below 0.13. For clusters with a redshift greater than this the *HR_Red Grism* and *GG475* filter (spectral resolution of $\sim \Delta\lambda/\lambda \sim 3100$ over a wavelength range 6450–8600 Å) were used to sample the Hα. The setup used was selected such that the spectra obtained would cover a spectral range which should include the principle lines of Hα, [OI], [NII] and [SII] assuming they are present in each objects spectrum. As this project was proposed as a bad weather backup project, the observations were taken in a range of conditions, with a mean seeing of ~ 1.4 arcsec in the range ~ 0.5–2.6 arcsec. The seeing quoted is

the mean of the DIMM seeing measured for each of the three exposures. Both the *HR_Orange* and the *HR_Red* modes offer a 27" × 27" field of view which is covered by 1600 fibres. Each fibre is coupled to a micro-lens to give near-continuous sky coverage with each fibre observing a region of 0.67" in diameter. The total field of view is split into four quadrants of 400 fibres each and as such each quadrant required separate reduction. Details of the observations are summarised in Table 3.1.

The raw data from VIMOS were reduced using the VIMOS specific recipes in the ESO Recipe Execution Tool ESOREX. This package performed the basic data reduction on each data cube (a total of 12 for each object, one for each quadrant from the three pointing's) including bias subtraction, flat fielding, and the wavelength and flux calibration. To subtract the sky point–like objects were masked to remove any stars within the field. Such objects were defined as having a roughly 2d-Gaussian intensity profile with a FWHM on the order of the seeing and were removed out to the diameter of the seeing. The BCG was then removed by masking all pixels within an isophote of half its peak intensity. This level was chosen empirically as the best compromise to allow a good sampling of sky pixels while removing the majority of the BCGs light. The sky level for each quadrant was then calculated by taking the median value of the remaining pixels at each wavelength increment. This sky spectrum was then subtracted from each pixel in the four quadrants before they were combined into a single data cube. For low redshift objects ($z \lesssim 0.02$) the BCG easily fills a single quadrant so a higher flux threshold for removing the BCG must be used which can result in a substantial oversubtraction of the sky. For such objects continuum subtraction prior to the sky subtraction proved a more reliable means of isolating the emission line. The continuum was calculated from the spectrum at each spatial resolution element by taking the median of the emission either side of the lines of interest. The spectral range used to calculate the median were 120 Å in length and began 40 Å from the emission line on either side. Once the continuum had been subtracted the sky was subtracted in the same manner as the higher redshift objects before the lines are fit. The drawbacks of this method however are that it is only valid for a small spectral range so only one line complex can be fit for a given reduction, it also eliminates any information carried in the

objects continuum emission (such as dust absorption). Finally the three exposures were median combined for each pointing in order to eliminate cosmic rays. The exception to this was RXCJ2014.8-2430 which only had two pointing's so the mean of the two observations was used to produce the final cubes. The final mosaics provided cubes with a $\sim 30 \times 30$ arcsec field of view.

2.5 Analysis

2.5.1 IFU Data Cube analysis

Integral field spectroscopy is used to investigate the spatial variation of line emission and kinematics within cluster cores. This method took the IFU data cubes produced by the reduction of VIMOS, SINFONI and GMOS observations and fit spectral models to the key lines at each resolution element. The primary diagnostic line structure at optical wavelengths (VIMOS and GMOS) was the Hα (λ_{rest} 6562.8 Å) and [NII] (λ_{rest} 6548.1/6583 Å) complex. For the infrared observations (SINFONI) no such multi–line complex was available so the primary diagnostic line used was the Paschen-alpha (n=4 to n=3) transition of hydrogen (hereafter Pα).

To fit these lines we extracted a region of the spectrum in each resolution element (lenslet) that was 240 spectral resolution elements in length ($\sim$ 144 Å for VIMOS and GMOS, $\sim$ 528 Å for SINFONI) centred at the wavelength of principle line of interest at the cluster redshift. We then fitted Gaussian emission-line profiles to these extracted regions using a χ^2 minimisation procedure. To the [NII]–Hα triplet of lines we fit three separate Gaussian profiles on top of a flat continuum and compare this to just a flat continuum fit. While the continuum will not always be flat the short wavelength range used for the fitting routine mean there is little variation making a flat continuum a good approximation (Figure 2.2)

The fitting routine was given an array of first guess variables which were then used to produce the fit. For the Hα-[NII] triplet these variables were the redshift of the emission (first guess set to the cluster redshift), the flux of the Hα line (first guess set to the average line flux across the whole cube), the sigma width of the lines (first guess set to the width of a skyline, $\sim$2.0 Å or three resolution elements in VIMOS), the continuum flux level (first guess set to 0) and the flux of the bright
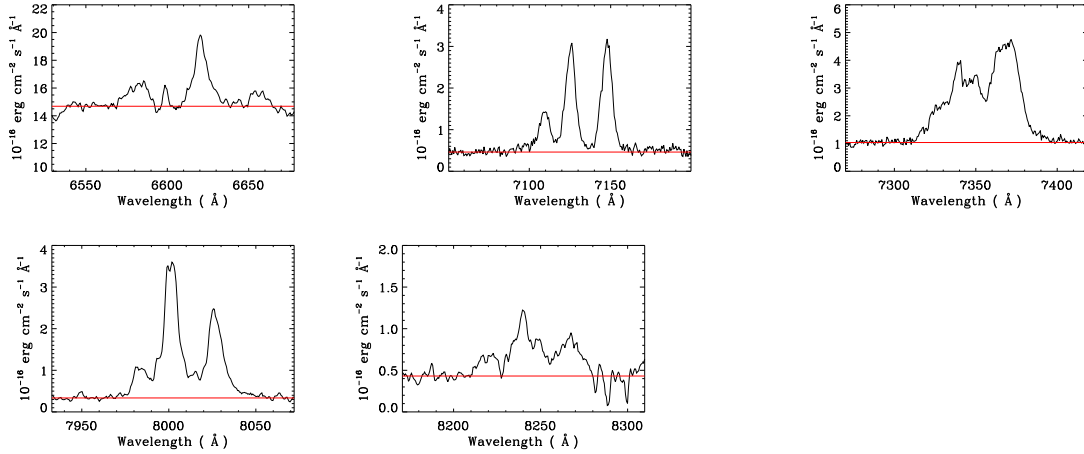
Figure 2.2: Here we show several spectra which represent the sample. The spectra are of the central region of five objects and the wavelength coverage is the same as the region used by the fitting routine. From left to right, top to bottom the redshifts of the objects are ≈ 0, ≈ 0.08, ≈ 0.13, ≈ 0.21 and ≈ 0.26 so are representative of the whole sample. As can clearly be seen from these spectra the continuum level over the short wavelength ranged used by the fitting routine is well approximated by a constant value (shown by the red line).

[NII] (λ_{rest} 6583 Å) line (first guess set to be the same as the Hα flux. The redshift and width of the [NII] lines were set to match the Hα and the flux of the [NII] (λ_{rest} 6548.1 Å) was fixed to $1/3^{rd}$ of the [NII] (λ_{rest} 6583 Å) flux. After producing the first guess the redshift, flux and linewidth of the Hα line, as well as the continuum level and [NII] (λ_{rest} 6583 Å) flux were allowed to vary until the model minimised to best fit the data. These profiles were initially fitted to the spectrum from each 0.67 arcsec lenslet and adaptively binned to 2.0 arcsec in regions with lower Hα flux, as such the low surface brightness emission has a lower resolution than the brightest regions. The fitting routine used for the SINFONI observations works in exactly the same way however due to the separation of the lines each is fit independently as a singlet.

We accepted these fits as representing the data when they provided an improvement over a continuum only fit at the 7σ significance level. When an acceptable fit was found the parameters of the best fitting model were stored and the 1σ errors were calculated by varying each parameter slightly form the best fit and allowing all others to re–minimise. For each pixel where an acceptable fit was found we attempted to fit a second model which included an additional line component with a redshift, intensity and width independent of the initial fit. This extra component

was allowed to become much broader than the initial fit and was included as a means to test the spectra for additional velocity components and broad line features. This model was then accepted when it provided an improvement over the single component fit at the 8σ significance level. For pixels where a second component was found to be significant the errors were recalculated to account for the new model.

The parameters of the fits were then used to produce maps of the line flux, line-of-sight velocity and linewidth (full width at half-maximum (FWHM) deconvolved for instrumental resolution). The velocity zero point was determined as the median of the measured velocities after removing the highest 2.5% and lowest 2.5% of them. A retrospective clipping method was used to remove pixels in which the fitting routine had returned parameters with unphysical properties. Continuum images of the region covered by the observations were produced by taking the median from each lenslet over a region of the spectra containing no emission lines or sky line residuals (here after referred to as collapsing the cube).

2.6 Afterword

Throughout this thesis we assume a standard cosmology with $\Omega_m = 0.27$, $\Lambda = 0.73$ and $H_o = 71$ km s^{-1} Mpc^{-1} throughout.

Chapter 3

Sample Analysis

3.1 Overview

This Chapter presents the analysis of all 73 BCGs in our IFU sample beginning with the details of the observations. We will then present maps of the continuum, line emission, [NII]/Hα ratio, mean velocity and velocity dispersion for each object in the sample. The parameters of the individual objects are extracted and presented before the statistics of the sample are discussed. We will present evidence of the ordered nature of the velocity structure seen in the ionised gas and show that, for at least a few objects, it is inconsistent with the velocity field of the stellar component of the BCG suggesting that the stars and the gas are decoupled. We will also identify a rare subset of objects which show a substantial offset between the centre of the BCG and the majority of their Hα emission.

3.2 Observations

The sample selection, observations and details of the data reduction of the IFU sample are outlined in Chapter 2. Due to the flux limited nature of the sample the Hα luminosity of the systems has a dependance on redshift as shown in Figure 3.1 with the most luminous systems being those at higher redshift. Table 3.1 outlines the key observational parameters of each objects in the sample. The redshift quoted in Table. 3.1 is the average redshift of the Hα line in the object. Most of the objects in the sample had all pointings performed on the same day, or at least in similar conditions. However, RXCJ2014.8-2430 had one of its pointings performed in very poor conditions. As such we have only used two of the pointings to make the final cube. RXCJ2101.8-2802 had pointings which were taken on different days, it had 4 pointings total all of which were in consistent conditions and showed no other
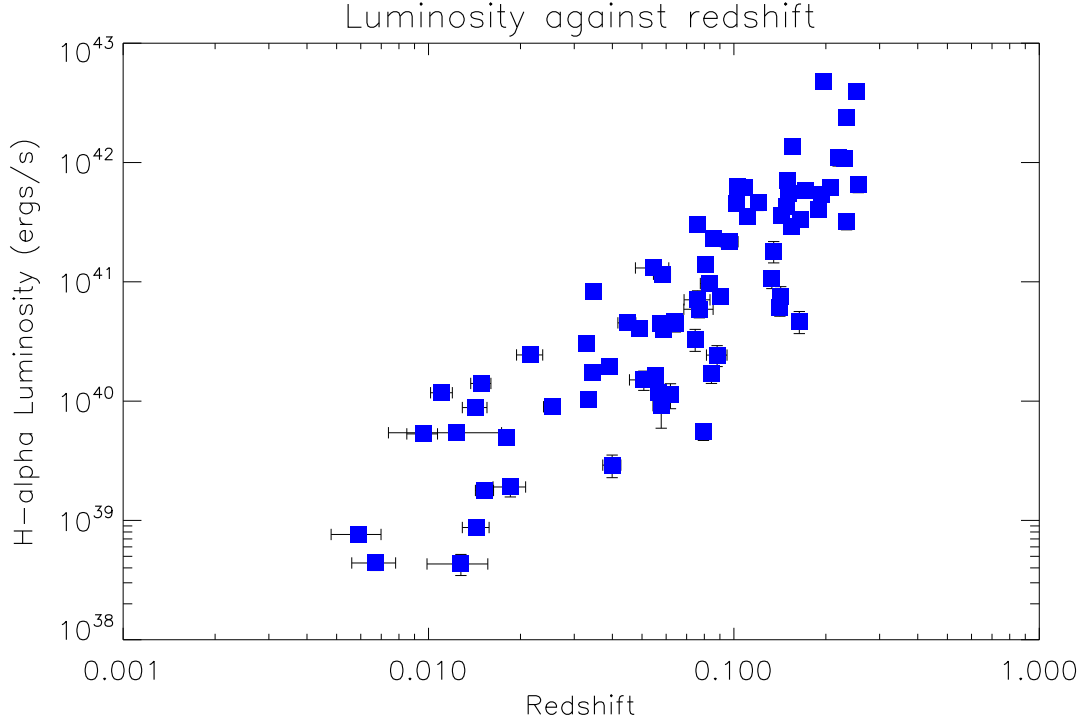
Figure 3.1: Here we plot the Hα luminosity against the redshift of each cluster. As would be expected for a flux limited sample a clear trend can be seen with the more distant objects generally having higher luminosities

problems in the spectra, as such we choose to use all 4 pointings giving this object a slightly longer integration time. We calculated the mean seeing of all observations to be ∼ 1.5 arcsec. Before the full fitting routine was run on an object its spectrum was studied to identify the presence of additional emission lines (lines other than Hα and [NII]), these additional lines are listed in Table. 3.1.

3.3   Maps

Here we present the maps of the parameterised fits to the Hα and [NII] triplet. The five panels show the continuum emission, the Hα flux map, the ratio of the [NII] to Hα, the line of sight velocity field and the line widths. It should be noted that in some systems where the continuum is very high and Hα flux is low not all of the Hα is recovered due to the underlying absorption feature caused by Hα in stellar atmospheres. In such cases the Hα line often appears very weak or even completely absent from some parts of the cube where it is otherwise expected to be (such as regions were the other ionised lines are strong). For these objects, rather than trying

TABLE 3.1.
THE OBSERVATIONAL PARAMETERS LISTED FOR EACH OBJECT IN THE VIMOS SAMPLE

Cluster	Redshift	Grating	Exposure(s)	Mean Seeing(")	Lines Detected
Abell 1060	0.012626	HR-orange	3×600	0.79	
Abell 1084	0.133013	HR-red	3×600	0.68	[OI]
Abell 11	0.149098	HR-red	3×600	0.77	[SII]
Abell 1111	0.165182	HR-red	3×600	0.85	[OI], [SII]
Abell 1204	0.170573	HR-red	3×600	0.81	[OI]
Abell 133	0.056650	HR-orange	3×600	0.93	[SII]
Abell 1348	0.119851	HR-orange	3×600	0.87	Hβ, [OIII], [NI], [OI]
Abell 1663	0.084330	HR-orange	3×600	2.46	
Abell 1668	0.063546	HR-orange	3×600	1.21	[OIII], [SII]
Abell 194	0.018199	HR-orange	3×600	1.17	
Abell 1991	0.059011	HR-orange	3×600	0.68	
Abell 2052	0.034354	HR-orange	3×600	1.89	[SII]
Abell 2390	0.230405	HR-red	3×600	1.41	[NI], [OI], [SII]
Abell 2415	0.057594	HR-orange	3×600	1.51	[SII]
Abell 2495	0.079323	HR-orange	3×600	0.92	
Abell 2566	0.083007	HR-orange	3×600	0.99	Hβ, [OI], [SII]
Abell 2580	0.088109	HR-orange	2×600	1.85	
Abell 2734	0.062036	HR-orange	3×600	1.81	[SII]
Abell 291	0.196026	HR-red	3×600	1.05	
Abell 3017	0.219269	HR-red	3×600	1.39	[OI],[SII]
Abell 3112	0.076016	HR-orange	3×600	2.25	[SII]
Abell 3378	0.141321	HR-red	3×600	1.32	
Abell 3444	0.255504	HR-red	3×600	0.51	
Abell 3574	0.014090	HR-orange	3×400	0.92	[SII]
Abell 3581	0.021600	HR-orange	3×600	2.03	[OI], [SII]
Abell 3605	0.064302	HR-orange	3×600	0.69	[SII]
Abell 3638	0.076867	HR-orange	3×600	1.04	[OIII], [NI], [OI], [SII]
Abell 3639	0.150512	HR-red	3×600	0.72	[SII]
Abell 3806	0.074599	HR-orange	3×600	0.56	[SII]
Abell 383	0.188691	HR-red	3×600	1.28	[SII]
Abell 3880	0.058350	HR-orange	3×600	2.57	[OIII],[NI],[OI],[SII]
Abell 3998	0.090187	HR-orange	3×600	2.01	
Abell 4059	0.048997	HR-orange	3×600	1.71	[SII]

Table 3.1: The observational parameters listed for each object in the VIMOS sample. The first column states the cluster designation as used throughout this thesis. The redshift is the median redshift acquired from the fits to the Hα-[NII] complex, the median is calculated from the fits after dropping the top and bottom 2.5% of the redshifts. The grating is the VIMOS grating used for the observations and the exposure lists the total integration time on target. The seeing is calculated as the mean of the DIMM seeing across all exposures for each object. The final column lists all lines apart from the Hα and [NII] lines that were detected by visual inspection, the Hα–abs line is included for systems which show some evidence of Hα self absorption.

Cluster	Redshift	Grating	Exposure(s)	Mean Seeing(")	Lines Detected
Abell 478	0.085558	HR-orange	3×600	1.95	Hβ, [OI]
Abell 496	0.032937	HR-orange	3×600	1.88	[OI], [SII]
Abell 795	0.134869	HR-red	3×600	1.17	
Abell 85	0.055327	HR-orange	3×600	1.00	[OI], [SII]
HCG62	0.014232	HR-orange	3×600	0.63	Hα–abs, [SII]
Hydra-A	0.053154	HR-orange	3×600	1.38	[OIII], [NI], [OI], [SII]
NGC4325	0.025474	HR-orange	3×600	2.39	[SII]
NGC5044	0.008941	HR-orange	3×600	2.23	[OI], [SII]
NGC533	0.018766	HR-orange	3×400	0.92	[SII]
NGC5813	0.006768	HR-orange	3×400	2.03	
NGC5846	0.006107	HR-orange	3×400	1.26	[SII]
RXCJ0120.9-1351	0.050603	HR-orange	3×600	0.92	
RXCJ0132.6-0804	0.148303	HR-red	3×600	0.75	[OI],[SII]
RXCJ0331.1-2100	0.192756	HR-red	3×600	1.63	[SII]
RXCJ0543.4-4430	0.163768	HR-red	3×600	1.32	
RXCJ0944.6-2633	0.142558	HR-red	3×600	0.43	[SII]
RXCJ1257.1-1339	0.014704	HR-orange	3×400	1.63	[SII]
RXCJ1304.2-3030	0.010925	HR-orange	3×400	1.97	[OI], [SII]
RXCJ1436.8-0900	0.080929	HR-orange	3×600	N/A	Hβ, [OIII], [NI] , [OI], [SII]
RXCJ1511.5+0145	0.039833	HR-orange	3×400	1.68	
RXCJ1524.2-3154	0.101902	HR-orange	3×600	1.27	Hβ, [OIII], [NI], [OI], [SII]
RXCJ1539.5-8335	0.075544	HR-orange	3×600	0.47	[OI](6300), [SII]
RXCJ1558.3-1410	0.096800	HR-orange	3×600	1.17	Hβ, [OIII], [NI], [OI]), [SII]
RXCJ2014.8-2430	0.155152	HR-red	2×600	2.00	[OI], [SII]
RXCJ2101.8-2802	0.033315	HR-orange	4×600	0.90	[SII]
RXCJ2129.6+0005	0.233940	HR-red	3×600	1.80	
RXCJ2213.0-2753	0.061279	HR-orange	3×600	1.27	
RXJ0000.1+0816	0.039267	HR-orange	3×600	1.48	[SII]
RXJ0338+09	0.034449	HR-orange	3×600	1.27	[NI], [OI], [SII]
RXJ0352.9+1941	0.108326	HR-orange	3×600	1.67	Hβ, [OIII], [NI], [OI], [SII]
RXJ0439.0+0520	0.207603	HR-red	3×600	1.27	[SII]
RXJ0747-19	0.102657	HR-orange	3×600	1.5	Hβ, [OIII], [NI], [OI], [SII]
RXJ0821+07	0.110876	HR-orange	3×600	1.25	Hβ, [OIII], [OI]
RXJ1651.1+0459	0.154666	HR-red	3×600	1.00	[SII]
S555	0.044841	HR-orange	3×600	1.75	[SII]
S780	0.234116	HR-red	3×600	1.50	[OI], [SII]
S805	0.015176	HR-orange	3×600	1.25	[SII]
S851	0.009414	HR-orange	3×600	1.25	[SII]
Z3179	0.142290	HR-red	3×600	1.00	[SII]
Z348	0.252854	HR-red	3×600	1.75	[NI], [OI], [SII]

Table 3.1: continued.

to model out the absorption we fitted the spectrum by forcing the spectral fit to be primarily constrained by the bright [NII](λ_{rest} 6583 Å) line. In such cases the maps in Figure. 3.2 show the [NII] flux rather than the Hα as the [NII] is substantially stronger in these systems.
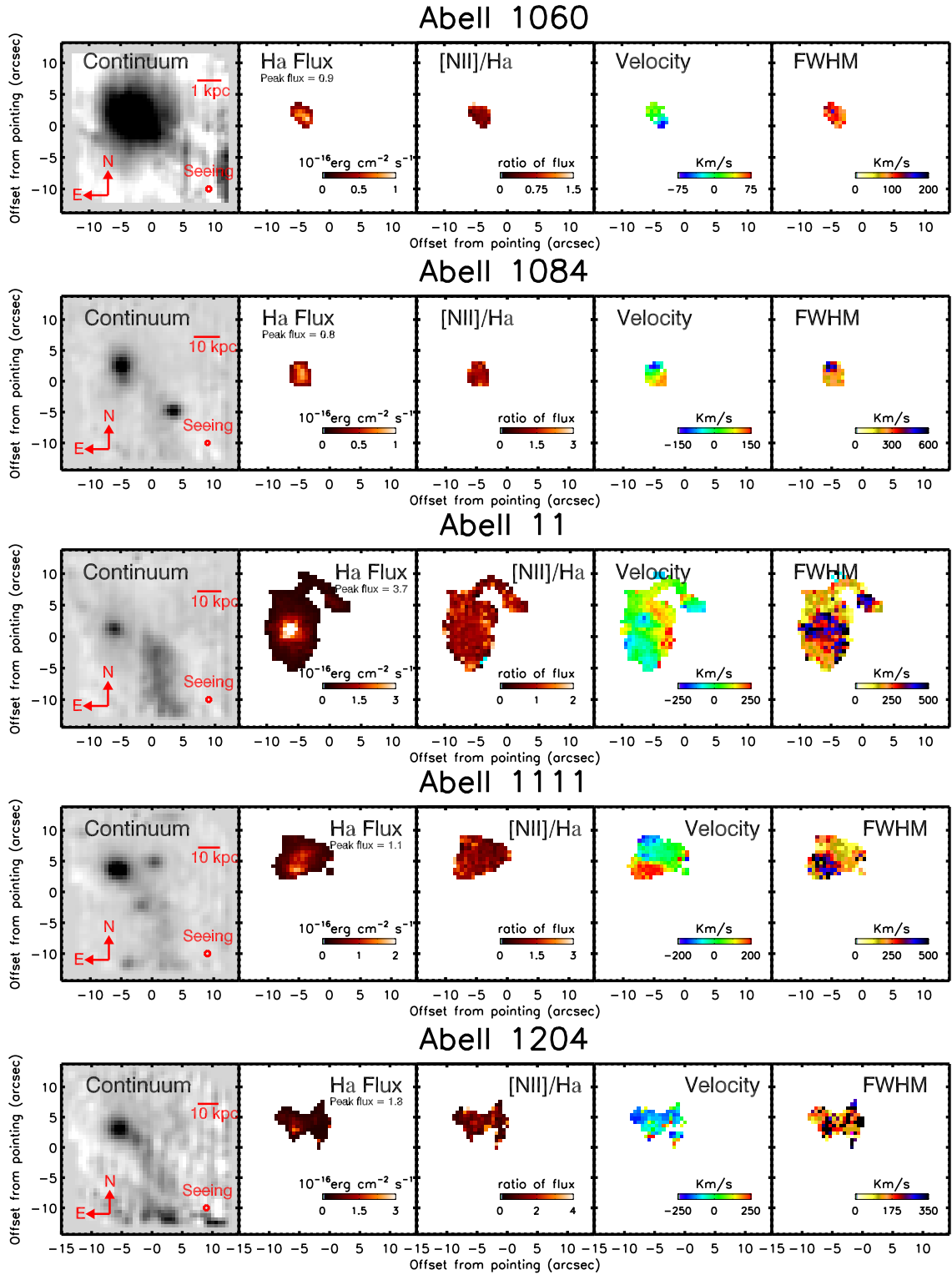
Figure 3.2: Maps of the spectral fits to the VIMOS data cubes for all 73 objects in the sample. From left to right the panels are: 1) A continuum image created by collapsing the cube over a wavelength range free of emission and sky lines, 2) The Hα flux map, 3) A map showing the ratio of [NII] to Hα flux, 4) the line of sight velocity profile of the Hα and [NII] emission, 4) the Full width at half maximum of the emission line deconvolved for instrumental resolution. For systems in which the Hα line appears self absorbed the flux, LOS velocity and FWHM are plotted for the [NII] line.
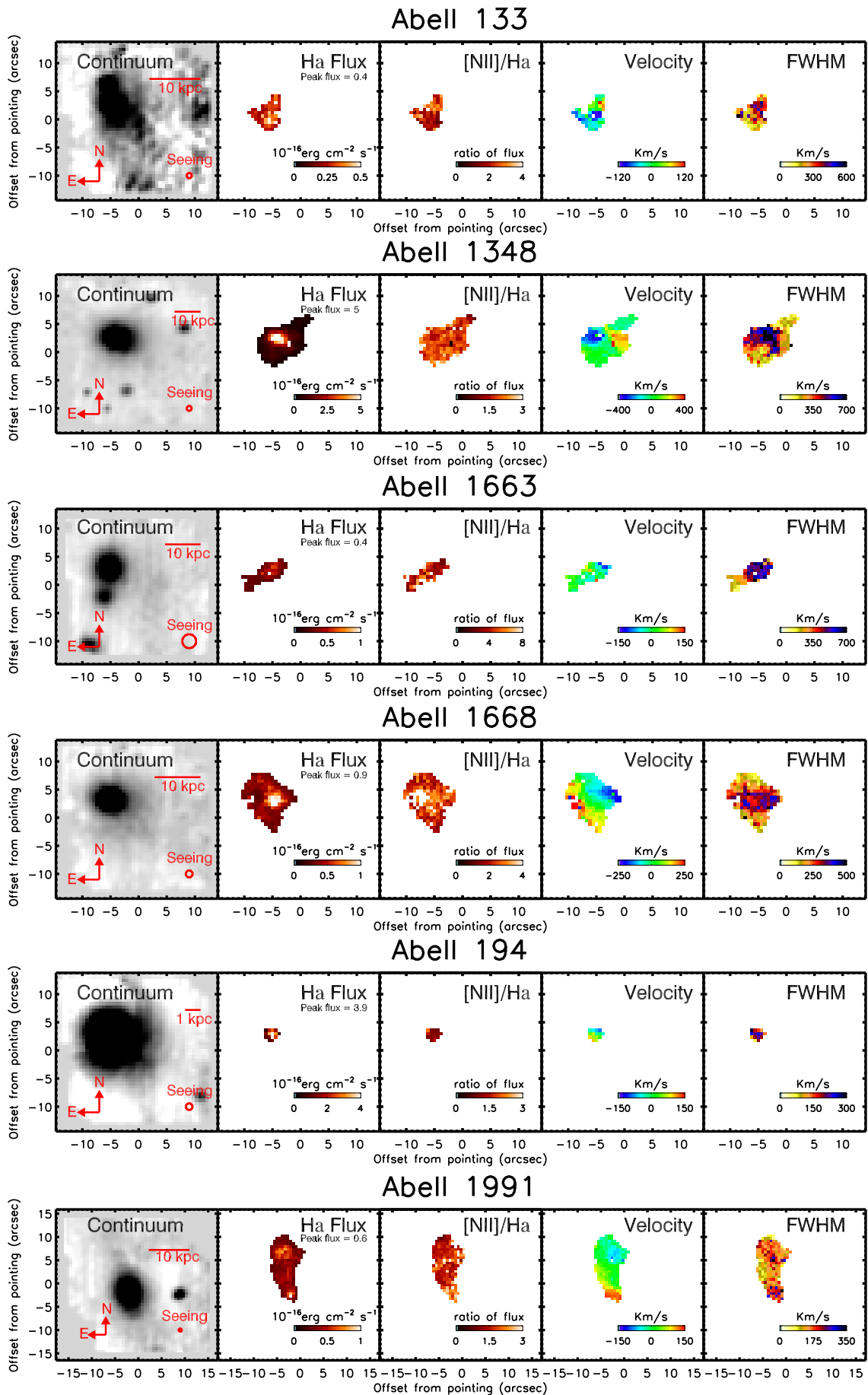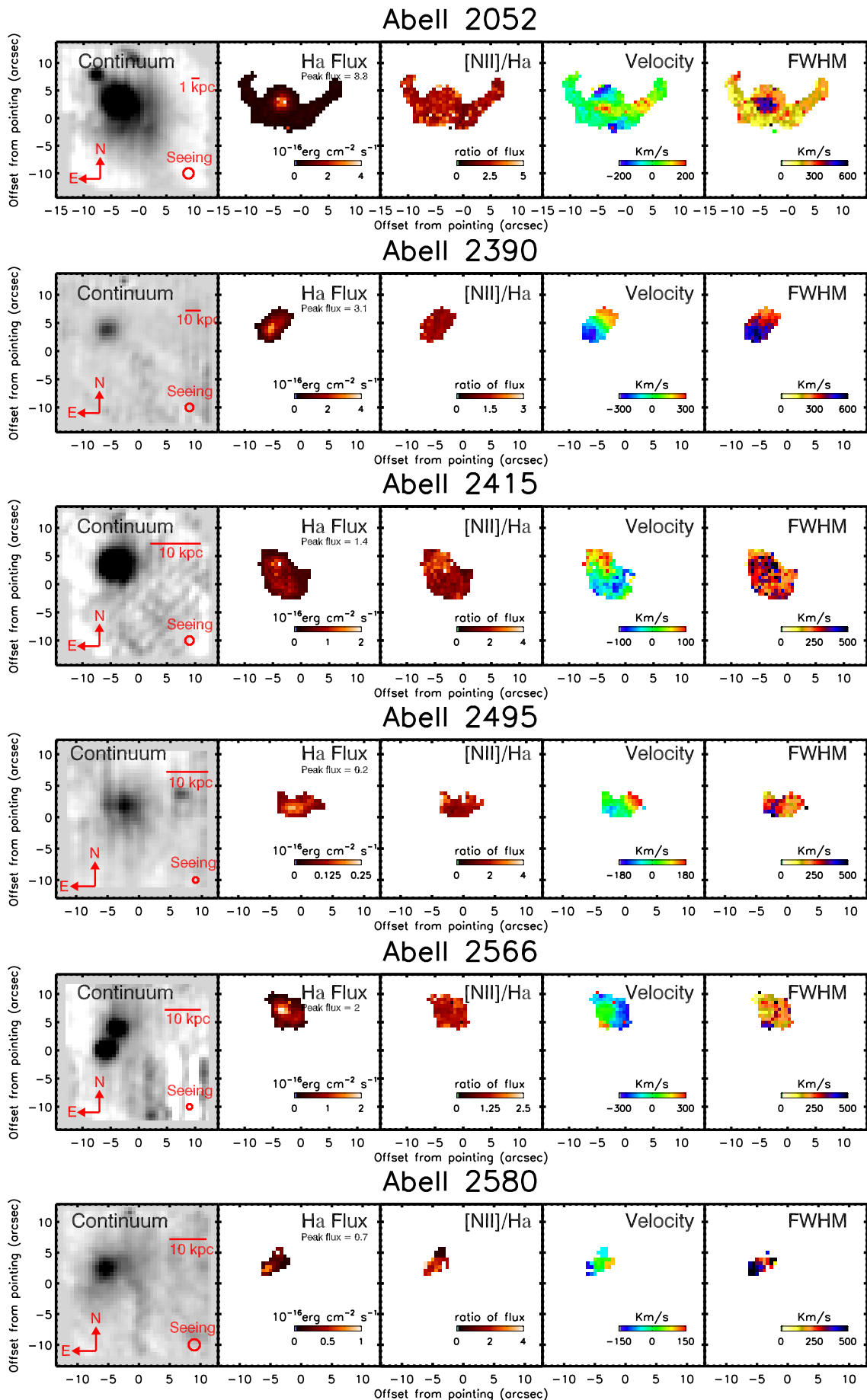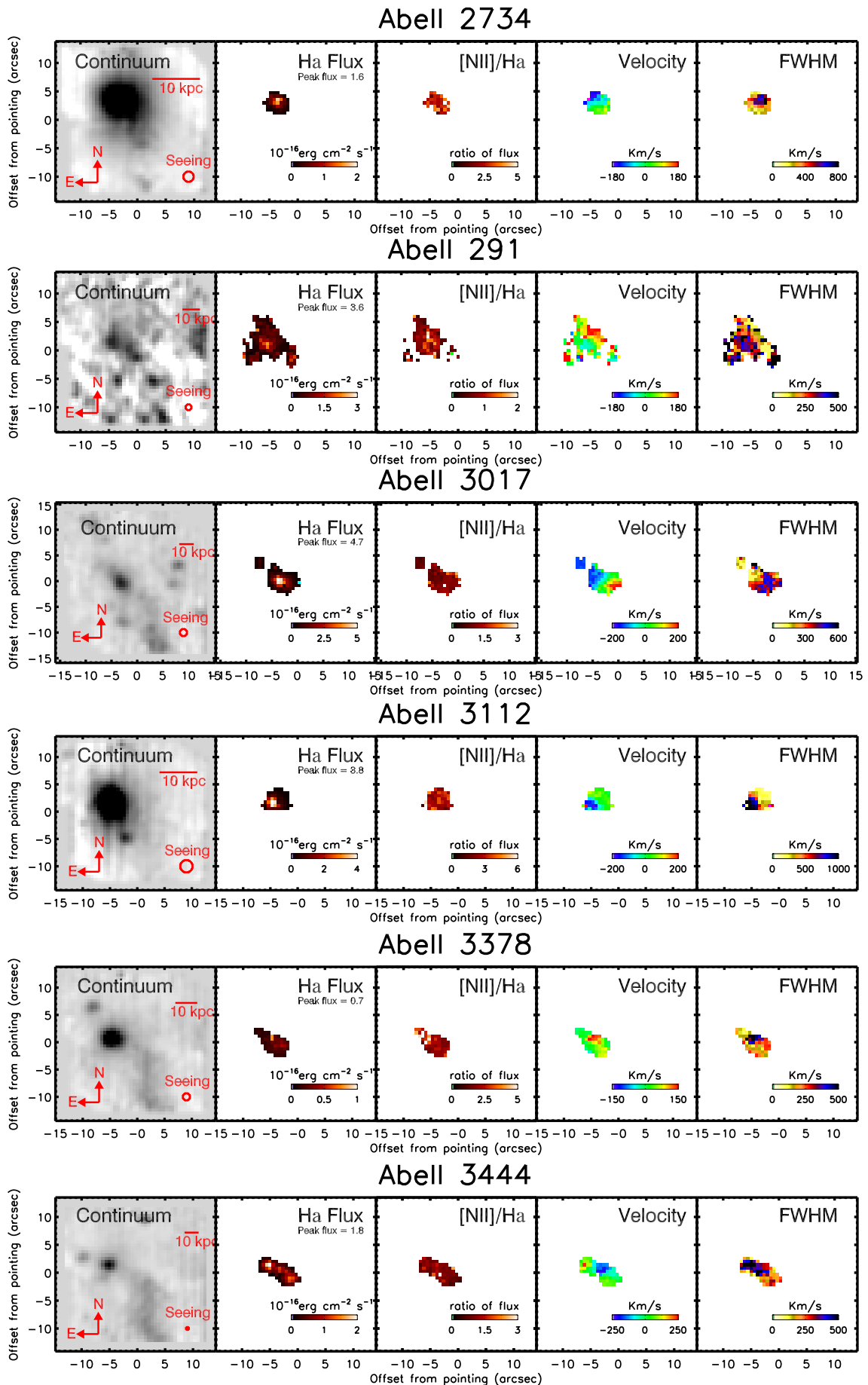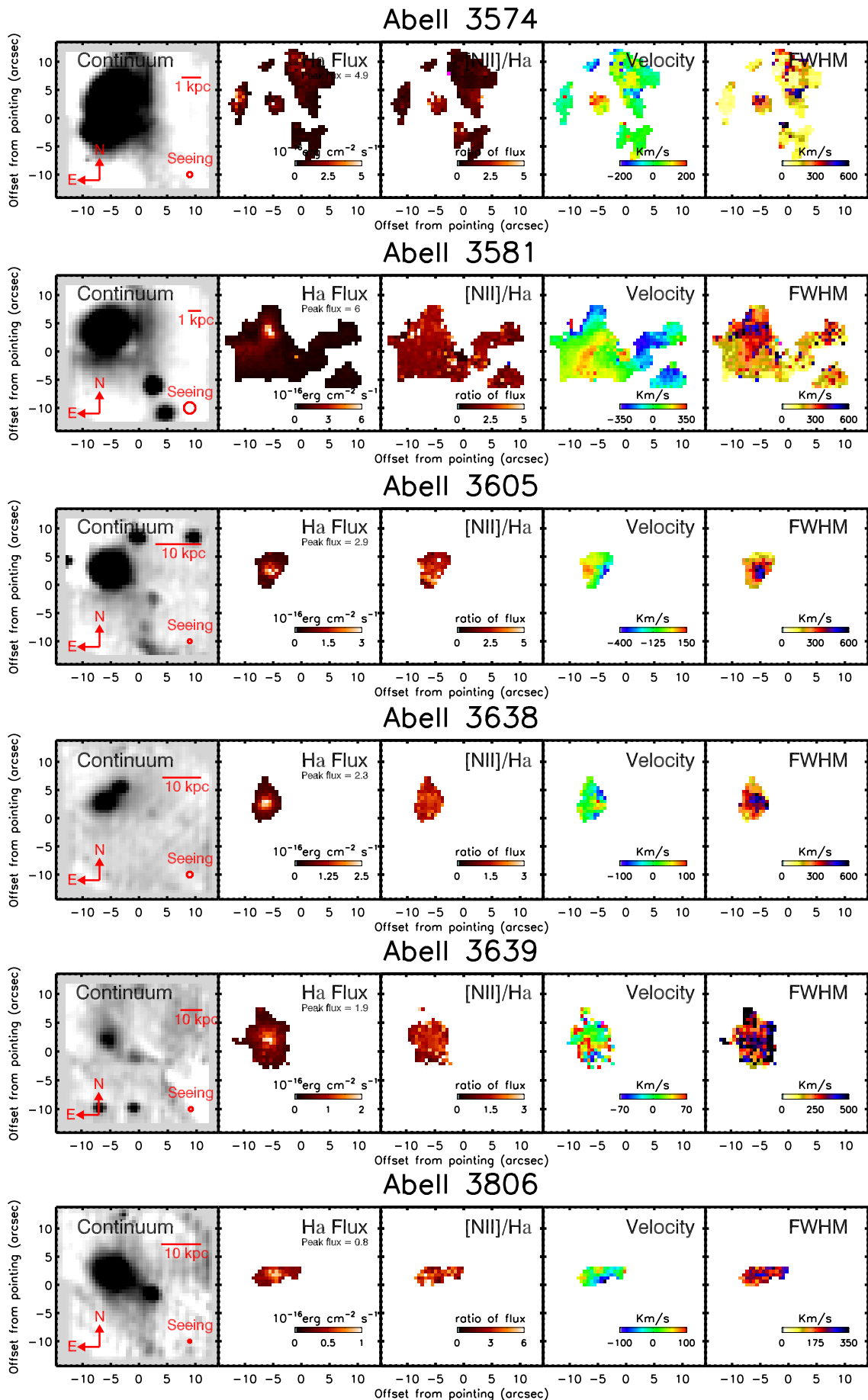
Abell 133

Abell 1348

Abell 1663

Abell 1668

Abell 194

Abell 1991

Figure 3.2: continued.

Figure 3.2: continued.

Abell 2734

Abell 291

Abell 3017

Abell 3112

Abell 3378

Abell 3444

Figure 3.2: continued.

Abell 3574

Abell 3581

Abell 3605

Abell 3638

Abell 3639

Abell 3806

Figure 3.2: continued.

Figure 3.2: continued.

Figure 3.2: continued.

NGC 533

NGC 5813

NGC5846

RXCJ0120.9−1351

RXCJ0132.6−0804

RXCJ0331.1−2100

Figure 3.2: continued.

RXCJ0543.4−4430

RXCJ0944.6−2633

RXCJ1257.1−1339

RXCJ1304.2−3030

RXCJ1436.8−0900

RXCJ1511.5+0145

Figure 3.2: continued.

RXCJ1524.2−3154

RXCJ1539.5−8335

RXCJ1558.3−1410

RXCJ2014.8−2430

RXCJ2101.8−2802

RXCJ2129.6+0005

Figure 3.2: continued.

RXCJ2213.0−2753

RXJ0000.1+0816

RXJ0338+09

RXJ0352.9+1941

RXJ0439.0+0520

RXJ0747−19
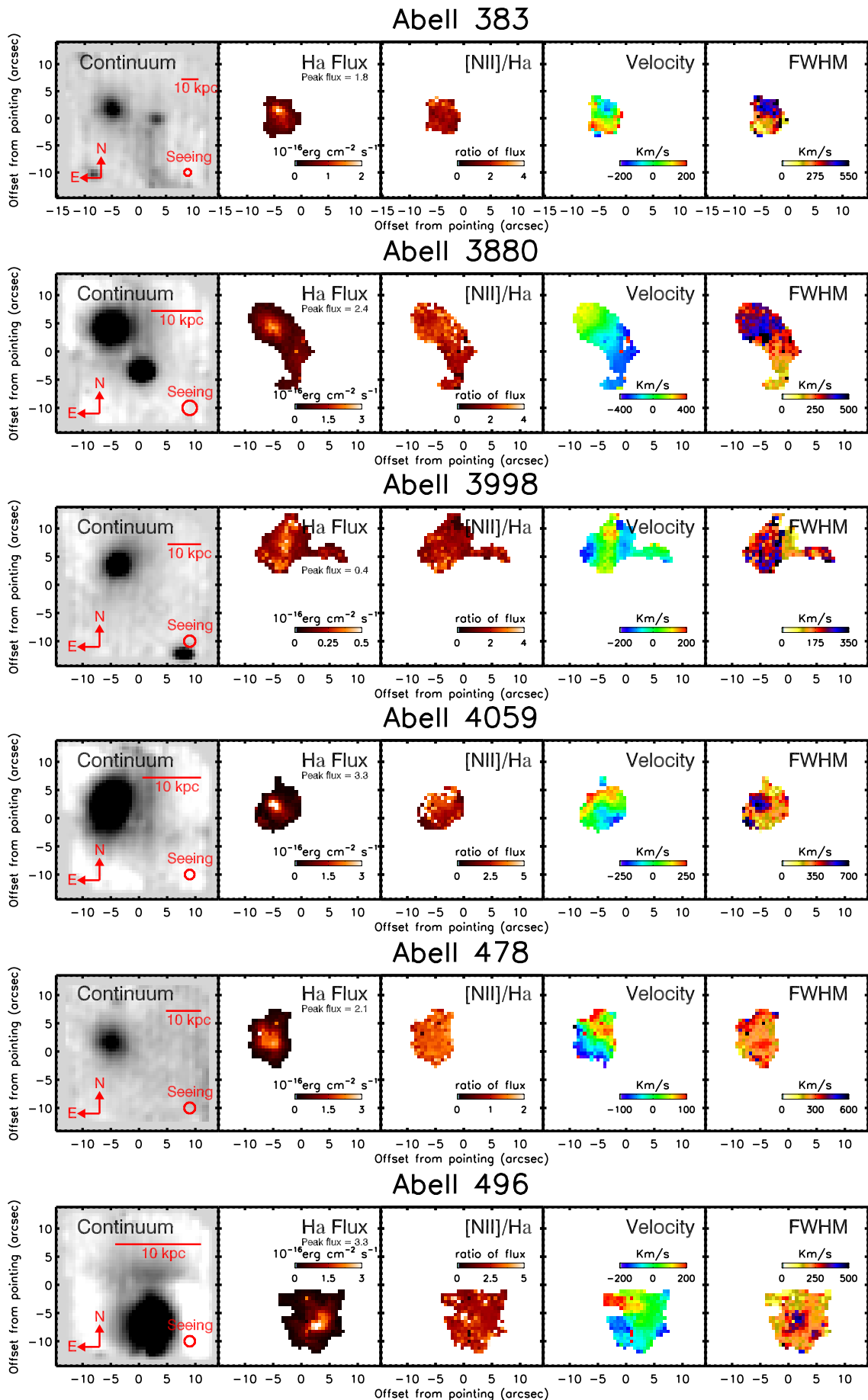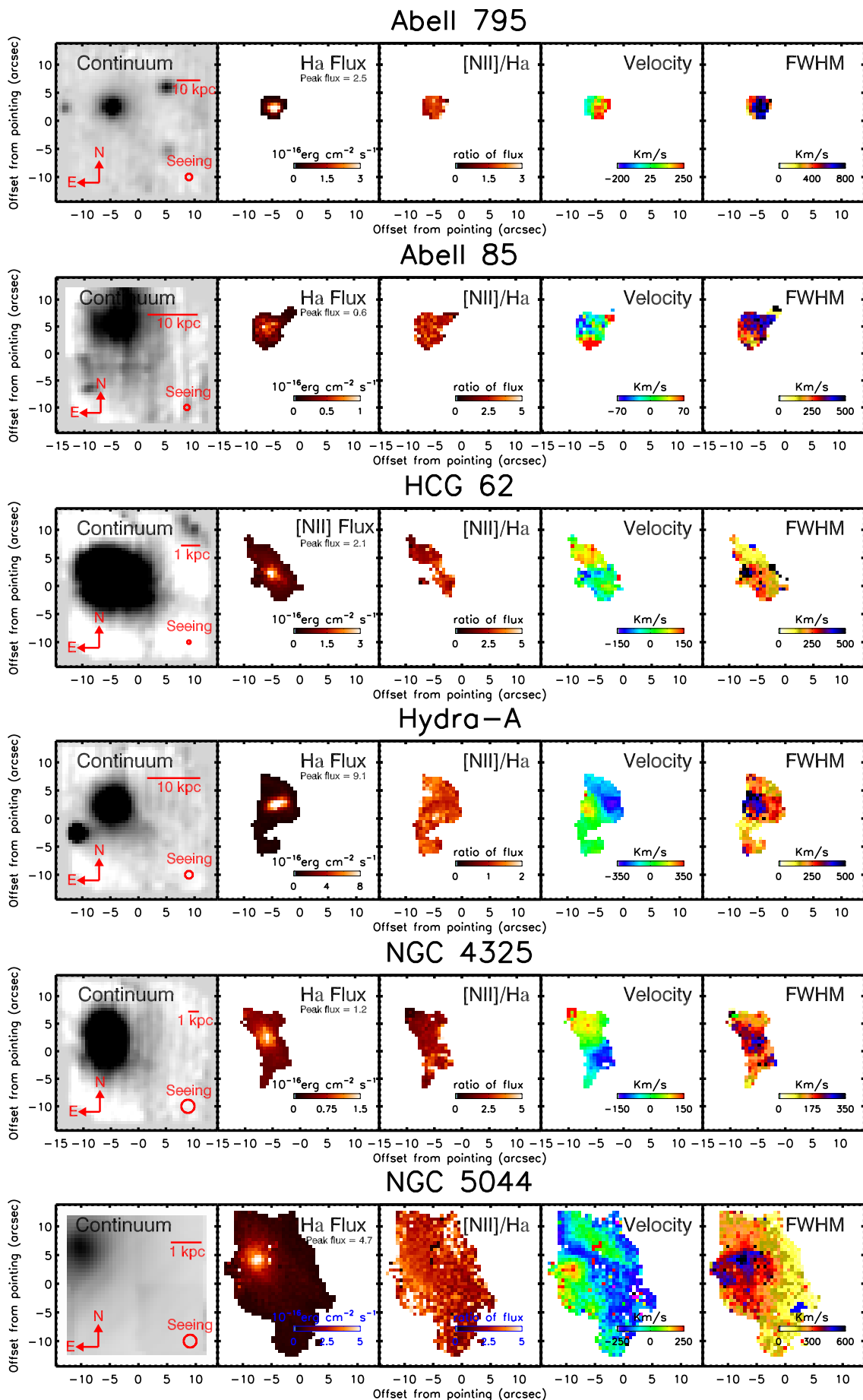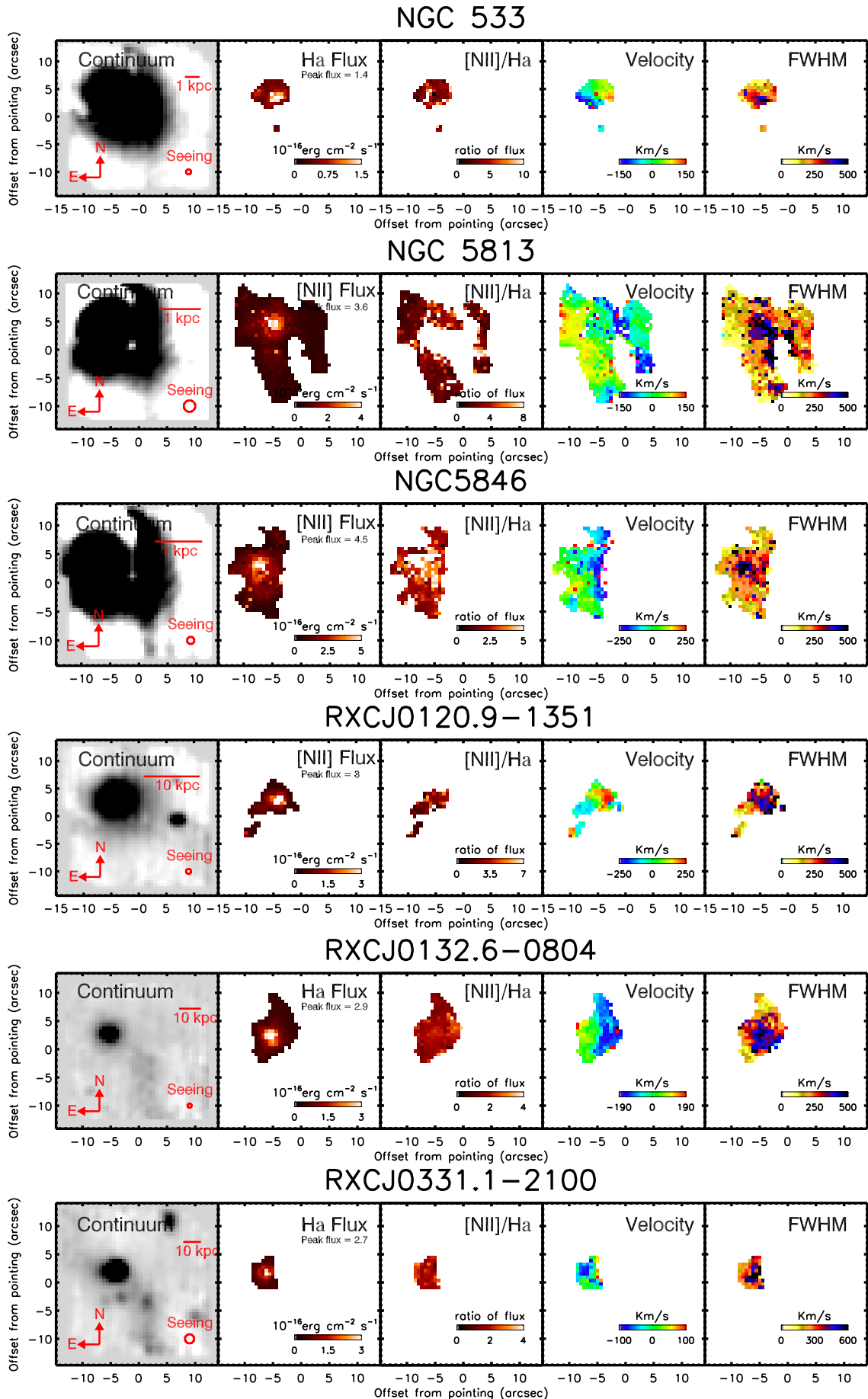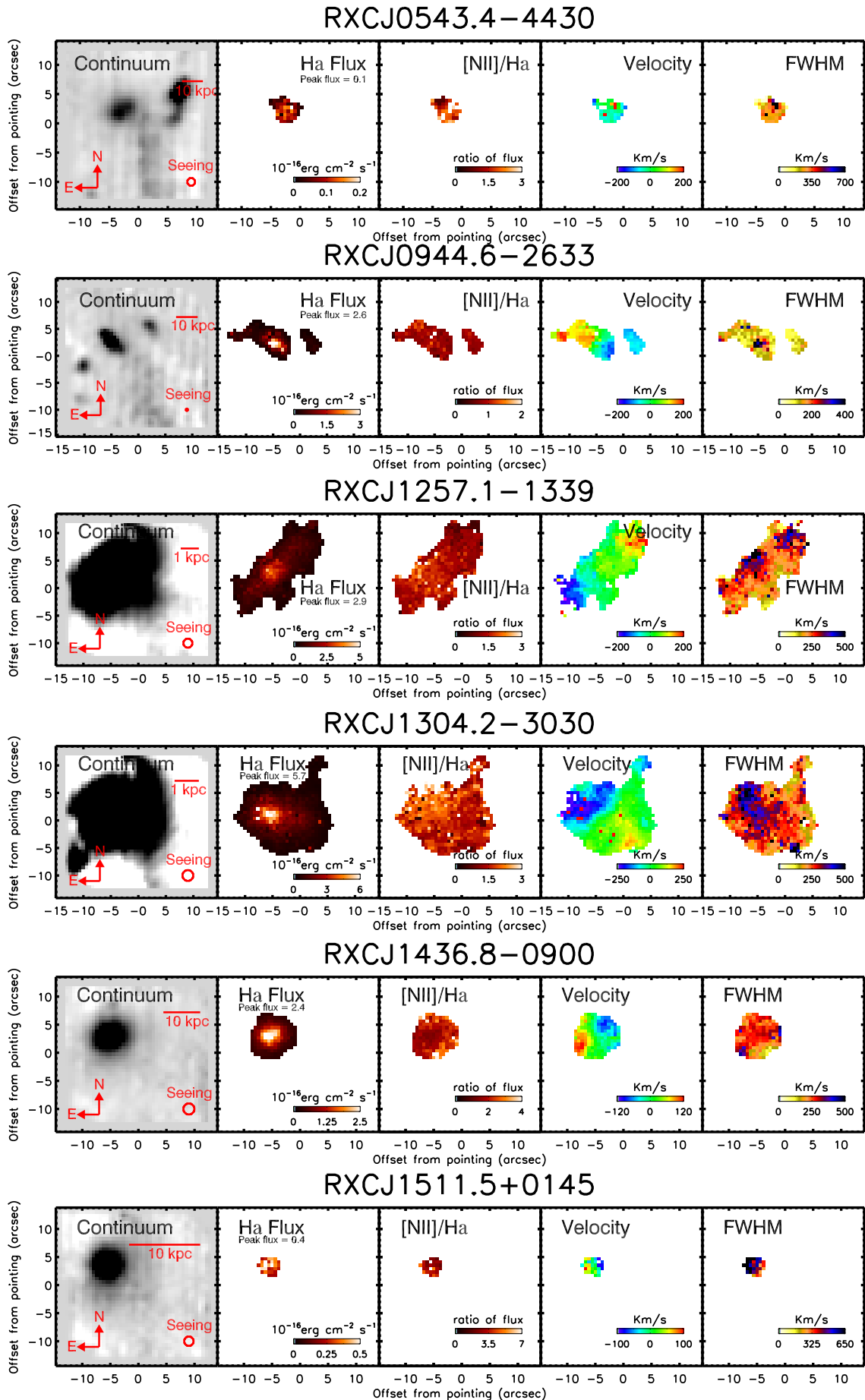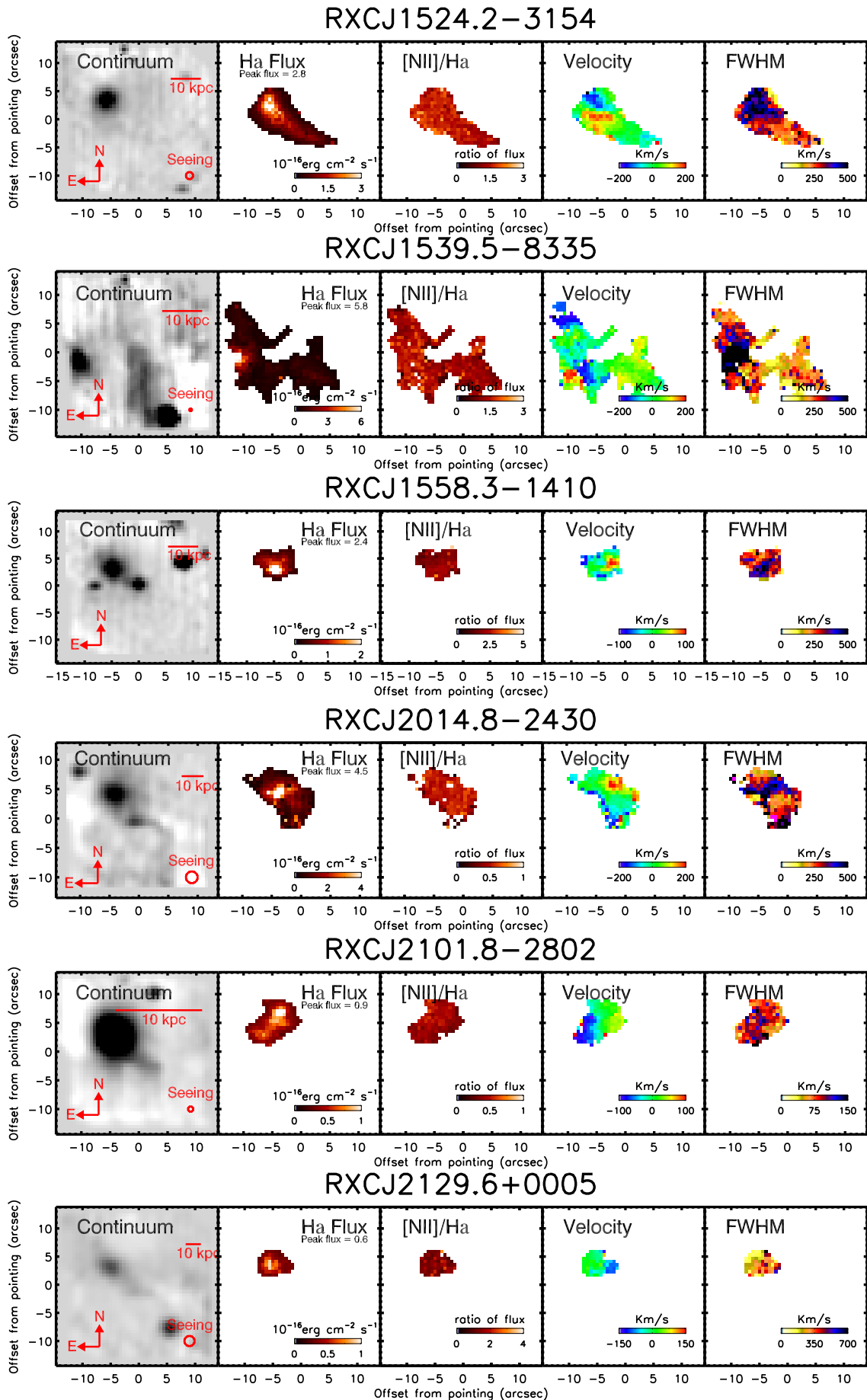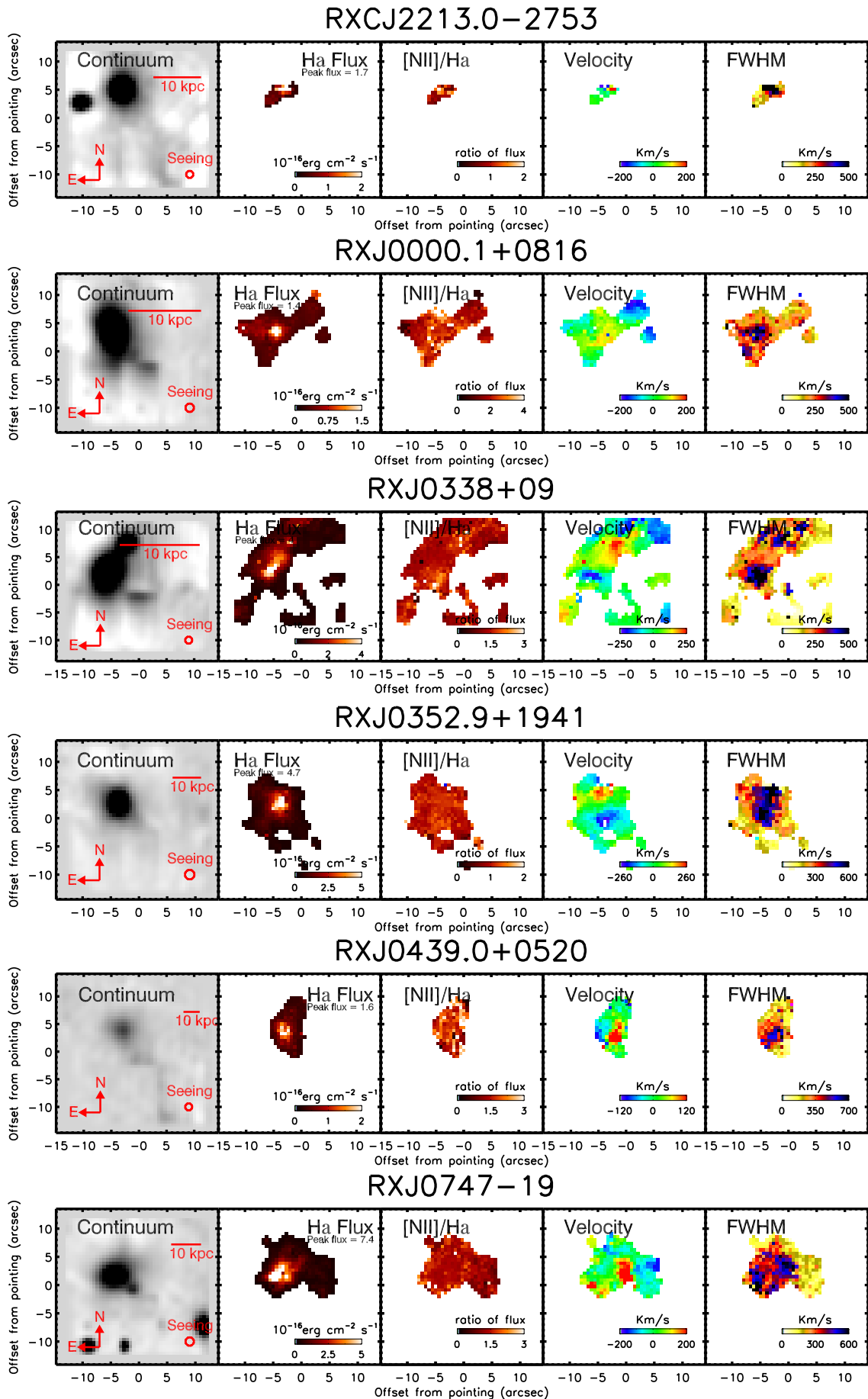
Figure 3.2: continued.
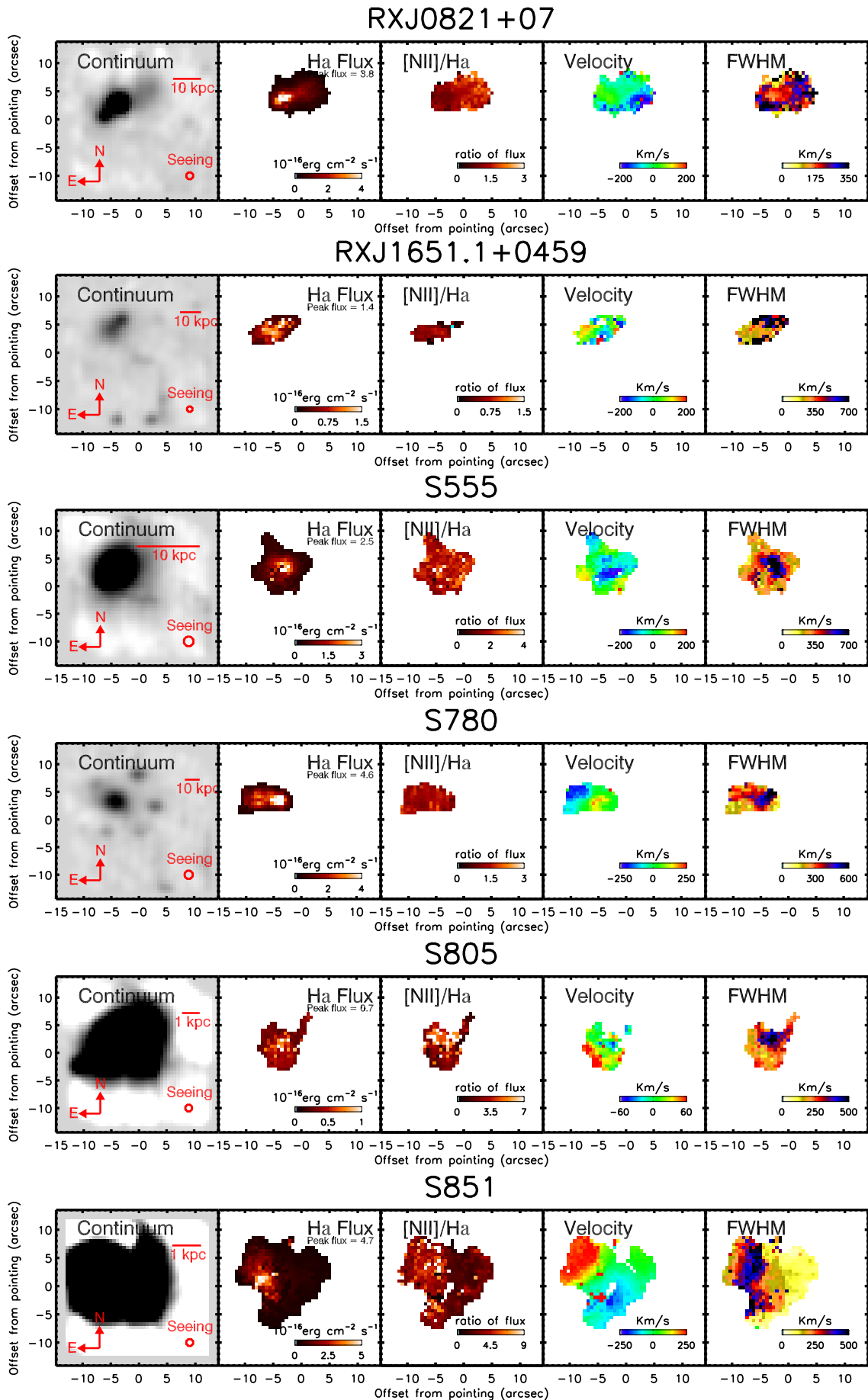
Figure 3.2: continued.
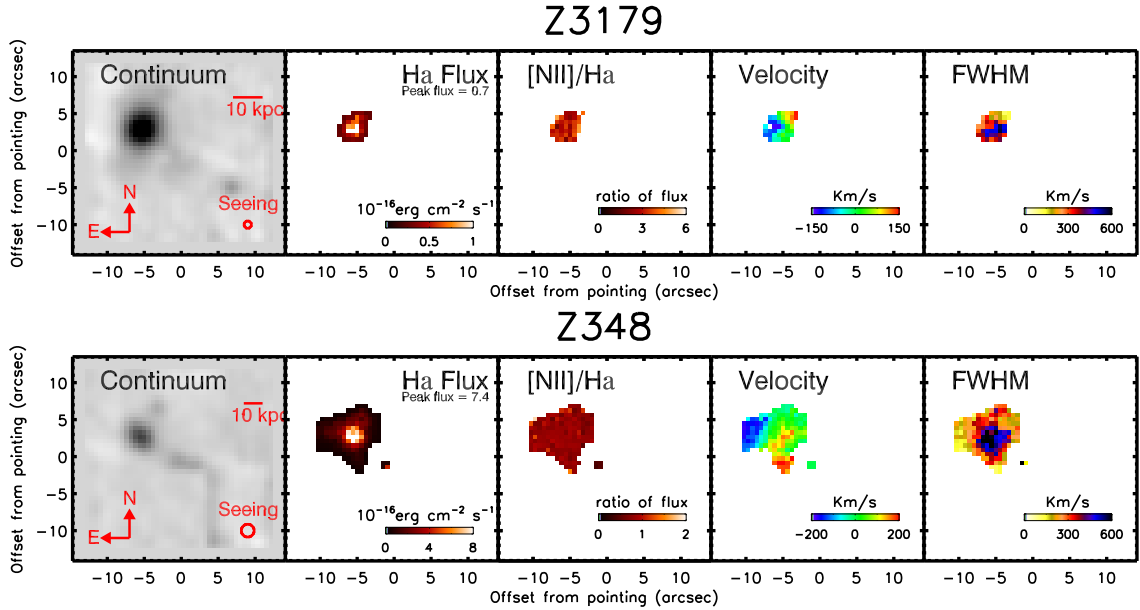
Figure 3.2: continued.

3.3.1 Hα morphology

From the maps shown in Figure 3.2 we can calculate the extent of the line emitting region for each object. We define the major axis to be the maximum length of continuous emission (at greater than 7σ) along a line drawn through the peak of the Hα emission (throughout this thesis we use extent and major axis interchangeably). The minor axis is then the maximum length of continuous emission perpendicular to the major axis (also through the peak of the Hα). This definition assumes that the distribution of Hα emission is well approximated by an ellipse. This is clearly not the case for all objects in the VIMOS sample though it is a good approximation to regions of uniform Hα distribution in most systems. We note however, that it is also important to characterize the overall distribution of the emission for those objects which are extended. As can be seen from Figure 3.2 the Hα morphology varies greatly from system to system. We categorise these morphologies into five distinct groups. It is important to note that the definitions are not all mutually exclusive, as such it is possible that a single object may exhibit a morphology which is consistent with two or more of the definitions given below. The classification assigned to each object in the sample can be found in Table 3.2.

Compact objects Compact objects are defined as objects in which the minor extent of the Hα emission above a significance of 7σ is less than twice the mean

of the DIMM seeing during the observation of that object. The selection criteria of the VIMOS sample required that every objects have an extent of more than 2" in the FORS spectra. As such very few objects should fall into this definition however we include it to account for observations taken in very poor seeing conditions. It is important to note that this definition of compact makes no consideration of the physical scale of the objects. However, it is an important classification as any apparent spatial variations along the minor axis seen for such objects cannot be believed. Objects are given this classification are also classified according to the structure seen along their major axis unless this too if less than twice the seeing.

Quiescent objects Objects classified as quiescent have Hα emission which is extended beyond twice the seeing and shows a simple elliptical and centrally concentrated morphology. The peak of the Hα emission must lie within the mean seeing of the peak in the continuum and the Hα flux must fall off uniformly as the continuum does (though not necessarily at the same rate as the continuum). Objects with a Hα morphology of this type are likely to be very relaxed with no major events having occurred recently enough to have disturbed the gas.

Plumes An object is classified as having a plume when the Hα emission shows a clear extent in one preferential direction which is not shared by the continuum emission. Typically with this type of object the peak of the Hα emission also shares the extent and shape of the plume which results in the peak of the Hα emission being slightly offset from the peak in the continuum. This offset is never a large physical separation ($\lesssim$ 7 kpc) but is an important parameter to distinguish plumes from quiescent objects in which Hα emission is only detected to one side of the BCG, the latter showing no offset larger than the mean seeing. For some objects classified as plumes a possible companion galaxy is present in the VIMOS field of view. For some such objects the plume can clearly be seen to extend towards the companion bridging the gap between the BCG and the companion (see Abell 3880 in Figure 3.2 for a prime example of this) suggesting the possibility that such plumes are caused as the result of an interaction.

Offset objects Objects classified as offset show a Hα morphology in which either
all of the emission is offset from the peak of the continuum or that have a
second Hα peak which contains the majority (> 50%) of the Hα flux that
is substantially offset from the BCG (> 8 kpc). Although we classify both
of these definitions as offset they show distinctly different Hα morphologies.
The objects which are completely offset from the centre of the BCG appear
to be otherwise quite similar to quiescent objects in their morphology. The
latter kind however appear morphologically more consistent with plumes with
a clear extent of the low surface brightness Hα emission extending in a single
preferential direction. However, there are two key differences to plumes. First,
the extent seen in the low surface brightness emission is not shared by a similar
structure in the bright emission as is the case with plumes. Secondly, those
which are classified as offset have a second peak in the Hα emission which is
positioned at the end of the extended region of low surface brightness emission,
away from the BCG. For a more detailed analysis of nature of this offset
emission see Chapter 4.

Disturbed objects The final morphological classification we present are disturbed
objects. These are objects where the Hα flux typical peaks close to the peak
of the continuum but have lower surface brightness Hα emission which is ex-
tended and forms non-uniform structures around the BCG. This classification
of objects essentially includes all objects which are not classified under one
of the previous four categories. The extended and non-uniform nature of the
Hα emission in this class of objects suggests that some event has disturbed
the cold gas in the core of the cluster causing it to flow away from a uniform
distribution. Some of the objects which fall into this category are systems
which are well known to have active AGN which can be seen to be disturbing
the ICM (for example Abell 2052, Blanton et al. (2011)). This suggests the
possibility that objects which fall into this classification are currently under-
going feedback processes which has resulted in the disturbance of the cold gas
reservoir.

High resolution narrow-band imaging of Hα in cluster cores has shown the pres-
ence of filamentary structures surrounding the BCG. While a few objects in our

sample do show narrow filaments of emission which extend out into the ICM we do not resolve these structures in the majority of cases. Most likely this is a result of the poorer seeing of our observations smoothing the filamentary structures to such an extent that they appear blended as a continuous region of low surface brightness emission extended away from the BCG. A good example of this effect is NGC 5044 which is known to have filaments of Hα emission extended to the south-west of the BCG (David et al., 2011). Comparing to our Hα flux map shown in Figure 3.2 it is possible to see low surface brightness emission extended to the south-west over similar distances to the filaments, however, the details of the filamentary structures are not visible in the VIMOS observation. In the few cases where we do see structures which appear similar to filaments we note that the spatial width of them is substantially higher than those observed with narrow-band imaging. While this may be an effect of the seeing it is impossible to tell without high resolution Hα imaging of these systems.

3.3.2   Excitation state

The [NII] to Hα ratio is a good measure of the excitation state of the gas. Table 3.2 lists the [NII]/Hα ratio for all objects in our sample as calculated from the total spectrum of each. As can be seen from these values the ratio varies substantially between objects. Assuming that the metalicity is approximately the same in all of the objects (a fair assumption for cluster cores given the gas mass is dominated by the ICM at a constant $\sim 1/3$ solar metalicity (Loewenstein, 2004), then this difference in the [NII]/Hα ratio suggests that some objects are substantially more highly ionised than others. As noted earlier some of the objects showed Hα emission which was self absorbed, this will have the effect of artificially rising the [NII]/Hα ratio calculated from fits to the total spectrum. We clearly indicate which objects show Hα self absorption in Figure 3.2 by plotting the [NII] intensity in place of Hα. For these objects the [NII]/Hα ratio calculated and presented in Table 3.2 can at best be considered an upper limit.

Figure. 3.2 shows the maps of the [NII]/Hα ratio for each object in the central panel. For the majority of objects the ratio can be seen to vary within these maps suggesting that the ionisation state is not constant throughout the objects. This

TABLE 3.2.
THE DERIVED PARAMETERS LISTED FOR EACH OBJECT IN THE VIMOS SAMPLE

Cluster	Velocity km s^{-1}	Extent kpc(arcsec)	L$_{H\alpha}$ 10^{40} erg s^{-1}	FWHM km s^{-1}	[NII]/Hα	Morphology
Abell 1060	68 $\pm$ 11	1.24(4.8)	0.043 $\pm$ 0.0086	107 $\pm$ 17	0.7 $\pm$ 0.3	Quiescent
Abell 1084	269 $\pm$ 30	11.34(4.8)	11 $\pm$ 1.8	275 $\pm$ 108	0.9 $\pm$ 0.5	Quiescent
Abell 11	247 $\pm$ 15	29.65(11.4)	70 $\pm$ 6.5	340 $\pm$ 61	0.9 $\pm$ 0.5	Quiescent
Abell 1111	478 $\pm$ 22	22.08(7.8)	33 $\pm$ 3.9	297 $\pm$ 75	1.1 $\pm$ 0.5	Plume
Abell 1204	490 $\pm$ 29	26.49(7.2)	59 $\pm$ 5.4	514 $\pm$ 355	1.7 $\pm$ 0.6	Disturbed
Abell 133	210 $\pm$ 32	7.25(6.6)	1.2 $\pm$ 0.16	308 $\pm$ 14	1.7 $\pm$ 0.2	Plume
Abell 1348	755 $\pm$ 40	18.15(8.4)	46 $\pm$ 6.3	513 $\pm$ 153	1.6 $\pm$ 0.5	Quiescent
Abell 1663	225 $\pm$ 45	14.25(9.0)	1.7 $\pm$ 0.29	526 $\pm$ 120	3.4 $\pm$ 0.4	Quiescent/Compact
Abell 1668	302 $\pm$ 22	11.00(9.0)	4.7 $\pm$ 0.45	339 $\pm$ 28	2.2 $\pm$ 0.7	Quiescent
Abell 194	85 $\pm$ 7	1.11(3.0)	0.50 $\pm$ 0.071	211 $\pm$ 122	0.8 $\pm$ 0.23	Compact
Abell 1991	124 $\pm$ 10	16.43(14.4)	4.0 $\pm$ 0.35	209 $\pm$ 64	1.5 $\pm$ 0.3	Offset
Abell 2052	268 $\pm$ 18	6.57(9.6)	1.8 $\pm$ 0.18	454 $\pm$ 105	2.2 $\pm$ 1.1	Disturbed
Abell 2390	490 $\pm$ 29	26.5(7.2)	109 $\pm$ 15	422 $\pm$ 52	0.95 $\pm$ 0.48	Quiescent
Abell 2415	186 $\pm$ 37	11.38(10.2)	4.5 $\pm$ 0.42	275 $\pm$ 180	1.5 $\pm$ 0.55	Plume
Abell 2495	201 $\pm$ 16	8.99(6.0)	0.56 $\pm$ 0.090	235 $\pm$ 38	1.5 $\pm$ 0.074	Quiescent
Abell 2566	325 $\pm$ 22	10.30(6.6)	9.7 $\pm$ 1.2	172 $\pm$ 74	0.91 $\pm$ 0.56	Offset
Abell 2580	203 $\pm$ 24	9.88(6.0)	2.4 $\pm$ 0.48	340 $\pm$ 157	0.75 $\pm$ 0.55	Compact/Plume
Abell 2734	210 $\pm$ 20	6.46(5.4)	1.1 $\pm$ 0.27	551 $\pm$ 105	2.5 $\pm$ 1.0	Quiescent
Abell 291	294 $\pm$ 70	23.39(7.2)	480 $\pm$ 31	626 $\pm$ 371	0.99 $\pm$ 0.55	Disturbed
Abell 3017	390 $\pm$ 31	25.51(7.2)	110 $\pm$ 17	366 $\pm$ 106	0.62 $\pm$ 0.33	Quiescent
Abell 3112	225 $\pm$ 19	9.51(6.6)	7.1 $\pm$ 1.3	893 $\pm$ 256	1.9 $\pm$ 1.2	Quiescent
Abell 3378	106 $\pm$ 15	20.89(8.4)	6.1 $\pm$ 0.95	422 $\pm$ 170	1.1 $\pm$ 0.39	Quiescent(Filament)
Abell 3444	428 $\pm$ 41	35.76(9.0)	66 $\pm$ 10	394 $\pm$ 140	0.67 $\pm$ 0.54	Offset
Abell 3574	161 $\pm$ 15	1.55(5.4)	0.88 $\pm$ 0.061	82 $\pm$ 16	0.56 $\pm$ 0.37	Disturbed
Abell 3581	464 $\pm$ 19	5.50(12.6)	2.4 $\pm$ 0.14	379 $\pm$ 69	1.6 $\pm$ 1.0	Disturbed
Abell 3605	269 $\pm$ 20	7.42(6.0)	4.5 $\pm$ 0.72	484 $\pm$ 130	2.4 $\pm$ 1.0	Quiescent
Abell 3638	111 $\pm$ 19	8.74(6.0)	5.9 $\pm$ 0.90	403 $\pm$ 67	1.3 $\pm$ 0.97	Quiescent
Abell 3639	150 $\pm$ 58	18.88(7.2)	56 $\pm$ 4.5	367 $\pm$ 73	1.4 $\pm$ 0.56	Quiescent
Abell 3806	136 $\pm$ 14	5.95(4.2)	3.3 $\pm$ 0.69	231 $\pm$ 52	2.9 $\pm$ 0.88	Quiescent
Abell 383	181 $\pm$ 52	24.58(7.8)	40 $\pm$ 5.0	386 $\pm$ 73	1.5 $\pm$ 0.64	Plume
Abell 3880	444 $\pm$ 20	13.55(12.0)	12 $\pm$ 0.89	438 $\pm$ 50	1.8 $\pm$ 0.95	Plume
Abell 3998	346 $\pm$ 66	18.17(10.8)	7.5 $\pm$ 0.57	253 $\pm$ 137	1.4 $\pm$ 0.18	Plume(Filament)
Abell 4059	396 $\pm$ 46	8.06(8.4)	4.1 $\pm$ 0.48	536 $\pm$ 97	2.5 $\pm$ 2.0	Quiescent

Table 3.2: Here we list the derived parameters for every objects from the VIMOS sample. The velocity column refers to the peak to peak velocity measured across the mean velocity map. The extent is the length of the major axis, The luminosity is calculated only for flux that appears at greater than 7σ significance. The FWHM is measured from the central 1.8×1.8 arcsec and the [NII]/Hα.

Cluster	Velocity	Extent	Hα Flux	FWHM	[NII]/Hα	Morphology
	km s^{-1}	kpc(arcsec)	10^{-16} erg cm^{-2} s^{-1}	km s^{-1}		
Abell 478	176 ± 12	17.33(10.8)	23 ± 2.3	261 ± 32	1.1 ± 0.92	Quiescent
Abell 496	252 ± 8	8.28(12.6)	3.1 ± 0.28	260 ± 46	2.1 ± 1.3	Quiescent
Abell 795	315 ± 38	11.48(4.8)	18 ± 3.7	755 ± 64	1.5 ± 0.85	Quiescent
Abell 85	217 ± 29	8.38(7.8)	1.6 ± 0.20	339 ± 54	2.3 ± 0.47	Quiescent(filament)
HCG62	168 ± 12	3.31(11.4)	0.087 ± 0.011	204 ± 101	3.0 ± 0.53	Quiescent
Hydra-A	556 ± 6	8.08(7.8)	13 ± 1.7	346 ± 58	0.86 ± 0.56	Quiescent
NGC4325	255 ± 10	6.77(13.2)	0.90 ± 0.089	236 ± 34	1.5 ± 0.59	Disturbed
NGC5044	277 ± 18	5.61(30.6)	0.54 ± 0.062	457 ± 99	2.5 ± 0.65	Disturbed
NGC533	211 ± 19	2.74(7.2)	0.19 ± 0.033	376 ± 218	3.1 ± 1.4	Quiescent
NGC5813	223 ± 24	1.51(10.8)	0.044 ± 0.0059	503 ± 81	2.1 ± 0.63	Disturbed
NGC5846	117 ± 12	1.28(10.2)	0.076 ± 0.0056	255 ± 63	3.0 ± 0.88	Quiescent
RXCJ0120.9-1351	345 ± 8	4.75(4.8)	1.5 ± 0.28	361 ± 40	2.2 ± 1.3	Quiescent(filament)
RXCJ0132.6-0804	452 ± 16	24.86(9.6)	43 ± 5.7	434 ± 66	1.5 ± 0.66	Quiescent
RXCJ0331.1-2100	125 ± 38	15.38(4.8)	54 ± 7.6	592 ± 184	1.2 ± 1.0	Quiescent
RXCJ0543.4-4430	245 ± 53	13.49(4.8)	4.7 ± 0.98	259 ± 169	1.9 ± 0.35	Quiescent
RXCJ0944.6-2633	289 ± 8	25.56(10.2)	36 ± 4.4	277 ± 132	0.58 ± 0.40	Disturbed
RXCJ1257.1-1339	468 ± 17	6.84(22.8)	1.4 ± 0.087	274 ± 116	1.1 ± 1.0	Quiescent
RXCJ1304.2-3030	343 ± 17	3.36(15.0)	1.2 ± 0.072	375 ± 41	1.5 ± 0.9	Quiescent(filament)
RXCJ1436.8-0900	199 ± 16	14.65(9.6)	14 ± 1.7	273 ± 14	1.4 ± 1.0	Quiescent
RXCJ1511.5+0145	138 ± 45	5.20(6.6)	0.29 ± 0.062	553 ± 113	3.0 ± 0.40	Quiescent
RXCJ1524.2-3154	310 ± 19	15.75(8.4)	46 ± 3.9	492 ± 47	1.3 ± 1.2	Plume
RXCJ1539.5-8335	333 ± 59	13.76(9.6)	30 ± 2.0	572 ± 123	1.1 ± 0.56	Disturbed
RXCJ1558.3-1410	275 ± 28	13.98(7.8)	22 ± 2.6	465 ± 103	1.2 ± 0.71	Quiescent
RXCJ2014.8-2430	539 ± 13	19.36(7.2)	140 ± 12	462 ± 92	0.78 ± 0.55	Quiescent
RXCJ2101.8-2802	169 ± 10	7.18(10.8)	1.0 ± 0.11	106 ± 17	0.54 ± 0.32	Offset
RXCJ2129.6+0005	157 ± 29	31.26(8.4)	32 ± 4.6	314 ± 64	0.93 ± 0.32	Quiescent
RXCJ2213.0-2753	185 ± 17	3.55(3.0)	0.92 ± 0.32	660 ± 372	1.4 ± 1.1	Compact/Quiescent
RXJ0000.1+0816	128 ± 3	3.73(4.8)	1.9 ± 0.17	388 ± 74	1.7 ± 0.57	Disturbed
RXJ0338+09	388 ± 6	8.64(12.6)	8.3 ± 0.50	327 ± 77	1.1 ± 0.96	Disturbed
RXJ0352.9+1941	244 ± 19	17.81(9.0)	62 ± 5.3	551 ± 45	0.79 ± 0.64	Quiescent
RXJ0439.0+0520	236 ± 54	26.50(7.8)	62 ± 7.1	559 ± 92		Quiescent
RXJ0747-19	354 ± 32	24.92(13.2)	63 ± 6.1	422 ± 83	1.7 ± 0.77	Disturbed
RXJ0821+07	270 ± 20	20.60(10.2)	35 ± 3.7	180 ± 49	0.84 ± 0.49	Plume
RXJ1651.1+0459	309 ± 25	17.70(6.6)	29 ± 4.0	276 ± 152	0.54 ± 0.39	Quiescent
S555	287 ± 20	11.64(13.2)	4.5 ± 0.44	578 ± 234	1.8 ± 1.1	Quiescent
S780	420 ± 17	33.51(9.0)	240 ± 28	490 ± 49	1.1 ± 0.95	Plume
S805	141 ± 22	2.78(9.0)	0.18 ± 0.018	227 ± 59	3.7 ± 0.95	Quiescent(filament)
S851	523 ± 17	3.59(18.6)	0.53 ± 0.039	425 ± 71	3.5 ± 3.1	Quiescent
Z3179	278 ± 15	15.01(6.0)	7.6 ± 1.5	482 ± 82	2.3 ± 0.97	Quiescent
Z348	226 ± 12	42.58(10.8)	390 ± 48	508 ± 71	0.57 ± 0.49	Quiescent

Table 3.2: continued.

is not surprising as sources of ionising radiation (AGN, star formation, etc.) are often seen to be localized to specific parts of a galaxy (AGN are localised to the centre of the galaxy, star formation is often seen to be clumpy rather then uniformly distributed (O'Dea et al., 2010)). These maps are also useful as they clearly indicate the regions of these objects which have substantial Hα self absorption. These regions have [NII]/Hα ratios which are extremely high, falling well off the top end of the colour scale. As such these regions appear as regions which show the presence of line emission (from the [NII] flux map in this case) but which do not show a value for the [NII]/Hα ratio.

While the [NII]/Hα ratio can be used as an indicator of how highly ionised the gas is it unfortunately cannot be used alone to determine the source of the ionising radiation. For this a comparison with other spectral lines, such as [OIII] and Hβ, is required. The other spectral lines present within the cube of each object are listed in Table. 3.1. Importantly we note that some objects do show the presence of [OIII] and Hβ, we study these objects in more detail in Section. 3.9 where their redshift allows.

3.4   Mean velocity profiles

The mean line of sight velocity (from here on the mean velocity) profiles are shown for each object in the maps in Figure 3.2. As can be seen from these maps the ionised gas in many of the cluster cores studied show a clear velocity gradient from negative to positive velocities relative to the systemic velocity. This velocity gradient is often seen to run across the bright peak of the line emission. Such an ordered and coherent velocity profile is often indicative of rotation but can also arise from uniformly entrained or out flowing material with an inclination to the plane of the sky. These velocity profiles and their possible link to rotation are discussed in greater detail in Chapter 6.

The maximum velocity difference across the line emission is given in Table 3.2. To calculate this the velocity maps were first median smoothed to eliminate any pixels with extreme velocities relative to their surrounding pixels. A 1.8 arcsec wide slit was then placed on the map centred on the peak of the line emission, in the case of objects with offset emission we use the peak of the continuum instead. This slit

is then rotated through 180° in 6° increments about the peak. At each position a profile of the velocity map was extracted by interpolating along the slit at 0.6 arcsec increments, the profile was then smoothed to 1.8 arcsec to reduce the noise. The profile with the maximum peak-to-peak velocity across the centre of the emission is the value given in Table 3.2.

Within the more extended and disturbed objects the velocity maps are much less ordered. However, under closer scrutiny many of these objects do still often show ordered velocity structures on smaller scales close to the centre of the system (defined by the location of the Hα peak). The bright central region of these systems show a coherent velocity structure with a strong gradient across the centre of the system. Away from this central region however, in the lower surface brightness extended emission the velocity field becomes much more chaotic. Abell 3581, NGC 5044 and RXJ 0338+09 are three good examples of such objects, each show extended low surface brightness emission with no coherence to the velocity structure. However, in the regions close (within $\sim$ 8 arcsec) to the peak of the emission the velocity is much more ordered. If it is the case that the extended emission is the result of some event which has disturbed the distribution of the cold gas then this small scale velocity structure may represent the overall velocity field of the object. Any event which disturbed the cold gas would initially affect the low density gas at the edges of the distribution. The disturbance can impart a velocity on this gas which is not consistent with the overall velocity field of the system. The densest gas however, is much more difficult to displace (Churazov et al., 2002) and, if it remains relatively undisturbed, should retain its previous velocity, which should be governed by the global velocity of the cluster core.

3.5   Velocity dispersion

The width (FWHM) of an emission line is a measure of the velocity dispersion of the gas from which it was emitted. In observations with ordered motions (such as a difference in the mean velocity) the velocity dispersion is a measure of the random motions of the particles which make up the gas. There is of course some care required in this interpretation as it requires the assumption that the variation of any ordered velocity field, within the region the line is emitted from, is negligible compared to the

random velocities within that same region. For IFU observations with a reasonable spatial and spectroscopic sampling this is generally the case for observations at low redshift except in the case of very high velocity gradients observed in poor seeing conditions. As such this assumption should be true for most of the systems in our VIMOS sample.

The line width (FWHM) maps for all objects in our sample are shown in the far right panels of Figure. 3.2. Most of the objects show a line width profile which peaks towards the centre of the system, where the flux maps peaks, and falls away as the surface brightness of the line emission does. This line width profile is exactly what is expected as in the central regions there should be more gas along the line of sight, which in turn allows for random motions which can contribute to the velocity dispersion. More interestingly some objects show additional peaks in the line width away from the central point suggesting the gas is more kinematically disturbed in these regions. Indeed the fact that most of these offset line width peaks appear in systems with disturbed morphologies (Abell 3574, RXJ 0338+09) would seem to support this assumption.

The spatially resolved nature of IFU observations makes a global measure of the velocity dispersion somewhat meaningless. The maps in Figure 3.2 clearly show that in most objects the line width varies considerably throughout the system. Also as previously mentioned the mean velocity profiles show substantial ordered variation which would artificially broaden the line width of the system if it is considered as a whole. As such in Table 3.2 we give the average line width measured within the central 1.8×1.8 arcsec region of the system. This definition should eliminate the effect of blending with the mean velocity in most systems allowing the variation of line width between systems to be compared.

3.6 Sample Statistics

In this section we will now look at what can be learned about the ionised gas within cluster cores when we consider the VIMOS sample as a whole. The objects in the sample showed a wide variation in both the peak–to–peak velocity (Table. 3.2) and extent of the emission. If the velocity field of each object was roughly consistent, then any observed peak–to–peak velocity difference between them would simply be

the effect of the gas sampling different regions of the velocity distribution. This would present itself as a clear trend between the extent of the line emission in a given object and the magnitude of the velocity difference observed.

In Figure 3.3 we show the peak–to–peak difference of the mean velocity field plotted against the maximum continuous extent of the line emission along the same direction as the peak–to–peak velocity was found. From Figure 3.3 it is apparent that for very compact objects the peak–to–peak velocity may be dependent on the extent of the velocity field sampled by the line emission. This lower velocity difference in very compact objects may be real, however, we note that very compact objects are much more susceptible to blurring caused by the seeing. If the velocity difference is being measured over a region comparable to the seeing it is possible that gas at each peak may be blended with some emission from the other peak, this would have the net result of shifting the best fitting models closer together thus reducing the measured velocity difference. For the most extended objects shown in Figure 3.3 there is no clear trend between velocity difference and extent. Greater than an extent of ~ 2 kpc the median velocity difference of the objects remains constant at ~ 250 km s^{-1} with a very large scatter. It is important to note however that if the ordered velocity structures seen in the velocity maps in Figure 3.2 are tracing a rotation then the inclination of that rotation away from edge–on will reduce the observed line–of–sight velocity, thus affecting the measured peak–to–peak velocity.

The ordered velocity structures seen for the majority of objects in the VIMOS sample are potentially caused by a rotation of the ionised gas within the cluster core. However, it is also possibly the effect of some other, less ordered, bulk motion of the gas (entrainment for example). The average velocity gradient of each system can be calculated from the peak–to–peak velocity difference and the extent over which that velocity difference is measured. On large scales gas rotating under gravity should form Keplerian disk about the centre of mass of the system. The rotation curves of disks are well understood and can be approximated to follow the curve of an arctan function (Courteau, 1997) of the form

$$V(r) = V_0 + \frac{2}{\pi} V_c arctan(R) \tag{3.6.1}$$

where R $= (r - r_0)/r_t$, V_0 is the velocity at the centre of rotation, r_0 is the
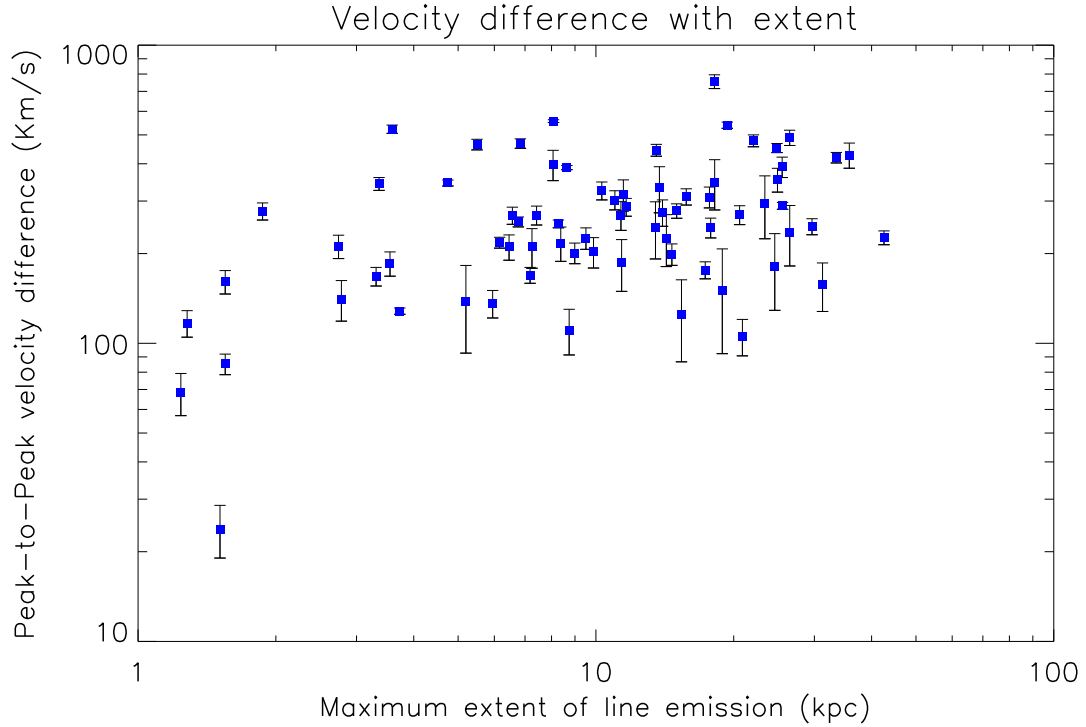
Figure 3.3: Here we plot the peak–to–peak velocity difference against the measured extent of each object. It is clear that there is no trend with the exception that very compact objects show a reduced velocity difference. This suggests that the different peak–to–peak velocities seen between objects in the sample are not simply the effect of having gas sample a larger portion of the velocity field in some objects than in others.

spatial centre of the galaxy, V_c is the asymptotic velocity and r_t is the radius at which the rotation curve transitions from rising to flat. Courteau (1997) show that this approximation provides a good fit to the rotation curves of galaxies. Thus for a rotating disk the velocity at a given distance from the centre of rotation can be assumed to be a function of that distance. As the mean velocity gradient of an object is defined as $\Delta V/\Delta r$ then, if the velocity difference is the result of a rotating disk, the velocity gradient should depend only with the extent over which it is measured. However, a velocity caused by bulk flows of the gas accelerated by means other than rotation should remain relatively insensitive to its radius, thus should have a velocity gradient which depends both on the velocity difference and the distance over which it is measured.

In Figure 3.4 we plot the calculated values of velocity gradient for each object. The top two panels of this figure show the velocity gradient plotted against the two parameters used to calculate it. It can be seen from these plots that the velocity

gradients of each object are well correlated with the extent over which they are measured with a smaller gradient in objects with a larger extent. By contrast the plot showing the velocity gradient against the velocity difference shows no obvious correlation. While a decrease in the velocity gradient with measured radius is what is expected if the velocity profile followed Equation 3.6.1 it can also be explained by random motions of the gas since the extent is the denominator used to calculate the gradient. However, in the latter case the velocity should also play an equal role in the determination of the velocity gradient, thus the gradient would be expected to correlate with both. So the fact that we only see a correlation with the extent is suggestive, though by no means compelling, that the ordered kinematics are the result of gas in a rotating disk. We will further explore the idea that the kinematics are related to a rotating disk later in Chapters 5 and 6. Figure 3.4 also shows a histogram of the mean velocity gradients for each object in the VIMOS sample. From this it can be seen that the velocity gradient for most objects is quite low with the distribution peaking at ~ 20 km s^{-1} kpc^{-1}.

If the assumption that the VIMOS IFU has sufficient spatial resolution to allow us to ignore the effects of blending gas at different mean velocities when calculating the velocity dispersion (see Section 3.5) then we would expect the velocity dispersion and peak–to–peak velocity to be unrelated. However, if the velocity dispersion measured by the fitting routine is subject to broadening through the blending of gas clouds with different mean velocities then we would expect to see some trend. We note that the gradient of the clusters velocity field should be highest in the centre where the mass concentration naturally peaks. It is within this region that the velocity dispersion is most likely to be broadened by the velocity gradient. In Section 3.5 we extracted the average velocity dispersion (FWHM) of the central 1.8 × 1.8 arcsec of each object, this region is comparable to the mean seeing (~ 1.5 arcsec) and is thus the scale on which we would expect the mean velocities to be blended.

In Figure 3.5 we show the average velocity dispersion within the central 1.8 × 1.8 arcsec of each objects plotted against the peak–to–peak of the mean velocity field. If we ignore the points with a peak–to–peak velocity below 100 km s^{-1} this plot would suggest that there is no obvious correlation between the average central
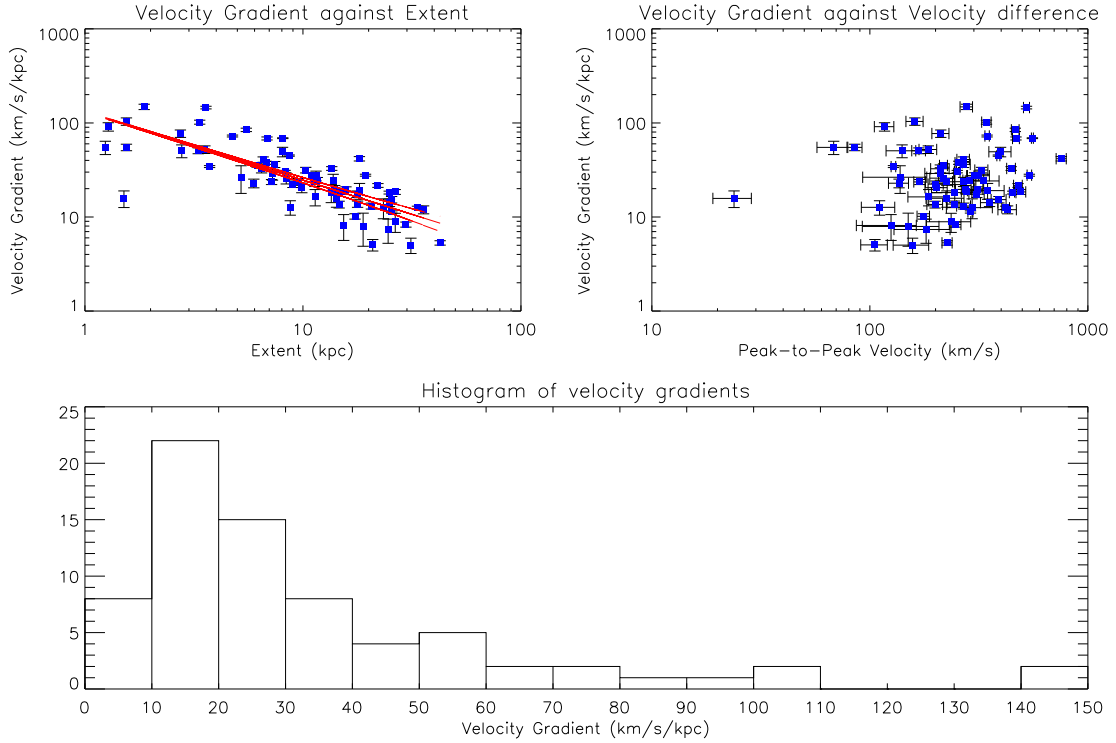
Figure 3.4: *Top Left* - Here we plot the velocity gradient of every object in the VIMOS sample against the extent of the objects line emission. A clear trend can be seen in this plot suggesting that the velocity gradient is dependant on the extent over which it is calculated. Alone this result is not unexpected given how the velocity gradient was calculated. *Top Right* - In this plot we compare the velocity gradient of our objects to the measured peak–to–peak velocity difference. We note that here there is no clear trend in this plot which suggests that the velocity gradient is independent of the peak–to–peak velocity. *Bottom* - This shows a histogram of the velocity gradients calculated for the objects in the VIMOS sample. A clear peak can be seen at ~ 15 km s^{-1} kpc^{-1} with a steady decrease towards higher velocity gradients. This suggests that the velocity gradients seen in the sample are sufficiently small that their effect on the velocity dispersion should be negligible. The combine interpretation from the top two plots is that the velocity gradient responds only to the extent of the gas and is largely unaffected by the velocity difference used to calculate it.

velocity dispersion and the peak–to–peak velocity difference for our VIMOS sample. However, if we include the points with a low velocity difference there is a hint at a possible trend in this data. Due to the low number of data points with a velocity difference below 100 km s^{-1} it is impossible to confirm if this trend is real and even if it is it would be weak suggesting that while the blending of mean velocities does affect the measured FWHM the value is still dominated by random motions within the gas.

The [NII]/Hα ratio can be used as a measure of ionisation state within an ionised
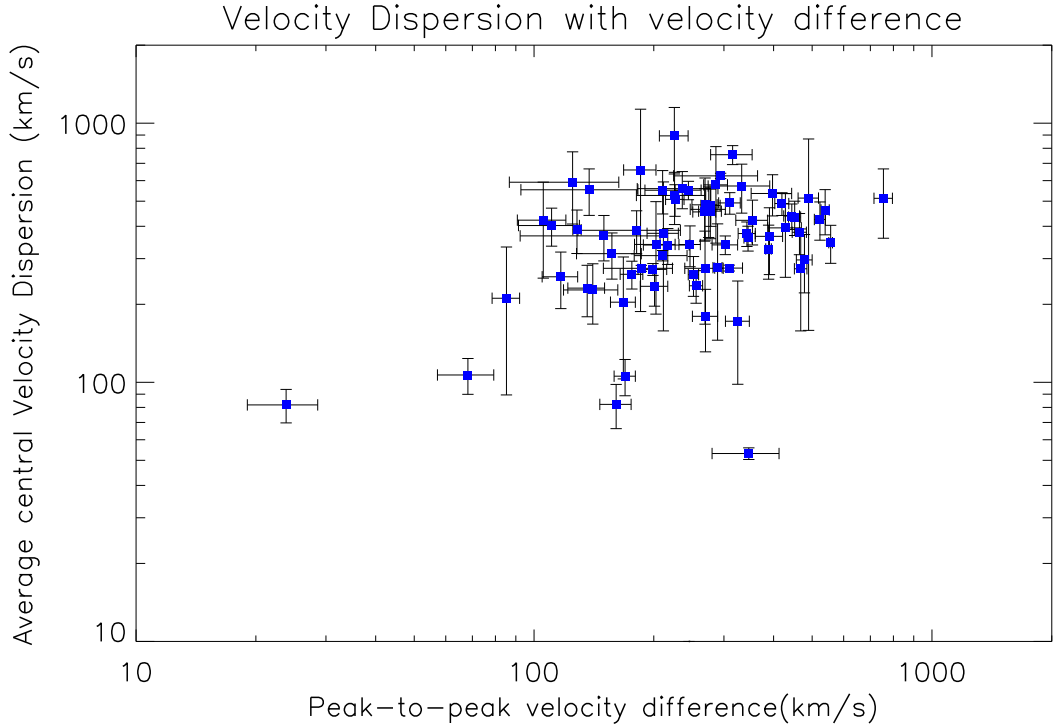
Figure 3.5: Here we plot the central velocity dispersion (FWHM) against the peak–to–peak velocity difference of each object. If the outliers with very low velocity dispersion (< 100 km s^{-1}) and/or low velocity difference (< 100 km s^{-1}) then there is no obvious trend suggesting the velocity dispersion is unrelated to the velocity across the object. This confirms the assumption that the velocity dispersion measured is real and not an effect of blending gas clouds with different mean velocities.

nebula. While alone it cannot be used to identify the source or the ionising radiation it does trace how highly ionised the gas is. The overall ionisation state of every object in the VIMOS sample was calculated in Section 3.3.2. While the maps in Figure 3.2 show a lot of variation of the ionisation state within different regions of each object the maps are very chaotic and do not show any obvious structures. Studying the overall ionisation state allows for a direct comparison between objects and with other global parameters. The ionising radiation within galaxies is believed to come from two primary sources, AGN and star formation (Baldwin et al., 1981). AGN typically produce a harder radiation field which results in a higher ionisation state while star formation has a softer radiation field. Thus one would expect gas ionised by AGN to have a high [NII]/Hα ratio while that ionised by star formation should have a lower value. However, this distinction is more complicated for gas in BCGs where both AGN and star formation are likely to be occurring.

In Figure 3.6 we show the global measure of the [NII]/Hα ratio of each system
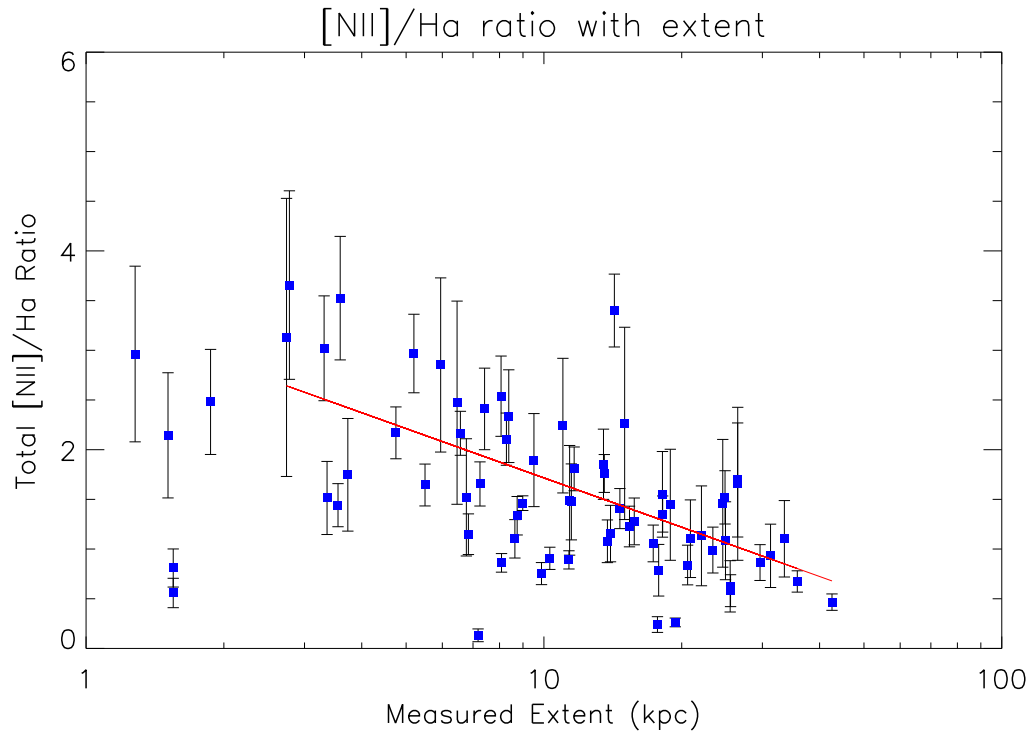
Figure 3.6: Here we show a plot of the overall [NII]/Hα ratio for every object in the VIMOS sample plotted against the extent of the line emitting region. A trend can be seen in this plot (indicated by the red line) which suggests that the overall [NII]/Hα ratio decreases as the extent of the emission line region increases. This suggests that the dominant source of the ionising radiation is harder in for compact objects than for extended ones. Likely the compact objects feel more influence from the central AGN while the extended regions are ionised by star formation.

as a function of the extent of its line emitting region. With the exception of a few outliers this plot shows a clear trend with the [NII]/Hα ratio decreasing as the extent increases. Since the ionising radiation in BCGs likely has contributions from both AGN and star formation (and potentially other sources, soft X-rays from the ICM cosmic rays etc.) this trend can be interpreted as an effect of the relative contributions of each. For very extended objects a lot of gas away from the central AGN is sampled, this gas will primarily be ionised by star formation due to its distance from the AGN. Thus the overall ionising radiation field will be dominated by star formation resulting in a lower [NII]/Hα ratio. By contrast in objects which are very compact we will only sample gas close to the AGN, thus it will have much more influence on the overall ionising radiation field resulting in a higher [NII]/Hα ratio.

In Figure 3.7 we plot the Hα luminosity against the extent for each object. As
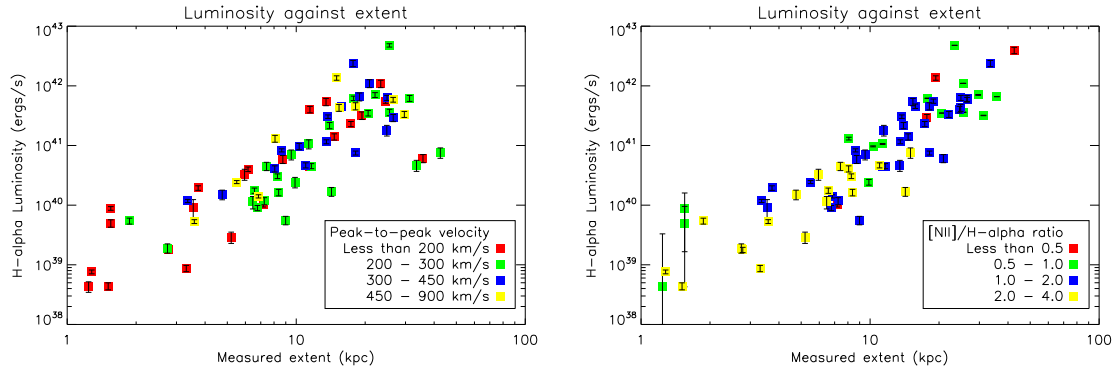
Figure 3.7: The Hα luminosity plotted against the extent of the line emitting region. A clear trend can be seen between the luminosity and extent as would be expected. *Left* - The points are colour coded into bins of peak–to–peak velocity. The velocity shows no clear trend on this plot however, we do note that the most compact (with an extent of less than 3 kpc) and least luminous objects have low velocities with all but 2 falling into the lowest velocity bin. *Right* - The points are colour coded into bins of overall [NII]/Hα ratio. The trend of [NII]/Hα ratio with extent can be seen in this plot. Again we see that the low luminosity compact objects typically have high [NII]/Hα ratios.

would be expected we see a clear trend in this plot with the more luminous objects being more extended. This is most likely a result of extended emission being easier to detect in the most luminous systems due to the increased surface brightness. The points on the plots in Figure 3.7 are also colour coded, on the left by the peak to peak velocity, and on the right by the [NII]/Hα ratio. The left plot of Figure 3.7 shows no general trend of the velocity on this plot, as might be expected from the lack of a trend in Figure 3.3. We do note however that the lowest luminosity ($< 10^{40}$ ergs s^{-1}), most compact objects (extent < 3 kpc) have low peak–to–peak velocities with all but two falling into the lowest velocity bin. The right hand plot of Figure 3.7 shows how the [NII]/Hα ratio varies with the extent and luminosity. Again we note that the objects to the lower left (compact and low luminosity) have quite consistent [NII]/Hα ratios with all but two falling into the highest bin. So collectively from Figure. 3.7 we can identify a collection of objects with low extent and luminosity, little velocity structure and high ionisation states. We would therefore suggest that the majority of the objects in Figure 3.7 below an Hα luminosity of $\sim 4 \times 10^{39}$ ergs s^{-1} with an extent less than 4 kpc are most likely to be LINERS as expected.

In Figure 3.8 we compare each objects Hα luminosity with its peak–to–peak velocity. There is no trend immediately apparent from this plot as might be expected

given the trend between luminosity and extent, and apparent lack of trend between velocity and extent. However, by binning the objects by luminosity and taking the average velocity in each bin a weak trend becomes apparent (the triple dot dashed line in Figure 3.8. When considering an observed velocity structure it is always important to consider the effects of inclination which can reduce the observed peak–to–peak velocity regardless of the origin of the velocity structure. The most likely inclination to view a velocity structure along, given a heterogeneous population and unbiased sample (a fair assumption for our objects given the minimal selection criteria), is 60 degrees to the plane of the sky. If we assume that the average velocity for each luminosity bin is from objects at this inclination, then we can show how this trend would be affected by the inclination. We selected a number of inclinations which would split the velocity range approximately into quarters, these inclinations are plotted as a series of lines in Figure 3.8. We can see that the same trend shifted to 90° encloses all of the objects in the sample bar one, S851. If we ignore the single outlier then it is possible to account for the different velocities seen in objects with similar luminosities as purely an effect of inclination.

If we assume this distribution in velocities to be a result of the inclination of the system then we can calculate the apparent inclination angle of each system using its luminosity and peak–to–peak velocity. In Figure 3.9 we show a histogram of this apparent inclination for the systems in the VIMOS sample. This plot shows that the velocity structure of the systems are distributed about an apparent inclination of 60° to the plane of the sky. There are very few objects with an apparent inclination around 0° and few with an inclination of greater than 80°. This distribution is consistent with what would be expected for a randomly selected sample. Thus it is possible to explain the differences in velocity at a given luminosity through the effect of inclination.

3.7   Offset Emission

In Chapter. 4 (Hamer et al., 2012) we report on the nature of objects from this sample which show a significant component (> 50 per cent) of their line emission significantly offset from the central BCG. Figure 3.10(top) shows a histogram plot of the apparent visible offset between the BCG and the majority of the clusters line
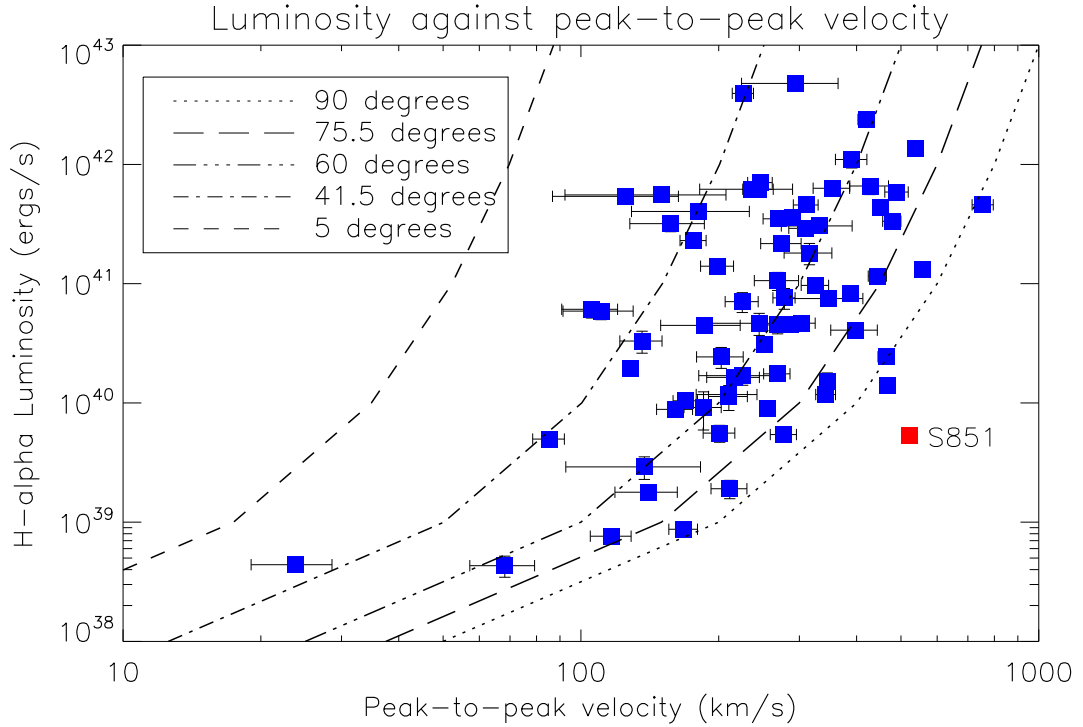
Figure 3.8: The Hα luminosity plotted against the peak–to–peak velocity. It is apparent from this plot that the mean velocity of the sample is dependent on the luminosity. This may be an effect of the more Hα luminous systems being more massive or that we can detect Hα sampling more of the velocity field in the more luminous systems. The lines on this plot show what the velocity would be at a given inclination if we assumed this trend was true and that the most likely inclination of an unbiased sample was 60 degrees from face on. In such a case the velocity of only one object in the sample, S851, cannot be explained by and inclination effect alone.

emission. It can be seen that almost all clusters show a small offset of less than 4" and most well below the seeing limit ($\sim$ 1.5 arc sec). Only one object (A1991) shows an offset of greater than this which makes it clearly stand out amongst our sample. In the bottom panel of Figure 3.10 we present the physical offset of the BCG from the majority of the line emission calculated at the redshift of the host cluster.

We draw three conclusions from this plot, the first is that the majority of the objects still show a small physical offset as is expected. Second, we note that there are now two objects showing a significant offset, one at $\sim$ 10 kpc and one at $\sim$ 12.5 kpc. One of these objects is A1991, the other is Abell 3444 one of the highest redshift objects in our sample (at z=0.2542). While A3444 actually has a larger physical offset than A1991 its higher redshift means its angular offset is only $\sim$ 3 arc sec and is not so obviously separated from the other objects in our sample. Finally, there is a cluster of objects with an offset of $\sim$ 6 kpc, studying the maps of these objects
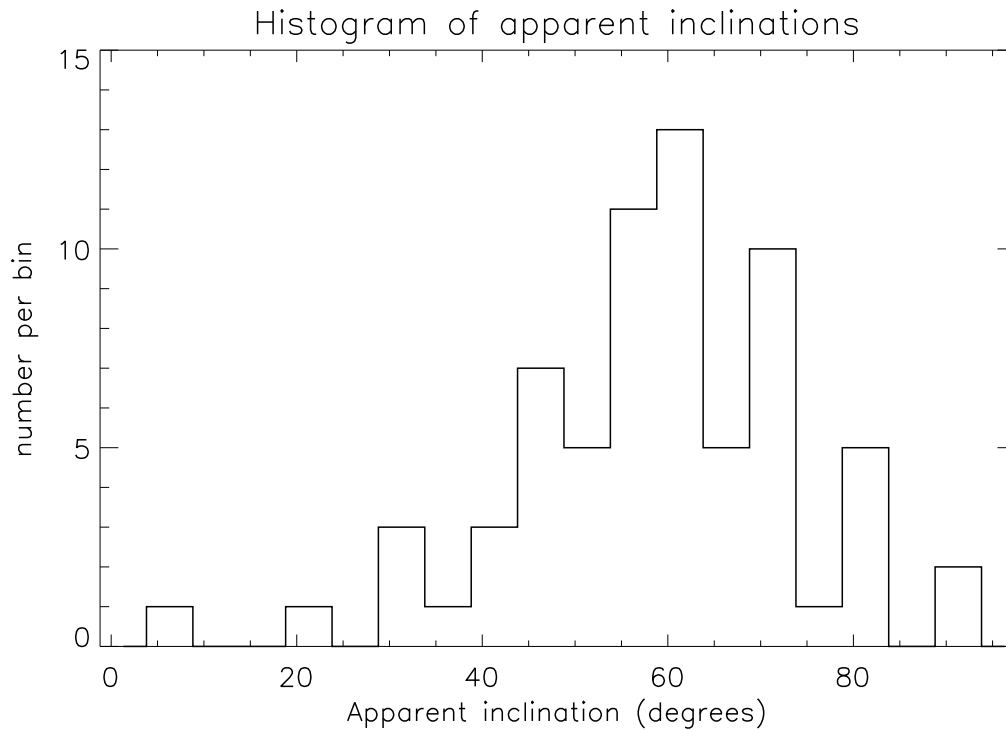
Figure 3.9: Here we show the apparent inclination of the objects in the VIMOS sample if it is assumed that the variation in their velocity at a given luminosity is a function only of inclination. The apparent inclination of the velocity is relative to the plane of the sky such that a velocity in the plane of the sky would have an inclination of 0 degrees. It can clearly be seen in this plot that there is a peak at $\sim$ 60 degrees around which the apparent inclinations are distributed.

we note they are mostly plumes of gas rather than separate offset emission such as that seen in A1991. One however, is Abell 2566 which is unique in our sample as it shows no line emission at the location of the continuum peak. In this respect it is similar to the Ophiuchus cluster identified by Edwards et al. (2009), however it was not included in the analysis presented in Chapter 4 (Hamer et al., 2012) as it lacked the supplementary *Chandra* data which allowed that analysis.

Figure 3.10 highlights the difficulty in detecting offset emission with VIMOS observations. Due to the limited field of view large offsets at low redshift would not be detected. Likewise a smaller physical offset at the higher redshift end of our sample would have an apparent offset on the scale of the seeing (A1991s offset is < 3 arcsec at the redshift of A3444 for example) preventing its detection. We also note that objects with an offset along the line of sight would not be easily detected by these observations.

Figure 3.11 shows the physical offset against the cluster redshift for the whole

sample. It can clearly be seen here that the offsets for the majority of the sample fall below the seeing limit of the VIMOS observations. A1991 and A3444 again clearly stand out from the sample, and we see the group of plumed objects (along with Abell 2566) at an offset of ~ 6 kpc. The dot-dashed line in Figure 3.11 marks the limit of the VIMOS field of view, assuming the BCG was at the centre of the pointing, objects with a separation placing them above this line would not be detected as the offset emission would fall outside the observed area of sky.

From Figure 3.11 it is apparent that there are other objects in which the line emission is offset from the BCG to a lesser extent than is present in A1991 and A3444. Of the objects which have an observed offset of greater than 1.5" (the average seeing limit) seven have a physical offset which puts them outside the effective radius of the galaxy (greater than about 3 kpc). The apparent offset in these objects however is still well below the offset of A1991 and A3444.

3.7.1   The unique properties of A2566

Abell 2566 differs from the other offset objects which are studied in Chapter 4 in that it has a strong, compact radio source that does not coincide with the brightest stellar component of the BCG but instead coincides with the location of the offset Hα emission (Figure 3.12). It is also apparent that the system shows a possible close companion which suggests the possibility that the two are strongly interacting. We were able to identify one other system in the literature (Zwicky 8193 in Wilman et al., 2006) which had properties similar to Abell 2566. Both have offset Hα emission and exhibit a very unusual offset between the radio source and the dominant stellar component. Unfortunately neither has high resolution observations of the ICM in the cluster core. So, while it may be tempting to speculate that the offset radio emission is evidence for the removal of the super massive black hole from the core of the BCG much more detailed observations are required before the true origin of the unique features in these systems can be determine.

Emission Line offset in arcsec

Emission Line offset in kpc
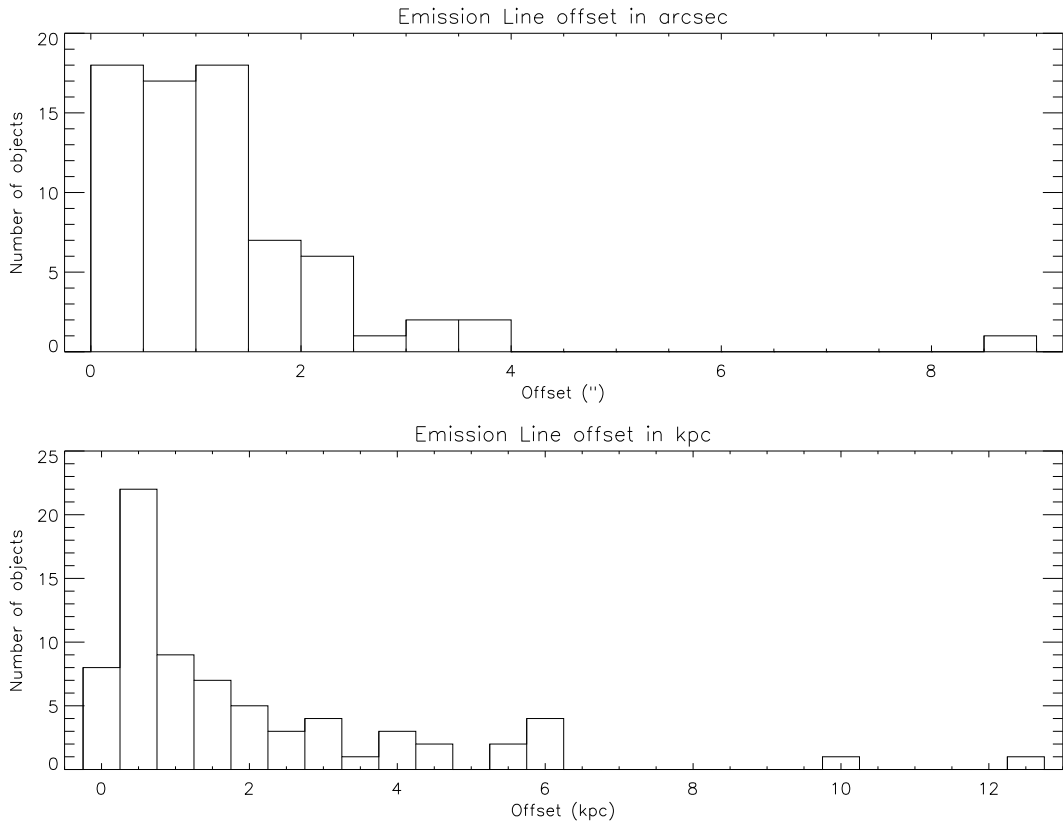
Figure 3.10: The top plot (a) shows the apparent offset between the continuum emission of the BCG and the centroided peak of the Hα emission for the full sample of objects. Almost all objects show small apparent offsets of less than 4". Only one object shows a significant apparent offset, this is A1991. The bottom plot (b) shows the physical observed offset of the BCG and the majority of the line emission. Here we see a more spread out distribution of objects but with the majority still showing small offsets.

3.8 Stellar Kinematics

The wavelength of the sodium D stellar absorption features (NaD$_1$ λ = 5895.9 Å and NaD$_2$ λ = 5889.9Å) was covered for most of our objects which allows for the extraction of stellar kinematics. Unfortunately the nature of the line makes it more difficult to characterise accurately than the emission lines. Primarily it requires the continuum emission to be bright in order for the absorption feature to be visible in the spectrum. It is also intrinsically a broad feature which makes contamination by sky lines a serious problem. From the VIMOS sample only 12 objects had spectra in which the NaD absorption was clear enough to be fitted at the 7σ significance level (so as to match the emission lines). Despite this we produce maps of the NaD feature for these 12 objects (Figure 3.13) and compare them to the line emission
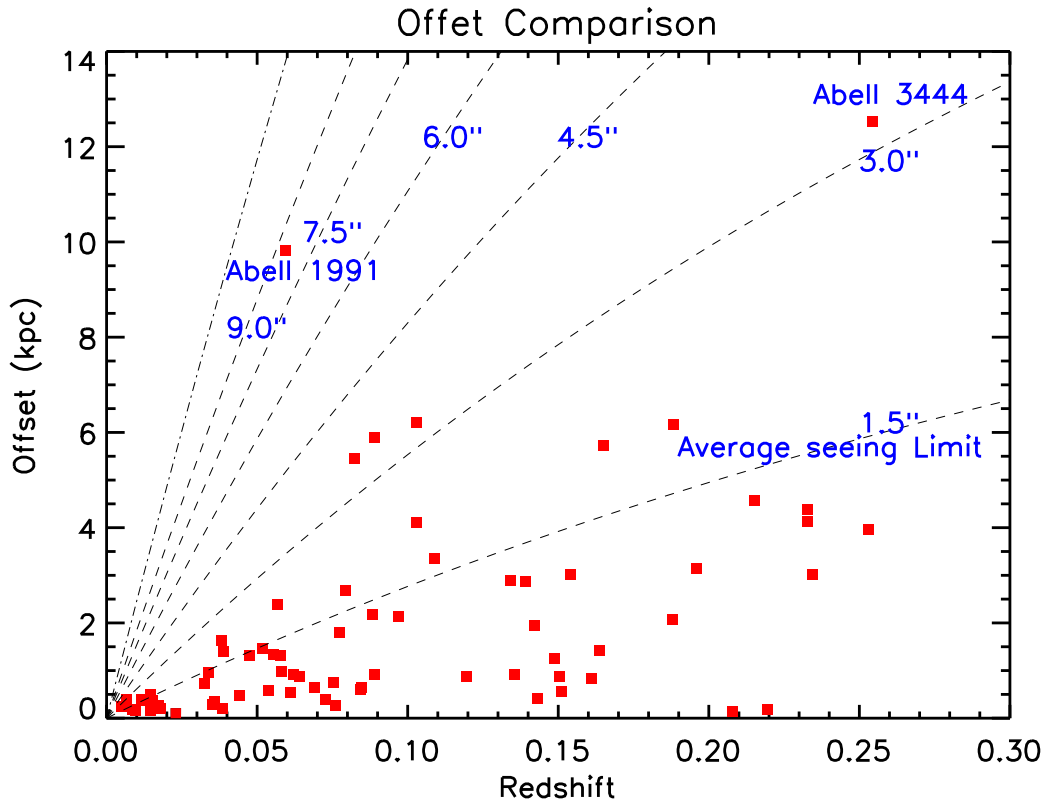
Figure 3.11: A plot of the observed physical offset between the BCG and the majority of the line emission and the cluster redshift. The dashed lines show constant visible offsets in 1.5" steps. We can see that the majority of objects fall well below the average seeing limit of 1.5". The dot-dashed line shows the extent of the VIMOS field of view (~ 12" as the BCG was positioned at the centre of the field of view)

maps (Figure 3.2).

One thing that is immediately apparent from studying the NaD absorption maps is that the stellar component of the BCGs shows no evidence of an ordered velocity structure. Indeed the mean velocity field appears to be completely random which is not unexpected for a massive elliptical galaxy such as a BCG. This is in stark contrast to the ordered velocity maps produced from the Hα emitting gas (Figure 3.2). We also note that although the line width maps do generally show a peak towards the centre of the object they are overall substantially more uniform than their counterparts from the line emission. This implies that the stellar component of the BCGs has a velocity field which is dominated primarily by random motion suggesting that the movement of the stars and gas in the galaxy are decoupled. Hydra-A is a clear example of this, it is one of the most ordered velocity fields in our sample and also has one of the largest peak–to–peak velocities. Moreover it is
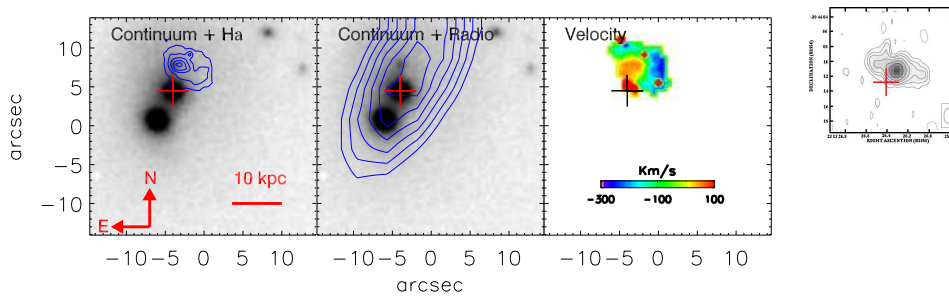
Figure 3.12: *Left* - FORS1 R band image of Abell 2566 with the Hα emission contoured in blue. A clear offset between the BCG and the Hα emission of $\sim$ 6kpc can be seen. *Centre Left* - FORS1 R band image of Abell 2566 with the National Radio Astronomy Observatory Very Large Array Archive Survey (NVAS) radio map contoured in blue. While the NVAS radio image is poorly resolved on the scales of this image it can be seen that the centre of its peak is offset from the BCG and more closely coincident with the position of the Hα emission. *Centre Right* - Hα velocity field of Abell 2566 as shown in Figure. 3.2. *Right* - A higher resolution radio image of the radio source in Abell 2566 taken from Owen & Ledlow (1997). This panel has been scaled to match the scale of the other panels. The Cross on each image marks the central position of the BCG.

known that the gas forms a rotating disk (Simkin, 1979), despite this however the stellar motions appear to remain random, producing a velocity field with no obvious order.

In Section 3.7 we identify A1991 as an object with offset line emission. The stellar absorption maps presented in Figure 3.13 when compared to the line emission maps in Figure 3.2 clearly show the extent of this offset. While both have a peak in roughly the same position, the line emission map shows little emission around this point with most of it located $\sim$ 10 arcsec to the north where it shows a second peak. By contrast the majority of the NaD absorption is centred almost uniformly around the southern peak of the line emission with possibly a slight extent to the south. The line emission map of RXJ0338+09 shows a very disturbed morphology suggesting that some major event is disrupting the line emitting gas within this system. Interestingly the stellar absorption map shows a secondary peak of absorption at $\sim$ 7 arcsec ($\sim$ 4.7 kpc) to the north-west of the BCG. This suggests the presence of a second galaxy very close in projection to the BCG. Consulting the stellar velocity map we find that this galaxy also has a velocity which is close to that of the BCG, redshifted by just a few hundred km s^{-1}. We interpret this as evidence that the BCG in RXJ0338+09 is currently interacting with (and possibly merging with) another cluster galaxy. It

therefore seems likely that this interaction is responsible for the disturbed structure of the clusters line emitting gas.
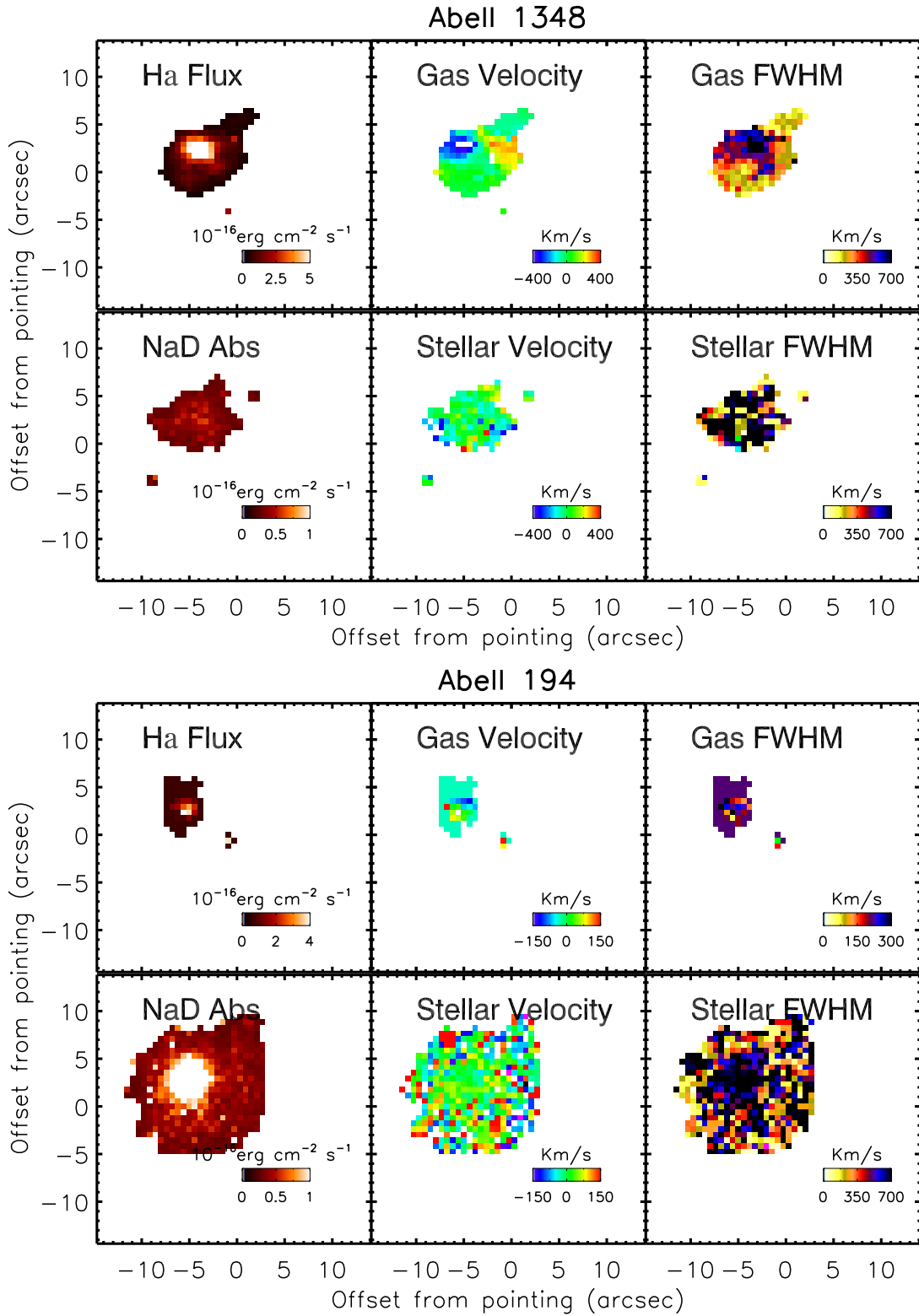
Figure 3.13: Here we show the stellar absorption and kinematics of each object from the sample in which the continuum was bright enough to allow the sodium D absorption feature to be fitted accurately. Fits to the Hα emission are included for comparison and the contrast in the mean velocity fields is very apparent clearly suggesting that the motion of the gas is decoupled from that of the stars.
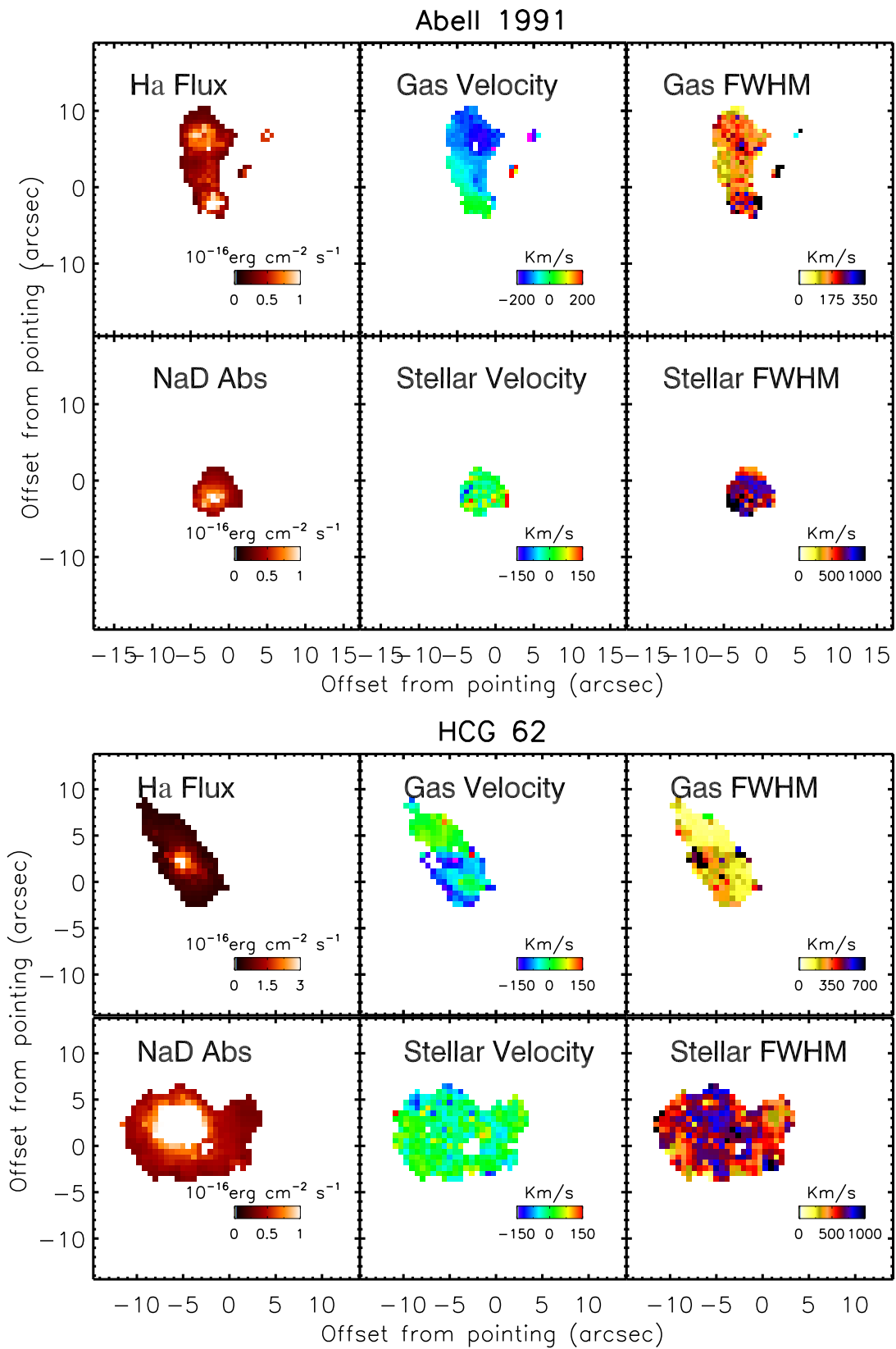
Abell 1991

HCG 62

Figure 3.13: continued.
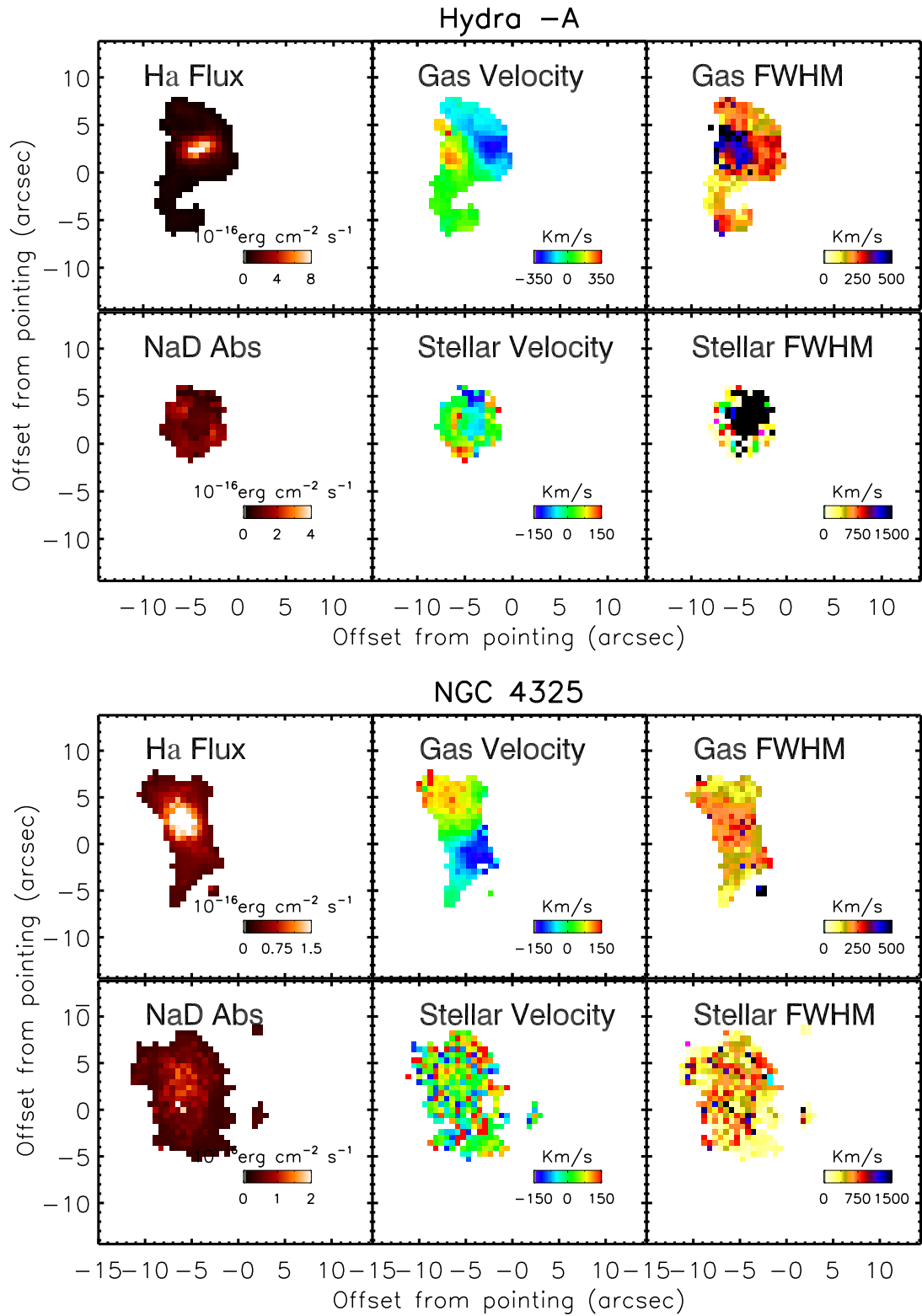
Figure 3.13: continued.
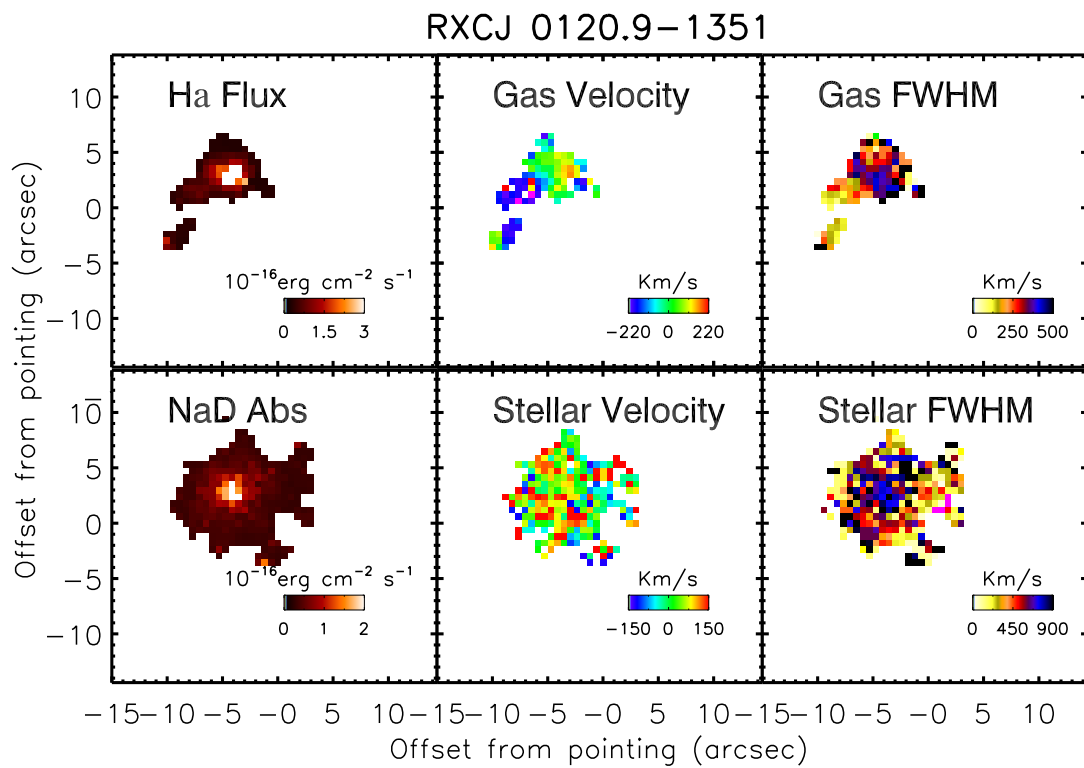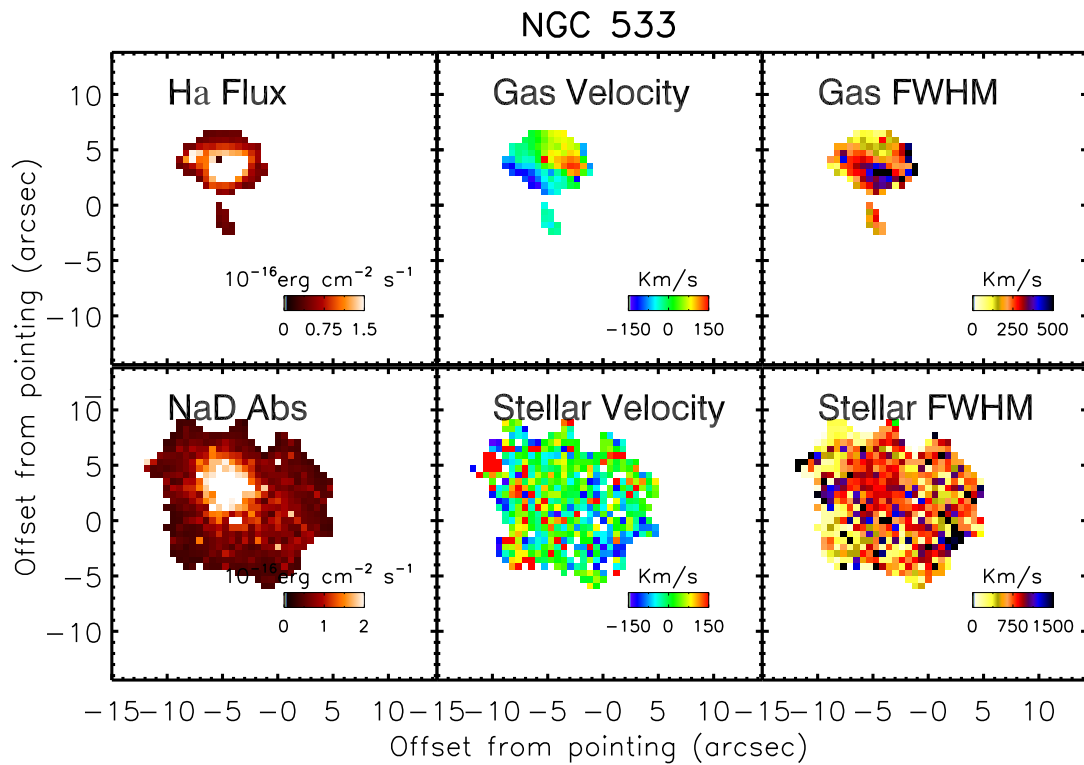
Figure 3.13: continued.
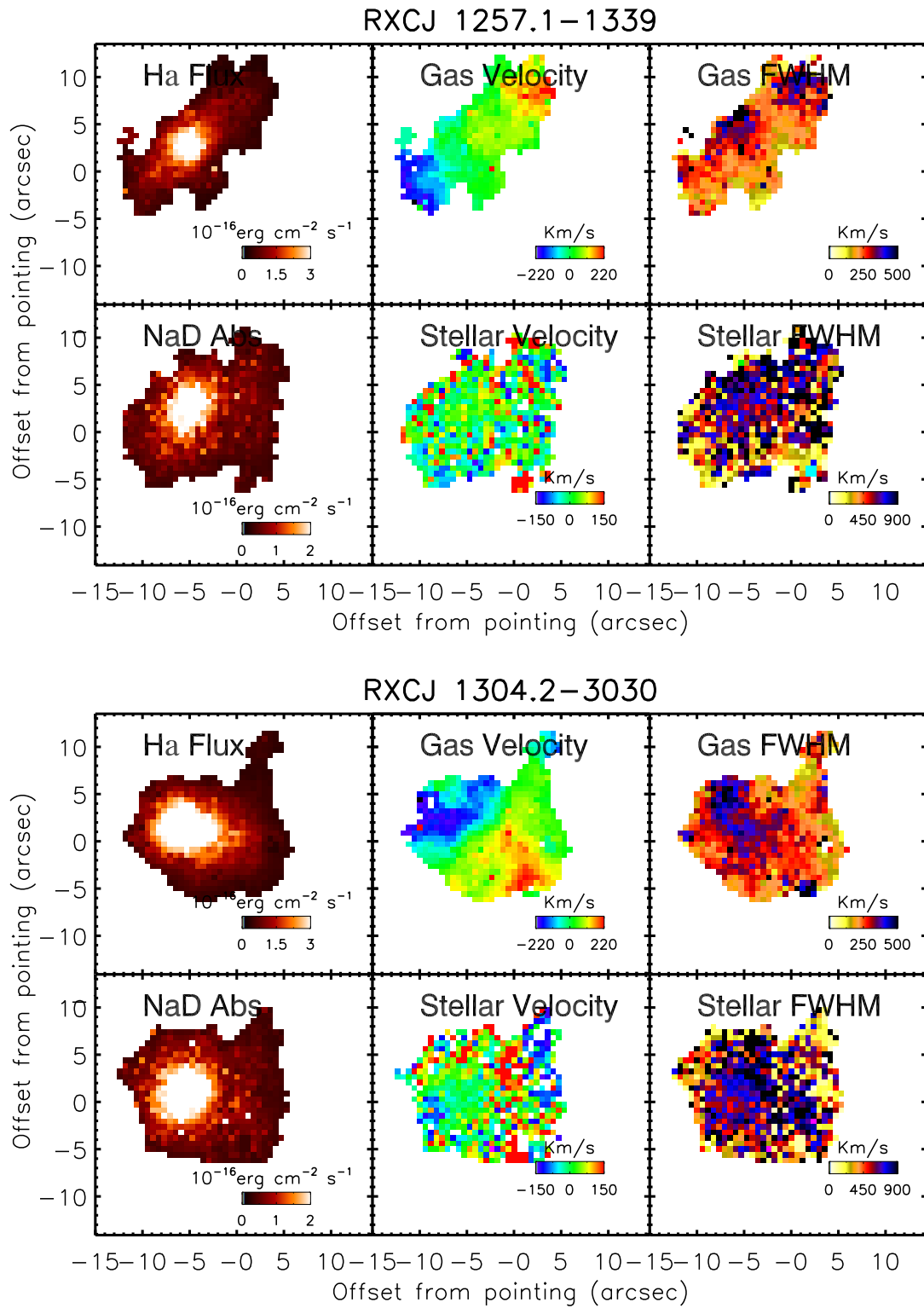
Figure 3.13: continued.
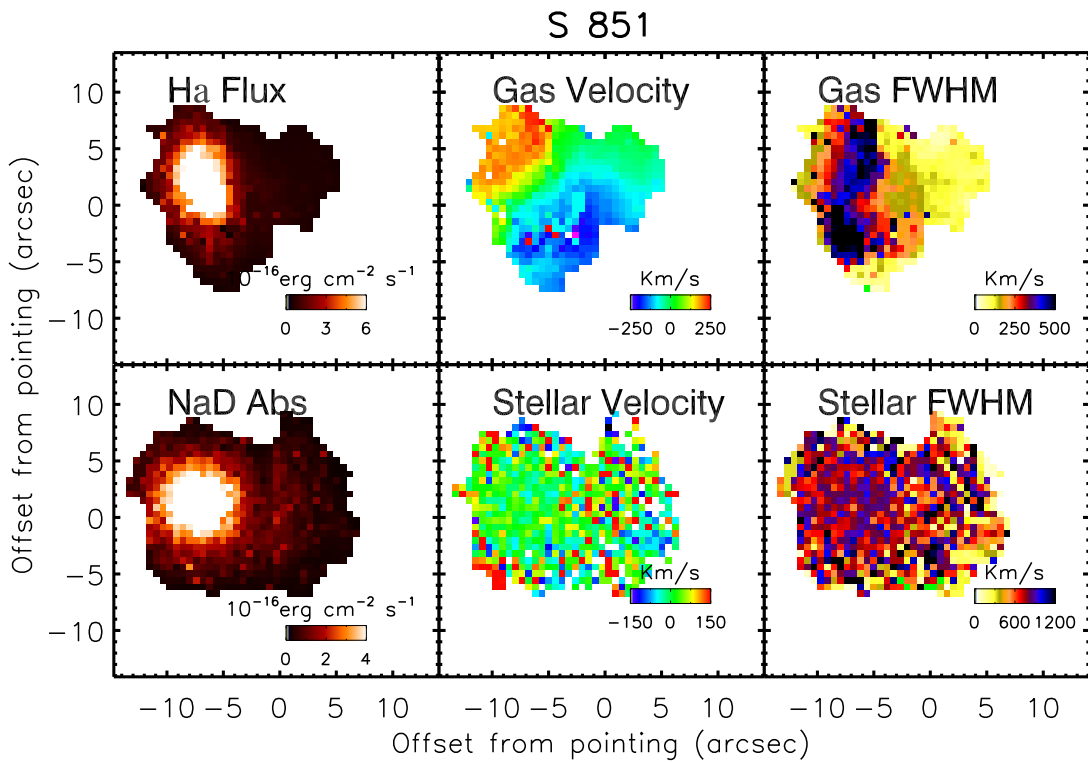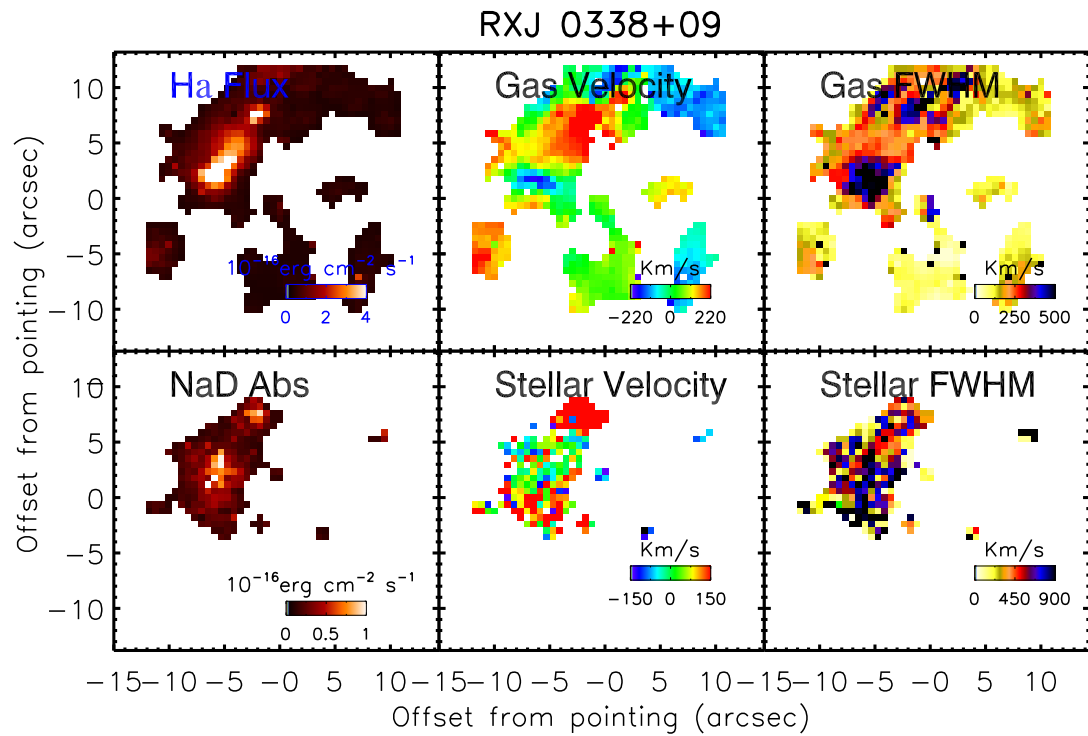
Figure 3.13: continued.

3.9 The source of the ionisation

We have already discussed the ionisation state of the gas in a previous section, however it is important to note that while the [NII]/Hα ratio can provide a measure of how highly ionised any gas is it cannot on its own be used to determine the source of the ionising radiation. For this other line ratios are also required (such as [OIII]/Hβ for a BPT analysis, Baldwin et al. (1981)) which can then be compared with the [NII]/Hα ratio to determine the source of the ionisation. Unfortunately for most of the objects in our sample the observations did not cover the wavelength range required to observe these lines. However, as can be seen from Table. 3.1 seven of the objects in our sample were at a redshift high enough to allow Hβ and [OIII] to be present at the blue end of the HR_orange grism.

We produced BPT diagrams for the 7 objects (Figure 3.14) which had both Hβ and [OIII] line present in the spectrum. From Figure 3.14 it is apparent that all 7 of these objects appear to have ionisation states which are consistent with being the result of AGN activity. While this is not unexpected as BCGs do host AGN, it is interesting to note that one of the objects for which the BPT analysis was possible was Abell 2566. Abell 2566 was discussed in Section 3.7 because the emission is completely offset from the BCG by $\sim$ 9 kpc. It was also noted that the radio emission appears to be centred on the offset line emission hinting at the possibility that the super massive black hole (SMBH) has been ejected from the BCG. The fact that the ionised gas shows evidence of being AGN ionised is also suggestive in favour of this scenario, however we note that the position of Abell 2566 on the BPT diagram is close to the border between AGN and star formation.
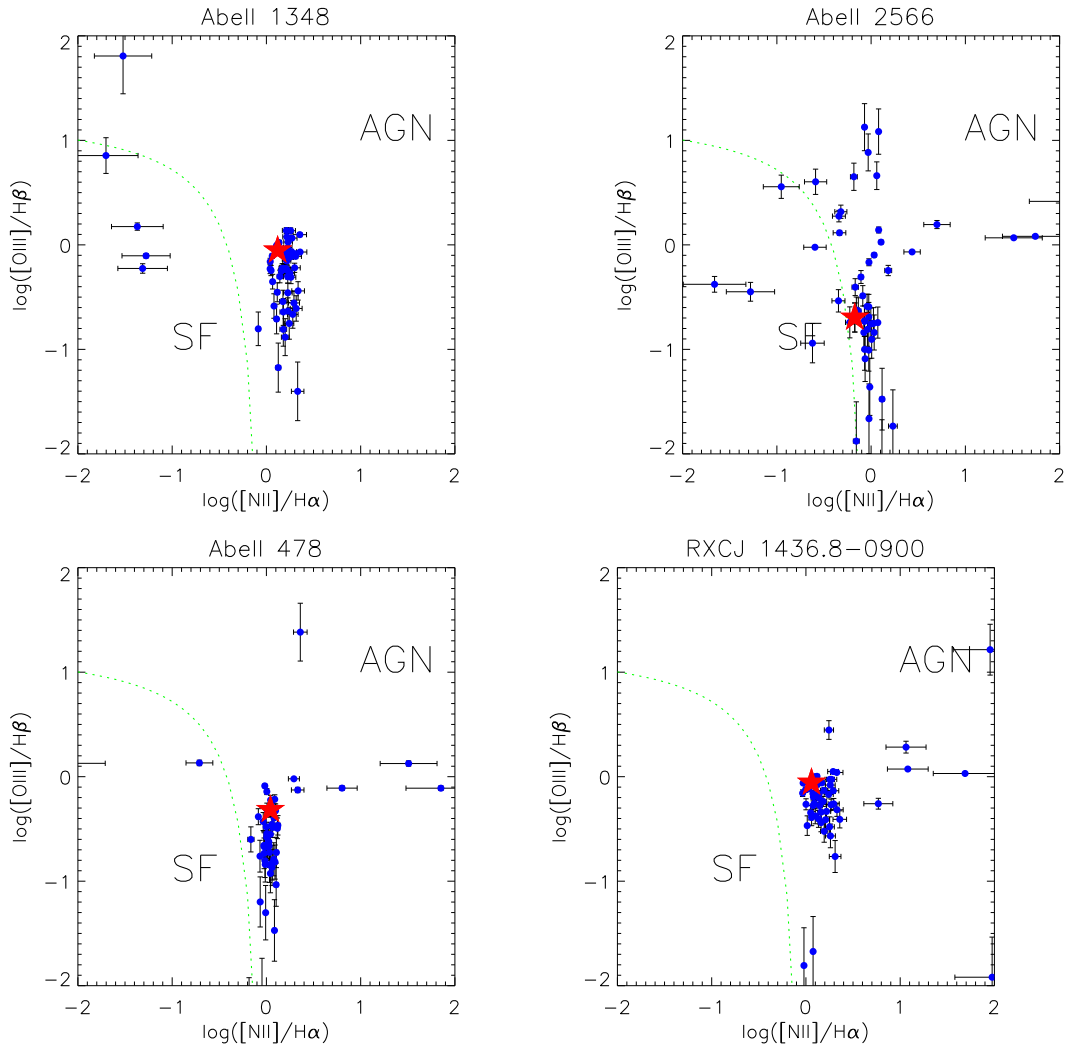
Figure 3.14: Here we show the BPT analysis of the objects from our sample which have redshifts that allow us access to the [OIII] and Hβ lines in our VIMOs observations. The blue points show the locations of every pixel of detected emission on the diagram, the red stars then show the location of the central 1.8×1.8 arcsec which should be the location of the AGN, The green dotted line marks the boundary between star formation and AGN dominated ionisation. Note that for Abell 2566 the emission was offset so the central region was determined from the Hα emission and not the continuum.
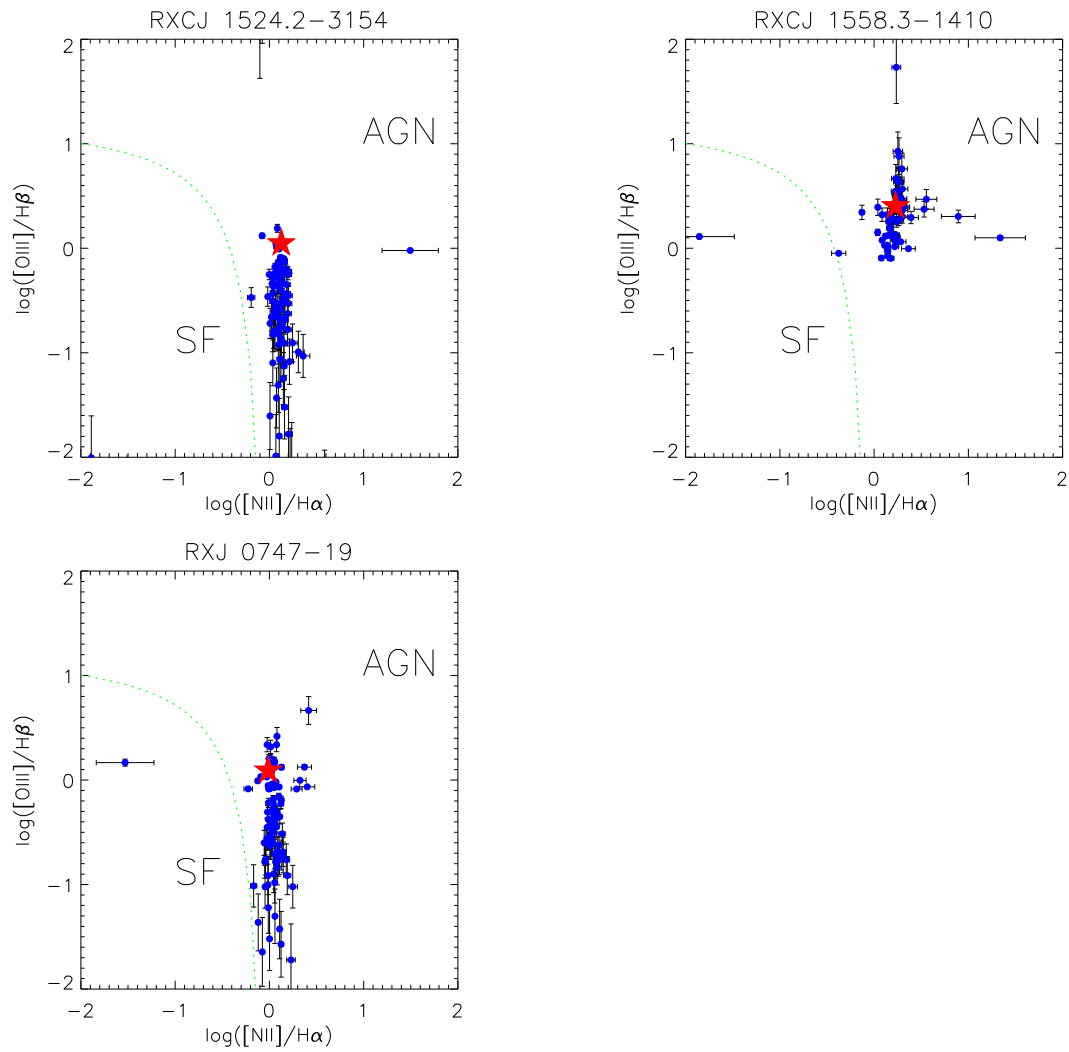
Figure 3.14: continued.

3.10 Summary

One of the key things found by this study was that the mean velocity of the ionised gas appears to trace a rotation. The maps shown in Figure 3.2 clearly show that the line emission for most systems traces an ordered velocity structure across the BCG. While most of the objects show other velocity structures in their more extended emission, the region around the peak of the Hα is, for the most part, consistent with that of a rotating disk, changing from red–shifted to blue–shifted across the core region. We also note that the velocity gradient is correlated with the extent of the object but not with the velocity difference. This is difficult to explain unless the velocity is also related in some way to the extent at which it is measured, which suggests an ordered motion such as a rotation of a disk. If the velocity structure is the result of a disk then its inclination will play a large part in the measure of its velocity. From Figure 3.8 we were able to show that if the velocity is dependent on luminosity then the implied inclinations to correct for the difference in velocities are consistent with those of a randomly selected sample from a heterogeneous population of inclined disks. We will address this issue of rotation in a Chapter 6 but what is clear from these results is that the kinematics of the line emitting gas are highly ordered and decoupled from the stellar component of the BCG.

We were also able to identify several objects which showed evidence of having a substantial fraction of their line emission offset from the BCG. In total we identify three objects from our sample of 73 which are substantially offset (> 8 kpc) from the BCG suggesting that such offsets are both rare and transient. Both Abell 1991 and Abell 3444 were found to have an offset between the peak of their line emission and their stellar centre of more than 10 kpc. These objects still showed line emission from the centre of the BCG but had the majority of it offset at a secondary peak. These two objects are studied in much more detail in Chapter. 4. The other offset object that was identified was Abell 2566 which was offset from the BCG by ~ 9 kpc. Interestingly, however, unlike Abell 1991 and Abell 3444 this object did not have any component of its line emission centred on the BCG. Comparison to radio data also showed the presence of a radio source centred not on the BCG but on the line emission. Unfortunately Abell 2566 lacks the high resolution X-ray data

required for a detailed analysis so it is easy to over interpret these data.

Chapter 4

The Relation Between Line Emission and Brightest Cluster Galaxies in Three Exceptional Clusters: Evidence for Gas Cooling from the ICM

4.1   Overview

In this Chapter we discuss a study of three exceptional clusters (Abell 1991, Abell 3444 and Ophiuchus) where there is a physical and kinematic offset between the BCG and the cooling, X-ray peak. We combine integral field spectroscopy, CO observations and X-ray data to investigate the connection between the cooling of the intracluster medium, the cold gas being deposited and the central galaxy. Within most clusters there is a strong spatial correlation between brightest cluster galaxies (BCGs) and the peak density and cooling rate of the intra-cluster medium (ICM). In these three systems this is not the case which allows the effects of the cluster core and the BCG on the ICM to be studied individually. We find the majority of the optical line emission is spatially coincident with the peak in the soft X-rays. In the case of A1991, we make separate detections of CO(2-1) emission on the BCG and on the peak of the soft X-ray emission suggesting that cooling continues to occur in the core

despite being offset from the BCG. We conclude that there is a causal link between the lowest temperature ($<2\,\mathrm{keV}$) ICM gas and the molecular gas ($\sim 30\,\mathrm{K}$). This link is only apparent in systems where a transitory event has decoupled the BCG from the soft X-ray peak. We discuss the prospects for identifying more examples of this rare configuration.

4.2 Introduction

Within the majority of clusters of galaxies the positions of the BCG and cluster core are strongly correlated (Peres et al., 1998; Sanderson et al., 2009a; Hudson et al., 2010). This correlation suggests a connection between the BCG and the cooling of gas from the ICM. Peres et al. (1998) found that within the ROSAT B55 sample most of the clusters have a BCG position within the uncertainty (~ 4–25 arc sec) of the peak in their X-ray surface brightness. Of the 55 clusters in the B55 sample, 65 per cent have a BCG within 10 arc seconds of the peak in X-ray surface brightness, although the authors note that no effort was made to correct the astrometry of the ROSAT images.

Sanderson et al. (2009a) find a clear correlation between Hα and radio emission in the BCG and the offset of the BCG from the X-ray peak. In their sample of 65 X-ray selected clusters all of the line emitting BCGs have an offset of less than 15 kpc from the peak of the cluster X-ray emission and only 4 have an offset of greater than 8 kpc. When extending their sample to all clusters (not just those with line emission) Sanderson et al. (2009a) find that only 3^{+4}_{-2} per cent have a BCG/X-ray offset of greater than $0.15r_{500}$. Hudson et al. (2010) study a sample of 64 galaxy clusters with high-quality Chandra X-ray observations and find that 88 per cent have a projected physical offset of less than 50 kpc. The authors note that all of the objects with a separation greater than this show evidence of an ongoing or recent major merger and suggest that such a major event in the clusters evolution is required to create such an offset between the BCG and cluster core.

The properties of the BCG (star formation, AGN activity, etc.) are also known to be closely related to the properties of the cluster core (cooling time, central entropy etc.) (Rafferty et al., 2008; Cavagnolo et al., 2008). These relations suggest a direct physical link and evolutionary relationship between the BCG and the cluster core.

Rafferty et al. (2008) find a clear link between a BCG's star formation and the central cooling time of the host cluster core, with star formation only occurring in systems with a central cooling times of less than $\sim 8 \times 10^8$ yr. This paper also finds that a small separation between the BCG and the cluster core ($\lesssim 20$ kpc) is required for a BCG to form stars suggesting a clear relation between the cooling of the X-ray gas in the core and the formation of stars in the BCG. A cluster central entropy of $\lesssim 30$ keV cm^2 was also found to be required for star formation in the BCG by Rafferty et al. (2008) which agrees with the findings of Cavagnolo et al. (2008) who also note that this is the upper boundary at which AGN feedback turns on.

The conclusions which can be drawn from this are that the gas cooling from the ICM is responsible for inducing the star formation and AGN activity within the BCG. The simplest mechanism to achieve this relationship is that as gas cools from the ICM it condenses and directly fuels the SF and AGN activity in these systems. If this is indeed the fate of gas cooling from the ICM it poses the question of whether the cooling and condensing of gas are related to the BCG or to the cluster core, a question which is difficult to answer in most systems due to the two being spatially coincident.

To disentangle the effects of the cluster core and BCG on the ICM, systems which show evidence of strong cooling but where the two are not coincident must be studied. An effect known as 'sloshing' (Ascasibar & Markevitch, 2006; Johnson et al., 2010; Million et al., 2010) can be generated in the ICM by a major event disrupting the centre of the cluster. Ascasibar & Markevitch (2006) show that gas sloshing occurs when the gas peak is offset from the DM peak and begins falling back. This paper also shows that if the sloshing is caused by a merger with a subcluster that has relatively little gas, the peak of the DM potential and the BCG associated with it can also be set in motion. As the DM and stars are relatively collisionless they would pass freely through the cluster while ram pressure will slow the gas core (Million et al., 2010). In such a case the BCG would be temporarily offset from the cluster core allowing their individual effect on the ICM to be disentangled. If cooling and condensing of gas is able to continue without the presence of the BCG we would expect to see cold gas at the location of the offset X-ray peak in systems where sloshing has decoupled the cluster core and the BCG.
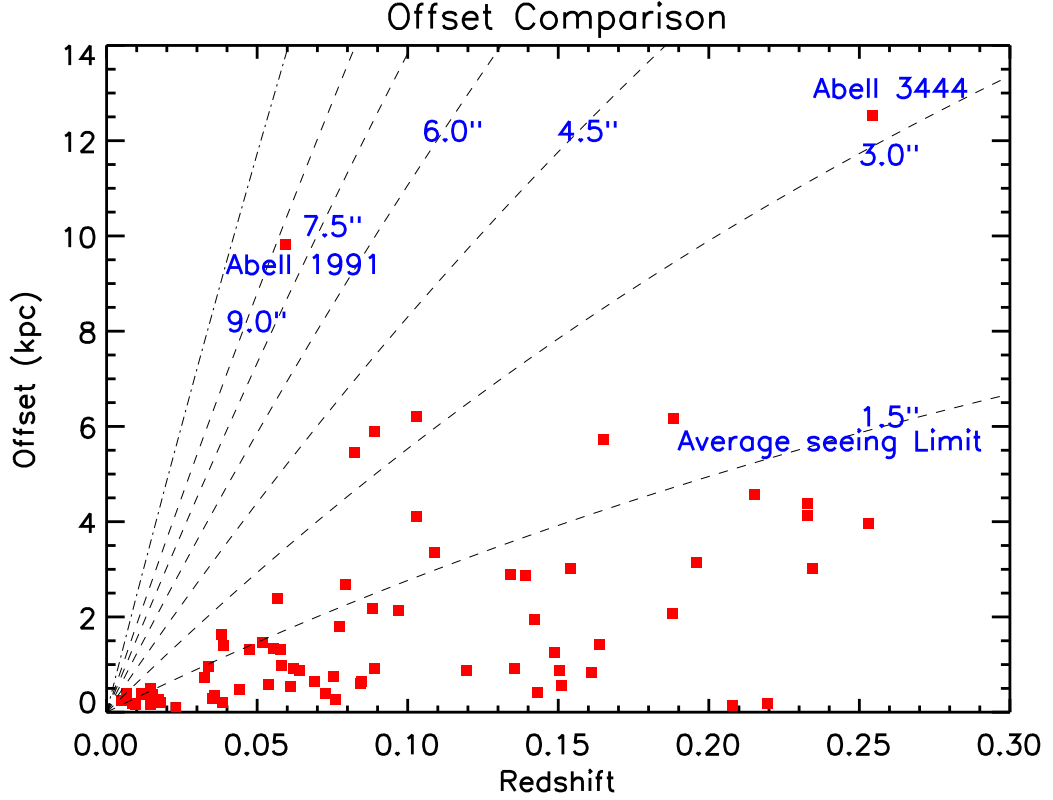
Figure 4.1: Observed physical offset between the BCG and the majority of the line emission in the parent sample of 73 BCGs Chapter 3). The dashed lines show constant offsets in 1.5″ steps. The dot-dashed line shows the extent of the VIMOS field of view ($\sim 12''$ as the BCG was positioned at the centre of the field of view). The majority of objects fall well below the average seeing limit of 1.5″ but A1991 and A3444 stand out with offsets of 9–13 kpc.

In this chapter, we report observations of three extreme systems (Abell 1991, Abell 3444 and the Ophiuchus cluster) from our parent sample which show a significant component (> 50 per cent) of their optical line emission significantly offset from the central BCG. A1991 and A3444 are unique from the rest of the sample in that the rest frame optical line emission is significantly offset from the BCG. Figure 4.1 shows the physical offset between the BCG and the peak Hα emission for the whole sample of 73 line emitting BCGs Chapter 3. It can clearly be seen here that the offsets for the majority of the sample fall below the average seeing limit of the VIMOS observations ($\sim$1.5″) with A1991 and A3444 having 9-13 kpc offsets. Ophiuchus was selected from the literature as it is the best other example of a BCG showing a significant offset between the BCG, the X-ray peak and the line emission (Million & Allen, 2009)

The separation of these three objects from the core of their host cluster presents
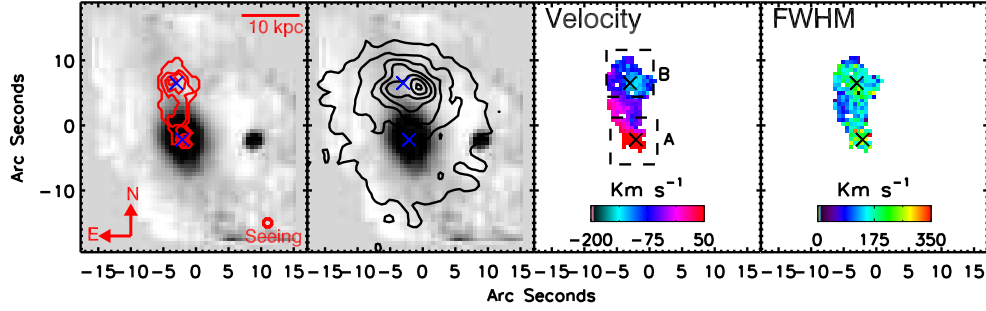
Figure 4.2: *Left:* A continuum image ($\lambda = 6000$-7000 Å) created from the VIMOS datacube. Over plotted as contours is the Hα emission at 6, 12, 18 and 24σ (with 1σ = 9.4×10^{-18} erg cm^{-2} s^{-1} arcsec^{-2}). The Hα emission is double peaked with one component on the BCG but extending north by $10''$ where a second component can be seen. *Centre-Left:* The continuum image showing the optical stellar component of the BCG with the X-ray map overlaid as contours. The peak in the X-rays is offset by $\sim 10''$ north of the BCG. *Centre-Right:* The Hα velocity field for A1991, as derived from fits to the Hα - [NII] complex. The velocities are given relative to a redshift z=0.0591. *Right:* The FWHM of the Hα line emission deconvolved for instrumental resolution. The crosses mark the location of the two Hα components on each plot. The plots are centred at RA = 14:54:31.567 and Dec = 18:38:32.70 (J2000). There is a component of Hα emission offset to the north of the BCG by $\sim 10''$ which coincides with the position of the peak in the soft X-ray emission. The velocity gradient along this offset shows a dynamical link still exists between the BCG and the Peak of ICM cooling.

a unique opportunity to study the cooling of the cluster gas away from the BCG. By disentangling the cluster core and BCG it is possible to determine if the cooling gas is related directly to the cluster core or to the BCG.

We first outline the observations and data reduction (§4.3) followed by a summary of how we completed the analysis (§4.4). In §4.5 we present the results before discussing their implications in §4.6. Finally a summary and conclusions are reported in §4.7 and we outline developments made since the submission of this paper in §4.8 along with discussing the future prospects for this study. We assume Ω_m =0.27, $\Lambda = 0.73$ and $H_o = 71$ km s^{-1} Mpc^{-1} throughout. This corresponds to a physical scale of $1.12\,\text{kpc}/''$ for A1991, $3.91\,\text{kpc}/''$ for A3444 and $0.55\,\text{kpc}/''$ for Ophiuchus.

4.3   Observations and Data Reduction

Observations of the BCG in A1991 were taken using the Visible Multiobject Spectrograph (VIMOS) instrument on the 8.2m Very Large Telescope (VLT) in April

of 2008 and May of 2010. Observations were made at two positions, one centred on the BCG and the second $\sim 10''$ north of the first to cover the peak in X-ray emission. At both locations a set of three 600 second exposures were performed with a pointing dither included between each exposure to account for bad pixels. The HR_Orange Grism and GG435 filter (spectral resolution of $R \sim \Delta\lambda/\lambda \sim 2650$ over the wavelength range 5250–7400 Å) were used to observe Hα ($\lambda_{\rm rest}$ 6562.8 Å) at the redshift of the cluster of 0.0587. Observations of A3444 were taken with VIMOS in June 2008 using the HR_Red Grism and GG475 filter (spectral resolution $R \sim \Delta\lambda/\lambda \sim 3100$ covering the wavelength range 6450–8600 Å) to observe Hα at the cluster redshift of 0.2533. The observations were taken in a range of conditions, with a seeing of $\sim 0.7''$–$1.3''$.

The raw data were reduced using the ESOREX package. This package performed the basic data reduction including bias subtractions, flat fielding and the wavelength and flux calibrations. To subtract the sky we masked any point-like objects to remove any stars within the field. The BCG was then removed from the field by masking all pixels within an isophote of half its peak intensity. The sky level for each quadrant was then calculated by taking the median value of the remaining pixels at each wavelength increment. This sky spectrum was then subtracted from each pixel in the four quadrants before they were combine into a single datacube. Finally we median combined the three exposures for each pointing in order to eliminate cosmic rays. To mosaic the two positions of A1991 we determine the exact offset between the BCG in both observations and combined them to create a cube with a $\sim 36'' \times 38''$ field of view.

The Ophiuchus cluster BCG (hereafter Ophiuchus) was observed by Edwards et al. (2009) using Gemini Multi-Object Spectrograph (GMOS) on the 8.1m Gemini South Telescope (Gemini). The observations of Ophiuchus consisted of four 1500 second exposures which were combined to give a total integration time of 6000 seconds. The R400+r grating (spectral resolution $R \sim \Delta\lambda/\lambda \sim 1918$ covering the wavelength range 5620–6980 Å) was used to ensure coverage of Hα at the cluster redshift of 0.0280 (Lahav et al., 1989). The seeing during these observations was $\sim 0.8''$ to $1''$.

The data were reduced using the GMOS specific tools in the Gemini IRAF pack-

age, which included bias subtraction, flat fielding and wavelength calibration. Sky subtraction was preformed by isolating the fibres from a secondary IFU situated $\sim$ $1'$ away from the primary IFU. These fibres were then used to create a sky spectrum which was subtracted from the fibres containing the observations. Cosmic rays were then rejected by comparing the spectrum from each fibre to that from neighbouring fibres and rejecting any element which had a value exceeding ten times the Poisson noise. The individual exposures were then combined into a single datacube which covers a region centred on the BCG of $\sim 5'' \times 7''$.

We obtained IRAM 30m data for the CO(1-0) and CO(2-1) lines in A1991 on 21st April 2010. The observations were performed in reasonable conditions ($\tau_{225\text{GHz}} \sim$ $0.1 - 0.2$) with the EMIR receiver using a 4 GHz bandwidth covering each line. Two positions were observed, the BCG and the optical line peak $11''$ north, each for 1 hour duration with wobbler switching with a $90''$ throw. The observations reached a noise level of 0.6 mK and 1.3 mK in 44 km s^{-1} bins (16 and 32 MHz) for CO(1-0) and CO(2-1) lines respectively. Both the 4 MHz and Wilma backends were used to sample the data but the noise performance of the 4 MHz backend was considerably better so only the 4 MHz data are presented here.

IRAM 30m observations of CO(1-0) in A3444 were obtained on 29th December 2006, before the VIMOS IFU observations, in very good conditions ($\tau_{225\text{GHz}} < 0.1$) with the A/B100 receivers with a 400 MHz bandwidth for 1 hour duration using wobbler switching with a $90''$ throw. These observations reached 0.8 mK in 52 km s^{-1} bins (16 MHz). At the time of writing, we are aware of no observations of CO in Ophiuchus.

4.4 Analysis

We use the integral field spectroscopy to investigate the spatial variation of line emission and kinematics within the clusters. We fitted Gaussian emission line profiles to the region of the spectra containing the Hα (λ_{rest} 6562.8 Å) and [NII] (λ_{rest} 6548.1/6583 Å) in each lenslet. We used a χ^2 minimisation procedure and allowed the velocity, intensity and linewidth of the Hα line, as well as the continuum level to vary independently. The [NII] lines were fixed to the same velocity and linewidth as Hα, the [NII] intensity was allowed to vary but the ratio of
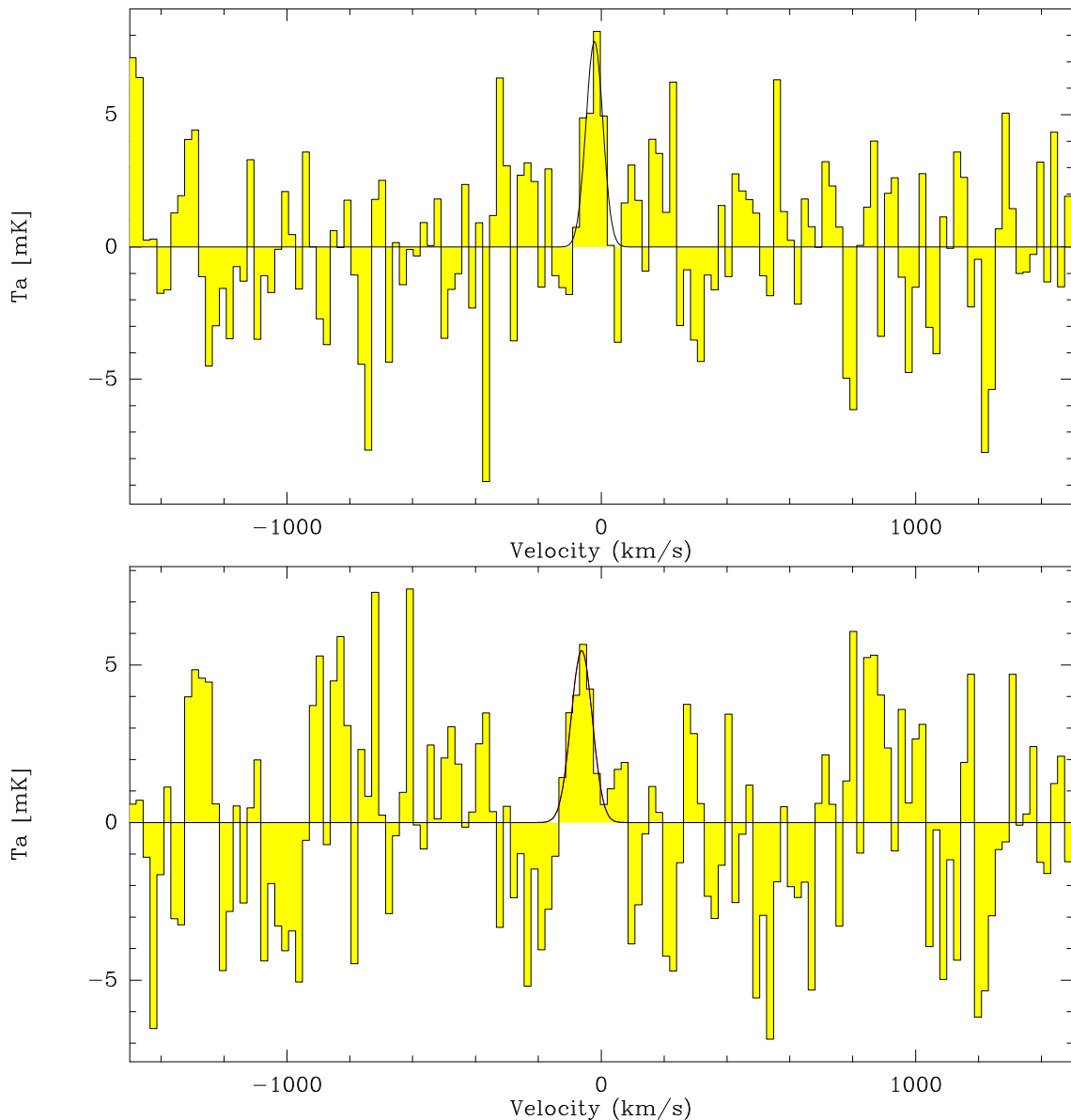
Figure 4.3: *Upper* IRAM 30m EMIR spectrum for A1991 on the BCG. *Lower* IRAM 30m EMIR spectrum for A1991 on the offset optical line peak. The plots show the CO(2-1) line in antenna temperature scale. Significant CO emission is detected at both the position of the BCG (3.8σ) and the offset Hα emission (3.0σ) and there is a small velocity offset in the line centroid between them.

[NII]6548.1/[NII]6583 was fixed to 1/3. The profiles were fitted to each $0.6''$ pixel and adaptively binned to $1.8''$ in regions with lower Hα flux. As such the low surface brightness emission has a lower resolution than the brightest regions.

These fits were accepted as representing the data when they provided an improvement over a continuum only fit at the 7σ significance level and when an acceptable fit was found the parameters of the best fit model were stored. These parameters were then used to produce maps of Hα flux, relative velocity and linewidth (FWHM

deconvolved for instrumental resolution). Continuum images of the region covered by the observations were also produced by taking the median of the emission from each lenslet over a region of the spectra containing no emission lines or sky line residuals (here after referred to as collapsing the cube).

TABLE 4.1.

PROPERTIES OF THE ON SOURCE AND OFFSET COMPONENTS

Target	Redshift	Velocity (km s^{-1})	Hα Flux (10^{-16} erg cm^{-2} s^{-1})	[NII] Flux (10^{-16} erg cm^{-2} s^{-1})	Continuum (10^{-16} erg cm^{-2} s^{-1} Å^{-1})	FWHM (km s^{-1})
Abell 1991						
BCG	0.05935[3]	0 ± 11	10.3 ± 0.7	23.7 ± 0.68	6.41 ± 0.27	205 ± 9
Offset	0.05893[2]	124 ± 10	22.5 ± 1.2	35.1 ± 0.87	0.76 ± 0.41	152 ± 5
Connecting	0.05910[3]	71 ± 11	7.48 ± 0.4	10.1 ± 0.35	2.15 ± 0.19	133 ± 7
Abell 3444						
BCG	0.25583[6]	0 ± 25	15.5 ± 0.7	8.3 ± 0.6	1.0 ± 0.2	490 ± 21
Offset	0.25550[3]	100 ± 19	16.5 ± 0.5	7.8 ± 0.5	< 0.5	273 ± 9
Connection	0.25503[6]	241 ± 26	10.0 ± 0.6	8.2 ± 0.6	0.4 ± 0.2	450 ± 26

Table 4.1: Results from the fit to the Hα [NII] triplet for the total spectrum of each object listed. The values in Square brackets are the errors on the last decimal place. For A1991 the BCG emission was defined as coming from a 8″ by 7″ region centred on the on BCG Hα peak, shown in Figure 4.2 as region A, the offset emission was defined in a similar manner about the offset Hα peak (region B in Figure 4.2). Similarly for A3444 the on–BCG emission was defined as coming from a 4″ by 5″ region centred on the BCG Hα peak and the offset was defined as an equally sized region about the offset Hα peak (region A and B in Figure 4.4 respectively). For both objects the connection is defined as the emission which was not in these previous two regions and consists of the low surface brightness emission joining the two peaks.

TABLE 4.2.
PROPERTIES OF THE CO(2-1) LINE IN A1991

Target	Significance Sigma(σ)	CO(2-1) Line Intensity (K km s^{-1})	Velocity (km s^{-1})	Line width (km s^{-1})	Peak intensity T$_{mb}$ (mK)	H$_2$ gas mass (10^8 M$_\odot$)
On BCG	3.8	0.52±0.16	-22±10	60±18	7.8±2.2	9.9±3.0
Offset	3.0	0.46±0.19	-62±17	79±35	5.5±1.8	8.8±3.6

Table 4.2: CO(2-1) line parameters for the IRAM 30m EMIR observations corrected for beam efficiency. The equivalent analysis for the data for CO(1-0) finds an upper limit of <0.15 K km s^{-1} which is consistent with the CO(2-1) detection given the observed range of line intensities for these lines in cluster cores (Edge 2001, Salomé & Combes 2003).

4.5 Results

4.5.1 Abell 1991

In Figure 4.2 we show the continuum image of A1991 (collapsed over $\lambda_{observed} = 6000$-7000 Å) and overlay contours of Hα line emission. It is apparent that while there is a component of the Hα emission centred on the BCG, a more extended clump is present $9''$ north lying off the bright stellar component, a projected physical offset of $\sim 10\,$kpc at the cluster redshift of 0.0587 (Struble & Rood, 1999).

Table 4.1 shows the values of the variable parameters for the minimised fits to the emission on the BCG, off the BCG (labeled on Figure 4.2 as regions A and B respectively) and the emission from the connecting gas. These fits show that the offset clump contains the majority ($\sim$55 per cent) of the Hα emission within the system.

A1991 also is known to have a significant offset ($\sim 10''$) between the position of the BCG and the X-ray peak (Sharma et al., 2004). Figure 4.2 shows that the bright peak in the X-ray gas lies roughly $10''$ ($11\,$kpc) to the north of the BCG and within $3\,$kpc of a similar peak in Hα emission. This bright X-ray peak corresponds to the lowest temperature gas in the cluster and the region where the gas is cooling most rapidly. This shows that the majority of the Hα emitting gas is related to the most rapidly cooling region of the ICM rather than being co-located with the BCG. Analysis of the *Chandra* data indicates that the pressure in the core of the cluster is relatively uniform between the BCG and the cooler, offset peak implying that the enhanced density at the peak is balanced by a lower temperature (Sharma et al., 2004).

In Figure 4.2 we show the velocity and linewidth maps produced from the fits to the individual lenslets. We note that the velocity map shows a continuous velocity gradient from the position of the BCG along a connecting filament to the offset emission. This suggests that the two components, while physically separated remain kinematically linked. To determine the velocity difference between the two components we extracted spectra from an $8''$ by $7''$ aperture centred on the BCG and on the offset component (marked A and B on the velocity map of Figure 4.2). We find a velocity difference of 124 ± 10 km s^{-1} between the two components. The

linewidth (FWHM) of the emission from the BCG is greater (205 ± 9 km s^{-1}) than that from the offset component (152 ± 5 km s^{-1}).

Next, we combine the Hα and the CO properties to investigate the relation between warm and cold gas within the cluster core. By virtue of the good conditions, the relative sensitivity between the two lines with EMIR strongly favours the CO(2-1) line. We obtain a significant detection of it in both positions (Figure 4.3) of 3.8σ on the BCG and 3.0σ on the offset line emission with the 4MHz backend. The CO(2-1) line also appears in the Wilma backend though at lower significance (2.9σ and 2.1σ) for the same binning due to the spectrum being substantial nosier. The significance of the line detection was calculated using the variance of the signal away from the line compared to the line strength. By this measure there are two candidate lines at -1250 and +930 km s^{-1} in the offset 4MHz backend spectrum presented in Figure 4.3. However, these features have no counterpart at the same velocity in the Wilma backend which suggests they are not real.

The separation of the two positions is just smaller than the IRAM beam at this frequency ($10.3''$ vs $10.9''$) and the measured velocity of the emission is offset by more than half the line width. From the separation and profile of the beam we estimate a less than 10 per cent contamination between the two pointings. Therefore the gas is likely to be spatially extended on a scale comparable, but not necessarily identical to, the optical emission lines. The velocity difference in CO(2-1) between the two positions is -40 ± 20 km s^{-1} in the same direction as the shift we observe in Hα but 84 km s^{-1} lower. This difference may be related to the bulk flow of the cold molecular gas or a different overall distribution with respect to the BCG compared to that traced by the optical lines. The significance of this velocity difference and its potential origin are beyond the scope of these single dish observations but could be addressed with deeper interferometry with PdBI or ALMA.

The detection of CO $10''$ north of the BCG in A1991 makes this the fourth system where extended CO has been found (e.g. NGC1275 Salomé et al. (2006), A1795 Salomé & Combes (2004) and RXJ0821+07 Edge & Frayer (2003)). In all of these systems the extended CO coincides with extended Hα emission. Within the system as a whole the implied total molecular gas masses of $\approx 1.9 \times 10^9$ M$_\odot$ for A1991 is consistent with the correlation of molecular gas mass and optical line
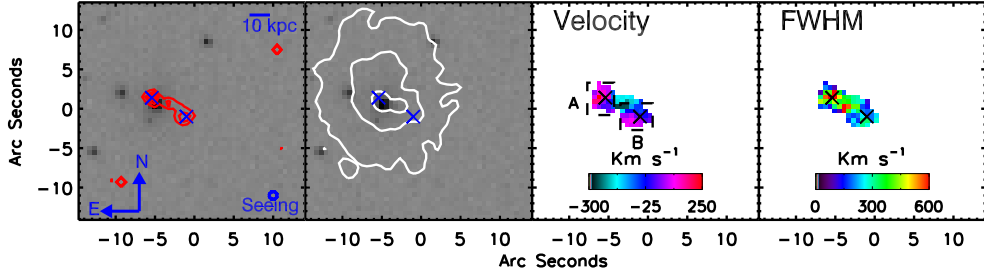
Figure 4.4: *Left:* This shows a FORS2 R band image of the central region of A3444. Over plotted as contours is the Hα line emission at 6,12,18 and 24 σ (with 1 σ = 0.021×10^{-16} erg cm^{-2} s^{-1}). The Hα emission is present towards the centre of the BCG but extends ∼ 5″ to the south west where it shows a second peak. *Centre Left:* The FORS2 R band image showing the BCG in A3444 with the *Chandra* X-ray map contoured over it. While the peak in the X-ray emission lies on the BCG a clear extent can be seen in the south westerly direction in the brightest emission traced by the inner most contour. *Centre Right:* The Hα velocity field for A3444, as derived from fits to the Hα - [NII] complex. The velocities are given relative to a redshift of z=0.2555. *Right:* The FWHM of the Hα line emission deconvolved for instrumental resolution. The crosses mark the location of the two Hα components on each plot. The plots are centred at RA=10:23:49.945 Dec=-27:15:25.34 (J2000). A component of Hα emission is offset to the south west of the BCG by ∼ 5″. This component matches the direction of an extent in the soft X-ray emission.

luminosity in Edge (2001) and with the star formation rate inferred from the MIR continuum (O'Dea et al., 2008a). However, current observations cannot spatially resolve whether the star formation in the offset gas follows the correlation found for gas within the BCG (O'Dea et al., 2008a).

4.5.2 Abell 3444

A3444 also shows a substantial fraction (∼63 per cent) of optical line emission offset from the BCG. In Figure 4.4 we show a FORS2 R band image of the central region of the cluster with contours from Hα line emission. A clear extension in the line emission can be seen to the south west where a secondary peak is apparent. This component is offset from the BCG by ∼ 3.2″ or ∼ 12.5 kpc at the cluster redshift of 0.2533 (Struble & Rood, 1999). In this cluster the line emission form the BCG and offset location are consistent within errors at ∼ 40% of the total line flux each (Table 4.1).

The X-ray observations of this system show a weak but significant point like source (L$_x$(0.5-10 keV) ∼ 4 × 10^{43} ergs s^{-1} in a 1.5″ aperture and a power law

spectrum) coincident with the BCG that has a relatively hard spectrum compared to the cluster emission (Figure 4.5) suggesting the presence of an AGN. While the point source is centred on the BCG (Figure 4.4), the soft X-ray emission shows an extension in the same direction as the offset optical line emission (Figure 4.4) although, like A1991, it is not exactly coincident with the offset peak in the line emission.

To determine the temperature of the gas at the location of the BCG we fit a mekal thermal plasma model (Mewe et al., 1985, 1986) to the 0.5–5.0 keV emission from a 1.5″ aperture centred on the BCG. This found the temperature of the gas to be > 7.5 keV which is high for a plasma model suggesting a contribution to the hard X-ray emission from an AGN component. The presence of an AGN in the BCG would produce increased X-ray counts which could shift the apparent centre of the cluster emission. As such the AGN contribution must be accounted for when determining the true centre of the ICM cooling.

To subtract the AGN emission from the soft X-ray emission on the BCG (and find the true level of the extended cluster emission) we determine the normalisation of the point source in the 2.0–5.0 keV band and apply this to the emission from the 0.5–1.5 keV band. To do this we first determine the properties of the cluster 2.0–5.0 keV emission from an annulus surrounding the point source. We then fit an absorbed power law plus an absorbed mekal plasma model to the point source 2.0–5.0 keV emission with the properties of the mekal component fixed to those from the surrounding annulus. Finally we apply the same model to the point source 0.5–1.5 keV emission with the normalisation and photon index of the power law set to the values determine from the hard X-rays and calculate the flux of the two components.

The total flux from the point source in the 0.5–1.5 keV band is $2.45^{+0.24}_{-0.20} \times 10^{-14}$ erg cm^{-2} s^{-1}, of which $0.55^{+0.16}_{-0.13} \times 10^{-14}$ erg cm^{-2} s^{-1} comes from the AGN contribution. We find that the cluster emission under the point source is $1.90^{+0.18}_{-0.15} \times 10^{-14}$ erg cm^{-2} s^{-1} while the extension to the south west has a flux of $2.4^{+0.20}_{-0.12} \times 10^{-14}$ erg cm^{-2} s^{-1} suggesting that it represents the peak in the soft X-ray emission. Analysis of the *Chandra* data also shows that the pressure in the core of A3444 is relatively constant when the AGN emission is excised. Therefore, A3444 shows very similar X-ray properties to A1991 with an offset peak in soft X-rays but a constant pres-

sure core on 50–100 kpc scales. In the case of A3444, where the AGN in the BCG contributes significantly to the X-ray emission, the offset position in the soft X-rays represents the region of maximum cooling of the ICM.

Within this system the BCG and offset component are separated by a velocity of 100 ± 19 km s^{-1}. We also note that the connecting emission has a higher velocity offset (241 ± 26 km s^{-1}) than the offset peak. The linewidths in this system are higher in the BCG (FWHM= 490 ± 21 km s^{-1}) than in the offset component (FWHM= 273 ± 9 km s^{-1}) suggesting the gas is more disturbed within the galaxy or that it is the combination of several, related gas clouds. We also note that the lenslet from the centre of the BCG has FWHM > 650 km s^{-1} suggesting possible contribution from the AGN detected in the X-ray imaging, that can be seen in the linewidth map in Figure 4.4.

In A3444, the smaller angular extent of the offset means that only a global measure of the cold molecular gas can be obtained from the IRAM observations in this system and its higher redshift restricts us to just CO(1-0). The observation provides a marginal (2.0σ) detection of 0.33 ± 0.11 K km s^{-1} and a width of 172 ± 69 km s^{-1} at the velocity of the BCG. However, the restricted bandwidth of the A/B100 receiver means that a broader line could be present but is lost in the baseline subtraction. The implied total molecular gas masses of $\approx 1.7 \times 10^{10}$ M$_\odot$ for A3444 is consistent with the correlation of molecular gas mass and optical line luminosity in Edge (2001).

4.5.3 Ophiuchus

Edwards et al. (2009) studied the properties of the Ophiuchus cluster with the GMOS IFU and found line emission with a substantial ($\sim 4''$) offset from the BCG (Figure 4.6). Edwards et al. (2009) attributed this offset line emission to another galaxy and not to the BCG itself but given the similarity with respect to the X-ray emission to A1991 and A3444 we reconsider this system. In our reanalysis of these data we also find that the line emission is offset from the BCG by $\sim 4''$ which, at a redshift of z=0.028, corresponds to a projected separation of ~ 2.2 kpc. The line emission within Ophiuchus shows no component on the BCG with 100 per cent of the Hα emission coming from the offset component.
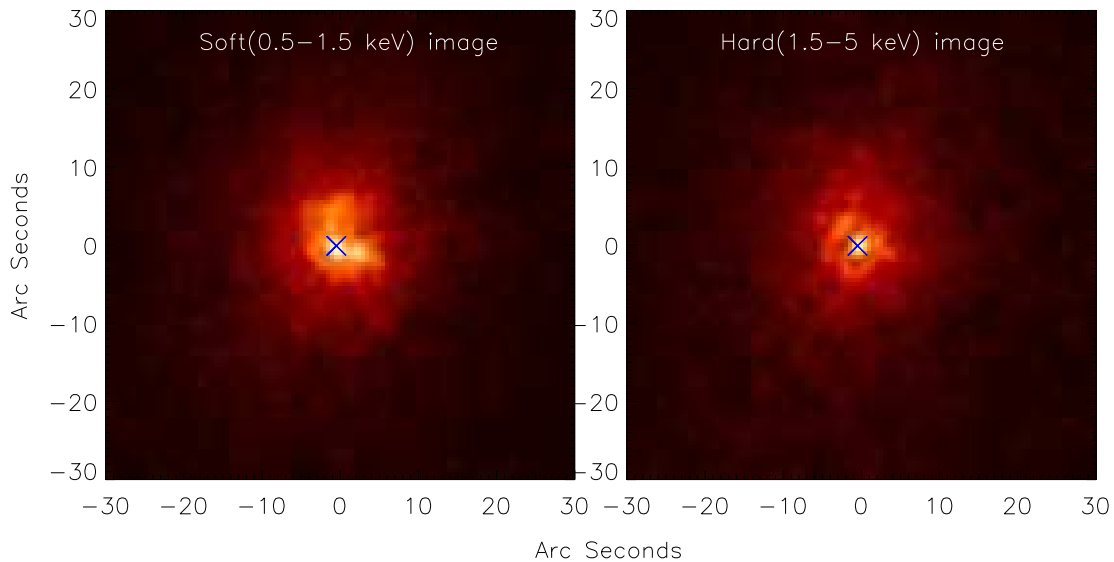
Figure 4.5: *Left* shows a soft (0.5-1.5 keV) X-ray image of the centre of A3444. A bright peak can be seen at the centre of the image which matches the position of the BCG. A secondary lower intensity peak can be seen to the west-south west of the central peak offset by ∼2-3 arcseconds. *Right* shows the hard (1.5-5 keV) image of the A3444 cluster core. A bright peak can clearly be seen at the centre of this image matching the position of the primary peak in the soft band. The crosses mark the location of the BCG on each image. The presence of this unresolved, hard emission on the central peak suggests this emission may be from an AGN component in the BCG.

Million et al. (2010) also analyse *Chandra* X-ray data and find that the X-ray peak in the Ophiuchus cluster is offset from the BCG by ∼ 4″, a similar offset to that seen in the line emission. In Figure 4.6 we compare the position of the X-rays and the offset line emission. We note that the *GMOS* field of view (shown by the dashed green line) ends along the north-east and north-west edges of the observed line emission but that otherwise the line emission lies towards the peak in X-ray surface brightness. While our analysis of these data find results consistent with those of Edwards et al. (2009) the alignment of the offset Hα and X-ray emission suggests a situation similar to that in A1991 and A3444.

In this system, there is sufficient S/N in the continuum that we can determine the stellar velocity. We extracted a spectrum of the BCG and used a penalised pixel-fitting method (Cappellari & Emsellem, 2004) to fit the Sodium D absorption from a catalogue of stellar templates. Comparison of the Hα line with the Sodium D(λ 5889,5895) stellar absorption find that the line emitting gas is offset from the

BCG by 603 ± 28 km s^{-1}. The velocity and line width maps are shown in Figure 4.7, the kinematics of the gas in this system are simple although some tentative evidence for a velocity structure is apparent to the east of the object (at the edge of the GMOS field of view). Other than this the velocity of the gas shows little variation ($\sigma = 31$ km s^{-1} which is half the velocity resolution of ~ 60 km s^{-1}) and the linewidth is uniform across the detected line emission (FWHM $= 235 \pm 38$ km s^{-1}). Future, wider field IFU observations are required to map the full extent and velocity structure of the line emission.

4.5.4   Time scales

The conclusion we draw from our extensive optical IFU sample (Chapter 3) is that the fraction of systems in which there is an offset between the majority of the optical line emission and the central galaxy of more than 8 kpc is relatively small (≈ 3 in 73). In the narrow-band imaging survey of 27 groups and clusters (McDonald et al., 2011), A1991 is the only object with a second component of the optical line emission that is offset from the BCG. Similarly, from X-ray observations of 24 line emitting clusters from the LoCuSS sample (Sanderson et al., 2009a) only four are offset from the X-ray centroid by more than 8 kpc (i.e. 15 per cent) (but none are offset by more than 15 kpc).

   We can use the statistics of offset line emission of the sample to estimate the lifetime of such offsets. Assuming that all clusters with a line emitting BCG may experience an offset at some stage, the fraction of BCGs showing this offset multiplied by the look-back time of the sample ($\sim$1 Gyr at the median redshift of the sample) gives an estimate on the lifetime of $\sim$40 Myr (3/77$\times$1 Gyr). With IFU observations, it is also possible to estimate the lifetime of the offset using the kinematics of the gas. Assuming the offset is orientated to the line of sight at an angle θ, the actual separation of the BCG and X-ray peak is $D = D'/sin\theta$, where D is the actual separation and D' is the projected separation that we observe. Similarly the projected and actual velocity difference is given by $V = V'/cos\theta$. We can determine the time scale of this separation to be $T = D'/V' \times cos\theta/sin\theta$.

   Assuming that the likelihood of any orientation is uniform over the area a hemisphere, then the median orientation angle will correspond to the angle that splits
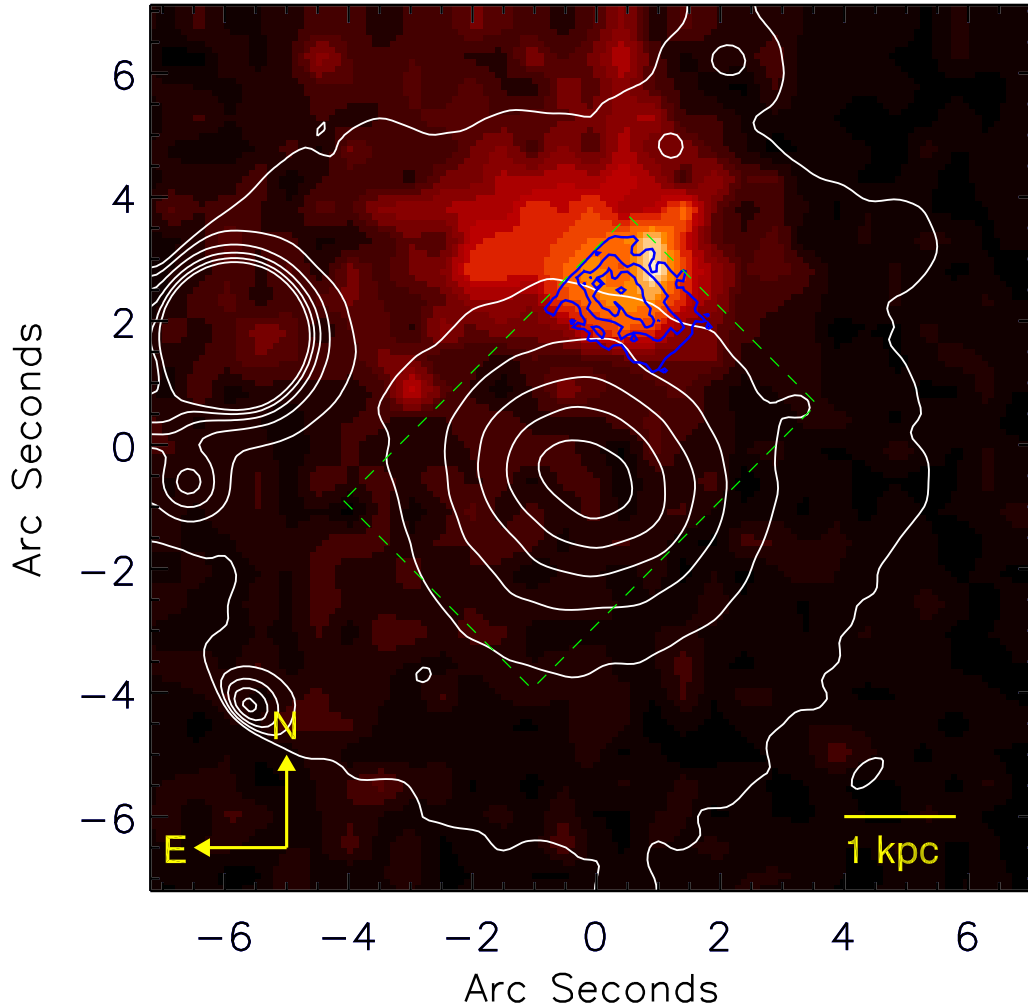
Figure 4.6: The colour scale shows the X-ray emission observed by Chandra with contours from the continuum emission from the *GMOS* R-band acquisition image of the Ophiuchus BCG. Blue contours show the position of the Hα line emission at 6, 12, 18 and 24 σ. The Hα line emission is offset to the north of the BCG. The position of the offset Hα emission lies near the peak in the X-ray surface brightness. It should be noted that the north-east and north-west edges of the line emission coincide with the edges of the *GMOS* field of view (shown as dashed green lines) so these contours may not represent the true extent of the Hα.

the hemisphere into two equal areas. This implies that $2\pi r^3 \cos\theta_2 = \pi r^3$ and hence $\theta = \cos^{-1} 0.5 \sim 60°$.

A1991 has the most well constrained parameters of the three objects and therefore by setting a limit on the offset velocity and distance we can limit the range of angles over which we expect the offset to be orientated. Assuming the maximum offset velocity to be 500 km s^{-1} and the offset distance to be no more than 20 kpc, we
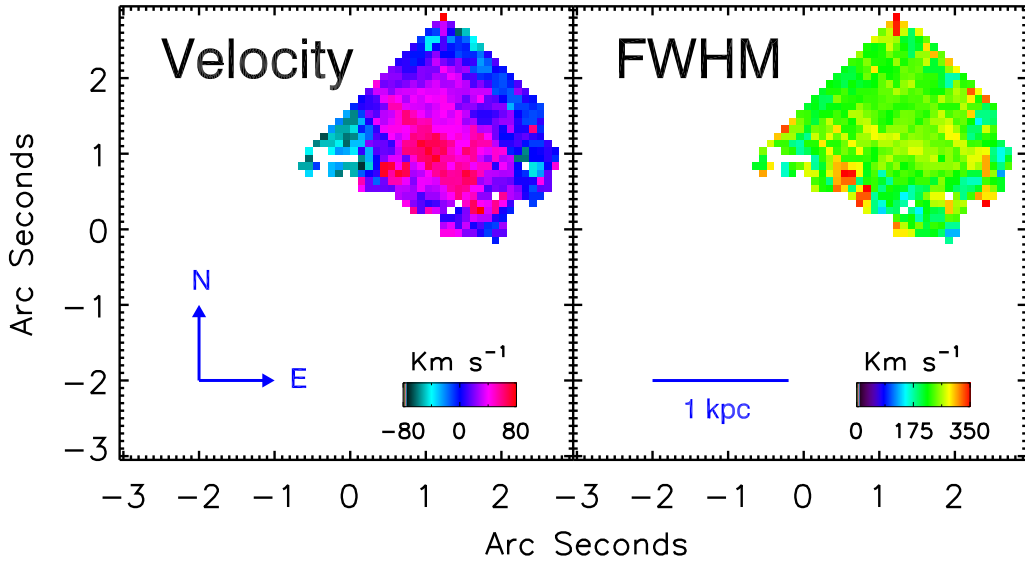
Figure 4.7: The Hα velocity field (*Left*) and FWHM linewidth (*Right*) for Ophiuchus, as derived from fits to the Hα - [NII] complex. The velocities are given relative to a redshift z=0.0304. The velocity and linewidths are simple and show little variation although tentative evidence for for a velocity structure is apparent to the east of the object.

calculate an orientation ranging from $30°$–$75°$. By applying the above equation with appropriate orientation angles we find that its most likely lifetime is 45 Myr with a possible range of 20–135 Myrs. These values are consistent with those calculated from the sample statistics suggesting that the lifetime of such offsets is a few tens to a hundred Myrs.

At a mass deposition rate of 10–$20 \, M_\odot \, yr^{-1}$ (Sharma et al., 2004) 2×10^7–2.5×10^9 $M_\odot$ could condense from the ICM within 20–135 Myr. With the most likely time scale of 45 Myr this corresponds to 5×10^8–10^9 $M_\odot$ so the expected mass of gas is comparable to our detected CO gas mass. It should be noted that the lower mass deposition rate represents gas centred on the BCG which is at a higher temperature and lower density than that at the offset position so should be considered a lower estimate.

4.6 Discussion

The most striking result from our observations is that the optical line emission is emitted predominantly from the region with the highest soft X-ray surface brightness and not the BCG. In the vast majority of clusters the peak in the X-ray emission is very close to the BCG (Peres et al., 1998; Hudson et al., 2010; Sanderson et al., 2009a) so determining whether the optical lines are primarily related to the cooling of the ICM or the BCG is not possible. The direct relationship between the core X-ray properties (e.g. cooling time or entropy) and the optical line emission in any BCG has been established (Rafferty et al., 2008; Cavagnolo et al., 2008). However, only in the very small minority of clusters where the 'sloshing' of the ICM resulting from major or minor cluster mergers (Ascasibar & Markevitch, 2006; Johnson et al., 2010; Million et al., 2010) or an episode of strong AGN activity temporarily results in the BCG not residing at the peak of the gas cooling is there an opportunity to make the direct test of whether the optical line emission is related primarily with the cooling gas or the BCG itself.

The presence of cold molecular gas in the cores of clusters can be explained through a number of mechanisms: mergers with gas-rich cluster galaxies or gas cooling from the intracluster medium. The gas mass observed in BCGs ($10^{9-11.5}M_{\odot}$) (Edge, 2001; Salomé & Combes, 2003) is too large to be explained by galaxy mergers or stellar mass loss but is consistent with heavily suppressed cooling from the ICM (Peterson et al., 2003; Peterson & Fabian, 2006; Sanders et al., 2010).

Given the close correlation between optical lines and CO found in other cluster cores the detection of ionised gas at the location of the X-ray peak suggests the presence of a reservoir of molecular gas offset from the BCG. We directly detect the presence of molecular gas in the form of CO in A1991 and make a tentative detection in A3444. In one system, A1991 we also detect CO at the offset position, with a molecular gas mass of $\sim 10^{9}$ $M_{\odot}$. The presence of such a high mass of molecular gas at the offset position clearly suggests that cooling is occurring despite the BCG and cluster core being separated.

Using the statistics from our sample we estimate that any offset of greater than 8 kpc can only remain for around 10^{8}yrs. This is consistent with the dynamical time

scale of the core implying that these "excursions" of the BCG from the X-ray peak are short-lived. If the molecular gas at the offset position is being produced in situ then it would have to cool from the ICM within this time frame. Within the central regions of the cluster core X-ray observations predict typical cooling rates of the order $\sim$ 1-10 M$_\odot$ yr^{-1} (Peterson & Fabian, 2006), at this rate of cooling the cluster core could deposit between 10^8 and 10^9M$_\odot$ of cold molecular gas in the $\sim 10^8$ yrs which it is not coincident with the BCG. As such, the offset molecular gas observed in A1991 is consistent with the upper band of cooling from the ICM of 25 M$_\odot$ yr^{-1} (Sharma et al., 2004).

Although A3444 and Ophiuchus do not have separate detections of cold molecular gas at the offset position, their similarities to A1991 suggest that it may be present. Due to the smaller angular offset between BCG and X-ray peak in A3444 and Ophiuchus, resolving the molecular gas is not possible with single dish observations. However, with the start of ALMA operations there is now the possibility to directly map the molecular gas in such systems allowing the separate components of the gas to be resolved.

An alternative explanation for the morphology of the extended molecular and ionised gas is ram pressure stripping of gas related to the BCG when a merger induces large motion of the ICM relative to the BCG. This requires an efficient mechanism to entrain the dense molecular gas into the much more tenuous ICM. The effect of magnetic fields could enhance this stripping but would have to be very effective to explain the acceleration observed in Ophiuchus. The observations presented here cannot rule out ram pressure stripping. However, future mm-interferometry should be able to map the cold molecular gas and allow us to distinguish between these mechanisms. If ram pressure stripping is responsible we would expect the molecular gas to be stripped less effectively than the optical line-emitting gas, while in the case of local cooling we would expect a similar morphology between the two phases.

4.6.1 Similar objects

The offset between the BCG and X-ray peak in clusters is not unique to these objects, both Abell 1644 (Johnson et al., 2010) and RXJ1347.5-1145 (Johnson et al., 2011) have a small offset and show evidence of sloshing similar to that seen here.

Markevitch et al. (2003) also find that two thirds of clusters classified as cool cores by (Peres et al., 1998) show evidence of cold fronts associated with sloshing. An offset along the line of sight is not always obvious suggesting the existence of more objects in which the BCG is dissociated from the cluster core but cannot be detected by observations due to projection effects.

There are also a number of other systems where the peak of the line emission is coincident with the BCG but have less intense offset line emission in the form of extended envelopes and filaments. A1795 (Crawford et al., 2005) and RXJ0821+07 (Bayer-Kim et al., 2002) both show very extended optical emission that follows the highest X-ray emissivity in the cluster and also has associated cold molecular gas emission (Salomé & Combes, 2004; Edge & Frayer, 2003). Most recently, Canning et al. (2011) present evidence for a filament of optical line emission extending from the BCG in A2146 which is undergoing a major merger where the peak in the X-ray emission is offset from the BCG by 37 kpc. The IFU data presented in Canning et al. (2011) doesn't cover the X-ray peak so it can't be established if A2146 is similar to the three clusters presented here but it illustrates that a significant merger is required to dissociate the BCG from the X-ray peak. In a major merger the disruption in the core will be significant. Russell et al. (2010) show that the pressure profile in the core of A2146 is very asymmetric, unlike that in A1991 which is dynamically more quiescent. Therefore, the process of cluster-cluster merging, and the longer lived sloshing that it induces, may be required to produce the brief decoupling of the peak in the intracluster medium density from the BCG observed in all of these systems.

Another viable mechanism for inducing bulk motion of the ICM in a cluster core is the inflation of cavities due to AGN activity in the BCG. Blanton et al. (2011) show a close correspondence between filaments of high X-ray surface brightness and optical line emission in A2052 (see Chapter 3) which has an extensive cavity network. The compressed gas in these filaments has a short cooling time so the optical line emission may also be related to local cooling. The systems presented in this Chaper do not resemble A2052 or exhibit the large cavities required to generate the observed offsets, so AGN feedback is unlikely to explain the lop-sided offsets we observe in A1991, A3444 and Ophiuchus. However, the small scale correlation between strongest X-ray

cooling and optical line emission suggests a common mechanism behind them.

The existence of cold gas that is 'orphaned' in the cores of clusters may have a number of implications for more distant systems. For instance, in the high redshift radio galaxy TXS0828+193 ($z = 2.6$), Nesvadba et al. (2009) find a cloud of cold molecular gas emitting at CO(3-2) that has no bright optical or near-infrared counterpart that is 80 kpc from the radio galaxy itself. They speculate that this may be analogous to low redshift clusters but note that the gas tends to be associated with the central galaxy. While the total gas mass and physical offset are substantially larger in TXS0828+193 than in A1991 or A3444, the similarity between the systems may point to a common mechanism.

4.7   Summary

Within the cores of most clusters there is a clear spatial coincidence between the position of the BCG and the peak of the ICM density. However there are a few clusters in which the BCG and cluster core are found to be decoupled. In such systems, it is possible to disentangle the effects of the cluster core and the BCG on the ICM and study each individually. Here we study three such systems selected from a parent sample of 73 massive X-ray selected clusters where we find that the optical, millimetre and X-ray observations of the cores show extended optical line emission and cold molecular gas directly related to the peak of the cooling of the intracluster medium and not the central galaxy. These three systems are the only clusters from our sample to show a significant offset between the BCG and cluster core suggesting that such a phenomenon is rare and transient. From the sample we find that a significant offset occurs in only 2–3 per cent of systems and that they likely have lifetimes lasting of the order of 20–100 Myr. We note however that it is possible for systems to have an offset along the line of sight which we would not detect so this fraction may be slightly higher and should be considered a lower limit.

The rarity of such significant offsets between the BCG, X-ray peak and optical line emission points to a large event in cluster evolution, a major cluster merger or possibly a powerful AGN outburst. Mergers are predicted to drive shocks through the core of the ICM at early times and cause sloshing as a later effect (Ascasibar & Markevitch, 2006; Johnson et al., 2010; Million et al., 2010; ZuHone et al., 2010,

2011) both of which are capable of separating the BCG from the cluster core. X-ray observations of A1991 suggest the passage of a cluster-wide shock through the core of the cluster and similar observations of Ophiuchus show sloshing of the ICM suggesting the possibility of a recent merger. Whatever the reason for the separation the gas cooling at the X-ray peak will continue and cooled gas will be deposited away from the BCG. This provides a unique opportunity to directly constrain the process of gas cooling without the presence of a BCG.

4.8   Afterword

Since completing this study a number of objects which show evidence of a velocity offset between the BCG, line emission and apparent cluster velocity have been identified. We postulate that these are analogous the Abell 1991, Abell 3444 and Ophiuchus but viewed along the direction of the offset. These other objects show a large velocity offset but very small or no apparent spatial offset. Obtaining the cluster and BCG velocities for the objects in this study would allow us to test if these also exhibit an offset in velocity space. We can obtain the BCG velocity by fitting the stellar Sodium D, g-band and H+K absorption features. To find the cluster core velocity requires spectroscopic redshift measurements to be obtained for a substantial fraction of cluster members within the gravitational influence of the core (~ 10 kpc). These galaxies will follow the large scale gravitational potential of the cluster so their mean velocity should trace the centre of the DM distribution.

Chapter 5

Cold gas dynamics in Hydra-A: evidence for a rotating disk

5.1   Overview

In this Chapter we present multi-frequency observations of the radio galaxy Hydra-A (3C218) that lies in the core of a massive, X-ray luminous cluster of galaxies. Hydra-A was identified in Chapter 3 as having one of the largest peak–to–peak velocities of all objects in the VIMOS sample and our observations indicate that there is an extended ($\sim$ 5 kpc) disk of cold, molecular and atomic gas in the core of Hydra-A that rotates perpendicular to the orientation of the radio jets. The detection of broad, double-peaked lines of CO(2-1) with IRAM 30m and [CII]157μm and [OI]63μm with *Herschel* PACS allow us to estimate the mass of the cold gas within the region covered by the disk to be $M_{gas} = 2.33 \times 10^9 \pm 0.28$ M$_\odot$. Optical and NIR IFU spectroscopy with VIMOS and SINFONI on the VLT trace the dynamics of the ionised gas and warm molecular Hydrogen. The line profiles and kinematics of these gas phases can be interpreted as a rotating disk within the BCG. These high spatial resolution observations demonstrate that the complex line profiles found in the cold atomic and molecular gas are related to the disk. Finally, an *HST* image of the galaxy shows that this gas disk contains a substantial mass of dust. We conclude that the cold gas originates from the direct cooling of the intra cluster medium. This suggests that it should therefore retain the velocity of the cluster which could result in two velocity components if the BCG is not at rest with respect to the cluster. We note the alignment between the axis of rotation of the disk and the axis along which the AGN is inflating cavities in the ICM which hints at a possible conection

between the gas cooling on kpc–scales and the accretion of material onto the black hole. We finish by discussing the implications of these observations for models of cold accretion, AGN feedback and cooling flows.

5.2 Introduction

The symbiotic relationship between the brightest cluster galaxy (BCG) and the dense intracluster medium (ICM) that surrounds it has important implications for our understanding of the formation and evolution of massive galaxies (see Fabian, 2012; McNamara & Nulsen, 2012, for reviews). The energetics of the gas show that the different gas phases are connected, for instance the close correlation between the X-ray properties (cooling time, central entropy etc.) of the cluster core and the detection of optical lines in the BCG as shown by Cavagnolo et al. (2008) and Sanderson et al. (2009a). Hence, the implicit connection of the optical emission to the cold (Edge, 2001; Salomé & Combes, 2003) and warm (Edge et al., 2002; Egami et al., 2006)(Donahue et al. 2009) molecular gas, suggests that there is a direct link between the rapidly cooling gas in the ICM ($t_{cool} < 10^9$ years) and the presence of cold molecular gas. However, any model positing that the cool gas in the BCG condenses from the hot ICM must also satisfy stringent observational constraints on the rate of energy loss from gas at temperatures above $\sim \frac{1}{3} T_{\text{cluster}}$ and strong limits on cooling of gas below that temperature. (Peterson et al., 2001; Sanders et al., 2010). AGN in the BCG may supply the heat required to curtail radiative cooling. While the global AGN energy budget seems sufficient, the details of how the AGN prevents the ICM from rapidly cooling are not yet settled.

Feedback of energy from AGN outbursts has been invoked both to provide a potential source of the heating required to truncate the cooling of the ICM and to resolve the over-production of massive galaxies in semi-analytic models (Bower et al., 2006; Croton et al., 2006). This AGN feedback injects mechanical energy into the ICM as outflows from the black hole inflate kpc–scale cavities in the X-ray atmosphere (McNamara & Nulsen, 2007). One of the most striking examples of these cavities is Hydra-A (3C218 McNamara et al., 2000; Wise et al., 2007), which has clearly defined X-ray surface brightness depressions in the ICM that spatially correlate to the complex radio structure in this radio source. Hydra-A is the central

galaxy of an X-ray luminous cluster which exhibits strong optical line emission which shows a complex velocity structure that clearly indicates evidence of rotation (Simkin, 1979; Ekers & Simkin, 1983) and dust (Hansen et al., 1995). McNamara (1995) identified the presence of excess blue light from the central $\sim 8'' \times 6''$ (8.4$\times$6.3 kpc) region which is spatially coincident with the rotating emission line nebula. This region has a major axis which in projection is aligned almost perpendicularly to the radio jet axis and suggests the presence of a young stellar population within the rotating ionised gas which they attribute to locally enhanced star formation fuelled by either the cooling flow or in–falling material. McNamara (1995) also noted that this configuration is similar to the standard model of AGN disk accretion, although the scales involved in this system are much greater.

The detection of HI absorption (Dwarakanath et al., 1994, 1995; Taylor, 1996), CO line emission (Salomé & Combes, 2003), PAH features (Donahue et al., 2011) and warm H_2 ro-vibrational and rotational lines (Edge et al., 2002; Donahue et al., 2011) all suggest a significant mass of atomic and molecular gas at a range of temperatures in the core of the galaxy. The dynamics of this phase and its relationship to the optical lines and associated star formation are open issues given that most observations are from a single dish or single line of sight.

In this paper we present new data over sub-mm to optical wavelengths that shed new light on the nature and dynamics of the cold gas in Hydra-A. In particular, new data from *Herschel* (Pilbratt et al., 2010) and IRAM 30m combined with Very Large Telescope (VLT) integral field data provide a much clearer picture of the dynamics of the cold gas. In §5.3 we outline out observations and analysis techniques. Next we outline our results (§5.4) before discussing their implications in §5.5. Finally a summary and conclusions are reported in §5.6. In the assumed cosmology, (Chapter 2) $1''$ corresponds to a physical scale of 1.053 kpc at the redshift of Hydra-A, z=0.054878 (Smith et al., 2004).

5.3   Observations and Data Reduction

5.3.1   VIMOS

Optical IFU observations of Hydra-A were taken using the VIMOS (Visible Multi-object Spectrograph) instrument on the 8.2m (VLT) in October 2007. Three 600 second exposures were taken with a pointing dither included between each exposure to minimise the effect of bad pixels. The HR_Orange Grism and GG435 filter (spectral resolution of $R \sim \Delta\lambda/\lambda \sim 2650$ over the wavelength range 5250–7400 Å) were used to observe Hα ($\lambda_{rest} = 6562.8$ Å) at the redshift of the cluster. The observations were taken in moderate seeing conditions with a mean seeing of $\sim 1.25''$.

We reduced the raw data using the ESOREX package. We performed the basic data reduction including bias subtractions, flat fielding and the wavelength and flux calibrations. In order to prepare the data for sky subtraction we masked any point–like objects to remove any stars within the field. The BCG was then removed from the field by masking all pixels within an isophote of half the peak flux. This level was chosen empirically as the best compromise to allow a good sampling of sky pixels while removing the majority of the BCG light. The sky level for each quadrant is then the median value of the remaining pixels at each wavelength increment. This sky spectrum was then subtracted from each pixel in the four quadrants before they were combined into a single datacube. Finally, we median combined the three exposures for each pointing in order to eliminate cosmic rays. To mosaic the three pointings we determine the exact position of the BCG in each observation and combine them centring on this position to create a cube with a $\sim 29'' \times 28''$ field of view.

5.3.2   SINFONI

The SINFONI (Spectrograph for Integral Field Observations in the Near Infrared) instrument on the VLT was used to take H and K band IFU observations of Hydra-A (programme 082.B-0671, PI Nesvadba) in November 2008 and February 2009. The observations consist of three visits in each band, with each visit comprising six 300 second exposures, four centred on the BCG and two on an offset sky region. The

observing conditions were similar to those of the VIMOS observations with a mean seeing of $\sim 0.59''$.

The ESOREX package was set up for SINFONI IFU observations and used to reduce these data. We corrected for dark current, the linearity of the detector, optical distortions between the slitlets and performed the basic calibration steps as for VIMOS. The sky reduction was also performed using this package for the separate sky observations taken during each pointing. The individual pointings in each band were then combined into a single cube in the same manner as the VIMOS observations. This procedure produced cubes with a $\sim 8'' \times 8''$ field of view.

5.3.3 Analysis of the IFU data

The spectral cubes produced by the reduction processes were unwrapped into two dimensional spectral images so that the presence of emission lines could be identified by eye. Spectral models were fitted to each line at each spatial position so that maps of the spectral properties could be produced. The fitting was performed on a small region of the spectrum around the line to enable the fitting routine to work more effectively. This region corresponded to 160 Å (240 wavelength elements) for VIMOS and 490 Å (200 wavelength elements) for SINFONI. The noise level was calculated using a second such region near the first that contained no emission lines or sky features. The median value of the spectrum within the extracted region was taken as a continuum model against which to compare a fit to the line. The fits to the line were made using Gaussian models in which the parameters were allowed to vary. These fits were accepted when they provided a 7σ better fit than the flat continuum alone. The primary fit to the VIMOS data was to the Hα/[NII] triplet. The models were fit to the rest wavelength of the line and the redshift was allowed to vary, the three lines relative rest frame positions were fixed. The total flux in the Hα line and strong [NII]λ_{rest} 6583 Å line were allowed to vary independently, the flux in the weaker [NII] line was set at one third the flux of the brighter line. The line widths were allowed to vary between pixels but the [NII] was forced to have the same width as the Hα. The continuum was typically "flat" over the short wavelength ranges being studied. As such the continuum level was set to a constant value throughout each spectral model. However, the value was allowed to

vary between spatial resolution elements. In lower flux regions where a 7σ fit could not be obtained the routine binned the surrounding 8 pixels and attempted the fit again. In the SINFONI observations the brightest lines are from Paschen α (Paα) and molecular hydrogen. The rest frame wavelengths of these lines are sufficiently separated to allow each line to be fitted independently from the other lines. A single Gaussian model was fitted to the line at the rest wavelength and the redshift, flux, width and continuum level were allowed to vary. Again the routine binned pixels together in the event a 7σ fit could not be obtained. When a line was detected in this way the single Gaussian model (or the triplet in the case of Hα and [NII]) was tested against a two component model to check for extra velocity components. This second Gaussian was varied independently of the other model (central redshift, intensity and line width) and was allowed to be much broader. When all the parameters were re-minimised, the χ^2 of the new fit was calculated and compared to the original models. Although this provided a better fit to the data the extra components were found to not be significant due to the reduction of the degrees of freedom.

5.3.4   IRAM 30m

We obtained IRAM 30m data for the CO(1-0) and CO(2-1) lines in Hydra-A in April 2010. The observations were performed simultaneously in exceptional conditions ($\tau_{230\mathrm{GHz}} \sim 0.05$) with the EMIR receiver using a 4 GHz bandwidth covering each line (Carter et al., 2012). The observation was of 2 hours duration with wobbler switching with a $90''$ throw. The observations reached a noise level of 0.3 mK in 100 $\mathrm{km\,s^{-1}}$ bins.

5.3.5   Herschel

Hydra-A was observed with *Herschel* as part of an Open Time Key Project to observe a statistical sample of cooling flow clusters (programme OTKP_aedge1, PI Edge). We used the PACS instrument to obtain spectral observations of the two principal atomic cooling lines, [OI] (OD:536, OBSID:1342207793) and [CII] (OD:538, OBSID:1342207817) at 63 and 157 μm respectively. The lines were observed in line spectroscopy mode using the chopping and nodding implementation to account for the background and dark current. These were then analysed using the standard

pipeline routines included in the latest release of the Herschel Interactive Processing Environment (HIPE *v. 7.1.0*). A detailed description of the Herschel data reduction can be found in Mittal et al. (2011). The full analysis of these spectral data and the additional PACS and SPIRE photometry will be made elsewhere (Oonk et al., in preparation).

5.3.6 HST

An *HST* ACS image of Hydra-A was obtained on the 16th April 2011 using ACS with the WFC detector and F814W filter for an exposure time of 2367s. Standard calibrations were then applied including subtraction of the bias, correcting for dark current and flat fielding. This observation was taken as part of a programme to obtain high resolution imaging of all the *Herschel* OTKP clusters (Proposal ID 12220, PI Mittal).

5.4 Results

5.4.1 IFU Maps

In Figure 5.1 we show the HST F814W image of Hydra-A. It is apparent from this image that there is a surface brightness depression running across the BCG at $\sim$ 70 degrees to the north-south line. The VIMOS Hα flux map (Figure 5.2) shows a bright elongated region which is coincident with and shares the same PA as the Paα and dust lane as shown in Figure 5.1. Lower surface brightness Hα emission is also present extended to the north and south of the BCG.

The Hα velocity map shows a continuous velocity gradient across the BCG of $\sim$ 600 km s^{-1}. This velocity gradient runs across the BCG along the major extent of the elongated high surface brightness region. We note that the extended emission to the north and south is slightly blue shifted from the velocity of the BCG but is constant and consistent with the median velocity of the Hα emitting gas. The line width (FWHM) of the emission is greater ($\sim$ 390 km s^{-1}) in the redshifted emission than in the blue-shifted emission ($\sim$ 270 km s^{-1}) which may be due to greater absorption on the blue-shifted side that limits the range of radii sampled by
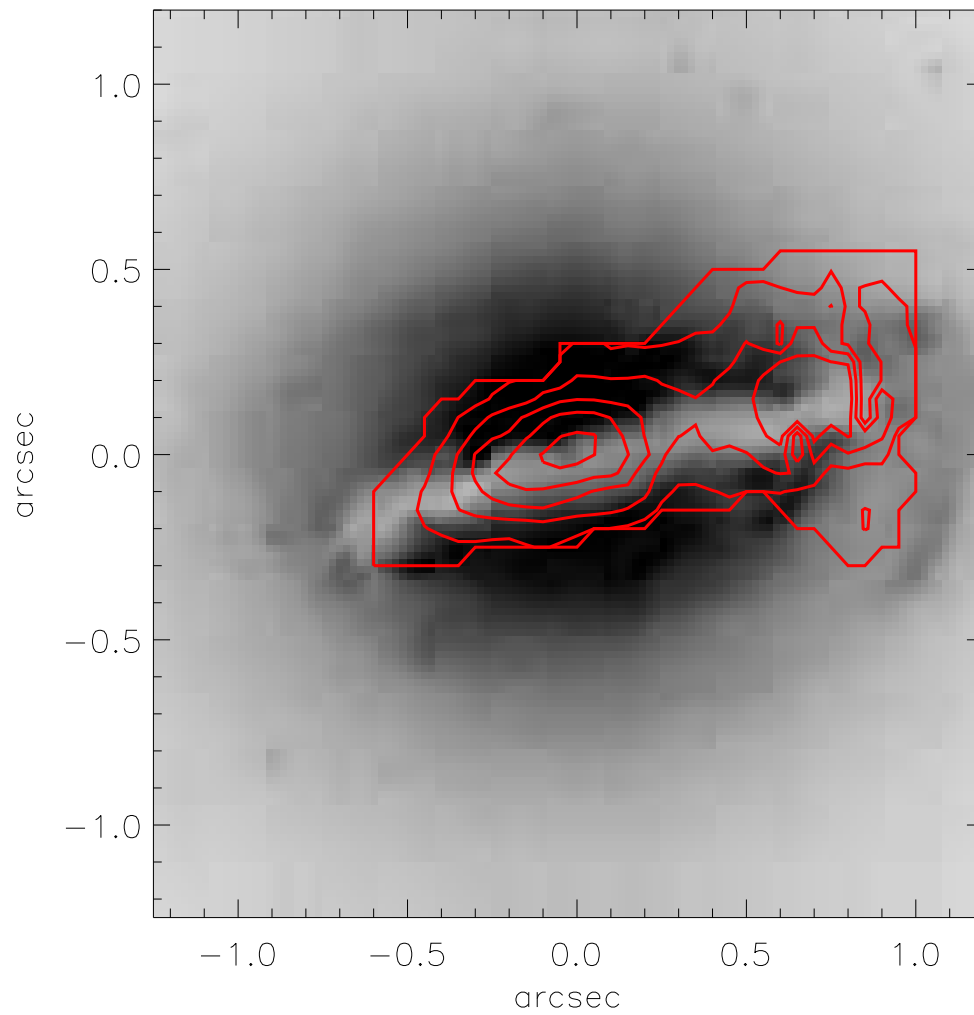
Figure 5.1: .
A HST F814W image of Hydra−A showing a clear dust lane across the centre of the BCG. Contoured over this is the Paα intensity which can be seen to run along the length of the dust lane.
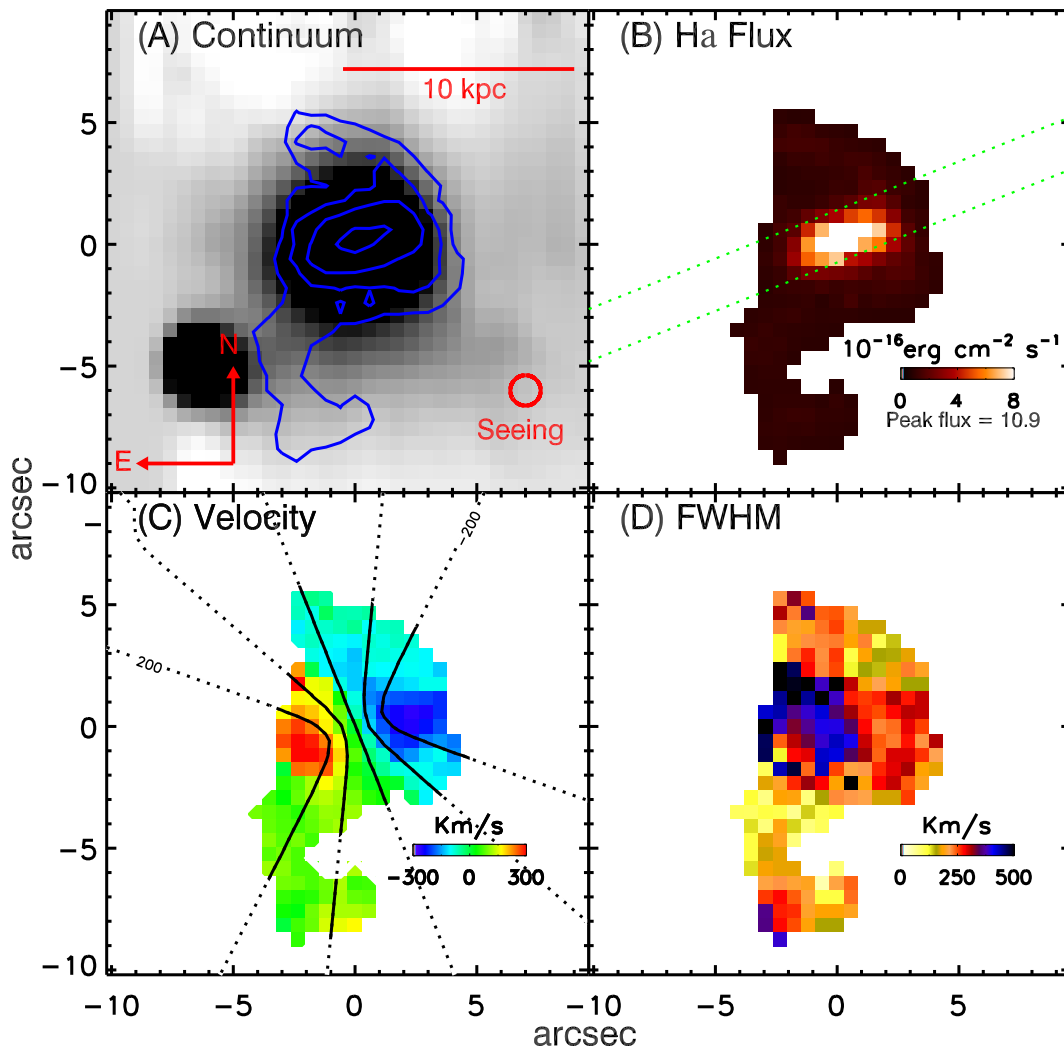
Figure 5.2: This figure shows the IFU maps of the Hα emission as taken from fits to the Hα/[NII] triplet observed in the VIMOS cubes. Panel (A) shows a continuum image made by collapsing the cube The contours show the Hα emission clearly centred on the BCG. Panel (B) is a Hα Flux map which shows a disc of bright emission running across the BCG. In panel (C) we show the relative velocity of the Hα line to the galaxy redshift, a strong velocity gradient of ∼ $600 km s^{-1}$ can clearly be seen. Contoured on this plot are lines of constant velocity created by fitting a disk model to the velocity map. The final panel (D) shows the measured Full Width Half Maximum (FWHM) of the line which can be seen to broaden to the left hand side of the disc.

our line of sight in that region.

Figure 5.3 shows a K-band continuum image produced by collapsing the K-band SINFONI observation over a region free of telluric absorption ($2.07 - 2.32\ \mu$m). The dust lane seen in the optical image is also present in the IR but is much weaker and less prominent due to emission from a point source at the centre of the BCG and the weaker dust absorption. The Paα map shows emission elongated across the galaxy in the same direction as the surface brightness depression. The emission shows a two component structure with a depression in the Paα emission separating two bright components. The mass of ionised hydrogen in a system can be estimated from the Paα flux (Oonk et al., 2010) as

$$M_{HII} = 2.41 \times 10^{18} \left(\frac{F_{Pa\alpha}}{ergs^{-1}cm^{-2}} \right) \left(\frac{D}{Mpc} \right)^2 \left(\frac{n_e}{cm^{-3}} \right)^{-1} \qquad (5.4.1)$$

where $F_{Pa\alpha}$ is the Paα flux, D is the distance in Mpc and n_e is the electron number density. Assuming an electron density of $n_e = 200$ cm^{-3} as in Oonk et al. 2010, a distance of 242 Mpc and the measured Paα flux of 6.31×10^{-14} erg s^{-1} cm^{-2} we find a H$_{II}$ mass of 4.5×10^7 M$\odot$. The Paα shows a similar velocity structure to the Hα with a continuous gradient of $\sim$ 500-600 km s^{-1} running across the emission. The line width (FWHM) of the Paα is slightly higher in the centre of the emission ($\sim$ 280 km s^{-1}) than on the edges ($\sim$ 140 km s^{-1}). This velocity width pattern is consistent with observing through a rotating disk where we sample less random velocity components through the edge of the disk than through the centre.

The H$_2$ 1-0 S series lines sample the warm (1–2×10^3 K) vibrationally excited molecular gas within the BCG. Within the K-band spectrum of Hydra-A we find four strong lines associated with the molecular gas, H$_2$ 1-0 S(0) to S(3) (Figure 5.4).

Of these lines, S(0) is the least reliable since it is located at the noisy red edge of the spectrum. As such, fits could only be obtained at the 5σ significance level for this line. The separate component seen in the Paα map does not appear in the 1-0 S(0) emission. This non-detection of 1-0 S(0) is likely to be due to the lower signal–to-noise as the line is present within the total spectrum of this region though the line is weak compared to Paα. The S(0) fits do not show as extreme a velocity gradient as seen in the Paα but they do show a similar velocity structure with a continuous velocity gradient running almost east to west across the emission. We
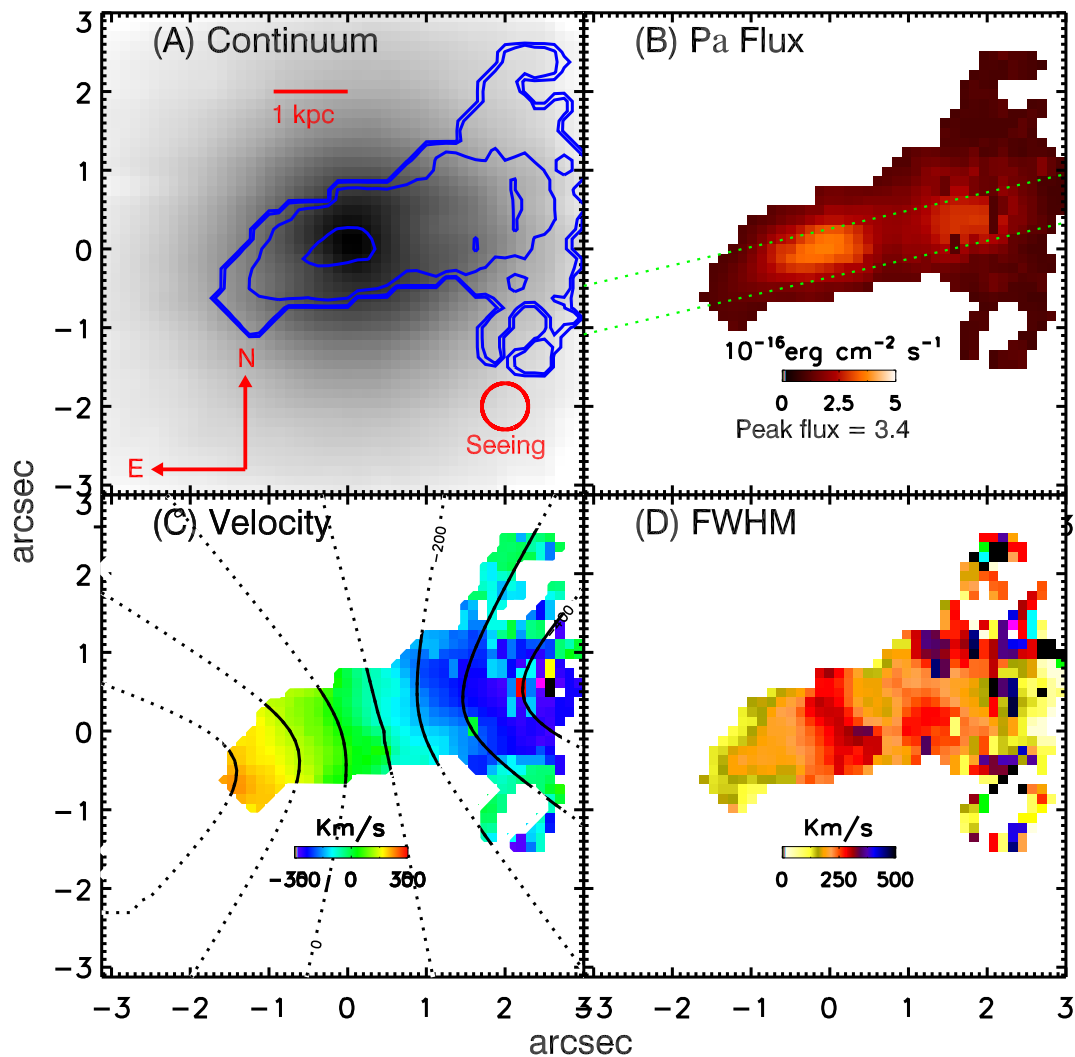
Figure 5.3: This figure shows the IFU maps of the Paα emission as taken from fits to the Paα emission line observed in the SINFONI cubes. Panel (A) shows a continuum K-band image created by collapsing the cube with contours of the Paα emission. In panel (B) is a Paα Flux map which shows an elongated structure across the BCG. In panel (C) we show the relative velocity of the Paα line to the galaxy redshift, a strong velocity gradient of ∼ 600 km s⁻¹ can be seen along a similar PA to the Hα. Contoured on this plot are lines of constant velocity created by fitting a disk model to the velocity map. The final panel (D) shows the measured Full-Width Half-Max of the line which seems largely uniform.

Figure 5.4: This figure shows the IFU maps of the 1-0 S(0) to 1-0 S(3) emission as taken from fits to the emission lines observed in the SINFONI cubes. From top to bottom the panels are arranged in order from S(0) to S(3). The Far left panels (A) show a continuum K-band image created by collapsing the cube with a flux map for each line contoured in blue. The centre left panels (B) show the Flux maps which typically show an elongated structure across the BCG. The dotted lines on these panels show the region from which the rotation curves were extracted and represent the position angle of the disc as determined by the disc fitting. In the centre right panels (C) we show the relative velocity of each emission line to the galaxy redshift. A strong velocity gradient of ~ 600 km s^{-1} can be seen along a similar PA to the Hα. Contoured on these plots are lines of constant velocity created by fitting a disk model to the velocity maps. The far right panels (D) show the measured Full-Width Half-Max of the lines. Each line shows an increase in the FWHM at the point where the flux map appears brightest, for the S(1) and S(3) lines this point also matches the dynamical centre (the point at which the velocity of the disk model goes through 0). However the S(0) and S(2) lines also show enhanced line width along the edges of the emission, though this is likely a result of the lower signal to noise and therefore not real. The consistency of the velocity structure of these lines with those of the ionised Hα and Paα suggests that the warm molecular gas occupies the same rotating disc as the ionised gas.

note that the S(0) emission is not as extended (likely due to lower signal–to–noise) along this direction as the other K-band lines which may account for this. The FWHM of the S(0) line is highest at a position centred on the peak of the emission, which is consistent with being at the centre of the BCG. However, the map shows regions of similar linewidth throughout the structure. The similarity of linewidths is possibly due to blending with noise spikes that artificially broaden the line fit.

Figure 5.4 also shows the S(1) line emission, which is one of the most reliably characterised molecular lines due to being strong and isolated from other lines and telluric features. For consistency with the other molecular lines however we present a map of the fits to emission above the 5σ significance level. The S(1) emission shows a clear extent, matching that seen in the Paα and dust lane. In contrast however the S(1) flux map does not show the double component structure seen in the Paα. However, the velocity structure of the S(1) matches that seen in the ionised lines with a clearly visible velocity gradient of ~ 600 km s^{-1} running along the long axis of the emission. The FWHM of the S(1) emission peaks at ~ 375 km s^{-1} in the centre of the BCG. This width is substantially higher than that seen in the Paα but is consistent with that seen in Hα. The width falls to ~ 200 km s^{-1} at the edges which is consistent with both the ionised lines.

The mass of warm molecular hydrogen can be estimated from the H$_2$ 1-0 S(1) flux using equation 4 from Oonk et al. (2010)

$$M_{H_2} = 5.08 \times 10^{13} \left(\frac{F_{H_2 1-0\ S(1)}}{\mathrm{erg s^{-1} cm^{-2}}} \right) \left(\frac{D}{\mathrm{Mpc}} \right)^2 \tag{5.4.2}$$

where $F_{H_2 1-0\ S(1)}$ is the flux in the S(1) line, and D is the distance in Mpc. Again using a distance of 242 Mpc and the measured $F_{H_2\ 1-0\ S1}$ flux of 142×10^{-16} erg s^{-1} cm^{-2} we find a H$_2$ mass of 4.2×10^4 M$\odot$.

The S(2) emission is shown in Figure 5.4. While the S(2) emission from Hydra-A was weaker than the S(0) its observed wavelength put it in a significantly less noisy part of the spectrum resulting in the detection of more emission at 5σ. As such its structure more closely matches that of the S(1), suggesting the structure in the S(0) map is likely the result of incompletely detected emission and is not real. As expected from the other molecular lines the velocity structure of the S(2) emission matches that of the ionised gas with a ~ 600 km s^{-1} gradient running along the line

of the dust lane. The linewidth of S(2) appears considerably higher than the S(1). This is however likely a result of the binning used by the fitting procedure to obtain the required signal to noise. By binning together pixels at substantially different velocities before fitting the line width can be artificially increased. Consulting the integrated spectrum suggests that there is no significant difference in the warm molecular line widths as is expected since they are emitted from the same gas. The S(3) line (Figure 5.4) is another strong molecular line. However, its position in the spectrum places it near a strong telluric feature. The removal of this telluric feature results in an increase in noise compared to other parts of the spectrum. While the line is clearly detected at greater than the 5σ significance limit, the physical properties derived from the fit are less reliably determined than those of the S(1) line. We also note that in the nuclear regions the S(3) emission appears to be blended with HeI emission, requiring that the two lines have been fitted together fixing the rest wavelength separation. The velocity profile of the S(3) line is consistent with that from the other molecular lines and ionised lines presented so far, with a velocity gradient of $\sim$ 500–600 km s^{-1} running along the direction of the dust lane. The linewidth of S(3) is mostly consistent with that of S(1) peaking at $\sim$ 500 km s^{-1} near the centre of the emission and falling to $\sim$ 250 km s^{-1} at the edges.

[FeII] emission was the only line detected in the H-band observations. The maps presented in Figure 5.5 show that the [FeII] emission is compact and located at the centre of the BCG as is expected for a high ionisation line. Despite being compact the line does appear to be extended to the east on scales slightly greater than the seeing. Within this small extent there appears to be a velocity change of $\sim$ 200 km s^{-1} across the emission. This velocity gradient is consistent with that found from the other ionised and molecular lines across a similar extent. However higher resolution observations of this emission are required to confirm this velocity gradient is real. If it is, it presents a direct link between the gas on galaxy–wide scales and the nuclear region. The peak FWHM of the [FeII] line is greater than that seen in the other lines, at $\sim$ 700 km s^{-1}, as would be expected if this emission came from the denser nuclear region. The component extended to the east has a substantially lower width ($\sim$ 300 km s^{-1}), which is more consistent with the width seen in the molecular emission lines.
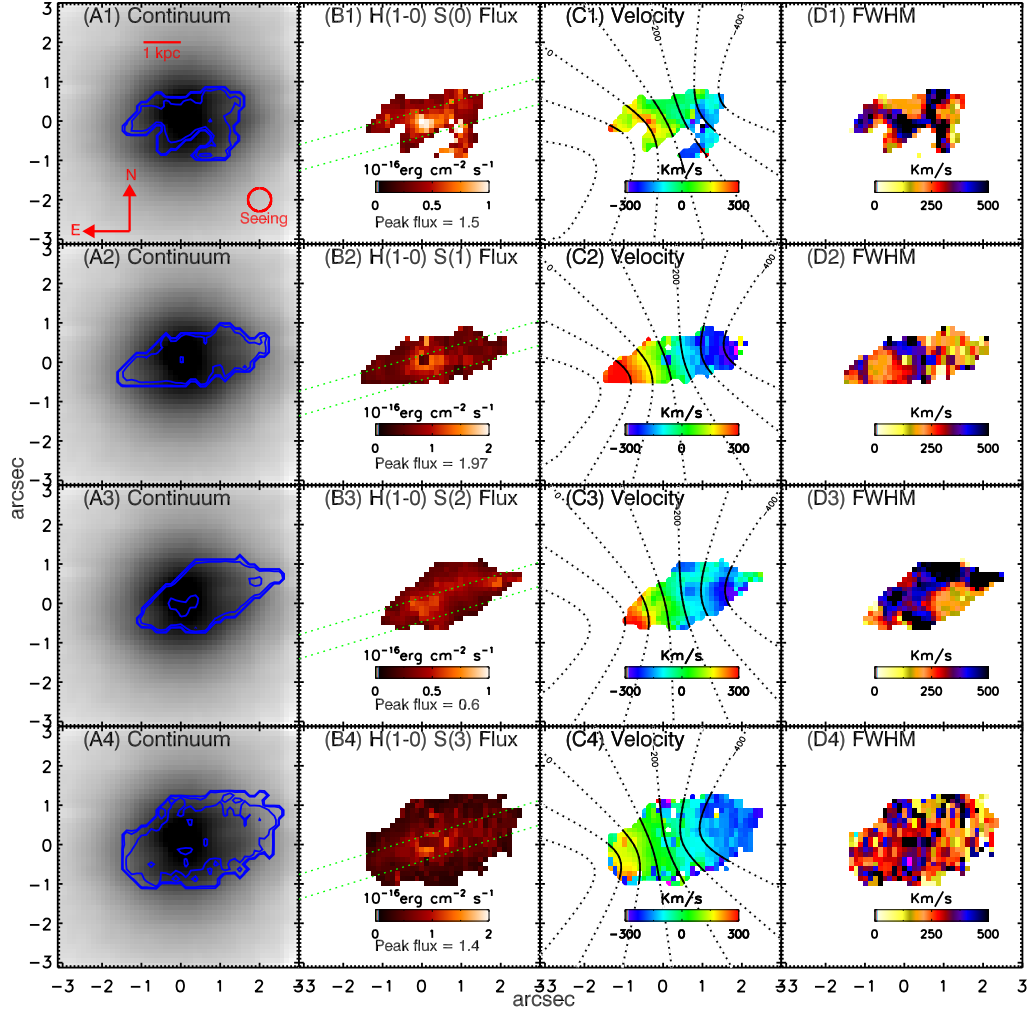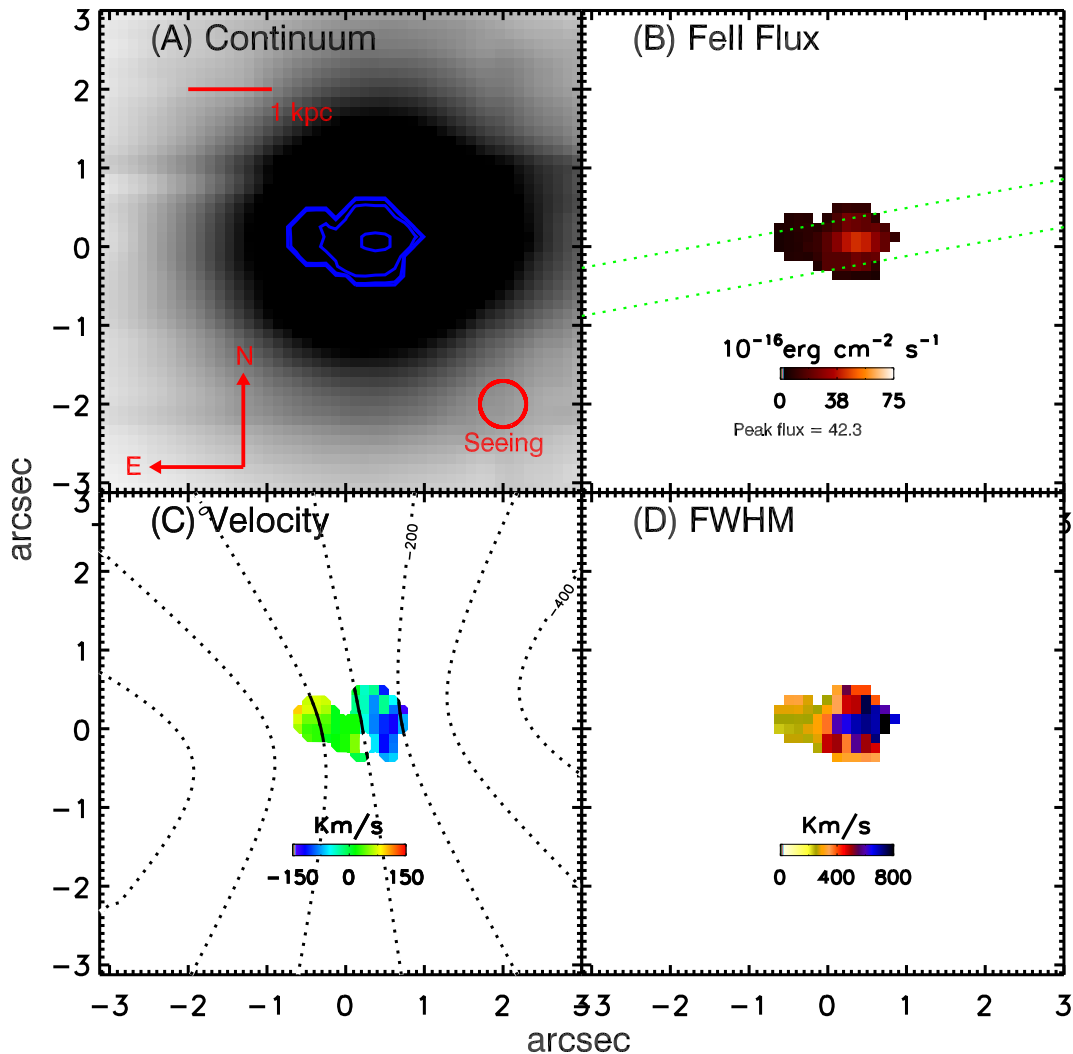
Figure 5.5: This figure shows the IFU maps of the [FeII] emission as taken from fits to the [FeII] emission line observed in the SINFONI cubes. Panel (A) shows a continuum K-band image created by collapsing the cube with contours of the [FeII] emission. In panel (B) is a [FeII] Flux map which shows an elongated structure across the BCG. It can be seen from this that the [FeII] emission is much more centrally concentrated than the other lines, which is expected as it is associated with regions of the strongest photoionisation. In panel (C) we show the relative velocity of the [FeII] line to the galaxy redshift, a strong velocity gradient of ~ 200 km s^{-1} can be seen along a similar PA to the Hα. Contoured on this plot are lines of constant velocity created by fitting a disk model to the velocity map. It should be noted that the [FeII] emission is barely resolved at just twice the seeing so this velocity gradient may not be real. The final panel (D) shows the measured Full-Width Half-Max of the line which shows a much broader profile in the central regions than the other lines.

TABLE 5.1.
PROPERTIES OF THE SEVEN EMISSION LINES FIT WITH DISK MODELS

Line	Position angle (Degrees)	Inclination (Degrees)	Transition R (kpc)	Luminosity (10^{40} erg s^{-1})	$V_{2.2}$ (km s^{-1})	Redshift (At zero velocity)
Hα	164 ± 22	56 ± 13	2.00 ± 0.75	14.22 ± 0.76	397 ± 49	0.05490[12]
Paα	167 ± 20	69 ± 15	1.97 ± 0.55	45.24 ± 2.83	341 ± 36	0.05452[8]
H(1-0) S(0)	156 ± 21	65 ± 19	1.46 ± 0.41	5.16 ± 1.11	384 ± 25	0.05439[5]
H(1-0) S(1)	164 ± 19	64 ± 18	1.48 ± 0.38	15.58 ± 5.94	381 ± 65	0.05440[5]
H(1-0) S(2)	168 ± 38	64 ± 23	1.76 ± 0.80	7.69 ± 1.14	369 ± 42	0.05438[6]
H(1-0) S(3)	163 ± 18	66 ± 14	1.54 ± 0.35	25.80 ± 1.34	421 ± 66	0.05439[3]
[FeII]	170 ± 5	56 ± 9	1.70 ± 0.13	—	355 ± 33	0.05473[10]

Table 5.1: The [NII] and Hα have the same PA and Velocity as they are fit as a triplet. The Transition radius is measured as the point at which the fit rotation curve begins to flatten. A suitable standard star for the [FeII] was not taken so no value of the luminosity could be obtained. $V_{2.2}$ is defined as the inclination corrected velocity at $R_{2.2}$, with the values of $R_{2.2}$ set to 2.95 and 2.20 kpc for VIMOS and SINFONI, respectively.

5.4.2 Rotation of the ionised gas

The ionised and warm molecular gas emission lines all show kinematics which are consistent with an ordered rotation. Disk models were fit to the velocity maps shown above in order to determine the consistency of this rotation between the different lines. These disk models were constructed such that the velocity profile follows an arctan function. This model is none physical but was found to be a good approximation of the velocity curve of disk galaxies by Courteau (1997). Table 5.1 gives the position angle and rotation velocity measured by the fit. The fits find position angles consistent to within $\sim 15°$ and rotation velocities consistent to within ~ 60 km s^{-1} (roughly twice the maximum spectral resolution). Given the small spatial scale of the [FeII] emission compared to the seeing, there are very few uncorrelated data points in the disk fit so we constrained the disk model for [FeII] to have an inclination and PA consistent with the other lines. We use the sodium–D absorption feature (λ_{rest} 5895.92, 5889.95 Å) from a FORS observation to determine the central redshift of the BCG. From this fit we find the stellar component has a redshift of $z = 0.05434[38]$. Combining the information from the seven lines suggests the presence of a disk of ionised and molecular gas in the centre of the Hydra-A BCG which is rotating with a peak-to-peak velocity of ~ 700 km s^{-1} separated by 5 ± 0.7 kpc.

Figure 5.7 shows rotation curves extracted from the velocity maps along with profiles derived from the models using the same PA estimate, which was consistent
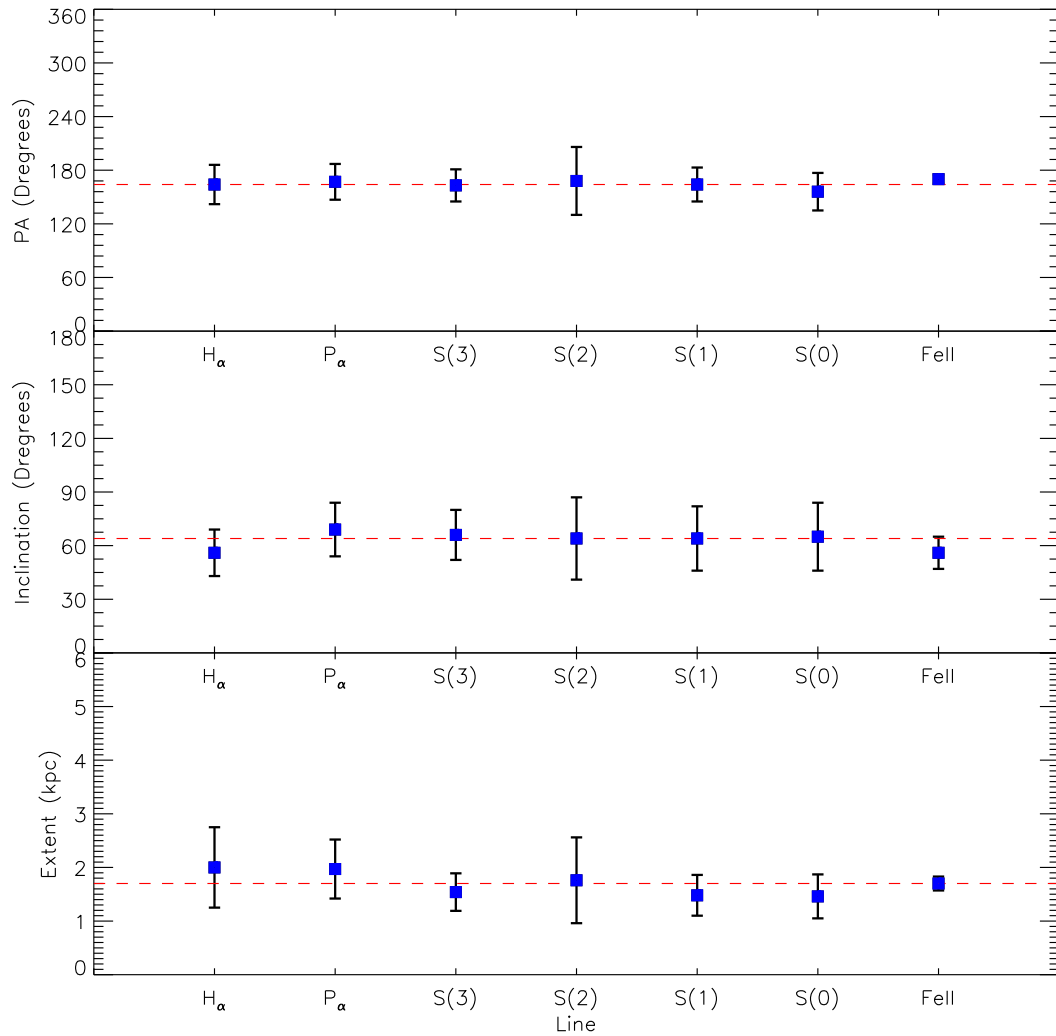
Figure 5.6: Here we show a comparison of the key parameters of the best fit for the disk model for each line (Note that the rotation velocity comparison is shown later in Figure 5.10). The top panel shows a comparison of the position angle, the middle shows the inclination angle and the bottom shows the distance at which the velocity curve turns over. The dashed line on each plot shows the median value. The errors are calculated from the Monte Carlo fitting routine and are the maximum deviation from the best fit parameters with a $\Delta\chi^2 < 1$ one assuming all other parameters are allowed to minimise. Note the smaller error on the FeII is a result of having to use more constrained limits on the parameters in order to get a fit. For each of these three parameters the disk models show a good consistency between the lines.
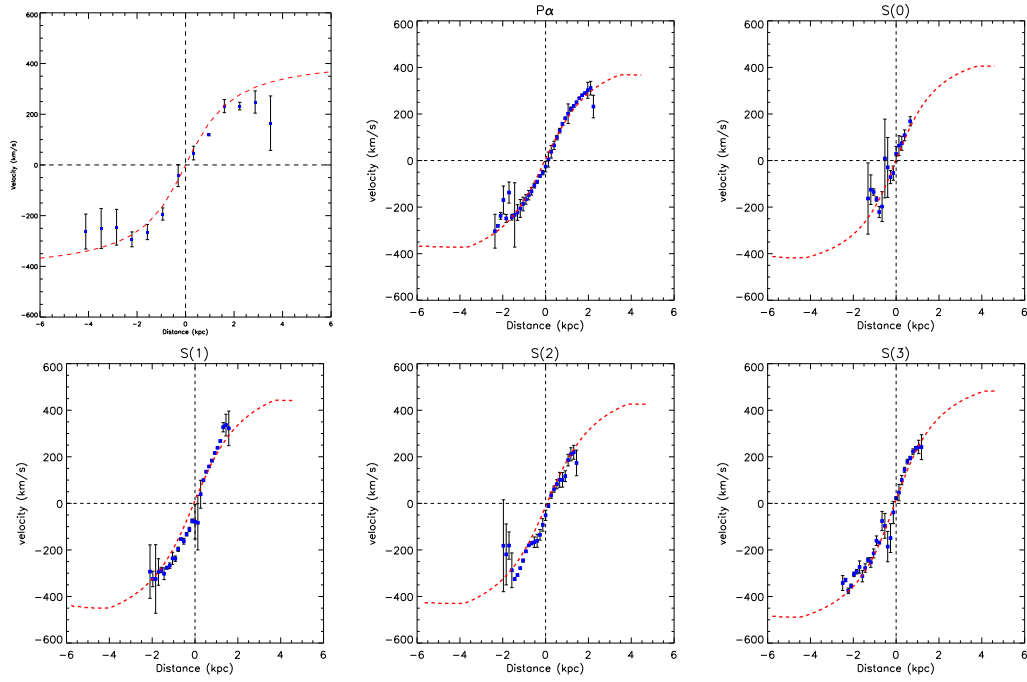
Figure 5.7: Velocity profiles for the six brightest lines from our VIMOS and SINFONI observations. The profiles are presented as observed (not inclination corrected), the errors are 1σ. The dashed line shows the velocity profile of the disk model taken along the same line as the data. For each line the model provides a good fit to the data suggesting the velocity is well fit by a disk model, however we not that for none of the lines do we reach the flattened part of the velocity profile.

for the disk models for each line. The extracted rotation curves all show little deviation from the models except at the edges where the line fits are not as precise due to the lower signal–to–noise. The S(0) line velocity profile appears less consistent with the model than the velocity profiles of the other lines displayed in Figure 5.7. However, as discussed in section 5.4.1 the map of this line is noisier than the others and it is consistent with the model within errors. Due to the [FeII] line being barely resolved we do not show its rotation curve.

We use these rotation curves to directly constrain the dynamical mass of the BCG within the radius enclosing the disk. We define the position $R_{2.2}$ as a distance from the centre of rotation equal to $2.2 \times$ the disk scale length and calculate the mass within this region (as in Miller et al., 2011). If the disk were purely exponential, this point would correspond to the peak rotational amplitude (Freeman, 1970; Binney & Tremaine, 1987). The inclination–corrected velocity at this point ($V_{2.2}$) is then used to calculate the dynamical mass within the disk. For the Hα emission we find $R_{2.2} = 3.2$ kpc and $V_{2.2} = 397$ km s^{-1} which corresponds to a dynamical mass of $1.2 \times 10^{11}\,M_{\odot}$. However, we note that the spatial resolution of the Hα map is 0.6 kpc. By contrast the Paα map has a spatial resolution of 0.26 kpc and we find $R_{2.2}$ = 2.2 kpc, $V_{2.2} = 340$ km s^{-1} and a dynamical mass of $6.0 \times 10^{10}\,M_{\odot}$. As the Pa$\alpha$ map has a higher spatial resolution we use this as $R_{2.2}$ and thus find the dynamical mass within $R_{2.2}$ to be $M_{dyn,2.2} = 5.96 \times 10^{10}\,M_{\odot}$.

5.4.3   Cold molecular emission

In Figure 5.8 we show the CO(2-1) spectrum of Hydra-A which shows a strong and broad line present within the cluster. This detection is notable for several reasons, not least the remarkable width of the line. The full width zero intensity of 1200 km s^{-1} is comparable to the bandwidth of the past attempts to detect CO in this system (O'Dea et al., 1994; Edge, 2001; Salomé & Combes, 2003) so it would have been impossible to detect the full line flux before the advent of the wide bandwidth receivers such as EMIR. The line is broader than all previous CO detections in BCGs by a factor of 30 per cent and it suggests there may be a potentially significant number of systems that have escaped detection due to their intrinsic line width.

The spectrum also points to considerable velocity structure within the line. There are only two published double-peaked CO detections in BCGs (3C31 and 3C264, Lim et al., 2000) so the discovery of a third in a 3C radio galaxy points to a potential connection between powerful radio emission and cold gas disks.

The total CO(2-1) line intensity of 1.87±0.24 K km s^{-1} in units of measured antenna temperature (T_A^*) implies a molecular gas mass of $2.2 \pm 0.28 \times 10^9$ M$_\odot$ assuming a conversion factor of 3.0×10^{20} cm^{-2} (K km s^{-1})$^{-1}$, and a CO(2-1)/CO(1-0) ratio of 0.7 following Edge (2001). This gas mass is comparable to the gas mass found in most other CO detected BCGs (Edge, 2001; Salomé & Combes, 2003) and consistent with the dynamical mass of the disk (M$_{dyn,2.2} = 5.96 \times 10^{10}$ M$_\odot$).

Finally there is significant radio continuum at both 3 and 1 mm detected as an excess baseline in the EMIR observations (285±30 and 128±18 mJy at 3 and 1 mm, respectively). This emission is consistent with recent high frequency observations of the core and lobes with MUSTANG on the GBT (Cotton et al., 2009) and implies that the vast majority, if not all, of the detected 850 μm SCUBA flux of 69.3 mJy (Zemcov et al., 2007) is from the radio continuum and not from dust emission.

5.4.4 Atomic Gas

We show the [OI] spectrum of Hydra-A taken with *Herschel* in Figure 5.9. The spectrum shows a striking similarity to the velocity structure of the CO(2-1) line implying that they trace the same cold gas clouds. This correspondence between atomic and CO velocity profiles has also been observed in other BCGs at the centre of cooling flows (for example A1068 and A2597, Edge et al., 2010; Tremblay et al., 2012)). The intrinsic velocity resolution of the PACS spectrograph at the longest wavelengths makes it harder to match the velocity structure of the [CII] line (Edge et al., 2010). However, if the CO(2-1) and [OI] lines are smoothed to the intrinsic resolution of PACS at [CII] then the three lines are consistent. From these observations it is possible to estimate the mass of atomic gas present in the BCG. Following Wolfire et al. (1990), and assuming the cooling rate and C$^+$ abundance determined therein, one can estimate the atomic gas mass as deduced from CII to be

$$M_{HI} = 2.7 \times 10^6 \left(\frac{D}{\text{Mpc}} \right)^2 \left(\frac{F_{\text{CII}}}{10^{-17}\text{Wcm}^{-2}} \right) \tag{5.4.3}$$
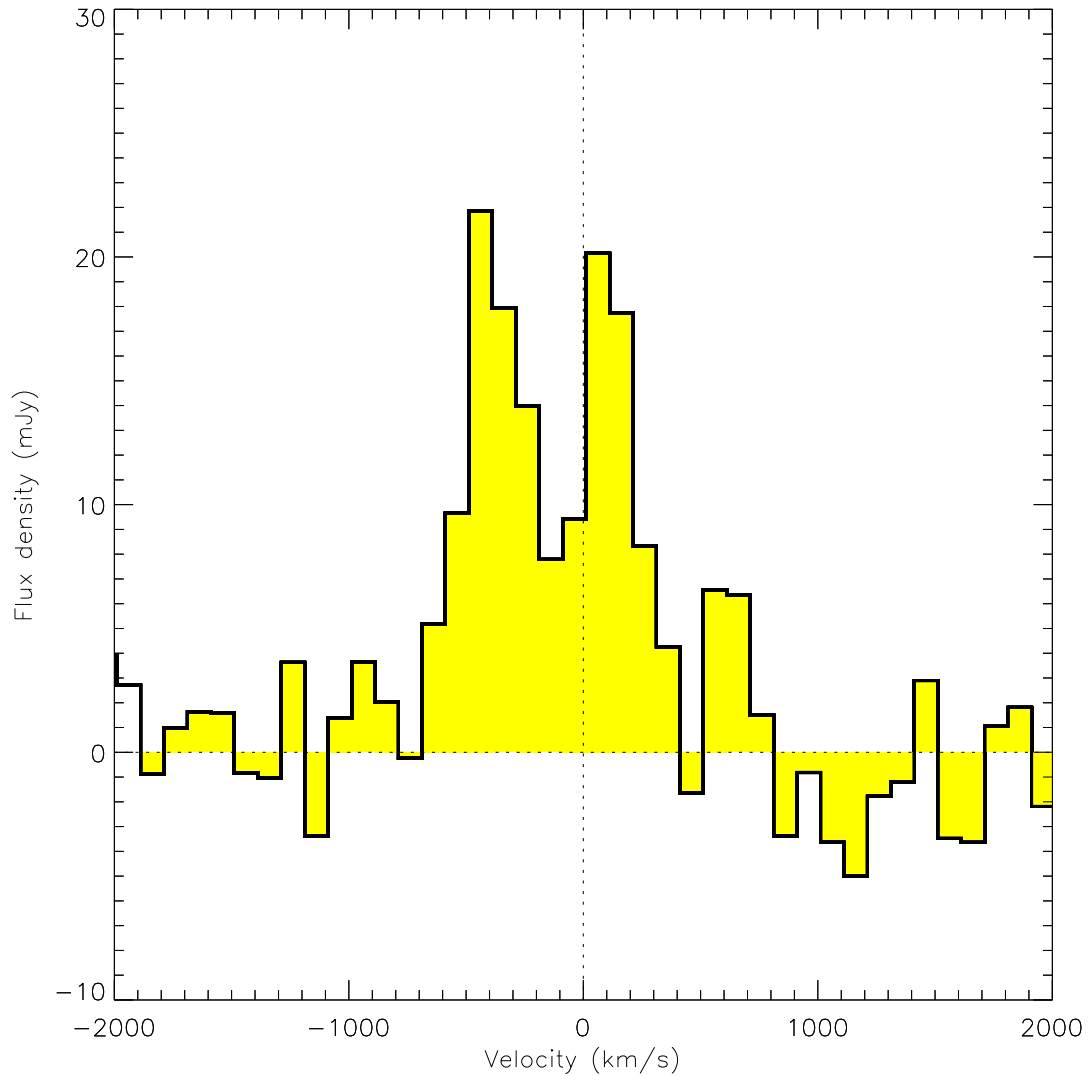
Figure 5.8: This is the CO(2-1) spectrum of Hydra-A taken from the 4 MHz backend on IRAM 30m. The line shows a width of 500 to 600 km s^{-1} consistent with the rotation velocity seen in ionised lines. A double peak structure is present with the trough between peaks situated at the dynamical centre of the system

where D is the distance to the cluster in Mpc, and F_{CII} is the flux of CII in W cm^{-2}. We measure a CII flux of 5.3×10^{-21} W cm^{-2} and use a distance of 242 Mpc, which gives an atomic gas mass of $8.4 \ 10^7$ M$_\odot$. The assumptions going into this estimate make it rather uncertain (perhaps by as much as an order of magnitude) but this mass is just below the upper limit of 4×10^8 M$_\odot$ derived from HI absorption by Dwarakanath et al. (1994).

5.5 Discussion

The results presented above build directly on the previous studies of Hydra-A and confirm unambiguously that there is a coherent and large amplitude velocity gradient (~ 700 km s^{-1}) in the gaseous disk across the galaxy. Importantly, the major axis of this velocity gradient is aligned perpendicular to the axis of the radio jets. The addition of the multiple molecular and atomic line detections allows us to connect the cold gas to the observed emission line dynamics from IFU observations. The complex, double-peaked velocity profile seen in both the CO and [OI] lines is consistent with the cold gas being distributed throughout the disk. This match extends to both the ionised Hydrogen (traced by Hα and Paα) and the CO and [OI] gas sharing a significant asymmetry to the blue that appears to be localised to the western edge of the gas disk.

The prominence of the gas disk in Hydra-A is accentuated by the fact that it is being viewed close to edge-on and appears as a striking dust lane in HST (Fig 1, Mittal, et al., in preparation) and ground-based imaging (Ramos Almeida et al., 2011). Similar gas disks are known in other brightest cluster galaxies at the centre of cooling flows, e.g. NGC1275 in Perseus (Wilman et al., 2005; Lim et al., 2008) and NGC383/3C31 (Lim et al., 2000; Okuda et al., 2005; Ocaña Flaquer et al., 2010). The prevalence of these disks in radio luminous systems is suggestive but may be an observational selection effect as many of the galaxies with known disks were selected for HST imaging on the basis of their radio power(de Koff et al., 2000; Verdoes Kleijn & de Zeeuw, 2005; Tremblay et al., 2007).
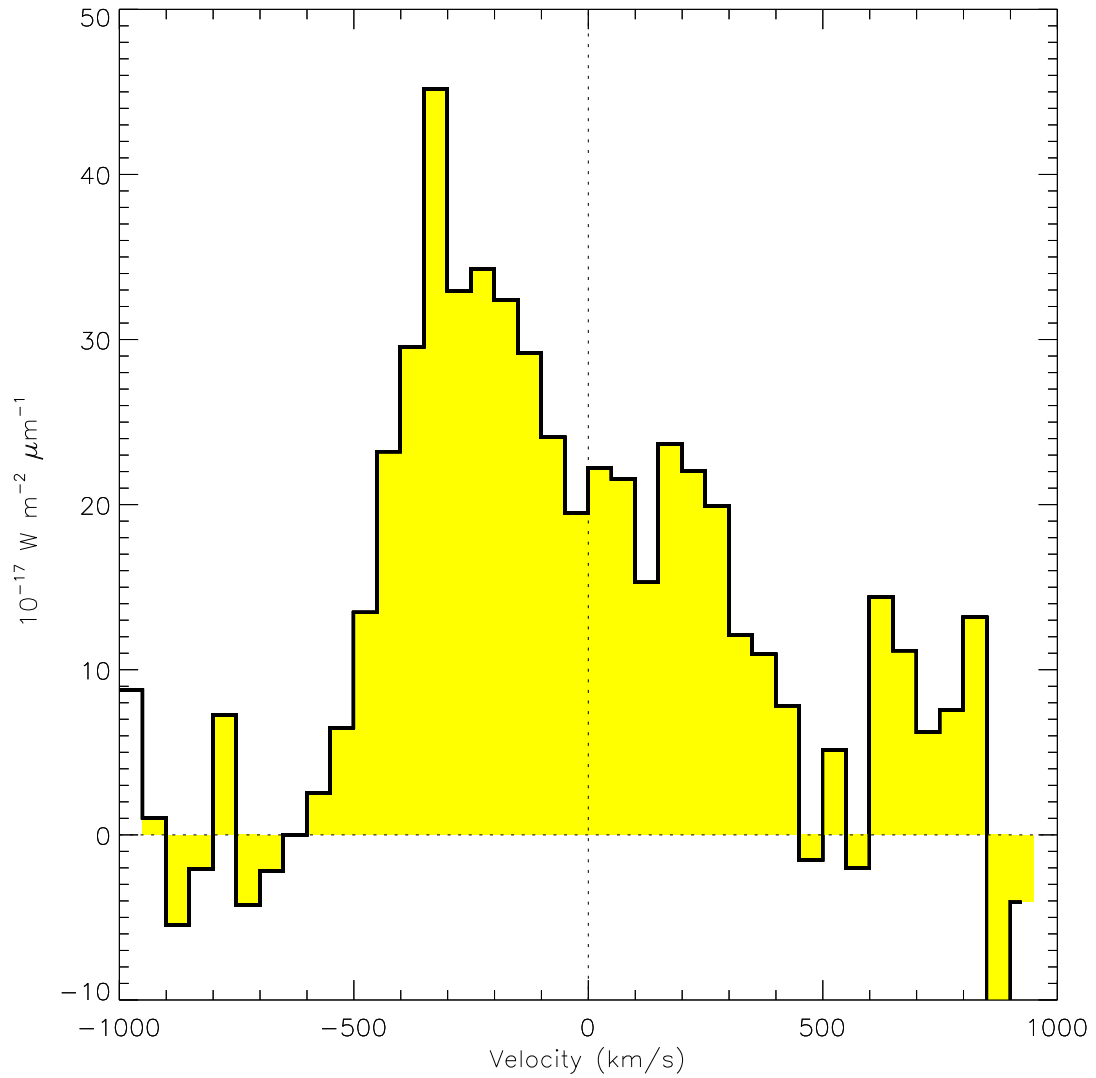
Figure 5.9: Here we show the far infrared [OI] spectrum of Hydra-A taken with the PACS spectrometer on the *Herschel* space telescope. The width and structure of the line are consistent with the CO(2-1) although the ratio of the flux in the two peaks is different between the two lines.

5.5.1   Fuelling the feedback?

Hydra-A offers several significant insights into the nature of cooling flows and AGN feedback. The discovery of a distinct disk of cold gas in such a powerful radio galaxy can be used to assess the energetics and fuelling of AGN activity.

Studies of the cavities in the intracluster medium indicate that a substantial amount of energy is being transferred from the AGN into the surrounding gas through the mechanical work done by the radio lobes (McNamara et al., 2001; McNamara & Nulsen, 2007). The total energy of the outbursts is 10^{59-63} erg which corresponds to the accretion of $10^{6-7.5}$ $M_\odot$ of gas on to the central super massive black hole assuming an efficiency of 0.1. Combining our estimates of the gas masses in the various phases we calculate the total mass of cold gas in the disk to be 2.33×10^9. Oonk et al. (in prep) calculate that the dust mass is 1.2×10^7 at a temperature 26 K. Assuming that the dust lane in the disk contains the majority of this then the total mass of cold material detected in the disk is 2.34×10^9 $M_\odot$ which is sufficient to fuel a future outburst of comparable magnitude.

While this comparison is by no means proof that the cold gas was solely responsible for the fuelling of any outburst in Hydra-A, other systems may provide clues. Edge (2001) note that the BCGs with the most powerful extended radio emission (Cygnus-A, Perseus-A, M87 and Hercules-A) are less luminous in CO for their given optical line luminosity. If the radio emission is generated by the rapid depletion of the gas in the core of the galaxy then this could explain the weaker molecular gas emission.

The origin of the cold gas is another open question. While the accretion of cold gas from in–falling cluster members and through stellar winds can be invoked for lower luminosity systems like M87 and NGC4696 (Sparks et al., 1989, 2004), these stochastic and ad hoc processes struggle to explain the observation that the vast majority of BCGs in cooling flows exhibit optical line emission (Cavagnolo et al., 2008) and CO lines (Edge, 2001; Salomé & Combes, 2003) when the central cooling time or entropy is low or the large gas masses ($> 10^{10.5}$ $M_\odot$) found in many systems. Instead, the residual gas cooling that is not truncated by the AGN feedback is still significant (Wise et al., 2007; Sanders & Fabian, 2011) and the 10–100 $M_\odot$ yr^{-1} observed in the largest cool cores can result in the accumulation of sufficient cold gas

in $\sim 10^9$ yr. This reasonably constant supply of cold gas could in principle power the cores of all BCGs in the strongest cool cores all the time. The observation that all strong cool cores have a radio source (Mittal et al., 2009) may be an indication that this consistent accumulation of fuel for powering the black hole and star formation is indeed the case.

If the accretion of cold gas deposited from the cooling of intracluster gas is the dominant accretion mode in cluster cores, then what properties do we expect other systems to share with Hydra-A? The very large dust disk and the extremely broad line width in Hydra-A may be the product of a preferential viewing angle where the cold disk of gas and dust is being observed almost edge-on (Figure 5.1). This fortuitous viewing angle also maximises the visibility of the X-ray cavities if they are created perpendicular to the disk. NGC1275 does not show a similar dust lane but the presence of an inner spiral structure and a direct line of sight to the nuclear emission implies that we are viewing any disk at a substantial angle ($> 30°$).

5.5.2   The blue shifted line emission

The extended, one-sided nature of the blue shifted Paα line component implies that this emission is from gas that is not directly related to the gas disk or the disk is asymmetric. In NGC1275 gas on 5–20 kpc scales is observed which does not follow the rotation observed on smaller scales (Salomé et al., 2008; Lim et al., 2008; Mittal et al., 2012) so the presence of gas that has a substantial offset from the systemic velocity of the BCG is not unprecedented. Indeed, there are systems where the majority of the optical line emission lies off the BCG spatially and in velocity, such as A1991 and Ophiuchus (Chapter 4, Hamer et al., 2012). In these cases the peak of the X-ray emission is coincident with the line emission and not on the BCG. In the case of Hydra-A, the X-ray emission close to the BCG is strongly affected by the radio cavities but there is a relatively weak excess to the west of the BCG (Wise et al., 2007).

What are the possible origins of this additional gas component? One possibility is that it is related to the merger of another gas-rich galaxy with the BCG. However, we view this scenario as unlikely given the relatively large gas mass involved and the lack of any donor galaxy in the cluster core. The inference that the cold gas found

in the cores of most clusters is related to gas cooling rather than a merger with a gas-rich galaxy has been the subject of extensive debate over the past 3 decades (Sparks, 1992; Edge, 2001) but the close connection between the X-ray properties of the cluster core and the optical, infrared and radio properties of the BCG which is seen in the vast majority of systems clearly favours a sustained and non-stochastic explanation (Cavagnolo et al., 2008; Voit et al., 2008; O'Dea et al., 2008b; Sanderson et al., 2009a). Therefore, the origin of the cold gas from the direct cooling of the ICM best matches the observations.

One implication of the gas cooling from the ICM is that it will retain the velocity of the cluster and not necessarily the BCG. So, if the BCG is not at rest with respect to the cluster, then in principle it is possible that two velocity components could be observed, one associated with the cluster and one with the BCG.

To test whether this is the case in Hydra-A, we extracted the galaxies known within 15′ (940 kpc) from NED and find 20 potential cluster members (other than Hydra-A itself) and the mean redshift for these is 0.0529 so 450 km s^{-1} lower than Hydra-A and comparable to the blue-shifted line component. Some caution is required in interpreting this result given the number of galaxies is relatively small and that there is a second cluster of galaxies present (probably associated with Abell 780 that lies 11′ from Hydra-A and is frequently, and completely erroneously, equated to Hydra-A in the literature). However, there is some evidence that the second gas component could be related to the cluster velocity giving a natural explanation as to why two velocity components are present.

This conclusion requires the BCG to have a significant velocity with respect to the cluster. There is a considerable literature on "speeding cDs" (Beers & Geller, 1983; Zabludoff et al., 1993; Pimbblet et al., 2006) and there are a significant fraction of clusters with a velocity offset between the cluster mean and the BCG velocities of more than 300 km s^{-1}. The origin of this velocity offset is poorly understood but probably relates to a recent merger of a substantial subcluster that affects the cluster mean velocity with respect to the BCG. The presence of cold fronts and merger shocks could be used to support this interpretation (Markevitch & Vikhlinin, 2007; ZuHone et al., 2010, 2011). However, these are most prominent for mergers in the plane of the sky, whereas the observed velocity difference will be largest for

mergers along the line of sight so the lack of these features does not exclude the presence of a significant merger.

The implications for the interpretation of other clusters are significant. For instance, A1795 has a broad CO velocity width (Salomé & Combes, 2003) and a prominent tail of Hα line emission (O'Dea et al., 2004; Crawford et al., 2005; McDonald & Veilleux, 2009). The BCG is known to be offset from the cluster mean (Oegerle & Hill, 1994) and there is evidence for a merger from the X-ray imaging (Ettori et al., 2002). Also the velocity offsets between the stellar component of the BCG, the cold gas retained by the BCG, the mean of the cluster members and the cold gas outside the influence of the BCG that all need to be considered separately. The gaseous nature of the ICM and cold molecular gas mean that they can experience shocks and decouple from the dark matter and stellar components which are relatively collisionless and respond only to gravity. Therefore, it is possible that all four components could differ in velocity, with the BCG and cluster mean having the widest separation and the gas components falling between them. Accurate measurements of the stellar and ionised gas components of BCGs are relatively straightforward to obtain (e.g. Crawford et al., 1999) as are similar measures of the molecular and cool atomic gas. However, determining the mean velocity of cluster members requires at least 50 cluster members to ensure a statistically robust value so dedicated multi-object spectroscopy is required which has more demanding observing time requirements.

5.5.3 The balance of molecular, atomic and ionised gas

The SINFONI data provide a direct comparison of the molecular and ionised gas in Hydra-A from the Paα and 1-0 S Series H_2 molecular lines. The presence of a secondary peak in the Paα which is not present in the warm molecular gas suggests the western edge of the disk is either less molecular than the disk or that the molecular gas is cooler than the disk.

In order to compare the cold molecular, atomic and ionised gas directly we produced a reconstructed spectrum of the Paα by taking the measured velocity, linewidth and flux of the emission at each point used to produce the velocity profile and created a Gaussian with these parameters. The spectra of these individual
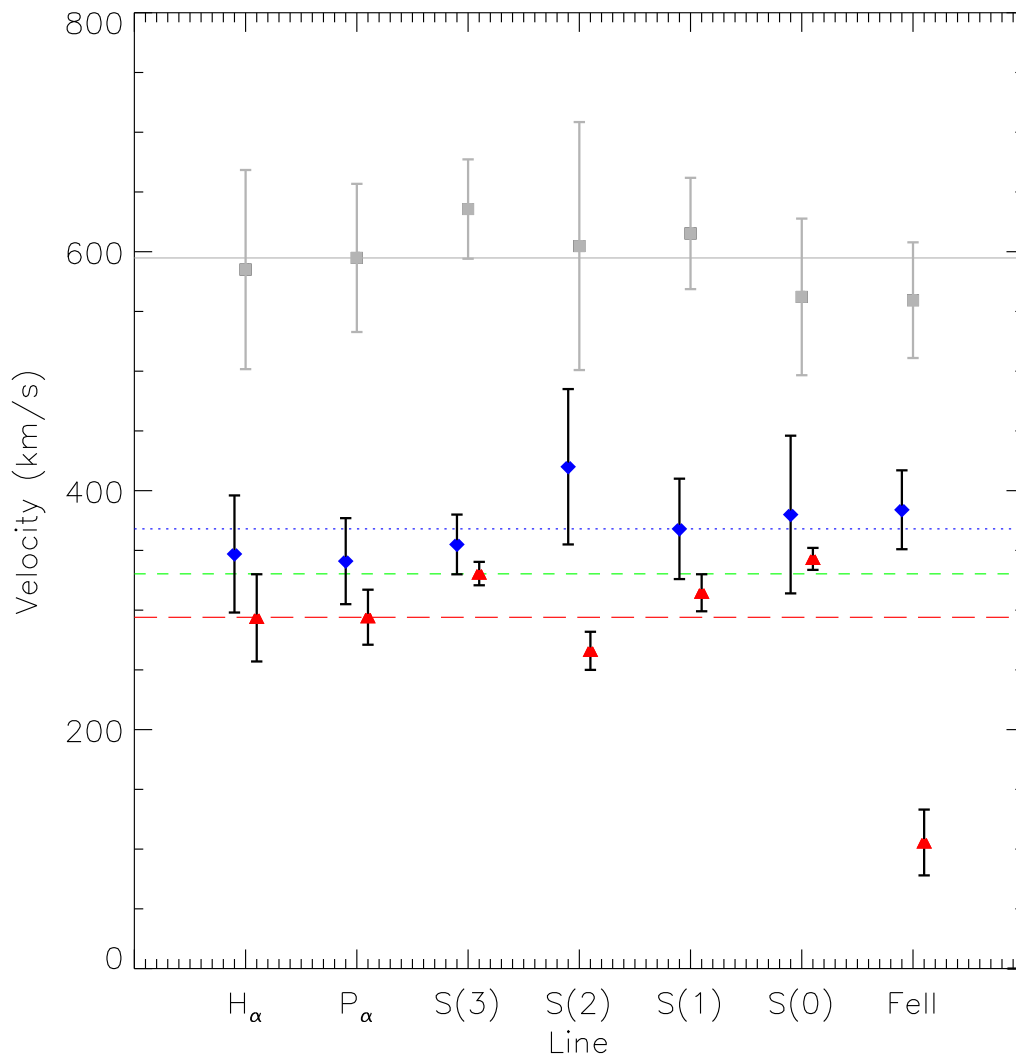
Figure 5.10: Here we present a comparison of the rotation velocity predicted by the disk fits for each line. The red triangles show the magnitude of the maximum velocity measured from the data, the long dashed red line shows the median of these values while the dashed green line shows the median corrected for the median inclination. The blue diamonds show the values of $V_{2.2}$ derived from the models with the dotted blue line set at the median $V_{2.2}$. The squares show the asymptotic velocity from the best fit model for each line with the solid line representing their median. All errors bars are to 1σ and it can be seen that within errors the value of $V_{2.2}$ are consistent with the inclination corrected maximum measured velocity.
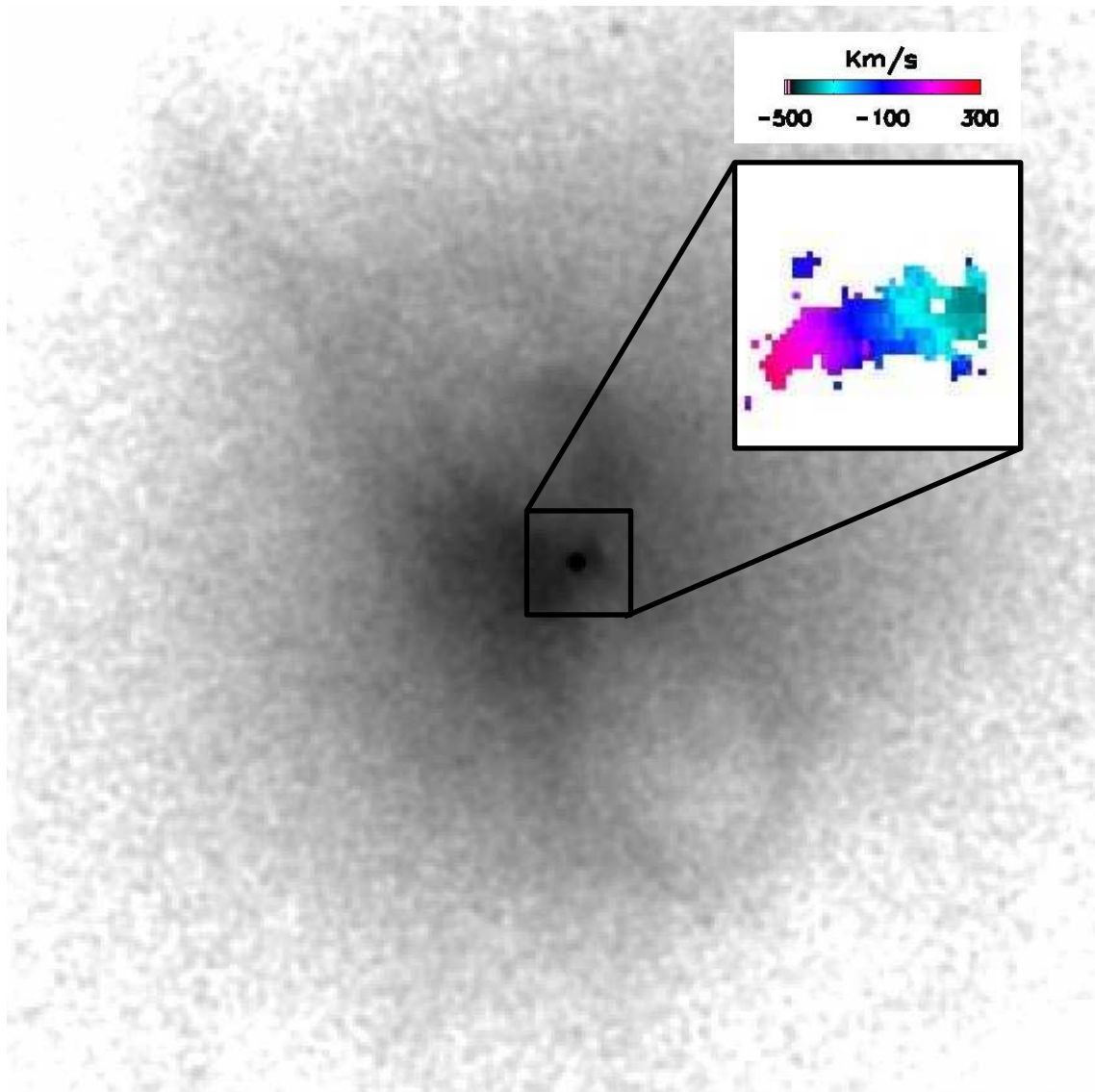
Figure 5.11: The central ∼2x2 arcmin region of the Hydra A cluster shown in a 221 ksec integration X-ray image. Two depressions in the X-ray emission show the location of cavities ∼20 arcsec to the north and south of the cluster centre. The inset shows the Paα velocity field in a ∼10x10 arcsec region centred on the BCG as derived from single component fits to the Paα line in Hydra A. The velocity field is with respect to the zero-point of the nominal cluster redshift of $z = 0.0549$. The velocity field shows an east-west alignment almost perpendicular to the alignment of the X-ray cavities.
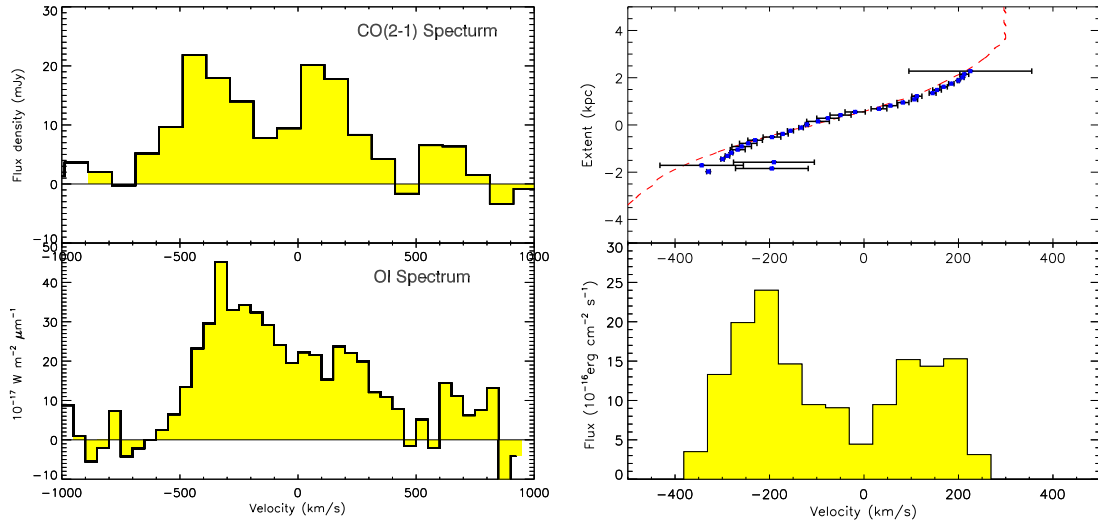
Figure 5.12: Here we show the spectrum of the CO and [OI] lines on the left. On the right we show the Paα velocity profile along with a reconstructed spectrum. The reconstructed spectrum of the Paα bears a remarkable resemblance to those of the atomic and molecular lines. Note that all three show a double peaked and asymmetric structures suggesting they trace the same reservoir of gas.

points were then summed to give the final spectrum of the Paα emission before being binned to a level comparable to the CO and [OI] spectra (50 km s^{-1}). As this reconstructed spectrum is produced from the emission detected by the fitting routine it only includes the high surface brightness ($\geq 7\sigma$ significance) Paα emission. A comparison of the CO, [OI] and reconstructed Paα integrated line velocity profiles is shown in Figure 5.12. It can be seen that the three profiles are remarkably consistent with each other. All three profiles show an asymmetric double peaked profile with a consistent separation between the peaks. We note that the Paα line appears narrower then the CO and [OI] however this is likely to be due to the fact it is reconstructed from the 7σ fits and as such has a sharp cut-off at low surface brightness. Therefore, we infer that the gas on the western edge of the disk does contain molecular gas implying that the weaker warm vibrationally excited molecular line emission is related to the excitation of the gas. This difference could be related to less shock heating (Jaffe et al., 2001; Wilman et al., 2002) or direct AGN heating away from the centre of the galaxy. However, equally large differences are seen in the ratio of Paα and the molecular lines in IFU observations of other systems with stronger cold molecular emission away from the central galaxy (Wilman et al., 2009; Oonk et al., 2010) and the ratio varies significantly between sources (Edge et al.,

2002) so one cannot draw universal conclusions from the line ratios in Hydra-A alone.

5.6 Summary

Mechanical feedback provided by AGN outbursts from BCGs is commonly believed to be the main contributing factor which prevents the catastrophic cooling of gas within cluster cores. For this process to work effectively a mechanism of self regulation is required to maintain the balance between the cooling gas and the feedback. This requires a direct link between the cooling gas (on kpc scales) and its supply to the super massive black hole be established which results in the activation of the AGN once cooling reaches a critical threshold. Here we study Hydra-A, a well known BCG in which AGN feedback appears to be currently active. We present clear evidence for a kpc scale rotating disk of ionised, atomic and molecular gas which has a rotation axis parallel to the axis along which the AGN is inflating cavities within the cluster core.

In addition, the agreement between the integrated line profile of the cold molecular and atomic lines and the ionised and warm molecular gas traced in the optical and NIR IFU observations (Fig 5.12) implies that the cold gas follows a similar ordered rotation. The existence of a relatively thin (<1 kpc) disk that has a velocity range of >700 km s^{-1} has profound implications for our understanding of Hydra-A in particular and radio galaxies in general.

5.7 Afterword

The alignment of the disks axis of rotation with the jets hints at a link between the kinematics of material on kpc scales and the accretion of material onto the central black hole. While this has interesting implications for Hydra-A it is suggestive given the high number of systems which showed an ordered velocity field in the maps presented in Chapter 3. Hydra-A was selected for this study as it is one of the most well studied objects in the VIMOS sample. This meant that a wealth of multi-wavelength data was available which allowed the kinematics of gas in many different phases to be studied in detail. Unfortunately as this was a study of just a

single object the scope with which these results can be interpreted is limited. We will attempt to address this in Chapter 6 by considering the full VIMOS sample in the light of what we have learned studying Hydra-A.

Chapter 6

The rotation of the ionised gas in galaxy cluster cores: a possible link between the cold gas on kpc–scales and the feedback from the central AGN

6.1 Overview

In this chapter the kinematics of the ionised gas within the core of the clusters presented in Chapter 3 are studied in detail. First the kinematics of each cluster are compared to those of an idealised disk to determine which show evidence of disk rotation. Next each disk is modelled with the disk model presented in Chapter 5 in order to parametrise it. Finally a comparison to CO and radio/X-ray observations is presented which suggests that the ionised gas kinematics directly trace the gas which is responsible for fuelling the feedback within cluster cores. 62% ($\frac{45}{73}$) of the VIMOS sample are identified as having kinematic structures which are consistent with a rotating disk and the comparison to CO line-widths suggests that the large reservoir of molecular gas follows a similar ordered rotation. The prevalence of these disks is discussed and an alignment to the jets and cavities is identified which indicates that they are clearly an important component of the feedback process.

6.2   Introduction

The interaction between BCGs and the dense ICM which surrounds them is an important consideration for our understanding of the formation and evolution of massive galaxies (Fabian, 2012; McNamara & Nulsen, 2012). A clear correlation is observed between the X-ray properties of the core regions of clusters (cooling time, central entropy etc.) and the presence of strong optical line emission from the BCG (Cavagnolo et al., 2008; Sanderson et al., 2009a). Thus the implicit connection of optical emission lines to the cold (Edge, 2001; Salomé & Combes, 2003) and warm (Edge et al., 2002; Egami et al., 2006; Donahue et al., 2011) molecular gas points to a direct link between the gas cooling from the ICM and the presence of cold molecular gas. There are however stringent observational constraints constraints on the rate of energy loss from the ICM at temperatures $\gtrsim \frac{1}{3}$ $T_{cluster}$ and strong limits on the cooling of gas below that temperature (Peterson et al., 2001; Sanders et al., 2010) which any model must satisfy. AGN feedback is commonly invoked to curtail radiative cooling, however the details of this mechanism are not yet settled.

AGN feedback refers to the injection of mechanical energy into the ICM through the action of outflows from the SMBH inflating kpc-scale cavities in the hot gas of the ICM (McNamara & Nulsen, 2007). In Chapter 5 the Hydra-A (3C218) cluster, which has some of the most striking examples of X-ray cavities (McNamara et al., 2000; Wise et al., 2007), is studied in detail. The line emitting gas in Hydra-A indicates clear evidence of rotation (Simkin, 1979; Ekers & Simkin, 1983). The kinematics of the line emission are found to be consistent with those of the warm molecular, atomic and cold molecular gas implying they all share the same kinematic structure, i.e. a rotating disk (Chapter 5). Importantly, the axis of rotation of this disk is determined to be aligned almost parallel to the axis along which the radio jets from the AGN can be seen to be inflating cavities in the ICM.

The fact that the mass of cold material in the disk is sufficient to fuel an outburst comparable to that which has already occurred (Chapter 5), coupled with the alignment hints at the possibility that the disk may be responsible for regulating AGN feedback. This is as expected in the unified model of AGN, but the scales involved are much larger. The findings in Chapter 3 indicate that the ionised gas

in the majority of BCGs shows an ordered velocity structure suggesting that the situation in Hydra-A may not be unique to that system. If that were the case it would have profound implications for our understanding of radio galaxies and the interaction of BCGs with the cores of clusters.

This Chapter presents a detailed analysis of teh kinematic structure of the full sample of BCGs presented in Chapter 3. Kinemetry (Krajnović et al., 2006) is used to determine the consistency of the samples kinematics with a rotating disk in §6.3. In §6.4.1 disk models are fit to the velocity maps presented in Chapter 3 to characterise the rotation for the objects which are identified as disks. The kinematics of these disks are then compared to those of the molecular gas in those systems. Finally a comparison of the axis of rotation with the axis of the AGN feedback is presented and discussed in §6.4.2. A summary and conclusions are then presented in §6.5.

6.3 Kinemetry

Kinemetry is a generalisation of surface photometry to the higher order moments of the line-of-sight velocity distribution of galaxies developed by Krajnović et al. (2006). The spectroscopic images provided by observations using integral-field spectrographs allow for the production of mean velocity and velocity dispersion maps (both stellar and gaseous) which allow the kinematics of a system to be studied in detail. The generalisation put forward by Krajnović et al. (2006) follows the approach of surface photometry by extracting profiles of these maps along ellipses which best fit the predicted profile. Following the conventions laid down in Krajnović et al. (2006), the surface brightness and velocity dispersion are even moments which would be expected to have profiles which are consistent with a constant value. The mean velocity however is defined as an odd moment, if it is assumed that the mean velocity map traces material in a thin disk inclined at an angle i to the line of sight then the predicted profile of the ellipse should be well represented by a simple cosine law of the form

$$V(R, \psi) = V_0 + V_c(R)\sin(i)\cos(\psi) \tag{6.3.1}$$

where R is the semi–major axis length of the ellipse, V_0 is the systemic velocity, V_c is the ring circular velocity and ψ is the azimuthal angle measured from the projected major axis. Any deviation from these expected profiles represents a deviation of the data from the idealised model of a thin disk. These deviations are characterised using a Fourier analysis with a harmonic expansion the form

$$K(a, \psi) = A_0(a) + \sum_{n=1}^{N} A_n(a)\sin(n\psi) + B_n(a)\cos(n\psi) \qquad (6.3.2)$$

where ψ is the azimuthal angle from equation 6.3.1 assuming the velocity field field represents a disk and a is the length of the semi major axis. We use the algorithm described in detail in Krajnović et al. (2006) to extract and characterise the profiles along each best fitting ellipse for all the objects in our VIMOS sample.

Shapiro et al. (2008) refine the kinematic process of Krajnović et al. (2006) in order to quantify how well the kinematic data represents a disk. To do this they measure the symmetries of the mean velocity and velocity dispersion fields. Any asymmetries in these fields represent deviations from the idealised model (a rotating thin disk) and as such the combined asymmetry of the two fields can fully describe how accurately a system is represented by an idealised disk.

Such an idealised rotating disk should have an ordered velocity field described by Equation 6.3.1 and a centrally peaked velocity dispersion field. The velocity field of an ideal rotating disk should peak at the semi-major axis of the ellipse and go through zero at the semi-minor axis. As such the profile extracted along an ellipse should be dominated by the first harmonic of the $\cos(n\psi)$ term. Thus the circular velocity of each concentric ring can be represented by just the B_1 term of the harmonic expansion. As such all higher order terms (n > 1) of the harmonic expansion represent deviations from an ideal disk. By contrast the velocity dispersion field, as an even moment of the velocity distribution, can be analysed in an identical manner to surface photometry. For an ideal disk the velocity dispersion will be constant along each ellipse and will decrease as the semi-major axis length of the ellipses increase. As such the profile should be dominated by the power in the A_0 term of the harmonic expansion with the higher order terms (n > 0) representing the deviations from the ideal model.

The amplitude coefficient of each order in the harmonic expression can be written

as the quadrature sum of the A_n and B_n coefficients as given in equation 6.3.3.

$$k_n = \sqrt{A_n^2 + B_n^2} \qquad (6.3.3)$$

Shapiro et al. (2008) then use the average of these amplitude coefficients, with an order greater than that of the dominant component (n > 1 for the mean velocity field and n > 0 for the velocity dispersion field), as a measure of the non-ideal components in a system at a given radius. As such the average deviations from an ideal disk at each radial increment of the mean velocity field and velocity dispersion field are given by

$$k_{avg,v} = (k_{2,v} + k_{3,v} + k_{4,v} + k_{5,v})/4 \qquad (6.3.4)$$

and

$$k_{avg,\sigma} = (k_{1,\sigma} + k_{2,\sigma} + k_{3,\sigma} + k_{4,\sigma} + k_{5,\sigma})/5 \qquad (6.3.5)$$

respectively. We follow the prescription of Shapiro et al. (2008) and normalise the average deviations for both to the circular velocity coefficient $B_{1,v}$ in order to assess the relative level of deviation at each radial increment. Finally the asymmetries in both the mean velocity and velocity dispersion fields are averaged across all radii to give a global measure of the asymmetry in each. By this definition the asymmetries in the mean velocity field (V_{asym}) and the velocity dispersion field (σ_{asym}) are given by the expressions

$$V_{asym} = \left\langle \frac{k_{avg,v}}{B_{1,v}} \right\rangle \qquad\qquad \sigma_{asym} = \left\langle \frac{k_{avg,\sigma}}{B_{1,v}} \right\rangle \qquad (6.3.6)$$

respectively.

We use the algorithm described in detail in Krajnović et al. (2006) to extract and characterise the profiles along each best fitting ellipse for all the objects in our VIMOS sample. We then follow the method of Shapiro et al. (2008) outlined above to measure the kinematic asymmetries of each object so as to characterise the velocity fields.

6.3.1 Kinematic modelling

Shapiro et al. (2008) use these criteria to distinguish between disks and merging systems for low signal to noise, high redshift (z $\sim$ 2) objects. The total kinematic asymmetry of the system is defined as

$$K_{asym} = \sqrt{v_{asym}^2 + \sigma_{asym}^2} \tag{6.3.7}$$

with the empirically selected value of K$_{asym}$ = 0.5 separating the model disks and mergers. We note however, several key differences between the objects in our sample and those of Shapiro et al. (2008)

- The cores of clusters are complex and dynamic regions in which there are many processes which could contributing to the line of sight velocity distribution beyond just disks and mergers. Entrainment by the expanding radio lodes, outflows caused by AGN or starbursts, shocks passing through the ICM and the flow of gas along filamentary structures can all increase the asymmetry of the velocity field without the need for the system to be merging.

- The objects in our sample are all massive elliptical galaxies in which there is possibly an embedded disk of gas. As such they will have radically different mass and continuum light profiles to the template disk galaxies used by Shapiro et al. (2008) which are local disks. For a spiral galaxy, the continuum and line emission from the disk should both have roughly consistent profiles both following an exponential decrease. For the elliptical galaxies in our sample however the continuum profile will decrease much more slowly than the line emission from the disk. While this should not affect the kinemetric process itself it could potentially affect the identification of kinematic features in regions where the spectrum is dominated by the continuum.

- The signal to noise of the line emission in our systems is high (at least 7σ in all pixels used to create the maps) due to the line emission being bright and the systems being relatively local (z $\lesssim$ 0.25). As such the kinematics of our systems should be less sensitive to noise than those of Shapiro et al. (2008). This should make identifying disk systems easier for our sample, especially in

near face on systems where much of the kinematic information from the disk is lost.

From this list we can see that there are several important considerations which must be made when calibrating the kinemetric analysis. Firstly just because we identify a system as being kinematically disturbed we cannot assume that this is the result of a merger. Indeed the mean velocity maps of objects such as Abell 2052 (see Chapter 3) show multiple velocity components but have clearly been disturbed by outbursts from the central AGN. As such we also use the kinemetric analysis to test models of isolated non-disk objects (objects whose line of sight velocity distributions are dominated by random motions) to test if these are distinguishable from mergers based on their kinematics alone. We also note one other important consideration in the identification of disks, the inclination. Near face on disks are difficult to detect, but to what inclination can we accurately detect them and what fraction does this suggest we are missing? In order to address this the kinemetric analysis is applied to a sample of model disks which are inclined to within 5° of face on.

For a single isolated galaxy the kinematics should be dominated either by an ordered velocity structure in the form of a disk, or random motions of the gas and stars within the galaxy. In order to assess the ability of kinemetry to distinguish between these possibilities we produced 500 artificial IFU observations for each possibility which could then be classified with kinemetry and compared to the input parameters. In order to test the methods ability to identify near face on disks we produced a further 500 idealised disks which were set to have a high inclination value. Finally, within the cores of clusters, galaxies are densely packed making the observation of several interactions and mergers likely in a large sample. During such an event, if both objects contain line emitting gas, the relative velocity of the two objects can potentially produce a projected mean velocity structure which appears ordered and could be mistaken for a disk (for example RXJ0338+09). As such 500 artificial mergers were produced to test the kinemetric procedure.

For each fake observation to be produced the variation across the field of view of the continuum, line flux, line of sight velocity and velocity width all had to be determined. The limits used to constrain each variable were selected to ensure the

fake observations are consistent with the sample of real objects presented in Chapter 3. The variation of the continuum determines the actual position of the BCG on which the pointing of each observation in the IFU sample was determined. For this reason the peak of the continuum emission, corresponding to the centre of the BCG, was set to be within the central $1/3^{rd}$ of the field of view. A two dimensional De Vaucouleurs' profile was then produced around this point with an effective radius ranging from two to four spatial resolution elements. This produced an array with a value corresponding to the continuum level at each point in the cube of the artificially produced observation.

The Hα peak flux was set to be between 5 and 50 times the peak continuum level. The Hα flux profile was set to a two dimensional profile which decreased exponentially from the peak with an effective radius between 2 and 4 pixels. The position of the peak in Hα flux was set to match the position of the continuum peak. The line flux profile was allowed to flatten along one axis so that profiles could be produced which were not purely circular. When producing a disk the flattening parameter (q) was set equal to $\cos(i)$ (where i is the inclination of the disk), for non-disks q is set to a random value between 0.1 and 1. The profiles thus followed the equation

$$F_{H\alpha}(x,y) = F_0 e^{-r} \qquad \text{with} \qquad r = \sqrt{(\tfrac{x-x_c}{r_e})^2 + (\tfrac{y-y_c}{r_e \times q})^2} \qquad (6.3.8)$$

where x_c and y_c are the x and y centre of the profile, r_e is the effective radius and F_0 is the peak flux.. The line width σ of the emission at each point in the field of view was set to follow the same exponential decrease as the Hα emission with the peak set to a value between 200 and 400 km s^{-1}.

The mean velocity profile was different for each type of object being produced (disk, edge on disk or non-disk). The magnitude of the largest velocity shift (v_{max}) allowed for each distribution was set to be between 300 and 600 km s^{-1}. For the objects which were set to show evidence of disk rotation the mean velocity profile was set to follow an arctan function. While this is a non–physical model of the rotation Courteau (1997) found it to be a good approximation of the velocity curve of disk galaxies. So the mean velocity field of each disk followed the equation

$$v(x, y) = v_0 + v_{max}\arctan(R/r_t) \times \frac{x - x_c}{R} \times \sin(i) \qquad (6.3.9)$$

with

$$R = \sqrt{(x - x_c)^2 + (\frac{y - y_c}{\cos(i)})^2} \qquad (6.3.10)$$

where v_0 is the systemic velocity of the system (determined for a redshift of 0.006<z<0.25), r_t is the transition radius between the rising and flat part of the rotation curve (set to a value between 1 and 5 pixels from the centre) and i is the inclination of the disk with respect to the plane of the sky (set to be between 90°, edge on, and 5°, near face on). The face–on disks were also given velocity profiles following Eq. 6.3.9 but with their inclination set to be within 5° of face–on. Finally for the non-disks the velocity at each point was set to a random value between v_{max} and $-v_{max}$.

To determine the parameters for a merger, two random galaxy types were selected (disk, non-disk or face on disk) and parameters for each were produced. A random velocity difference of between -150 and 150 km s^{-1} was then included. The parameters the second model were then adjusted to apply this shift between the two objects.

Once the parameters of each fake observation had been determined, a spectrum was produced at each point in the field of view. Each spectrum covered a wavelength range of 144 Å with a spectral resolution of 0.6 Å (a total of 240 resolution elements to ensure consistency with fitting to the sample as described in Chapter 2). The spectrum in each spatial resolution element had a flat continuum level with a Gaussian emission line in the centre that had the parameters that had just been determined. The spectrum was initially produced at the wavelength of H$\alpha(\lambda_{rest} = 6562.8$ Å) shifted to a systemic velocity that corresponded to a randomly determined redshift between 0.006 and 0.25 (the range in which the sample observations were taken). This process produced a cube with the x and y dimensions representing the spatial coordinates of the observations and the z-axis containing the spectral information. To ensure consistency with our observations the cubes were then Gaussian smoothed across the spatial dimensions at each position along the

z-axis. The FWHM of this smoothing was set to a value between 0.5 and 3.0 arcsec to be consistent with the range of seeing conditions that the sample was observed under.

The final step in producing the fake IFU cubes was to add 1σ noise to the spectrum at each resolution element. These fake IFU cubes approximate the observations of the sample presented in Chapter 3 with a few minor differences. The artificial observations took no account of sky lines or continuum features which may adversely affect the fitting routine. However, we do not see this as an issue as we are only considering how well the kinemetry can identify the different types of objects not in testing the fitting routine. The spectral range covered is very short, only 144 Å. This however is the range over which the fitting routine was used for VIMOS so should not be an issue. We do note that these fake observations do not include the [NII] lines which were fitted together with the Hα line for the real data. Finally the field of view of the fake observations is much smaller than that of the data. However, it is consistent with the average region of the VIMOS field of view in which we were able to detect Hα emission for the sample. These fake cubes were then fitted with single Gaussian lines following the method outlined in Chapter 2 to produce maps of the artificial observations which could then be used to test the kinemetry routine. An example of the maps produced for each type of object modelled can be seen in Figure. 6.1.

6.3.2 Constraining the analysis

Both Krajnović et al. (2006) and Shapiro et al. (2008) note that the higher order terms are susceptible to misaligned centring which induces artificial power in the kinemetry coefficients. This step is relatively straight forward for the high signal to noise objects in our VIMOS sample, which for the most part show a clear centrally peaked Hα flux distribution. The only objects for which this is non-trivial are those with an offset Hα morphology, for these objects we centre the kinemetry on the Hα peak which is most closely aligned to the peak of the continuum flux.

Running the kinemetry without the position angle and inclination of the system constrained allows these parameters to change substantially with each consecutive radial increment. In an ideal disk system the values should vary slowly throughout
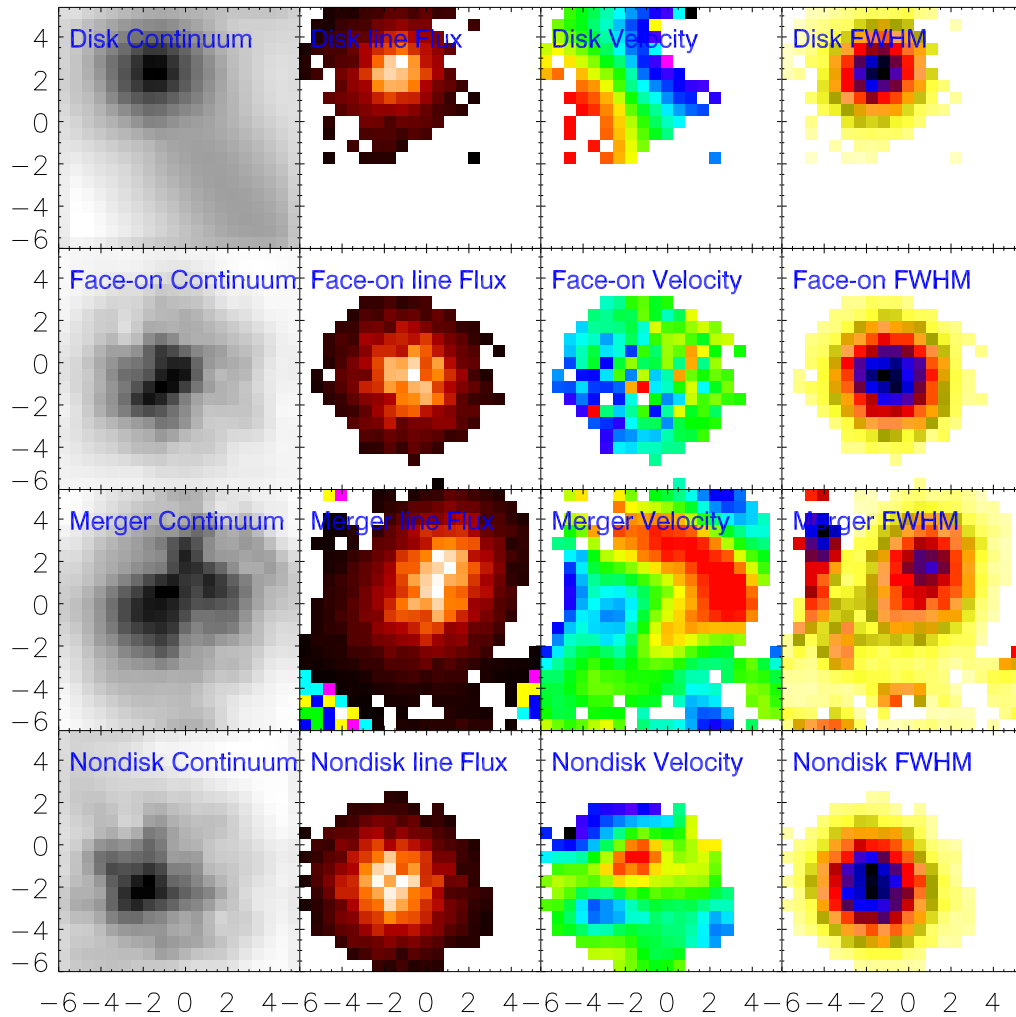
Figure 6.1: Here we show an example of the maps produced from each type of objects for which we produced artificial IFU observations. From left to right we show the continuum emission, the line flux, the mean velocity field and the velocity dispersion.

the system and as such any variation of these parameters during the kinometry suggest that the system may not be disk like. We found while performing kinometry on our VIMOS sample that the PA and inclination remained relatively stable during the fitting to the mean velocity map, varying on average by just a few degrees between consecutive radii. However, when performing the kinometry on the velocity dispersion maps the PA and inclination were much more unstable, varying by a few tens of degrees between radii. We also note that for several objects the average PA and inclination derived from the velocity dispersion map do not match their respective values derived from the mean velocity map. For these reasons we decided

to follow the approach of Shapiro et al. (2008) and fix the values of PA and inclination for each ellipse to a global value derived for each object. As the mean velocity map provided a more stable solution of these parameters, we use it to derive global values of both the PA and inclination before performing the full kinemetry analysis with these values fixed.

We first find the best fitting PA of the system using the known errors any mis-alignment induces. For a small misalignment of the PA during the kinemetry analysis we expect to increase the power in the A_1, A_3 and B_3 terms (Krajnović et al., 2006), while a large misalignment will increase the power in all terms with n > 0 except for the B_1 term which corresponds only to the maximum amplitude of the circular velocity. B_1 should thus only be dependent on the velocity gradient along the major axis of the ellipse. As such it should vary only with the PA and be relatively insensitive to changes to the inclination. Thus for a fixed inclination, the PA which maximises the power in B_1 and minimises the power in all other terms should be the global PA. To find the PA we perform the kinemetry on the velocity field with a PA fixed to -90° and the inclination fixed to a constant value ($\cos i = 1$, so the ellipse being fit is a circle). We then cycle through the PA range of -90° to 90° in steps of 3° and perform kinemetry at each increment. For each step in PA we calculate the quadrature difference between B_1 and all other terms, by maximising the total of these differences, we can identify the PA which gives the maximum power in B_1 while minimising all other terms. Thus we identify the global PA (PA_g) as the PA for which the value of

$$P_{PA} = \sum_{n=2}^{N} \sqrt{B_1^2 - B_n^2} + \sum_{n=1}^{N} \sqrt{B_1^2 - A_n^2} \qquad (6.3.11)$$

is maximised.

This however limits the accuracy of the global PA (PA_g) to $\pm 3^o$. We tested this procedure on some of the model disks for which the global PA is known and found that PA_g was consistent with the known PAs to within $\sim 2.5^o$. We then determined the global inclination (i_g) by running the kinemetry on the velocity field again, this time fixing the position angle to PA_g and leaving the inclination unconstrained. This allowed the procedure to determine the best fitting ellipse at each radii. i_g was then determined as the average inclination of the best fitting ellipse across all radii.

6.3.3   Kinemetric classification of objects

Our main aim of using the kinemetry analysis is to distinguish between systems which show a disk like rotation and those which do not. Thus we initially compare the kinemetric asymmetries of our model disks with those of our model mergers and non-disks (both of which are not disk like systems). Shapiro et al. (2008) use the total kinemetric asymmetry of each system (K_{asym}, Equation 6.3.7) to distinguish between disks and mergers in their model. In Figure 6.2 we show show a histogram of the total kinemetric asymmetries in the top left for disks (blue) and all models which are not disk like (red). It is apparent from this plot that the majority of disks have a low total kinemetric asymmetry and that there is a sharp fall in the number of systems as the value of K_{asym} rises. In contrast the models which are not disks show a more even distribution but notably show a drop off in the number of systems with a low kinemetric asymmetry.

We determine the value of K_{asym} which separates these two distributions to be $K_{asym} = 0.55$ which is consistent with the value found by Shapiro et al. (2008). This is shown as a dashed line in the top right panel of Figure 6.2. We note that while this value is slightly higher than that found by Shapiro et al. (2008) the higher signal to noise of our observations should make our measure of the kinemetric asymmetry less sensitive to noise. By using this value of K_{asym} we find we are able to correctly classify 72.8% of our simulated objects as disks. We show this in the top right hand panel of Figure 6.2 by a line indicating the value of K_{asym}=0.55. This value also correctly classifies 91.4% of systems which are not disks (95.4% of mergers and 87.4% of non-disks), shown in the bottom left hand panel of Figure 6.2. In the bottom right panel of Figure 6.2 we show distribution of both the model disks and models which are not disks along with the line that indicates the separation value of K_{asym}=0.55. We note that by using this distinction we misclassify 68% of the face–on disks models as systems without disks. However, as face–on disks are likely to make up only a small percentage of objects in an unbiased sample, we do not expect this to significantly affect our results.

In Figure 6.3 we test the ability of the kinemetric analysis to distinguish between the types of models which generally have a high value of K_{asym} (i,e, those which are not immediately identified as disks). In the left hand panel of Figure 6.3 we plot
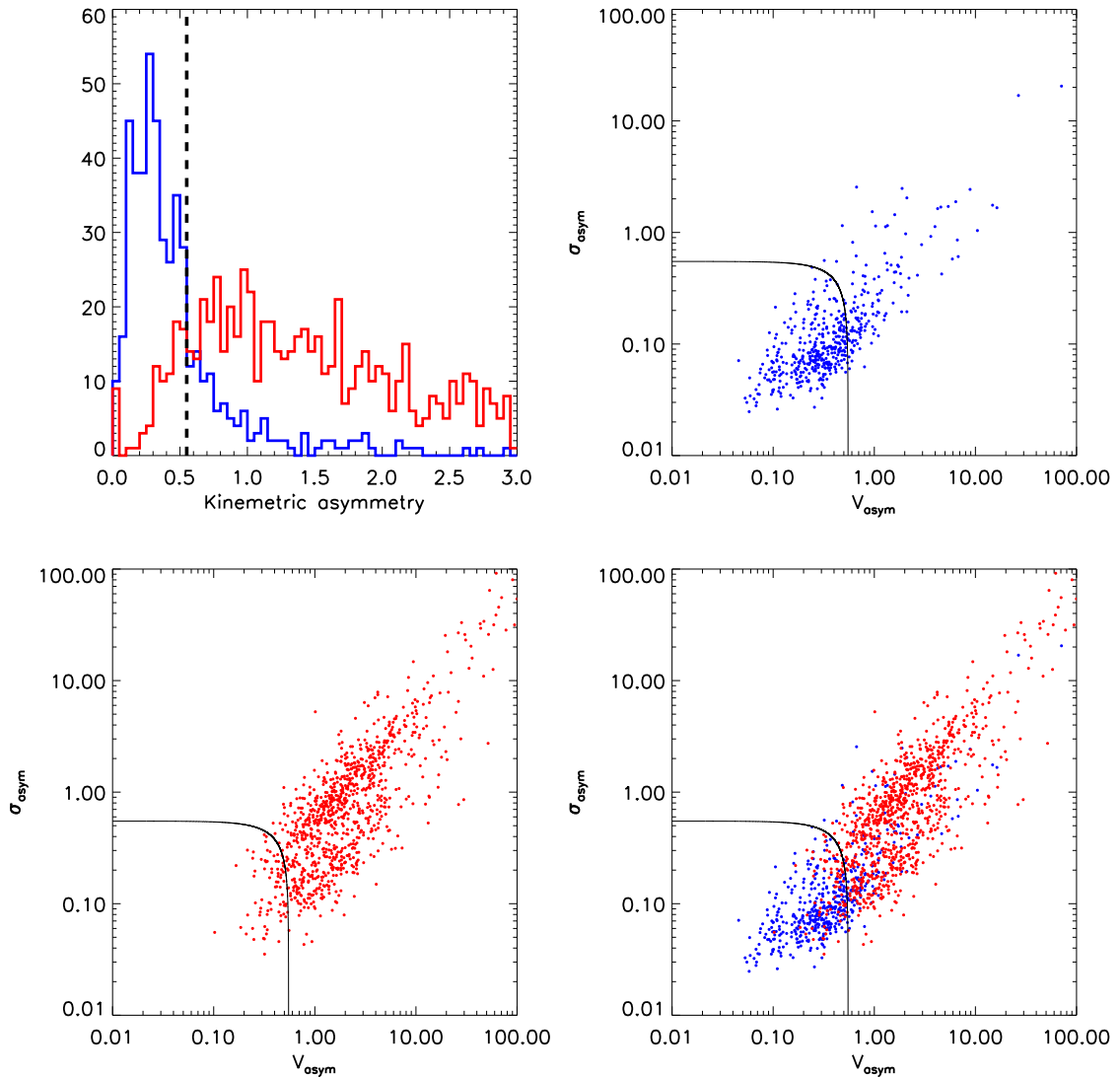
Figure 6.2: Here we compare the kinematic asymmetries of our model disks with the asymmetries of all models which are not disks (both non-disks and mergers. *Top Left* - A histogram of the total kinemetric asymmetry for disk models (blue) and non-disk/merger models (red). The disk models show a clear drop off at a kinemetric asymmetry of $K_{asym} = 0.55$ (shown by the dashed line), which is consistent with the value found by Shapiro et al. (2008). *Top Right* - Here we show a plot of the asymmetry in the mean velocity field against the asymmetry in the velocity dispersion field for the disk models. The line shows the cut of of $K_{asym} = 0.55$, which most of the disk models fall below. *Bottom Left* - A plot of the asymmetry in the mean velocity field against the asymmetry in the velocity dispersion field for the non-disk and merger models (mergers and non-disks). The line shows the cut of of $K_{asym} = 0.55$, which most of the models which are not disks lie above. *Bottom Right* - Asymmetry in mean velocity field and velocity dispersion field for both the disks (blue) and non-disks/mergers (red). The line shows the cut off of $K_{asym} = 0.55$ which clearly separates the two distributions.

the σ_{asym} against V_{asym} for the face–on disks, mergers and non-disks. It is apparent from this plot that the different types of model occupy different regions of this diagram. We note that the face on disks have values of V_{asym} and σ_{asym} which are roughly consistent. However, merging models appear to have slightly less asymmetry in the velocity dispersion field than in their mean velocity field while the non-disk models have substantially more asymmetry in their mean velocity field than velocity dispersion field. This suggests the possibility that the objects of these three models can be identified by the ratio of their σ_{asym} and V_{asym} values. We thus define the value

$$R_{asym} = \frac{\sigma_{asym}}{V_{asym}} \qquad (6.3.12)$$

with which we will attempt to classify our models. In the right hand panel of Figure 6.3 we show a histogram of σ_{asym}/V_{asym} for the models of face–on disks, non–disks and mergers. From this plot we can see that the three types of model clearly have distinct distributions of R_{asym}. We begin by considering the face–on disks (yellow) which show the highest values of R_{asym}. The number of objects with a given R_{asym} decreases substantially at $R_{asym} < 0.8$ (shown by the right hand dashed line in Figure. 6.3). Incidentally this is also the point at which the number of mergers shows a sharp rise. Next we consider the non-disks models (green), these have a distribution which clearly peaks at low values of R_{asym}. The non-disk models clearly dominate the overall distribution at values of $R_{asym} < 0.33$, the left hand dashed line on Figure. 6.3. Finally we note that the distribution of merger models (red) falls between these two limits with $0.33 < R_{asym} < 0.8$.

Less than 1% of our models had an R_{asym} of greater than 2.0, however, we note that noise in the data, or miscalculation of the objects centre, PA or inclination of the system could potentially increase the asymmetries in the mean velocity and velocity dispersion profiles. We thus imposed an upper limit on the distinction of our models, leaving those with $R_{asym} > 2.0$ as unclassified. Testing these limits on our models we find that 92.3% of the face–on disks had a value of $R_{asym} > 0.8$, 76.6% of non-disks had $R_{asym} < 0.33$ and 72.8% of mergers had $0.33 < R_{asym} < 0.8$. This clearly indicates the potential of the analysis in classifying objects with high total kinemetric asymmetries. However, we note three potential problems with

these distinctions

- Firstly, we note that our models are quite simple and often rely on non–physical empirical relations. Real galaxies are typically not so simple and as such it is possible that these distinctions may not be as clearly defined as they appear.

- We have assumed a high signal to noise to match that of our observations. As such the noise in the mean velocity field and velocity dispersion field does not contribute significantly to the measured asymmetries. If the signal to noise was lower we would expect noise to have a more substantial effect on the calculated asymmetries which may limit our ability to distinguish the models.

- Finally our models are made with good spatial sampling to be consistent with the observations in our sample. Objects with reduced spatial sampling (for example those at higher redshift) would have fewer independent data points from which to calculate the asymmetries which may make the distinctions identified here less robust.

The latter two points can easily be addressed with further modelling while the first would require these distinctions to be tested against a sample of real galaxies with known types. However, this is beyond the scope of this current work. We thus only use the value of R_{asym} to identify objects which are potentially face–on disks so that we can estimate the number of objects in our sample which are misidentified as not being disk systems due to inclination effects.

After being calibrated the kinemetric analysis was applied to the VIMOS sample presented in Chapter 3. The kinemetric asymmetries for every object in the sample are listed in Table 6.1 along with the objects classification based on its asymmetries. These asymmetries are then plotted in Figure 6.4 in black, and are compared to the models of disks (blue) and mergers/non-disks/face–on disks (red). The dashed line on this plot represents the division between the disks and the rest of the models, note that the majority of objects from the VIMOS sample fall below this line implying their kinematics are consistent with rotating disks.

For all objects not classified as disks in Table 6.1, R_{asym} was calculated to determine if they were possibly misclassified due to being near face–on. These values
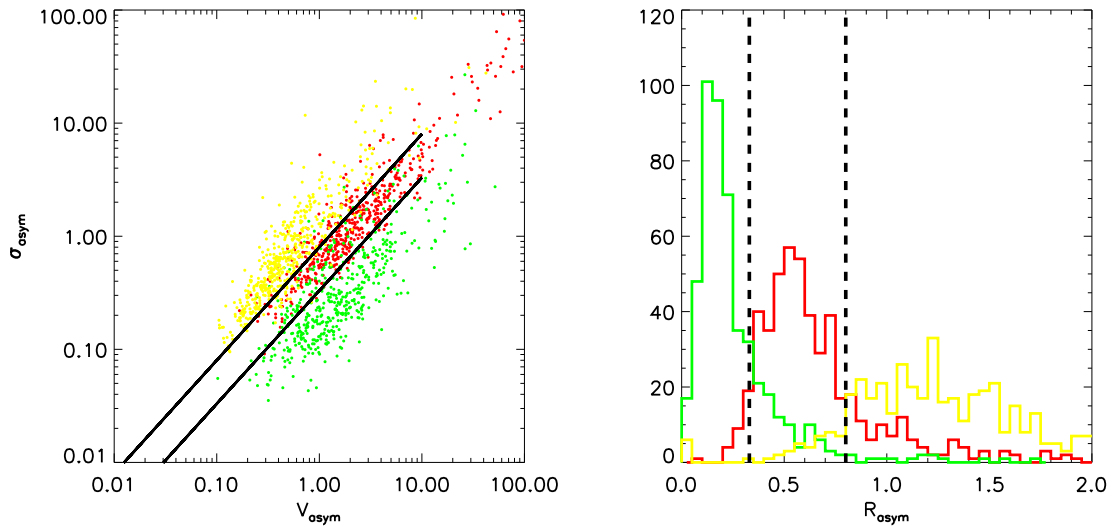
Figure 6.3: Here we show a comparison of the kinemetric asymmetries of objects which typically have a K_{asym} value of above 0.55, namely the face–on disks (yellow), mergers (red) and non-disk (green) models. *Left* - This shows a plot of σ_{asym} against V_{asym} for the face–on disks, mergers and non-disks. It can clearly be seen that these three objects types occupy different regions of the plot, roughly separated by the two lines. *Right* - A histogram of R_{asym} for the three types of model. The models are clearly separated in this plot, with non-disks having low R_{asym} values, face–on disks having high R_{asym} values and mergers lying between. The dashed lines separate the regions $R_{asym} < 0.33$ (non-disks), $0.33 < R_{asym} < 0.8$ (mergers) and $R_{asym} > 0.8$ (face on disks).

are presented in Table 6.2 and it can be seen that about half have values of R_{asym} which are consistent with the model face–on disks (Figure 6.3).

TABLE. 6.1.
THE KINEMETRIC ASYMMETRIES LISTED FOR EACH OBJECT IN THE VIMOS SAMPLE

Object	v_{asym}	σ_{asym}	k_{asym}	Classification
Abell1060	0.14 ± 0.084	0.11 ± 0.039	0.18 ± 0.045	Disk
Abell1084	0.39 ± 0.018	0.49 ± 0.027	0.63 ± 0.015	Not Disk Like
Abell11	0.39 ± 0.015	0.30 ± 0.22	0.49 ± 0.066	Disk
Abell1111	0.28 ± 0.034	0.12 ± 0.095	0.30 ± 0.015	Disk
Abell1204	0.059 ± 0.054	0.92 ± 0.16	0.92 ± 0.15	Not Disk Like
Abell133	0.40 ± 0.054	0.59 ± 0.075	0.71 ± 0.049	Not Disk Like
Abell1348	0.21 ± 0.0051	0.27 ± 0.0093	0.34 ± 0.0027	Disk
Abell1663	0.096 ± 0.041	0.36 ± 0.075	0.37 ± 0.027	Disk
Abell1668	0.27 ± 0.025	0.23 ± 0.061	0.35 ± 0.016	Disk
Abell194	0.18 ± 0.032	0.16 ± 0.064	0.24 ± 0.012	Disk
Abell1991	0.47 ± 0.032	0.39 ± 0.074	0.61 ± 0.033	Not Disk Like
Abell2052	0.59 ± 0.030	0.88 ± 0.18	1.1 ± 0.16	Not Disk Like
Abell2390	0.37 ± 0.028	0.22 ± 0.031	0.43 ± 0.012	Disk
Abell2415	0.73 ± 0.032	1.4 ± 0.041	1.5 ± 0.016	Not Disk Like
Abell2495	0.22 ± 0.025	0.40 ± 0.044	0.45 ± 0.018	Disk
Abell2566	4.1 ± 1.3	0.050 ± 0.041	4.1 ± 1.25	Not Disk Like
Abell2580	0.046 ± 0.030	0.0068 ± 0.023	0.046 ± 0.0014	Disk
Abell2734	0.20 ± 0.025	0.43 ± 0.060	0.48 ± 0.026	Disk
Abell291	0.12 ± 0.036	0.24 ± 0.074	0.27 ± 0.018	Disk
Abell3017	0.041 ± 0.033	0.11 ± 0.046	0.12 ± 0.0053	Disk
Abell3112	0.12 ± 0.025	0.021 ± 0.020	0.12 ± 0.0030	Disk
Abell3378	0.31 ± 0.10	0.73 ± 0.0529	0.79 ± 0.049	Not Disk Like
Abell3444	0.82 ± 0.031	1.2 ± 0.034	1.4 ± 0.046	Not Disk Like
Abell3574	0.78 ± 0.019	0.61 ± 0.091	0.99 ± 0.057	Not Disk Like
Abell3581	0.40 ± 0.028	0.14 ± 0.022	0.42 ± 0.011	Disk
Abell3605	0.25 ± 0.0050	0.20 ± 0.021	0.32 ± 0.0043	Disk
Abell3638	1.2 ± 0.16	1.5 ± 0.053	1.9 ± 0.20	Not Disk Like
Abell3639	0.65 ± 0.064	0.46 ± 0.018	0.80 ± 0.043	Not Disk Like
Abell3806	0.15 ± 0.12	0.35 ± 0.10	0.38 ± 0.041	Disk
Abell383	0.18 ± 0.031	0.63 ± 0.020	0.65 ± 0.014	Not Disk Like
Abell3880	0.19 ± 0.016	0.23 ± 0.061	0.30 ± 0.014	Disk
Abell3998	0.26 ± 0.064	0.75 ± 0.093	0.79 ± 0.071	Not Disk Like
Abell4059	0.10 ± 0.033	0.065 ± 0.46	0.12 ± 0.030	Disk
Abell478	0.22 ± 0.038	0.27 ± 0.11	0.35 ± 0.032	Disk
Abell496	0.094 ± 0.034	0.041 ± 0.019	0.10 ± 0.0033	Disk
Abell795	0.28 ± 0.040	0.56 ± 0.052	0.62 ± 0.031	Not Disk Like
Abell85	0.12 ± 0.024	0.039 ± 0.024	0.12 ± 0.0029	Disk
HCG62	0.52 ± 0.037	0.82 ± 0.45	0.97 ± 0.37	Not Disk Like
Hydra-A	0.23 ± 0.012	0.15 ± 0.051	0.27 ± 0.0082	Disk
NGC4325	0.18 ± 0.037	0.14 ± 0.073	0.22 ± 0.012	Disk
NGC5044	0.66 ± 0.021	0.80 ± 0.016	1.0 ± 0.019	Not Disk Like
NGC533	0.23 ± 0.099	0.45 ± 0.027	0.51 ± 0.026	Disk
NGC5813	0.78 ± 0.030	0.22 ± 0.062	0.81 ± 0.026	Not Disk Like
NGC5846	0.37 ± 0.023	0.079 ± 0.026	0.38 ± 0.0085	Disk
RXCJ0120.9-1351	0.21 ± 0.024	0.25 ± 0.13	0.33 ± 0.034	Disk
RXCJ0132.6-0804	0.26 ± 0.016	0.22 ± 0.012	0.34 ± 0.0050	Disk
RXCJ0331.1-2100	0.20 ± 0.049	0.45 ± 0.044	0.49 ± 0.022	Disk
RXCJ0543.4-4430	0.16 ± 0.050	0.10 ± 0.025	0.19 ± 0.0085	Disk
RXCJ0944.6-2633	0.16 ± 0.020	0.32 ± 0.058	0.36 ± 0.019	Disk
RXCJ1257.1-1339	0.24 ± 0.013	0.29 ± 0.055	0.37 ± 0.016	Disk
RXCJ1304.2-3030	0.25 ± 0.023	0.17 ± 0.16	0.30 ± 0.028	Disk

Table 6.1: The kinemetric asymmetries listed for each object in the VIMOS sample. The first column gives the clusters designation. The second column gives the measured asymmetry of the mean velocity field (v_{asym}) which the second gives the asymmetry in the velocity dispersion field (σ_{asym}). The final column shows the total kinemetric asymmetry of the system as defined by Equation 6.3.7.

The kinemetric analysis suggests that 45 of the 73 objects ($\approx 62\%$) in the VIMOS sample have a kinematic structure which is consistent with that of a rotating disk. The remaining 28 objects have total kinemetric asymmetries (K_{asym}) which are too

Object	v_{asym}	σ_{asym}	k_{asym}	Classification
RXCJ1436.8-0900	0.22 ± 0.067	0.34 ± 0.086	0.40 ± 0.032	Disk
RXCJ1511.5+0145	0.11 ± 0.020	0.085 ± 0.025	0.14 ± 0.0031	Disk
RXCJ1524.2-3154	0.35 ± 0.033	1.3 ± 0.019	1.3 ± 0.027	Not Disk Like
RXCJ1539.5-8335	2.0 ± 0.17	8.0 ± 0.045	8.2 ± 0.48	Not Disk Like
RXCJ1558.3-1410	0.40 ± 0.027	0.65 ± 0.052	0.77 ± 0.036	Not Disk Like
RXCJ2014.8-2430	0.29 ± 0.016	0.37 ± 0.033	0.47 ± 0.013	Disk
RXCJ2101.8-2802	0.29 ± 0.026	0.20 ± 0.19	0.35 ± 0.040	Disk
RXCJ2129.6+0005	3.9 ± 0.26	10 ± 0.020	11 ± 1.0	Not Disk Like
RXCJ2213.0-2753	0.62 ± 0.0023	0.17 ± 0.057	0.64 ± 0.0099	Not Disk Like
RXJ0000.1+0816	0.46 ± 0.071	0.39 ± 0.031	0.61 ± 0.035	Not Disk Like
RXJ0338+09	1.0 ± 0.037	2.4 ± 0.0095	2.6 ± 0.043	Not Disk Like
RXJ0352.9+1941	0.43 ± 0.014	0.34 ± 0.30	0.55 ± 0.10	Disk
RXJ0439.0+0520	0.14 ± 0.016	0.26 ± 0.0075	0.30 ± 0.0029	Disk
RXJ0747-19	0.099 ± 0.056	0.73 ± 0.16	0.74 ± 0.11	Not Disk Like
RXJ0821+07	0.066 ± 0.044	0.34 ± 0.023	0.34 ± 0.0082	Disk
RXJ1651.1+0459	0.11 ± 0.056	0.081 ± 0.018	0.14 ± 0.0065	Disk
S555	3.4 ± 0.037	2.5 ± 0.028	4.2 ± 0.14	Not Disk Like
S780	0.25 ± 0.053	0.11 ± 0.088	0.28 ± 0.017	Disk
S805	0.76 ± 0.010	0.81 ± 0.032	1.1 ± 0.027	Not Disk Like
S851	0.085 ± 0.060	0.082 ± 0.080	0.12 ± 0.0083	Disk
Z3179	0.23 ± 0.036	0.38 ± 0.016	0.44 ± 0.010	Disk
Z348	0.19 ± 0.082	0.45 ± 0.042	0.49 ± 0.025	Disk

Table 6.1: continued.

TABLE. 6.2.

THE RATIO OF KINEMETRIC ASYMMETRIES FOR OBJECTS NOT CLASSIFIED AS DISKS

Object	v_{asym}	σ_{asym}	R_{asym}	Possible Disk
Abell1084	0.39 ± 0.019	0.49 ± 0.027	1.2 ± 0.059	Yes
Abell1204	0.059 ± 0.054	0.92 ± 0.16	15.6 ± 0.060	No
Abell133	0.40 ± 0.054	0.59 ± 0.075	1.5 ± 0.13	Yes
Abell1991	0.47 ± 0.032	0.39 ± 0.074	0.84 ± 0.24	Yes
Abell2052	0.59 ± 0.030	0.88 ± 0.18	1.5 ± 0.14	Yes
Abell2415	0.73 ± 0.032	1.4 ± 0.041	1.9 ± 0.029	Yes
Abell2566	4.1 ± 1.3	0.050 ± 0.041	0.012 ± 73	No
Abell3378	0.31 ± 0.10	0.76 ± 0.052	2.3 ± 0.14	No
Abell3444	0.82 ± 0.031	1.2 ± 0.034	1.4 ± 0.034	Yes
Abell3574	0.78 ± 0.019	0.61 ± 0.091	0.78 ± 0.20	No
Abell3638	1.2 ± 0.16	1.5 ± 0.053	1.3 ± 0.11	Yes
Abell3639	0.65 ± 0.065	0.46 ± 0.018	0.70 ± 0.15	No
Abell383	0.18 ± 0.031	0.63 ± 0.020	3.5 ± 0.049	No
Abell3998	0.26 ± 0.064	0.75 ± 0.093	2.9 ± 0.096	No
Abell795	0.28 ± 0.040	0.56 ± 0.052	2.0 ± 0.086	Yes
HCG62	0.52 ± 0.037	0.82 ± 0.45	1.6 ± 0.35	Yes
NGC5044	0.66 ± 0.022	0.80 ± 0.016	1.2 ± 0.031	Yes
NGC5813	0.78 ± 0.030	0.22 ± 0.062	0.28 ± 0.026	No
RXCJ1524.2-3154	0.35 ± 0.033	1.3 ± 0.019	3.6 ± 0.027	No
RXCJ1539.5-8335	2.0 ± 0.17	8.0 ± 0.045	4.1 ± 0.021	No
RXCJ1558.3-1410	0.40 ± 0.027	0.65 ± 0.052	1.6 ± 0.063	Yes
RXCJ2129.6+0005	3.9 ± 0.26	10 ± 0.020	2.6 ± 0.026	No
RXCJ2213.0-2753	0.62 ± 0.0023	0.17 ± 0.057	0.28 ± 1.2	No
RXJ0000.1+0816	0.46 ± 0.071	0.39 ± 0.031	0.86 ± 0.20	Yes
RXJ0338+09	1.0 ± 0.037	2.4 ± 0.0095	2.4 ± 0.016	No
RXJ0747-19	0.099 ± 0.056	0.73 ± 0.16	7.4 ± 0.082	No
S555	3.4 ± 0.037	2.5 ± 0.028	0.73 ± 0.021	No
S805	0.76 ± 0.010	0.81 ± 0.032	1.1 ± 0.040	Yes

Table 6.2: Here we list all objects which were not classified as disks and calculate the value of R_{asym} for each. A substantial fraction have values between 0.8 and 2.0 suggesting their possible misidentification.

high to clearly identify them as disks. It should be noted however that $\approx$50% (13 of the 28) of objects identified as not being disks have kinemetric asymmetry ratios
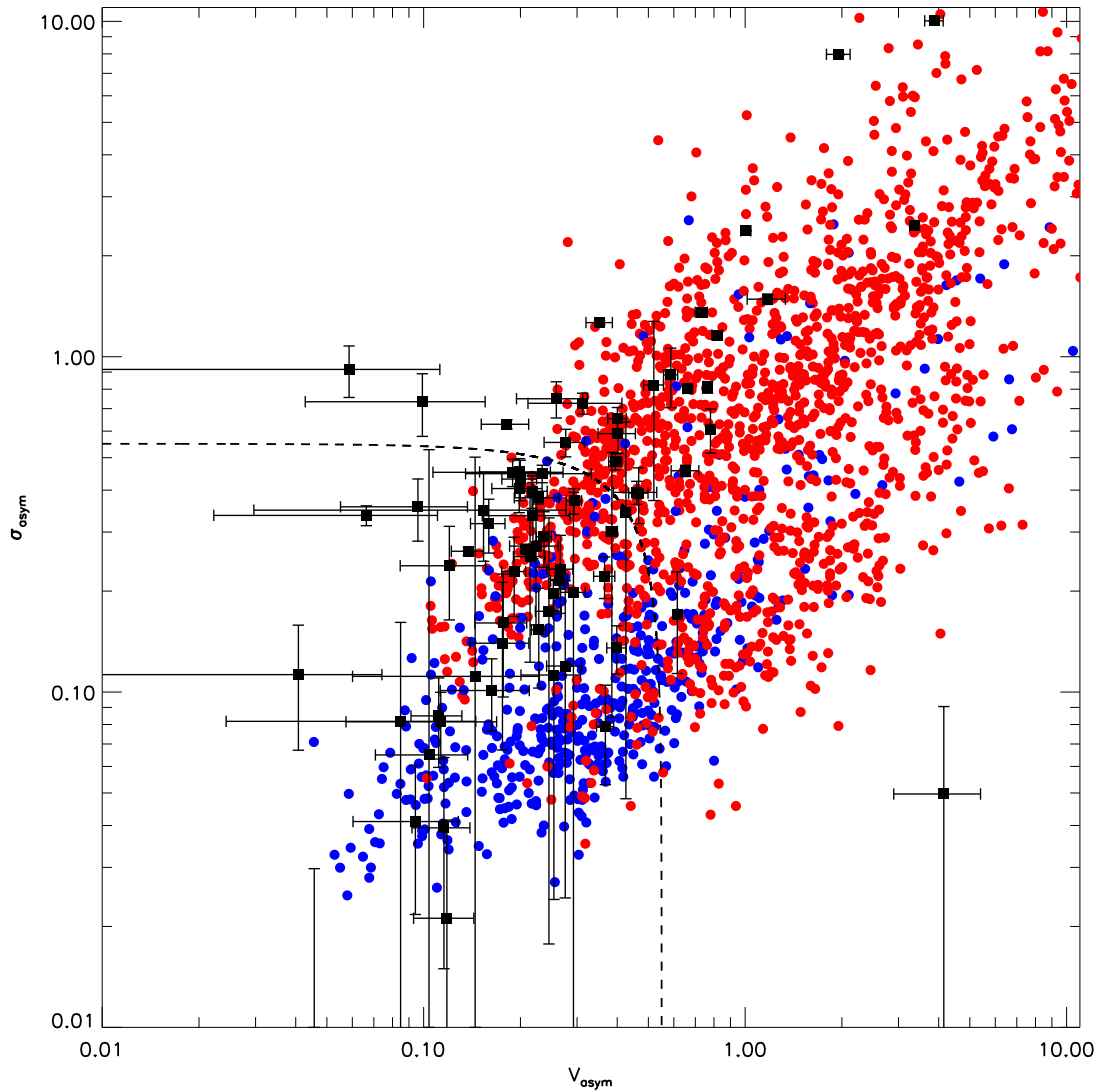
Figure 6.4: Here we compare the kinematic asymmetries of all objects in our VIMOS sample. The red points on the plot show the position of all models which were not disks (including the edge on disks) and the blue points show the position of the disk models. The dashed line shows the dividing line between the models of disks and the models of mergers/non–disks/face–on disks of $K_{asym} = 0.55$. The objects from the VIMOS sample are shown as black squares. The majority of the VIMOS sample ($\approx 62\%$) fall below the line of $K_{asym} = 0.55$ suggesting that their kinematics are consistent with rotating disks.

(R_{asym}) which are consistent with the models of near face–on disks suggesting that nearly a fifth of the sample have potentially been misidentified due to inclination effects. The distribution of position angles and inclinations for every object identified as a disk are shown in Figure 6.5. These distributions are consistent with those expected for a randomly selected sample of disks, having a uniform distribution in position angle and inclinations which are distributed about 60°. However, it
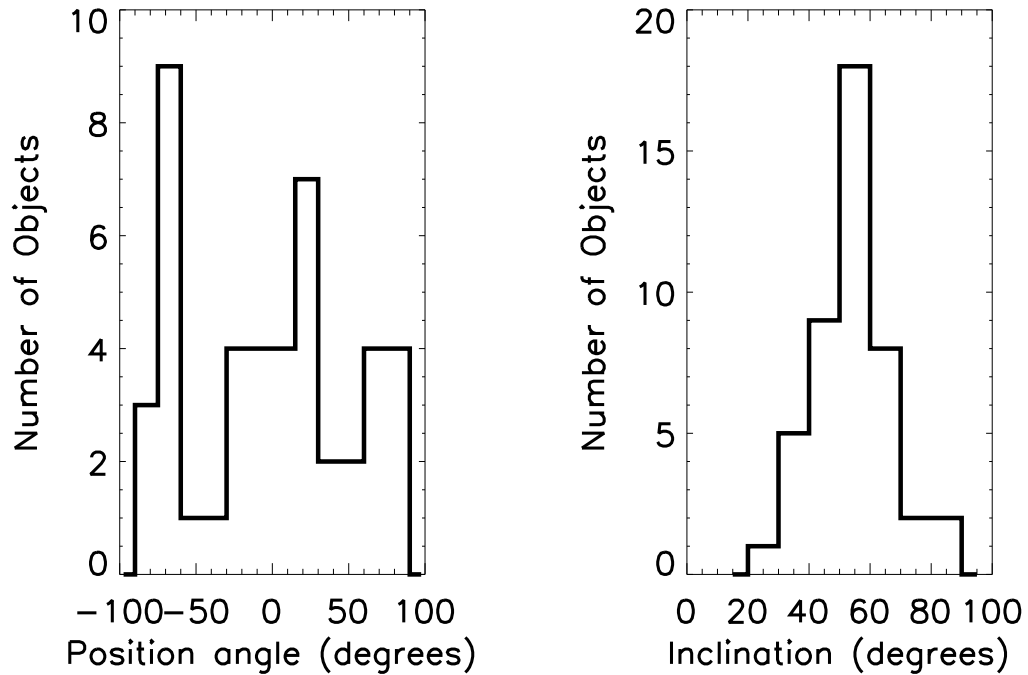
Figure 6.5: Histograms showing the distribution of position angle and inclination for the objects classified as disks in the VIMOS sample. *Left* - A histogram of the measured kinematic position angle, the distribution is largely uniform as would be expected for an unbiased sample. *Right* - A histogram of the measured inclination, the distribution peaks at $\approx 60^o$ as would be expected for a uniformly selected sample of disks. However, the distribution shows no objects with very low inclinations (close to face–on). While such objects are unlikely they should not be completely absent given the size of the sample. This is clearly a result of the difficulty in identifying face–on disks confirming that the kinemetric analysis is biased towards misidentifying face–on disks.

should be noted that no objects with an inclination of $< 20^o$ are identified. While the number of such objects should to be small they are not expected to be absent given the size of the sample. This suggests that the kinemetric analysis is indeed misidentifying disks with an inclination putting them close to face on.

6.4 Discussion

The results presented above build on the results presented in Chapter 3 confirming unambiguously that the ionised gas in many of the BCGs in the VIMOS sample have a coherent and ordered kinematic structure which is consistent with that of a rotating disk. The fact that such a large fraction ($\approx 62\%$) of the sample show such a

structure clearly suggests that this is the natural state of these systems. Considering these results in the context of the most well studied system in the sample, Hydra-A (Chapter 5), would suggest that these disks play an important role in the evolution of cluster cores. Unfortunately, the extensive multi–wavelength observations studied in Chapter 5 are not available for the full sample of objects making an analysis of the full sample to the same degree of detail impossible at this time. However, it is only by considering the sample as a whole that the importance of these disks can be measured.

6.4.1   Disk modelling

Disk models which followed an arctan function (Courteau, 1997) were fitted to the mean velocity maps of each object identified as a disk to parametrise their rotation. These models took the same form as the model disks produced in Section 6.3.1 and as such their mean velocity profiles were determined using Equation 6.3.1. The input parameters were varied through a Monte Carlo routine until the best fitting model was determined (by minimising the χ^2). These models were used to refine the PA used during the kinemetric analysis as well as to calculate $V_{2.2}$ and $M_{2.2}$ as defined in Chapter 5. In Figure 6.6 the mean velocity fields of each object from the sample classified as a disk are shown, the best fitting model is shown as contours of constant velocity. In the right hand panels of Figure 6.6 the rotation curves of each map, extracted along the best fitting PA, are shown along with the rotation curve of the best fitting model. The position of $V_{2.2}$ is shown on the plots in green and for most objects can be seen to fall close to the region of the velocity profile covered by the data.
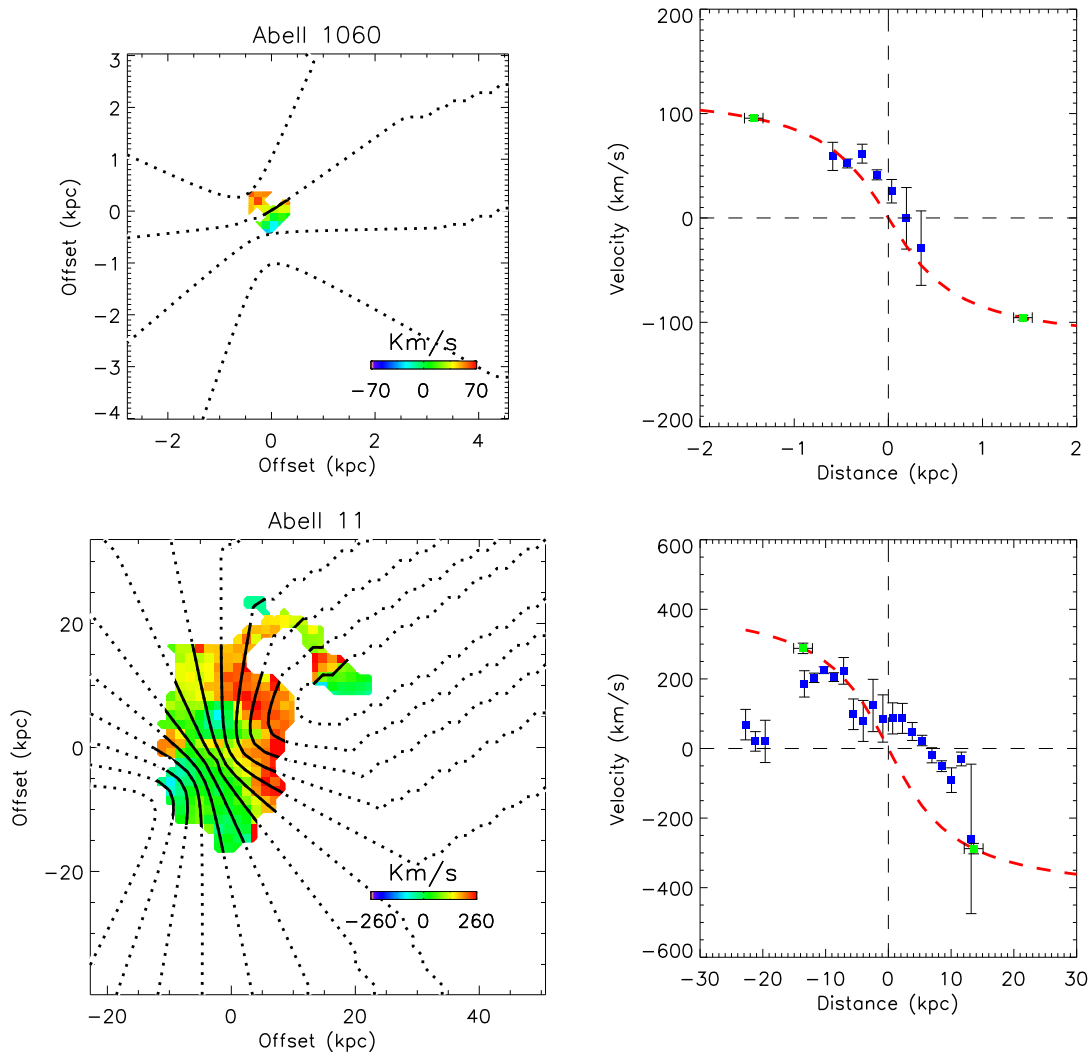
Figure 6.6: Here we show plots of the disk fits to each object identified as a disk. On the left we show the velocity maps with contours of the constant velocity from the disk models contoured on top. In the right hand panel we show the velocity curve of each object extracted along the PA determined but the disk models (blue points) along with the rotation curve of the best fitting disk models (red dashed line). The green points indicate the velocity at $R_{2.2}$. For the most part the models are good approximations of the rotation curves and it can be seen that the gas in the majority of objects samples out to $R_{2.2}$ allowing for an accurate determination of $V_{2.2}$ and the dynamical mass of the system.

Figure 6.6: continued.

Figure 6.6: continued.

Figure 6.6: continued.

Figure 6.6: continued.

Figure 6.6: continued.

Figure 6.6: continued.

Figure 6.6: continued.
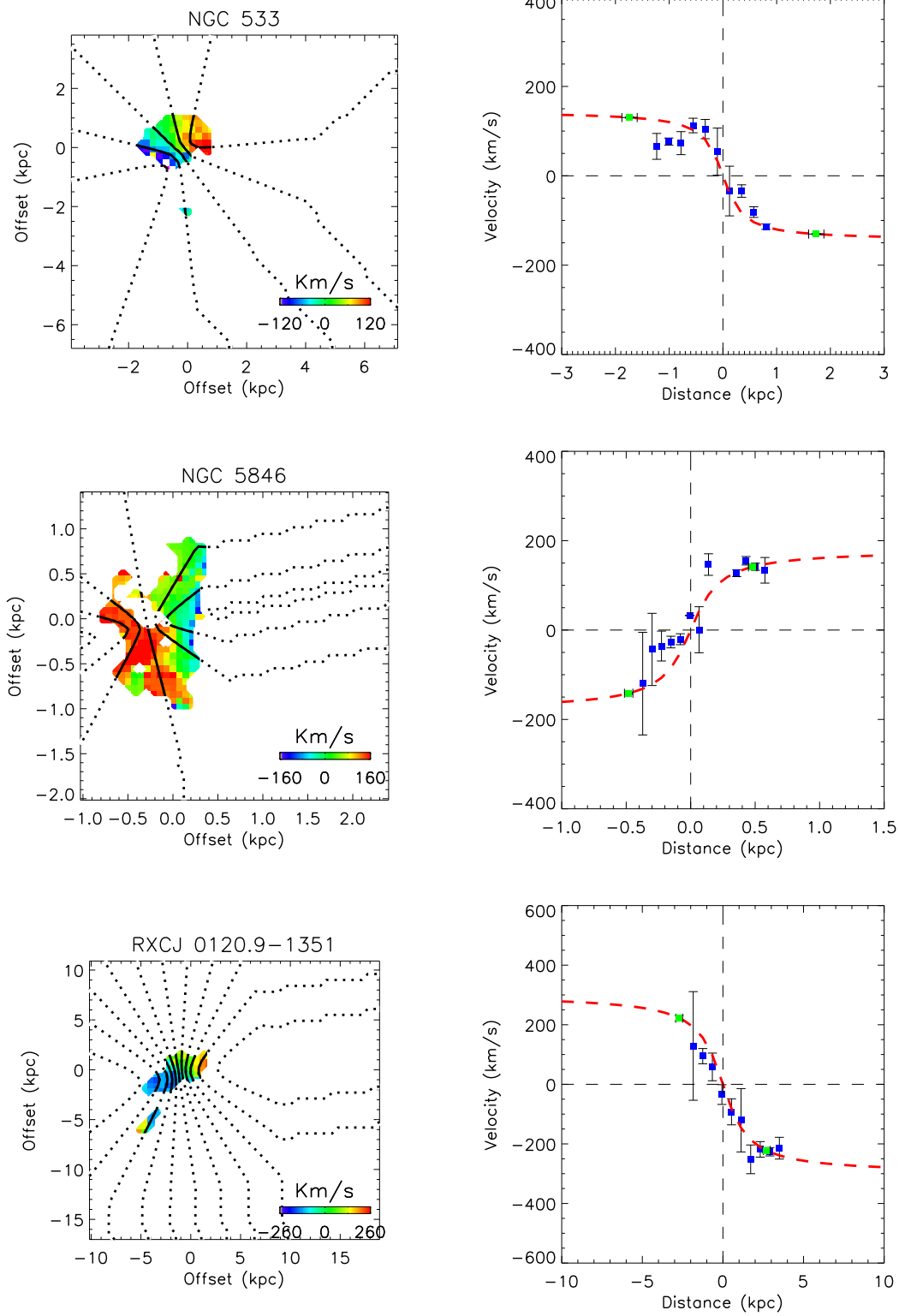
Figure 6.6: continued.
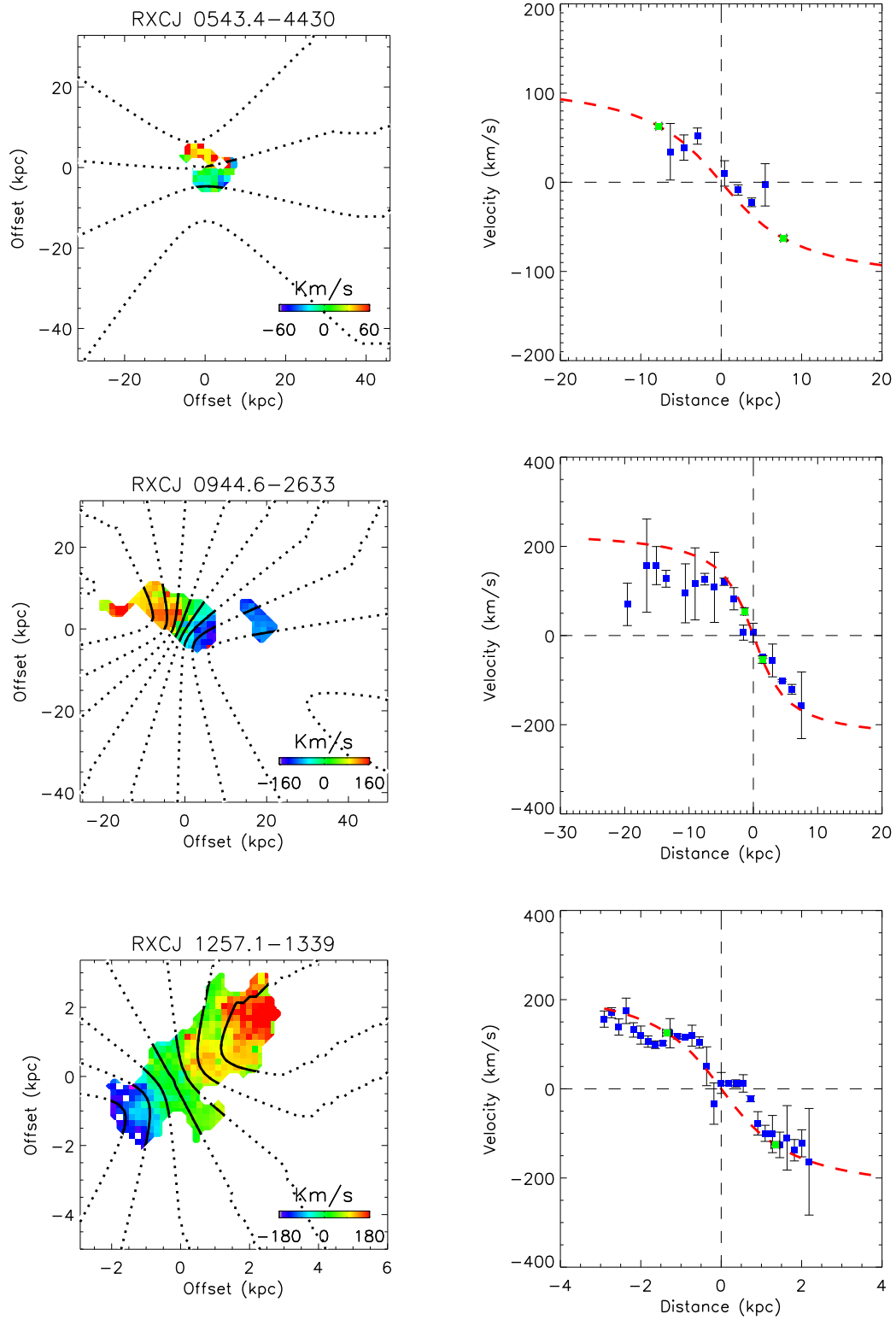
Figure 6.6: continued.
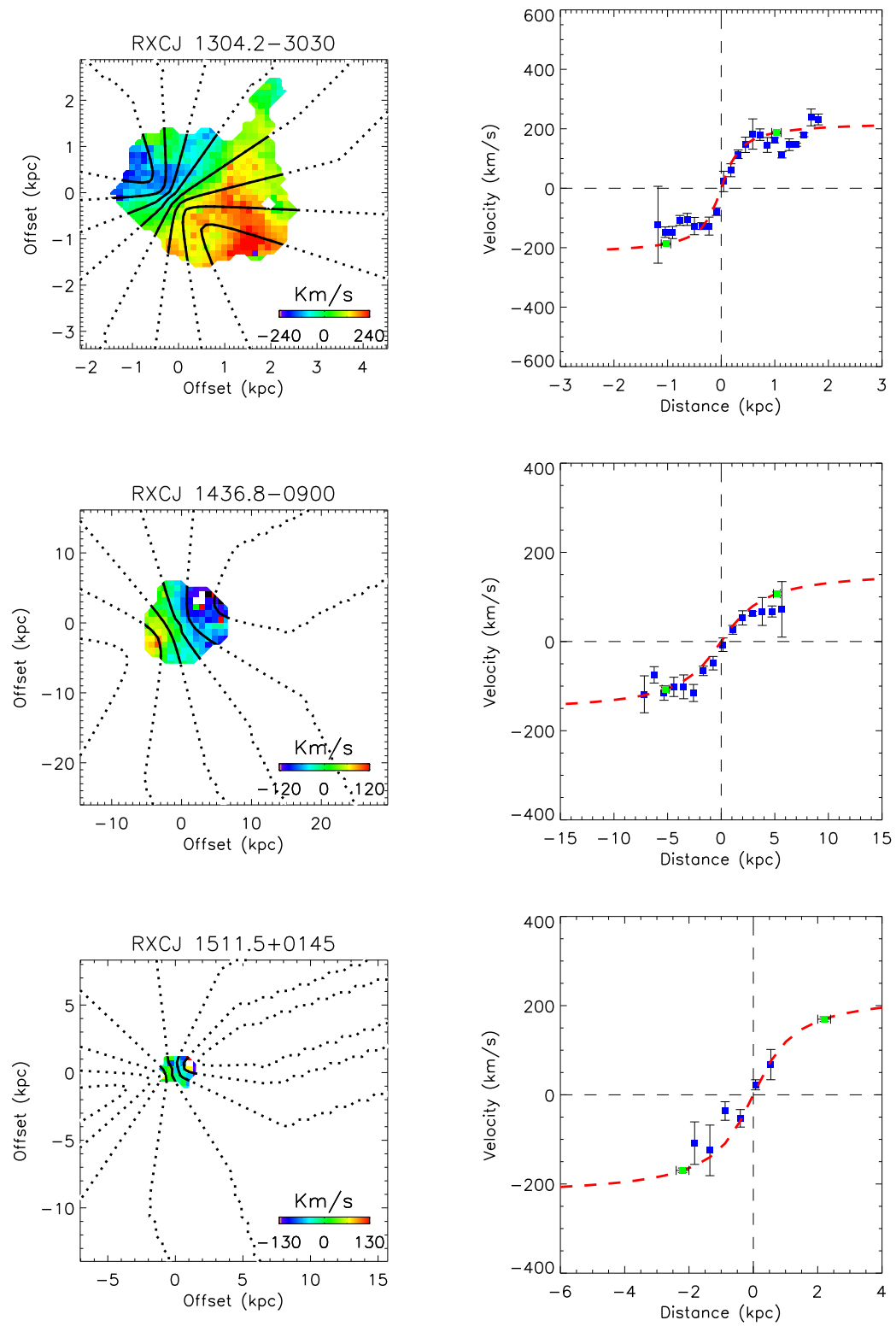
Figure 6.6: continued.
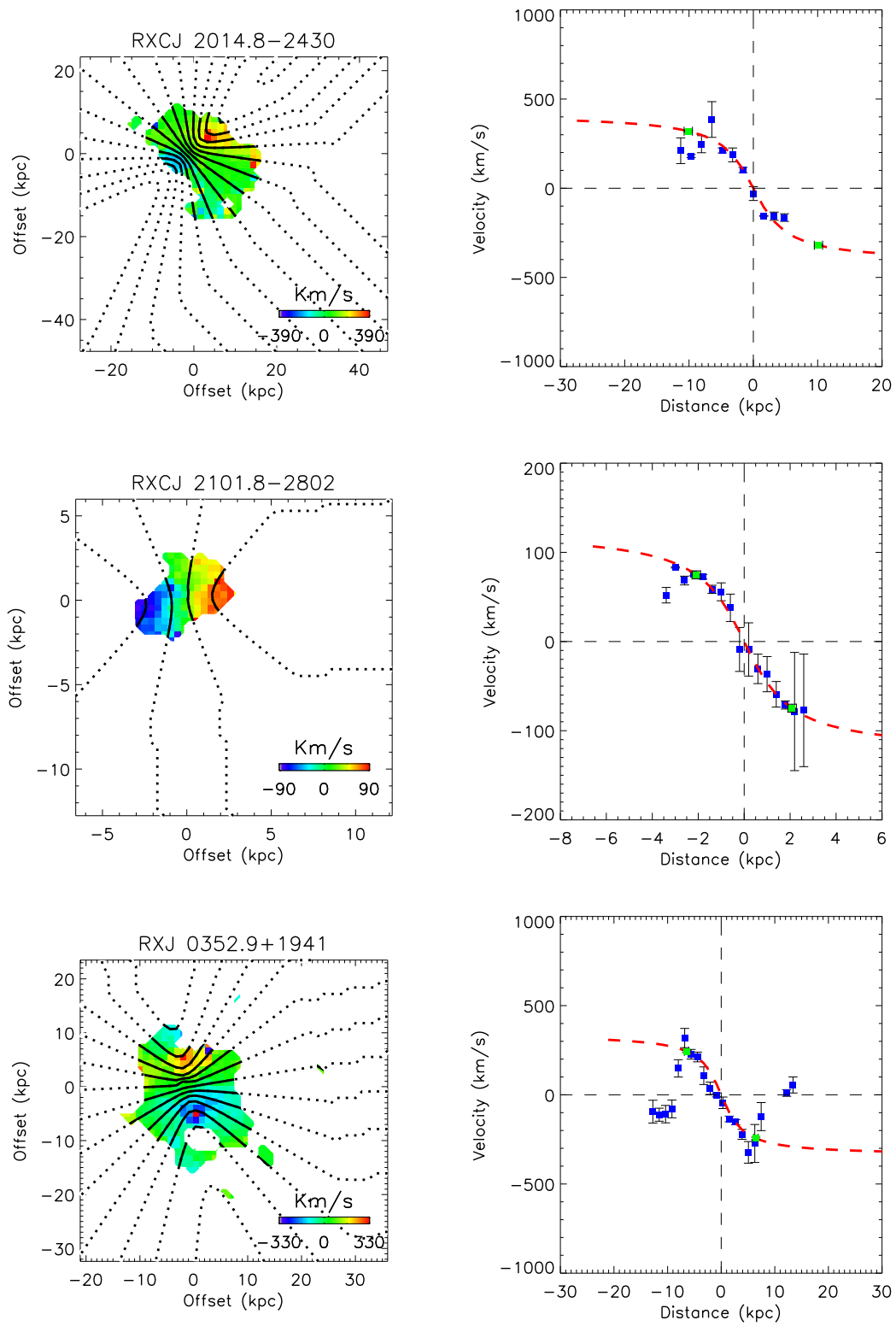
Figure 6.6: continued.
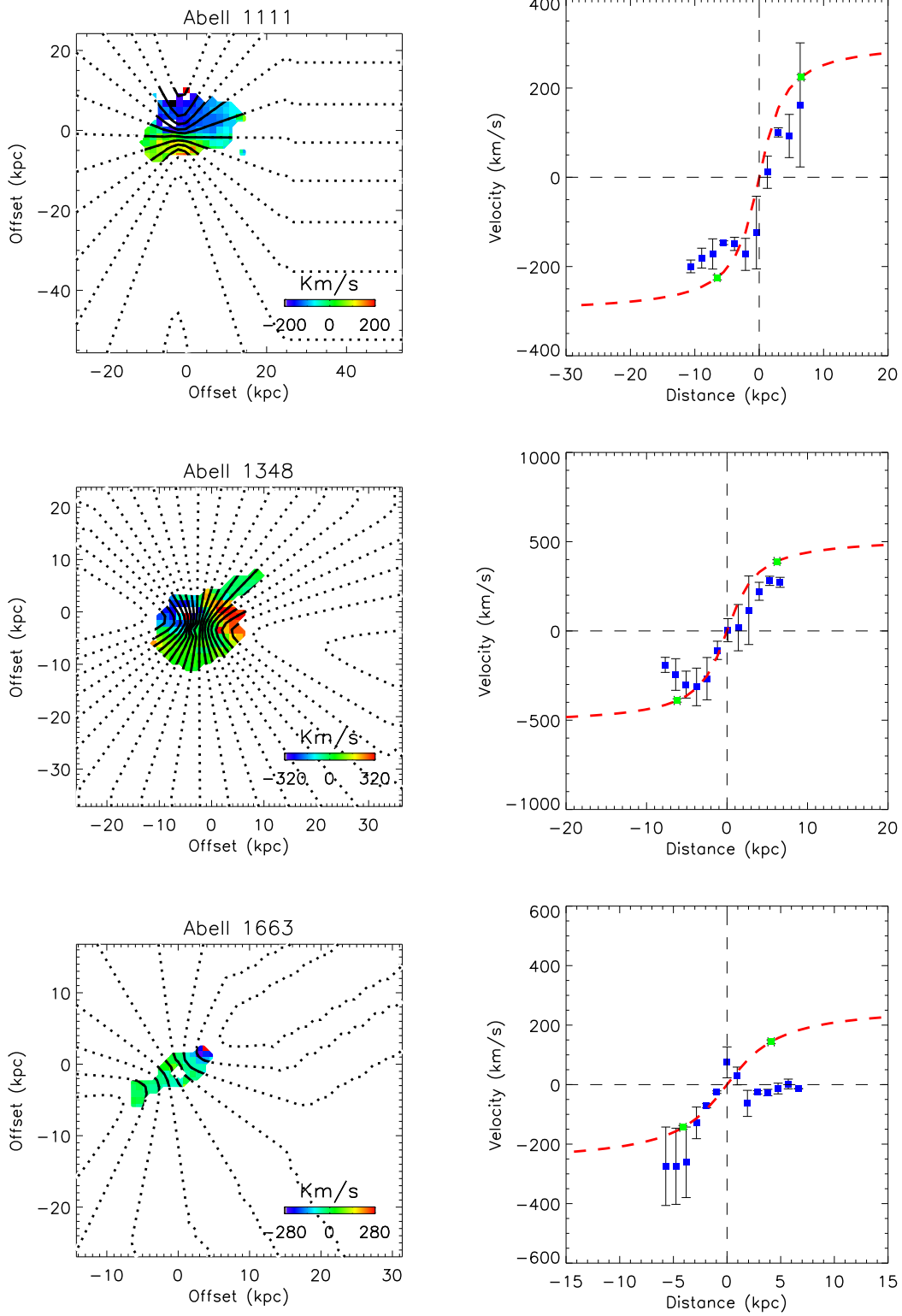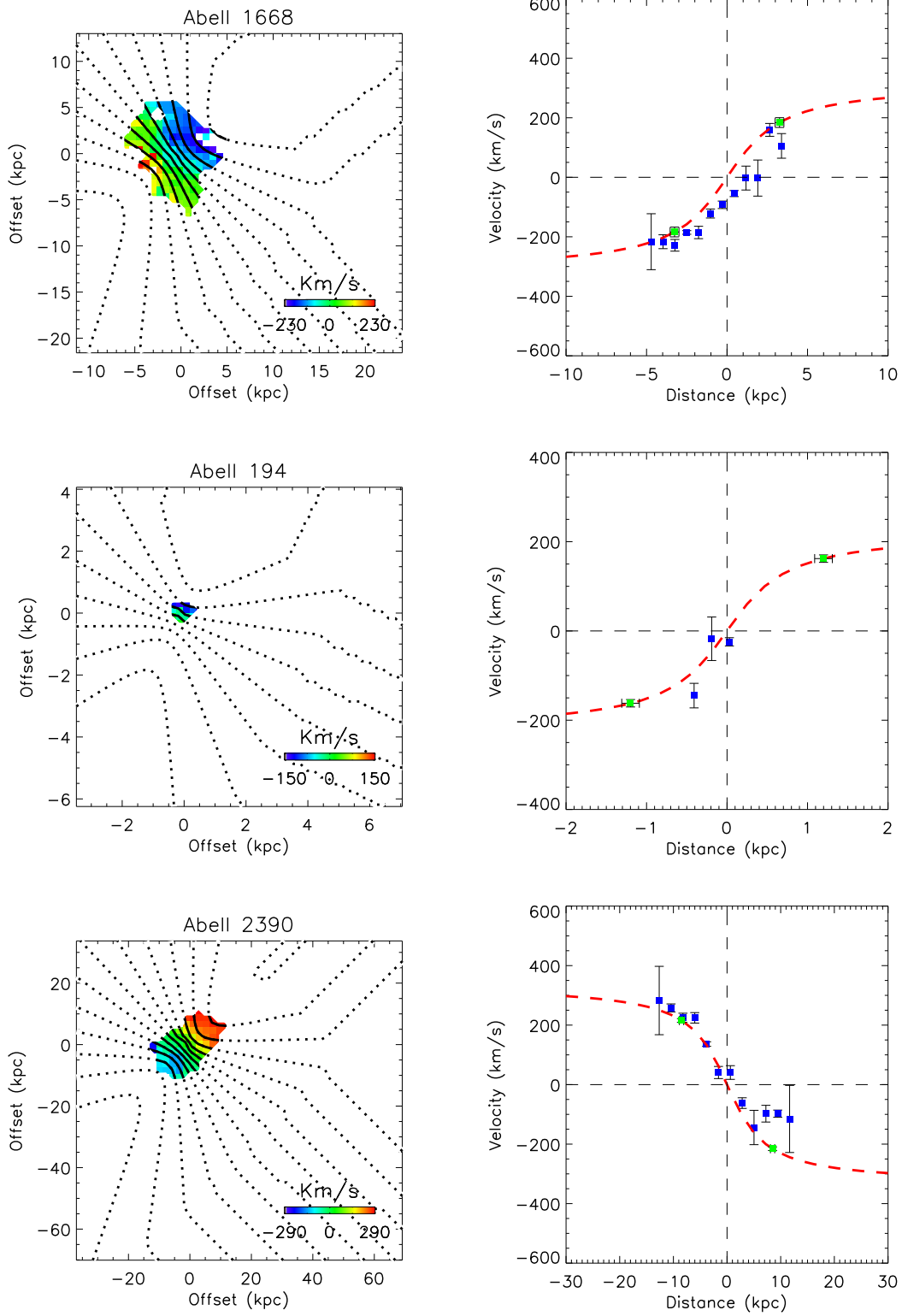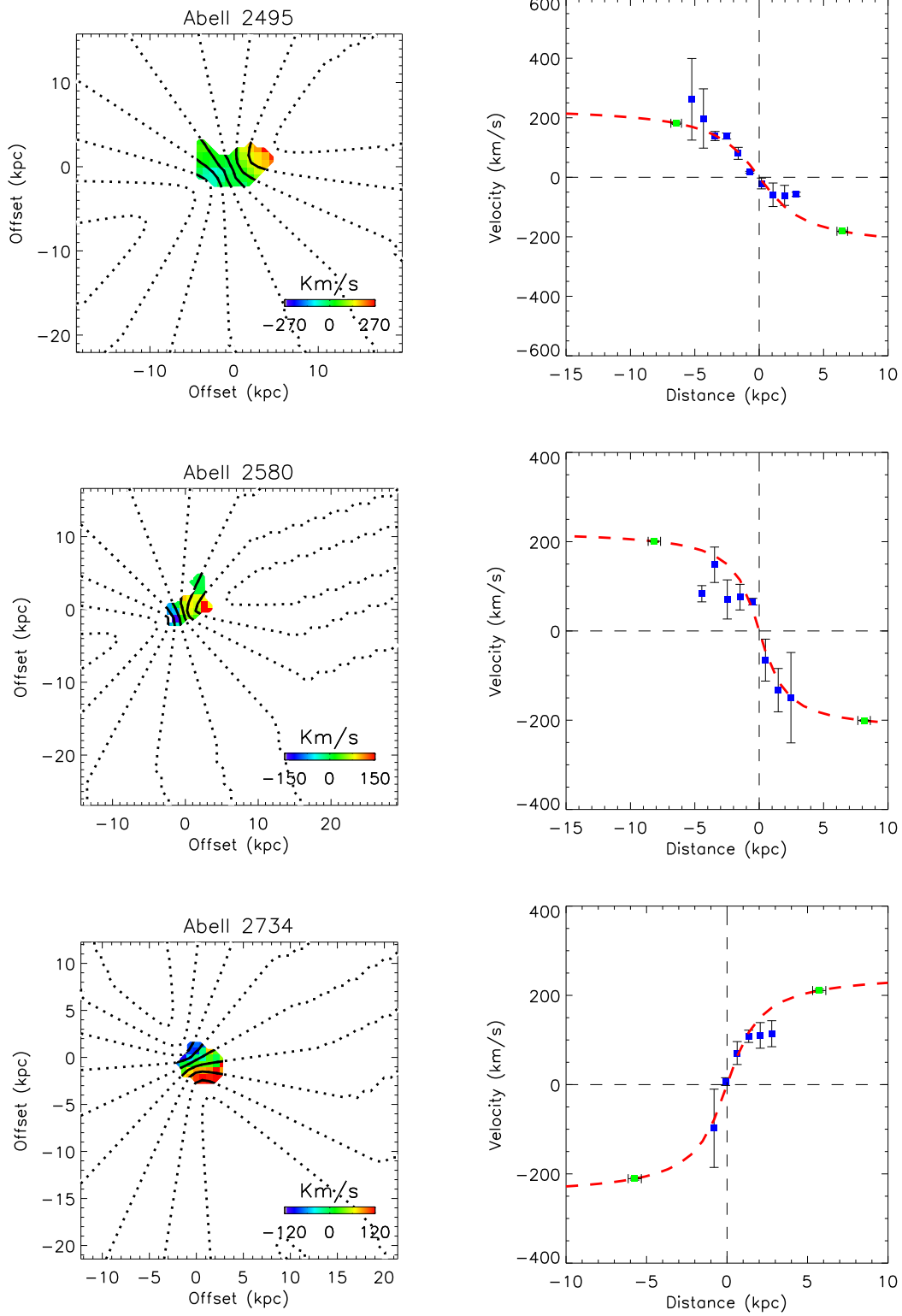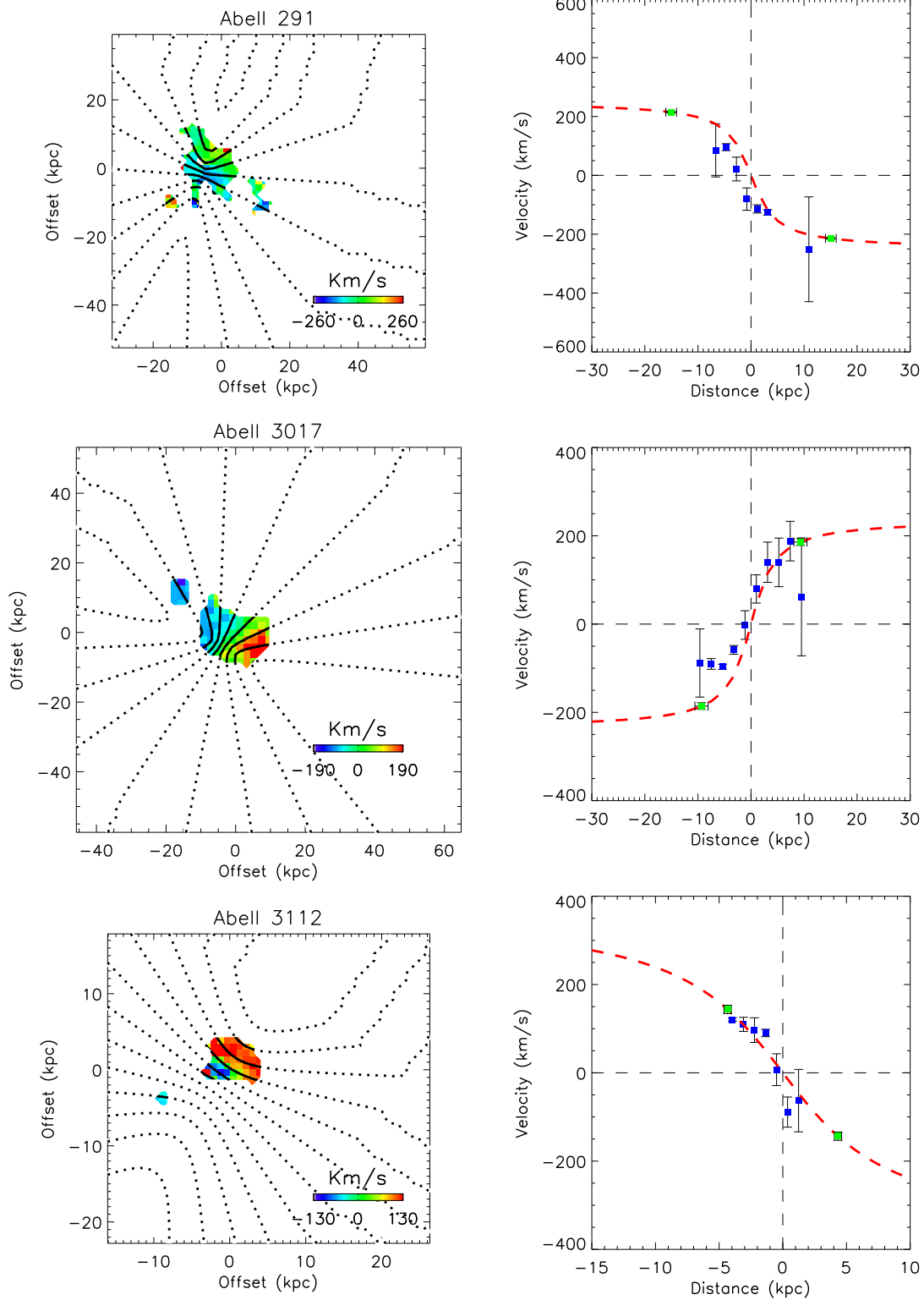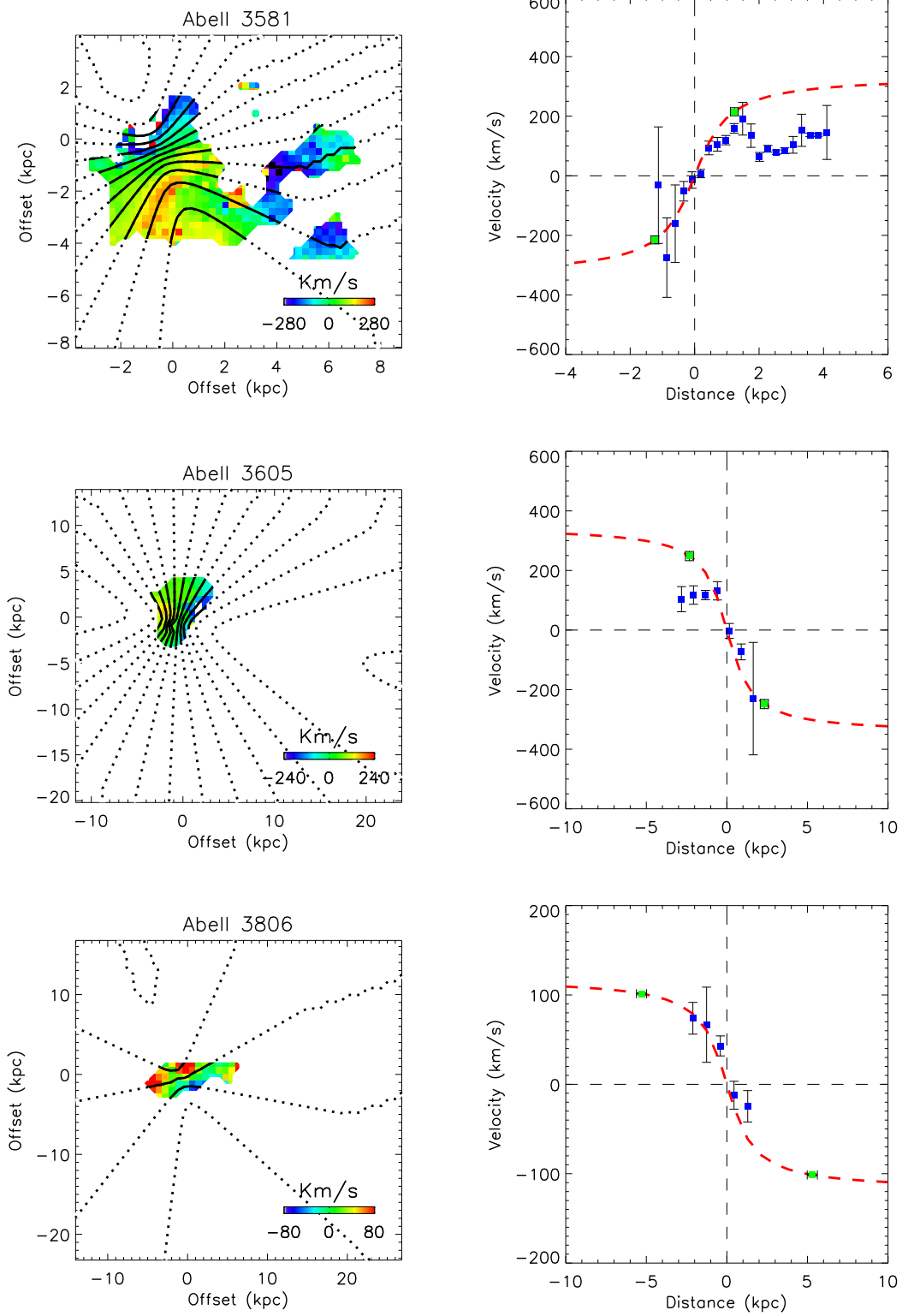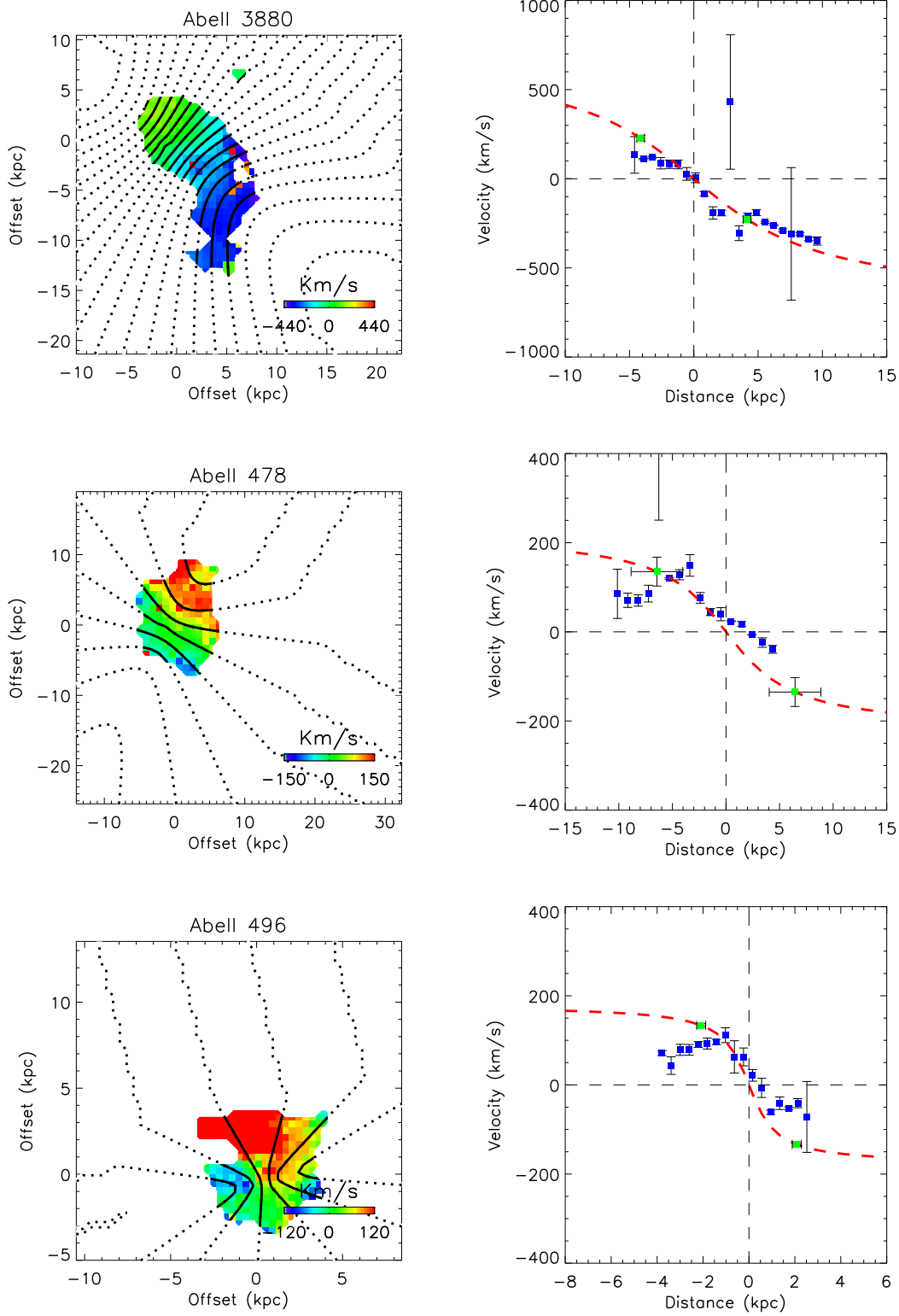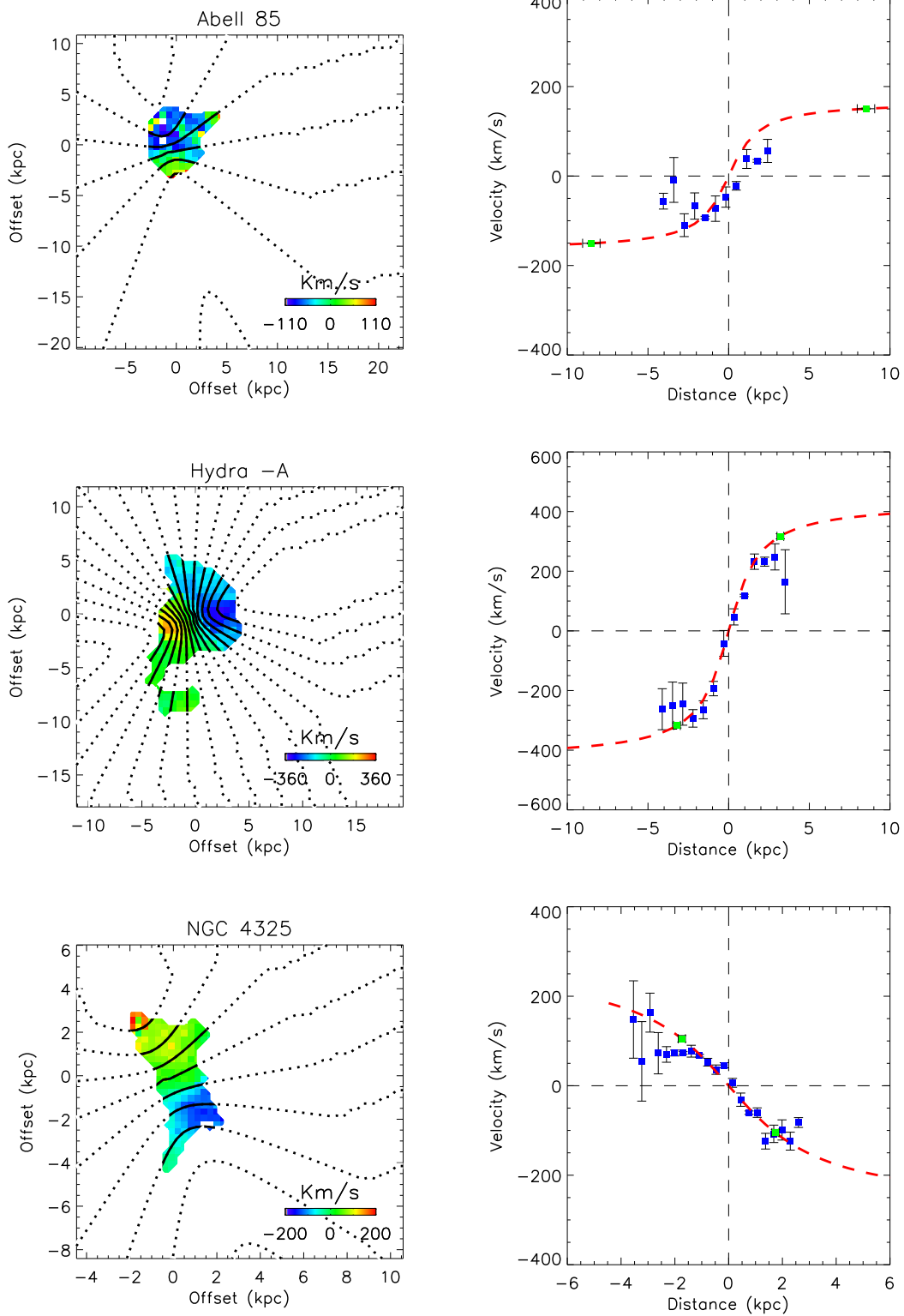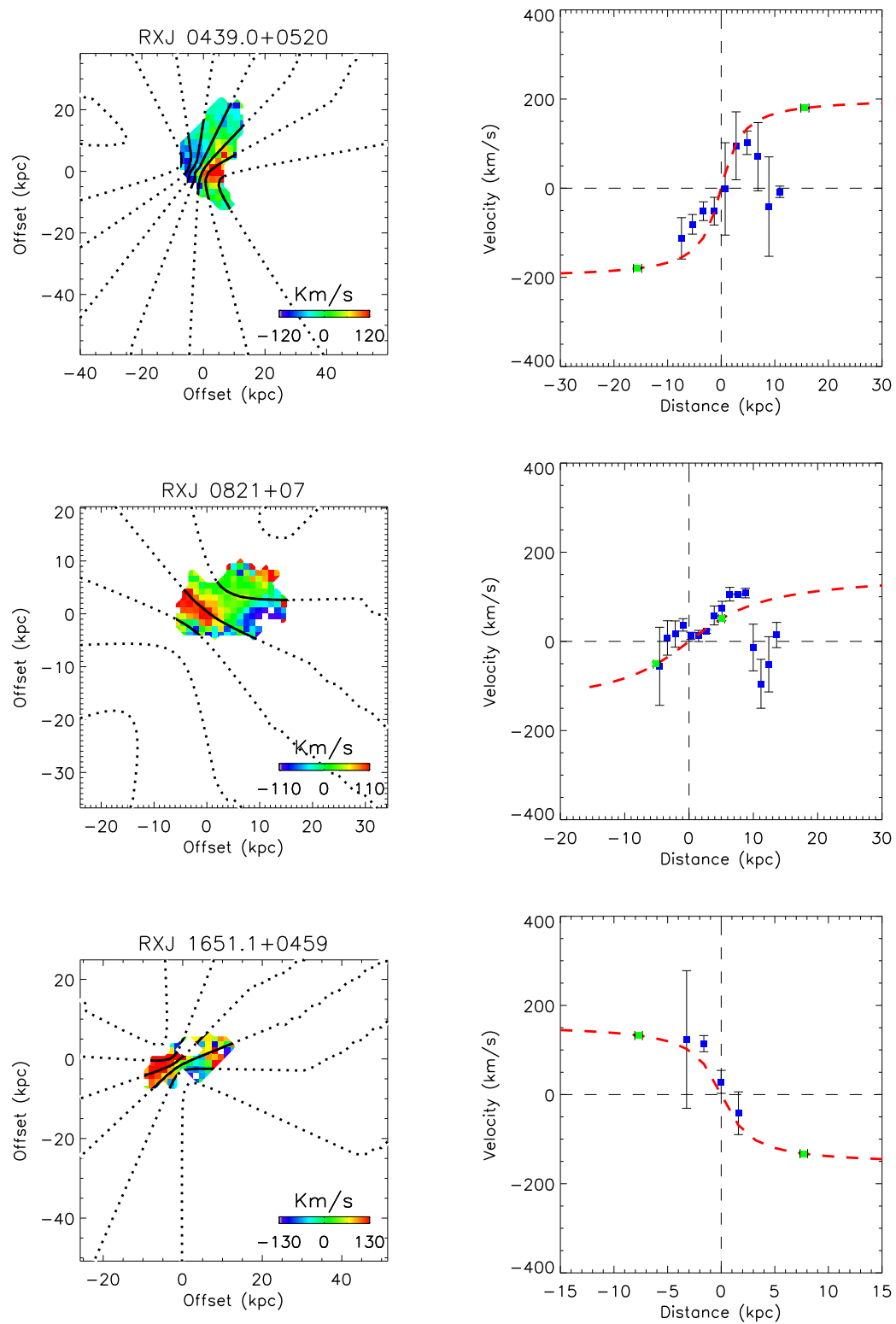
Figure 6.6: continued.
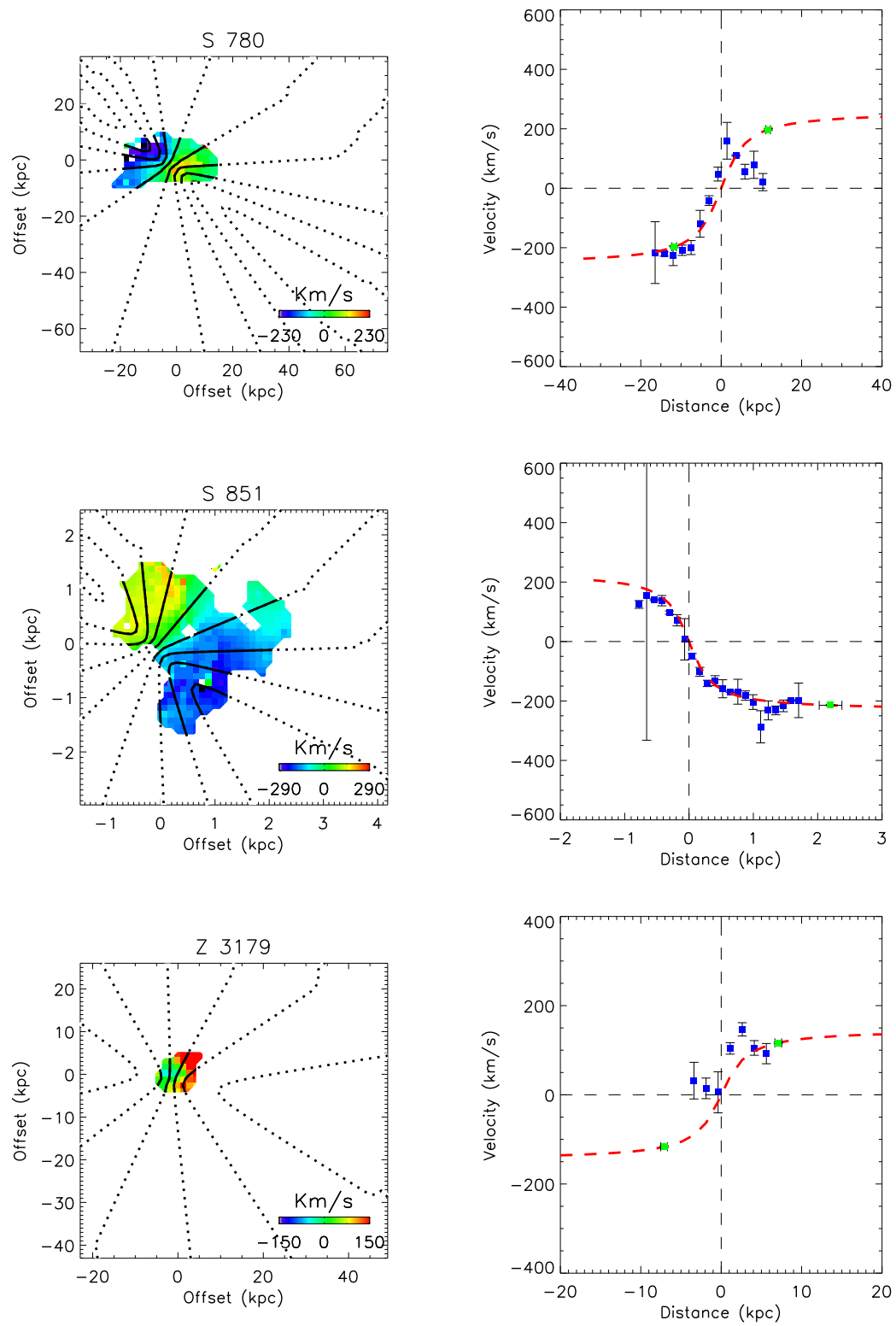
Figure 6.6: continued.
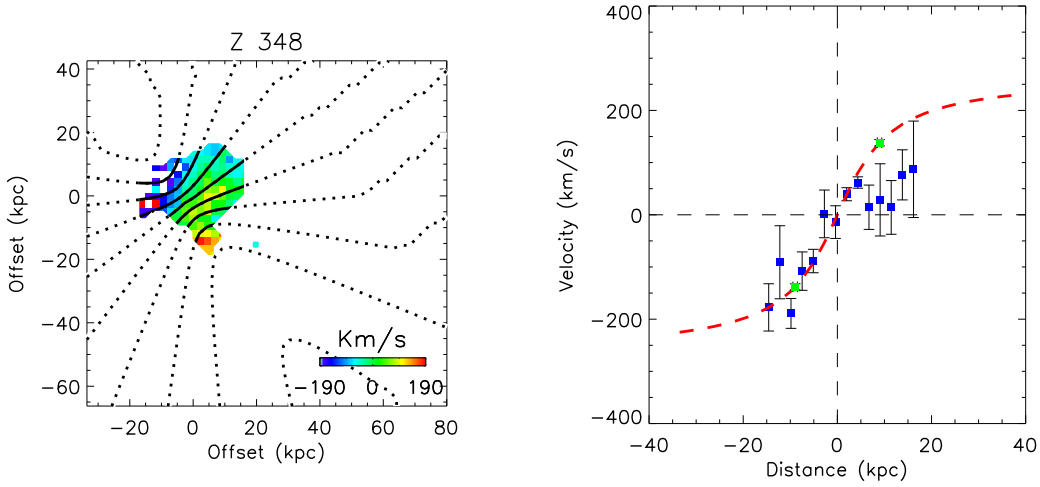
Figure 6.6: continued.

The calculated values of $R_{2.2}$, $V_{2.2}$ and $M_{2.2}$ are given in Table 6.3. $V_{2.2}$ is the most appropriate measure of the rotation velocity as it is expected to be the peak rotational amplitude if the disk is assumed to be purely exponential (Freeman, 1970; Binney & Tremaine, 1987). The values of $V_{2.2}$ quoted in Table 6.3 are corrected for the inclination of the system and thus will not match the position of the green points in Figure 6.6 except where the system is determined to be almost edge–on. It should also be noted that for some objects the detected ionised emission does not extend as far as $R_{2.2}$. In such cases the determination of $V_{2.2}$ requires extrapolation of the disk model. As can be seen from Figure 6.6 however, this extrapolation never extends beyond a few times the scale of the ionised gas emission. With $R_{2.2}$ determined from the continuum emission and $V_{2.2}$ estimated from the disk fit, $M_{2.2}$ is then the dynamical mass within $R_{2.2}$ assuming a keplerian orbit with low eccentricity (as would be expected for a disk). As such $M_{2.2}$ is simply given by

$$M_{2.2} = \frac{V_{2.2}^2 \times R_{2.2}}{G} \tag{6.4.13}$$

where G is the gravitational constant.

Due to the less comprehensive data a full comparison of the fraction of $M_{2.2}$ in each phase is not possible for each object the way it was for Hydra-A. However, the results presented in Chapter 5 suggest that the dominant component of the cool material ($\lesssim 10^4$ K) is the molecular gas as traced by the CO emission. For

TABLE. 6.3.
THE VELOCITY AT $R_{2.2}$ AND THE IMPLIED DYNAMICAL MASS

Object	$R_{2.2}$ (kpc)	$V_{2.2}$ (km s^{-1})	$M_{2.2}$ M$_\odot$	CO FWHM (km s^{-1})
Abell 1060	1.43 ± 0.099	123 ± 2.3	$5.1 \times 10^9 \pm 3.7 \times 10^8$	86 ± 20
Abell 11	13.6 ± 1.5	325 ± 15	$3.4 \times 10^{11} \pm 4.3 \times 10^{10}$	288 ± 53
Abell 1111	6.5 ± 0.42	252 ± 5.3	$9.7 \times 10^{10} \pm 6.9 \times 10^9$	—
Abell 1348	6.1 ± 0.35	487 ± 9.1	$3.4 \times 10^{11} \pm 2.1 \times 10^{10}$	418 ± 77
Abell 1663	4.1 ± 0.29	159 ± 6.4	$2.4 \times 10^{10} \pm 2.2 \times 10^9$	—
Abell 1668	3.3 ± 0.27	368 ± 13.7	$1.0 \times 10^{11} \pm 1.0 \times 10^{10}$	—
Abell 194	1.2 ± 0.11	268 ± 8.3	$2.0 \times 10^{10} \pm 2.0 \times 10^9$	—
Abell 2390	8.7 ± 0.42	311 ± 6.1	$1.9 \times 10^{11} \pm 1.0 \times 10^{10}$	—
Abell 2495	6.4 ± 0.41	209 ± 3.9	$6.6 \times 10^{10} \pm 4.6 \times 10^9$	—
Abell 2580	8.1 ± 0.48	228 ± 1.7	$9.8 \times 10^{10} \pm 5.9 \times 10^9$	—
Abell 2734	5.6 ± 0.37	244 ± 3.3	$7.9 \times 10^{10} \pm 5.8 \times 10^9$	—
Abell 291	15.0 ± 1.0	242 ± 2.7	$2.0 \times 10^{11} \pm 1.4 \times 10^{10}$	218 ± 93
Abell 3017	9.3 ± 1.2	219 ± 7.6	$1.0 \times 10^{11} \pm 1.5 \times 10^{10}$	—
Abell 3112	4.3 ± 0.29	182 ± 9.4	$3.4 \times 10^{10} \pm 3.3 \times 10^9$	—
Abell 3581	1.2 ± 0.12	311 ± 13.5	$2.8 \times 10^{10} \pm 3.2 \times 10^9$	156 ± 60
Abell 3605	2.3 ± 0.25	382 ± 15.5	$7.9 \times 10^{10} \pm 9.7 \times 10^9$	—
Abell 3806	5.3 ± 0.31	123 ± 1.2	$1.9 \times 10^{10} \pm 1.1 \times 10^9$	—
Abell 3880	4.1 ± 0.30	279 ± 16.7	$7.5 \times 10^{10} \pm 8.3 \times 10^9$	500 ± 117
Abell 4059	3.3 ± 0.23	343 ± 10.5	$9.0 \times 10^{10} \pm 7.4 \times 10^9$	—
Abell 478	6.4 ± 0.25	166 ± 3.1	$4.1 \times 10^{10} \pm 1.9 \times 10^9$	120 ± 16
Abell 496	2.1 ± 0.20	141 ± 4.2	$9.7 \times 10^9 \pm 1.0 \times 10^9$	—
Abell 85	8.5 ± 0.54	189 ± 1.3	$7.1 \times 10^{10} \pm 4.6 \times 10^9$	96 ± 37
Hydra -A	3.2 ± 0.21	397 ± 8.5	$1.2 \times 10^{11} \pm 8.5 \times 10^9$	571 ± 62
NGC 4325	1.7 ± 0.13	122 ± 7.2	$6.0 \times 10^9 \pm 6.8 \times 10^8$	168 ± 53
NGC 533	1.7 ± 0.14	163 ± 1.5	$1.1 \times 10^{10} \pm 8.8 \times 10^8$	—
NGC 5846	0.48 ± 0.032	149 ± 2.6	$2.5 \times 10^9 \pm 1.8 \times 10^8$	—
RXCJ 0120.9-1351	2.7 ± 0.21	355 ± 9.1	$7.9 \times 10^{10} \pm 6.7 \times 10^9$	—
RXCJ 0132.6-0804	2.5 ± 0.11	116 ± 3.4	$7.8 \times 10^9 \pm 4.7 \times 10^8$	—
RXCJ 0331.1-2100	17.4 ± 2.0	222 ± 2.9	$2.0 \times 10^{11} \pm 2.4 \times 10^{10}$	—
RXCJ 0543.4-4430	7.8 ± 0.37	96 ± 2.7	$1.7 \times 10^{10} \pm 1.0 \times 10^9$	—
RXCJ 0944.6-2633	1.4 ± 0.15	80 ± 8.1	$2.1 \times 10^9 \pm 3.7 \times 10^8$	—
RXCJ 1257.1-1339	1.3 ± 0.11	141 ± 7.2	$6.2 \times 10^9 \pm 6.7 \times 10^8$	—
RXCJ 1304.2-3030	1.0 ± 0.088	231 ± 3.8	$1.3 \times 10^{10} \pm 1.1 \times 10^9$	—
RXCJ 1436.8-0900	5.2 ± 0.32	157 ± 4.1	$3.0 \times 10^{10} \pm 2.1 \times 10^9$	187 ± 57
RXCJ 1511.5+0145	2.2 ± 0.20	177 ± 5.2	$1.6 \times 10^{10} \pm 1.6 \times 10^9$	—
RXCJ 2014.8-2430	10.1 ± 0.65	352 ± 6.1	$2.9 \times 10^{11} \pm 2.0 \times 10^{10}$	—
RXCJ 2101.8-2802	2.1 ± 0.19	97 ± 4.5	$4.6 \times 10^9 \pm 5.1 \times 10^8$	—
RXJ 0352.9+1941	6.5 ± 0.42	295 ± 6.5	$1.3 \times 10^{11} \pm 9.4 \times 10^9$	304 ± 65
RXJ 0439.0+0520	15.6 ± 0.77	288 ± 1.8	$3.0 \times 10^{11} \pm 1.5 \times 10^{10}$	—
RXJ 0821+07	5.1 ± 0.47	63 ± 4.8	$4.6 \times 10^9 \pm 6.6 \times 10^8$	126 ± 15
RXJ 1651.1+0459	7.7 ± 0.35	201 ± 1.9	$7.2 \times 10^{10} \pm 3.5 \times 10^9$	—
S 780	11.7 ± 0.58	205 ± 3.0	$1.1 \times 10^{11} \pm 6.1 \times 10^9$	252 ± 109
S 851	2.2 ± 0.18	237 ± 1.6	$2.9 \times 10^{10} \pm 2.3 \times 10^9$	—
Z 3179	7.1 ± 0.42	149 ± 2.1	$3.7 \times 10^{10} \pm 2.3 \times 10^9$	—
Z 348	9.0 ± 0.47	177 ± 5.9	$6.5 \times 10^{10} \pm 4.6 \times 10^9$	—

Table 6.3: The values or $R_{2.2}$, $V_{2.2}$ and the implied dynamical mass within $R_{2.2}$ ($M_{2.2}$) for the every object from the VIMOS sample identified as a disk. $R_{2.2}$ is determined from the continuum emission, $V_{2.2}$ is determined from the best fitting disk model and has been corrected for inclination. $M_{2.2}$ is then determined from $R_{2.2}$ and $V_{2.2}$ using Equation 6.4.13.

Hydra-A the kinematics of the ionised gas (measured by $V_{2.2}$) were consistent with the line width of the CO detection suggesting that both the line emission and the CO emission are from the same reservoir of gas. In such a case it is possible to use the ionised lines to trace the kinematics of the molecular reservoir within the cores of clusters. Figure 6.7 shows a comparison of the peak rotational amplitude of the
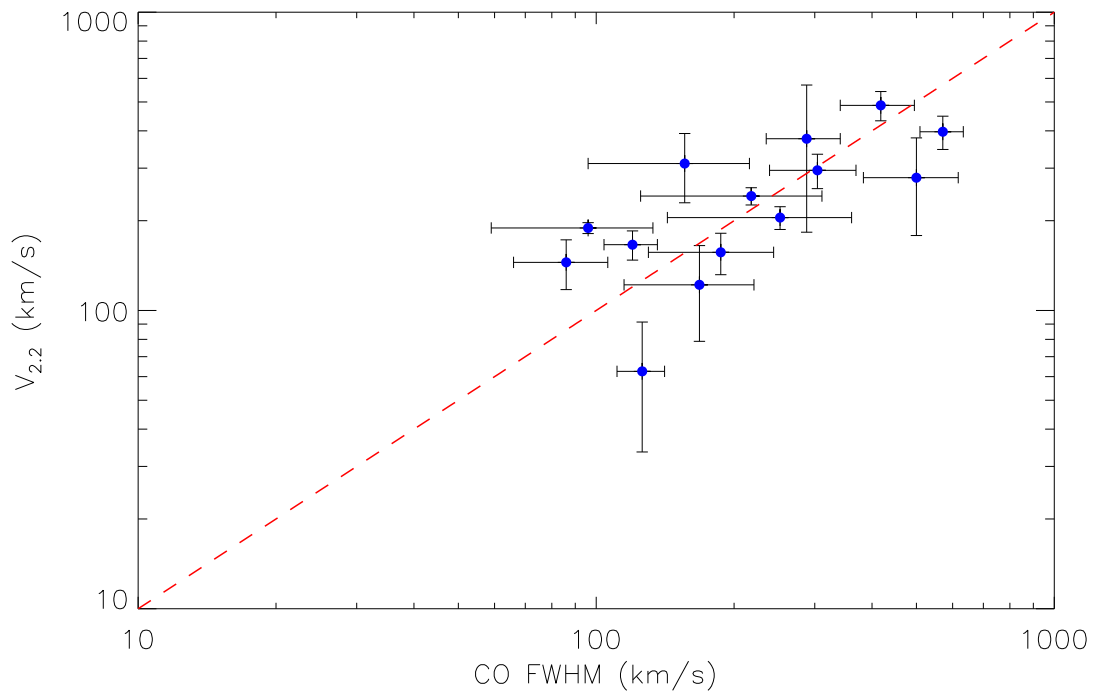
Figure 6.7: This plot presents a comparison of the peak rotation amplitude of the objects from the VIMOS sample identified as disks with the CO line width of those objects (in blue). Objects which here not identified as disks but which do have CO detections are plotted as well (in green), however for these objects the peak–to–peak velocity is used instead of $V_{2.2}$. A clear correlation can be seen in this plot suggesting that the ionised and molecular gas share the same kinematics and thus likely trace the same reservoir of gas.

disks in the sample against the FWHM of the CO line (for objects which have a CO detection). A clear correlation can be seen in this plot which implies that the molecular and ionised gas share the same kinematics thus suggesting they are part of the same reservoir of gas.

6.4.2   Alignment

The correlation of the CO line widths with the peak rotational amplitude of the ionised gas disk clearly suggests that the reservoir of molecular gas within the cores of clusters traces the same kinematic structure as the ionised gas. Thus implying that the majority of objects in the VIMOS sample ($\approx 62\%$) contain a kpc scale disk of cold material which is rotating about the centre of the BCG. This situation is similar to that seen in Chapter 5 for Hydra-A for which the axis of rotation of the disk was found to be aligned with the axis along which radio jets from the central

SMBH are inflating cavities in the ICM. This alignment hinted at a connection between the kinematics of cold material on kpc scales and the accretion of material onto the central SMBH and thus the feedback from the AGN. However, with just a single object it is difficult to say with any certainty whether this alignment is the result of an interaction between the disk and SMBH (i.e. the accretion of material from the disk is responsible for aligning the jet) or if it is simply coincidence.

Thus the identification of similar gas disks in the majority of systems ($\approx 62\%$) in the VIMOS sample begs the question, do they also show similar alignment between the axis of rotation and the axis along which the AGN is inflating cavities in the ICM. The axis of rotation for all objects classified as disks was calculated as part of the disk fitting routine discussed in Section 6.4.1. The axis along which the AGN is inflating cavities can be determined from either radio observations which identify jets, or X-ray observations which identify cavities in the ICM. Both of these identification methods are separated into two categories which loosely distinguish low powered and high powered outbursts. We distinguish jets based on their extent while we follow the convention of Hlavacek-Larrondo et al. (2012) in defining X-ray cavities.

Major Jets Major jets are defined as jets which extend over scales greater than a few arcsec. They thus require a substantial amount of energy be released consistently by the AGN over a sustained period of time to allow for their creation. The scale of these jets makes the axis along which they were emitted easy to identify even in relatively low resolution radio observations (from ATCA and VLA, Hogan et al. *in prep*).

Minor Jets Minor jets are jets which extend over less than an arcsec, and in some cases just a few milliarcsec. Thus the total energy input required to create them is substantially less than that of major jets. It is possible that minor jets are the precursors to major jets in systems in which the AGN has only been producing jets for a short time. The smaller scale of these jets means that their axis can only be determined from high resolution radio observations (i.e. from VLBA, VLBI etc.).

Clear Cavities Clear cavities are defined as being clearly visible in X-ray obser-

TABLE. 6.4.
THE AXIS OF ROTATION AND AXIES ALONG WHICH AGN JETS ARE INTERACTING WITH THE ICM

Object	Axis of rotation (Degrees)	Major Jet axis (Degrees)	Minor Jet axis (Degrees)	Clear Cavity axis (Degrees)	Potential Cavity axis (Degrees)
Abell 1348	-9.23 ± 7.8	—	50.5 ± 10	—	—
Abell 1668	37.5 ± 9.6	59.8 ± 10	—	—	—
Abell 2390	44.3 ± 9.9	—	—	—	73.4 ± 10
Abell 2495	31.7 ± 9.9	—	—	—	1.1 ± 10
Abell 3112	54.2 ± 9.98	—	-1 ± 10	—	—
Abell 3581	-65.75 ± 7.9	—	—	-108.9 ± 10	—
Abell 3880	-39.7 ± 9.9	27.5 ± 10	—	—	—
Abell 4059	-51.0 ± 22	-30.9 ± 10	—	-38.2 ± 10	—
Abell 478	57.8 ± 9.9	44.4 ± 10	—	—	—
Abell 496	17.9 ±	—	—	—	31.7 ± 10
Hydra-A	19.6 ± 5.0	24.2 ± 10	—	31.6 ± 10	—
NGC 4325	-65.0 ± 9.99	—	—	—	-50.0 ± 10
RXCJ 0132.6-0804	-4.85 ± 9.39	—	-75 ± 10	—	—
RXCJ 0331.1-2100	18.4 ± 8.8	24.0 ± 10	—	—	—
RXCJ 2014.8-2430	44.6 ± 5.9	46.4 ± 10	—	—	—
RXJ 1651.1+0459	-57.4 ± 4.2	-77.7 ± 10	—	—	—
RXJ 0352.9+1941	-77.0 ± 7.6	—	—	-33.2 ± 10	—
RXJ 0439.0+0520	-23.4 ± 7.7	—	-87.7 ± 10	—	-12.9 ± 10
S851	-43.13 ± 2.0	—	54.7 ± 10	—	—
Z348	-53.58 ± 1.4	—	—	—	-23.4 ± 10

Table 6.4: The axis of rotation as determined from the disk fitting for each disk which also has a detection of radio jets or X-ray cavities. Most objects only have either jets or cavities detected but note that two (Abell 4059 and Hydra-A) have both and they are consistent to withing $\sim 10^o$

vations, many such cavities are visible without the need for unsharp masking (Hydra-A, A2052 for example). Clear cavities require that a substantial mass of gas has been displaced within the ICM and thus require the injection of a lot of energy.

Potential Cavities Potential cavities are defined as being surface brightness depressions in the ICM which are not always clearly defined. Typically they require unsharp masking in order to be detected and even then are not always clearly defined.

The angles associated with the jets were then calculated as the position angle of a straight line drawn through the centre of the cluster and both of the radio lobes or cavities. The calculated angles for the axis of rotation, both types of jets and both types of cavities are given in Table 6.4. Note that data identifying jets or cavities was only available for a small sample of the objects which were identified as disks. Typically each object has either a detection of radio jets or X-ray cavities but a few have both and where they do these axis are consistent.

In Figure 6.8 the axis of rotation of the disks is compared to the axis of the jets

and cavities. The top left hand panel of Figure 6.8 compares the disk axis to the axis of the major and minor jets (in red and blue respectively). With the exception of one outlier the major jets are all closely aligned with axis of rotation of the disk. It can be seen from Table 6.4 that the outlying object is Abell 3880 which is identified as interacting with a cluster member in Chapter 3. This interaction can be seen in the form of a trail of ionised gas leading from the BCG to the companion galaxy. It is possible that this interaction affected the kinematics of the gas sufficiently to shift the axis of rotation of the disk without disturbing the system enough to completely disrupt it. What is perhaps more interesting about this plot however is the fact that the minor jets all appear to be misaligned with axis of rotation of the disk. The bottom left panel of Figure 6.8 is a histogram showing the distribution of offsets between the axis of rotation and the axis of the jets. The black line shows the overall distribution which has a clear peak at no offset and falls off sharply by an offset of 45°. There is a spike in the total distribution at an offset of $\sim 70^o$ which is dominated by the offset of the minor jets.

The central two panels of Figure 6.8 show the same plots for the X-ray cavities. The top plot shows the comparison of the axis of rotation with the axis of both clear (green) and potential (purple) cavities. Both types of cavities show a reasonable alignment with the axis of rotation as demonstrated by the histogram of offsets which again shows a clear peak at no offset and a sharp fall off at large offsets. The right hand two panels of Figure 6.8 show the same plots for the full sample (accounting for objects which have both jet and cavity detections). The comparison of the axes shows a clear trend with the cavities and majority of the major jets being aligned with the axis of rotation and the minor jets showing a misalignment. The histogram of offsets shows a distribution with a clear peak at no offset, again with the minor jets causing a spike at higher offsets. This result clearly shows that the alignment seen in Hydra-A is not unique to that system clearly suggesting that it is the result of the kpc scale disk interacting with the SMBH which is responsible for producing the jets.

It is interesting however that the minor jets do not share this alignment and in fact appear to be preferentially misaligned. The extent of this is illustrated in Figure 6.9 in which the distribution of offsets between the disk and jet/cavity axes
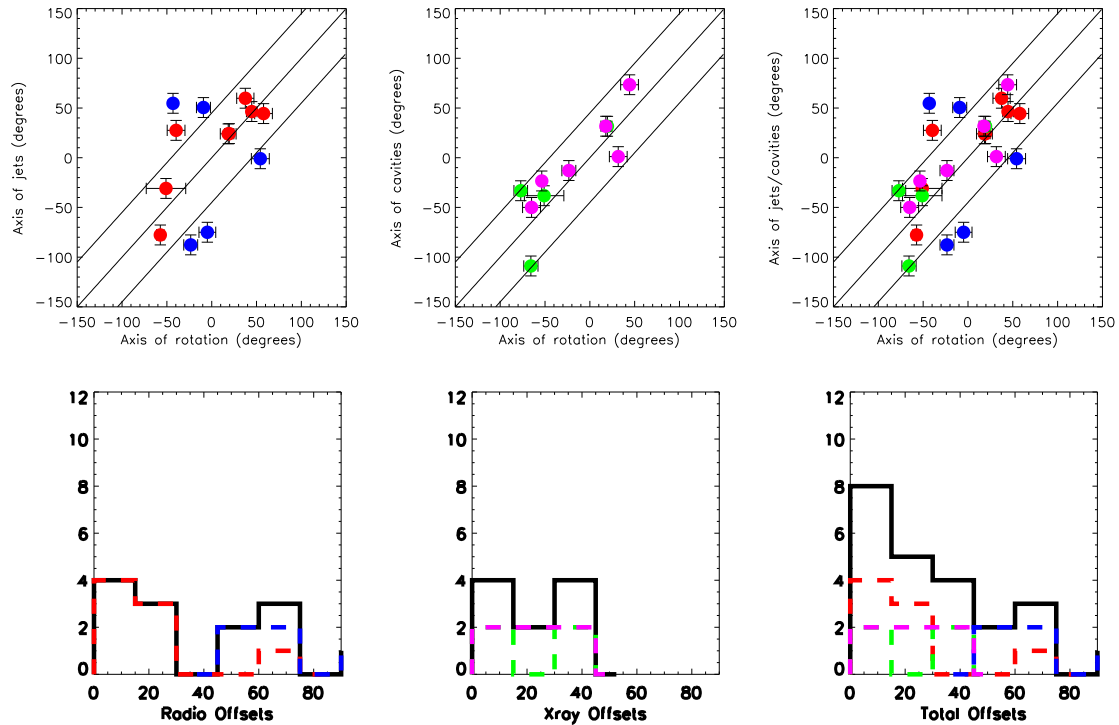
Figure 6.8: A comparison of the axis of rotation of the disks in the VIMOS sample with the axis along which the AGN is producing jets. *Top Left* - A comparison of the axis of rotation with the axis of major and minor jets (in red and blue respectively). The centre line represents a perfect alignment, while the outer lines enclose a region of ± 45°. *Bottom Left* - A histogram showing the offset between the axis of rotation and the axis of the radio jets. The total distribution is shown in black while the contributions from major and minor jets are shown in red and blue respectively. *Top Centre* - A comparison of the axis of rotation with the axis of clear and potential cavities (in green and purple respectively) with the lines identical to those in the top left. *Bottom Centre* - A histogram showing the offset between the axis of rotation and the axis of the X-ray cavities. The total distribution is shown in black while the contributions from clear and potential cavities are shown in green and purple respectively. *Top Right* - Combination of top left and top centre showing all alignments. *Bottom Right* - Histogram showing the total distribution of offsets (black) with the individual contributions in their respective colours. With the exception of the minor jets the axis of rotation and axis of the jets/cavities are well aligned in the majority of systems.

are separated, with the major jets and cavities shown on the left and the minor jets on the right. The major jets and cavities show a clear preference towards an alignment with the axis of rotation of the disk while the minor jets are preferentially misaligned. The reason for the contrast is beyond the scope of this work but may be related to the time scales involved. Large jets and cavities take time to form and thus have longer to be influenced by the kinematics of the disk on kpc scales. The smaller scale jets however could potentially have been formed more quickly
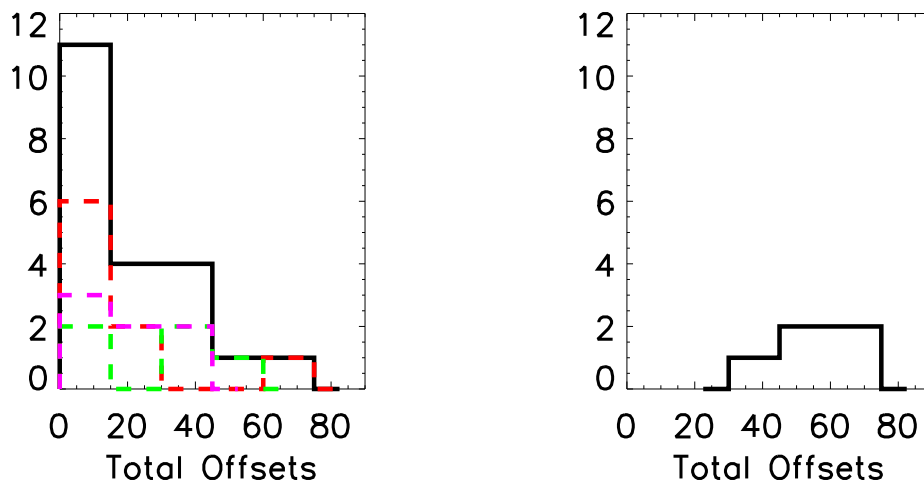
Figure 6.9: *Left* - Histogram showing the distribution of offsets between the angle of rotation of the disks and the axis of the major jets and X-ray cavities. *Right* - Histogram showing the distribution of offsets between the angle of rotation of the disks and the axis of minor jets. Note the stark contrast in the distributions, the major jets and cavities show a clear alignment with the peak of the distribution at no offset with a steep fall off towards higher offsets. The minor jets however show a clear misalignment to the axis of rotation of the disk.

making them more responsive to processes close to the SMBH. However, if this were the case, we would expect to see more scatter in their alignment while Figure 6.8 suggests that they are all misaligned.

6.5   Summary

It is commonly believed that the main contributing factor which prevents the catastrophic cooling of gas within the cores of clusters is mechanical energy provided by AGN outbursts. This AGN feedback requires a mechanism to self-regulate the feedback and cooling so that they remain balanced. As such a link must be established between the cooling of gas on kpc scales and its supply to the SMBH such that the AGN activates when cooling reaches a critical threshold. Here the BCG population has been shown to primarily contain rotating disks of ionised gas. The clear consistency of the peak rotational amplitude of this rotation with the line width of CO detections in these systems implies that the large reservoir of molecular gas follows a similar ordered rotation. In systems in which powerful radio jets are actively being produced and interacting with the ICM the axis of rotation of these disks has clearly

been shown to align parallel to the axis along which the jets are being produced. While it is tempting to note the similarity of such a system to the unified model of AGN it is important to note that the scales involved are much greater. Despite this the prevalence of these disks and their alignment to the jets and cavities indicate that they are clearly an important component of the feedback process.

Chapter 7

Summary and Future Work

7.1 Overview

In this Chapter we will summarise the data and results presented throughout this thesis. We will first recap the main questions which this study aimed to address before listing the main findings of the study. We will then discuss these findings in the context of the questions posed. A summary of future work relating to the sample and findings of this thesis will be presented before we finish with a brief conclusion which draws together the key points presented through this thesis.

7.2 Summary

The goal of this project was to study the spectroscopic and kinematic properties of the cold gas in a representative sample of cluster cores in order to address three key questions:

  i *Are all line emitting systems highly disturbed?* Previous IFU observations of just a handful of objects indicated the presence of gas at high velocity with structures and kinematics suggesting possible interactions with other cluster members (Wilman et al., 2006).

  ii *What role does the Brightest Cluster Galaxy play in the cooling of gas from the ICM?* Most clusters of galaxies have Brightest Cluster Galaxies whose positions are strongly correlated with the cluster core (Peres et al., 1998; Sanderson et al., 2009a; Hudson et al., 2010) which makes disentangling their respective roles in the cooling of gas difficult.

iii *What role does the cold gas play in the feedback process and what is its relation-ship to the fuelling of the AGN?* If radio jets are responsible for injecting energy into the ICM then the degree of fine tuning required suggests a link between the black hole in the Brightest Cluster Galaxy and the gas cooling from the ICM.

To this end we have assembled the largest collection of resolved spectroscopic IFU observations of BCGs to date using the VIsible Multi Object Spectrograph on the Very Large Telescope at the European Southern Observatory. These data formed part of a much larger multiwavelength campaign which provided supplementary data across a number of wavelength regimes which allowed for the multi phase gas to be studied in detail. These supplementary data included resolved spectroscopy of the warm molecular gas in the near infrared (SINFONI), submilimeter observations of the cold molecular gas (CO with IRAM 30m), far infrared spectroscopy of key atomic cooling lines (PACS on Herschel), radio observations to trace the activity of the AGN (VLA, ATCA, VBLA) and of course high spatial resolution X-ray observations of the hot gas in the Intra Cluster Medium. The study of these data has yielded many interesting results which we will now summarise:

1. The extent of the line emitting gas in cluster cores is highly varied from system to system. Some objects (Abell 194 for example) are barely resolved by VIMOS and have line emission which is concentrated around the brightest point of continuum at the centre of the BCG while others are extended over tens of kilo parsecs (S780, Z348 etc.) to where the line emission far outshines the continuum.

2. From the full sample of 73 objects we identify five distinct morphological states: (a) Compact emission concentrated on the core of the BCG (1/73 or 3/73 along a single axis); (b) Quiescent emission which is simple, roughly elliptical and centrally concentrated (45/73); Plumes which have the peak of their emission centred on the BCG but also show a clear extent in one preferential direction (10/73); Offset objects in which the peak and majority of the line emission is centred off the BCG (4/73); Disturbed objects in which the line emission peaks close to the centre of the BCGs continuum but which show extended non-uniform structures in the lower surface brightness emission (13/73).

3. We also identify the presence of filaments of Hα emission in six objects. While it is possible these are related to the filaments seen in narrow-band observations we note that the spatial width of these structures is substantially higher than that of those observed with narrow-band filters.

4. The objects in the sample are identified to have a wide range line ratios ([NII]/Hα) suggesting substantial variation in the ionisation states of different objects. More interestingly perhaps the [NII]/Hα can be seen to vary within a given object clearly suggesting that source of ionising radiation is not uniformly distributed.

5. Analysis of the few objects for which the redshift allows us access to the Hβ and [OIII] lines suggests that the gas is predominantly ionised by radiation from a central AGN. However, we note that the overall ratio of [NII]/Hα in the system shows a dependence on the extent of the line emitting nebula with more extended objects having a lower overall ratio. This would suggest that while the AGN dominates the ionisation star formation also plays a role and is more important in highly extended objects.

6. Studying the maps of mean velocity presented in Figure 3.2 suggest that the velocity structure of the ionised gas in the majority of the sample ($\sim \frac{2}{3}$rd) is highly organised. Most objects show a velocity map which indicates a continuous velocity gradient across the brightest region of the Hα emission. This is often true even in systems where the extended low surface brightness emission shows a highly disordered velocity structure. This is in stark contrast to the kinematics obtained for the stellar absorption in several objects which shows no coherent structure in their mean velocity maps.

7. Interestingly the overall velocity gradient of the systems (defined as the peak–to–peak velocity divided by the extent along which that velocity difference is measured) showed a correlation with the extent but not with the peak–to–peak velocity (Figure 3.4). Such a situation clearly suggests a system in which the velocity of the gas is dependent on its position in the system, such as a rotating disk.

8. Several objects are identified which show a clear offset between the peak of the Hα emission and the centre of the BCG as measured by the continuum. Such objects are rare accounting for only a few percent of the total sample. However, several of these objects were identified as having their offset Hα emission coincident with the peak of the X-ray emission from the ICM offering the opportunity to study its interaction with the BCG and cluster core separately.

9. By studying several such offset objects in detail we are able to identify the presence of cold molecular gas at the location of the offset emission that is associated with the peak of X-ray cooling and not the central galaxy. This clearly suggests that the cooling of the ICM continues at the X-ray peak despite absence of the galaxy which will result in cooled gas being deposited away from the BCG.

10. Although our observations of these offset systems do not allow us to directly constrain the reason for the offset, we are able to estimate the time scales of such offsets from the fraction of objects which show an offset and from the kinematics. The estimates from both methods are consistent suggesting that such offsets are transient, lasting only a few 10s to 100 Myrs.

11. We identify the presence of an extended ($\sim$ 5 kpc) disk of cold, molecular and atomic gas in the core of Hydra-A which is rotating about an axis that runs parallel to the radio jets. This alignment is highly suggestive bearing many similarities to the standard model of an AGN. However, we note that the scales of the disk in Hydra-A are far greater than those in typical AGN so caution is needed in this interpretation, especially for single object studies.

12. Using the wealth of multi-wavelength data available for Hydra-A we are able to perform a mass census finding a total of 2.3×10^9 M$\odot$ of cold material contained in the disk. While this accounts for only a small fraction of the total dynamical mass within $R_{2.2}$ we note that it is sufficient to fuel a future outburst from the AGN of comparable magnitude to the current outburst.

13. We use the kinemetry technique (which is the generalisation of surface photometry to higher order moments of the line-of-sight velocity distribution) to

characterise the kinematics of all objects in the VIMOS sample as either disk like or not disk like. Through this analysis we determine that the ionised gas in the majority ($\approx 62\%$) of BCGs has a kinematic structure which is consistent with that of a rotating disk.

14. From our modelling we identify a possible expansion of the kinemetric analysis to identify near face on disks which in our models typically have total asymmetries consistent with mergers and non-disks. However, the majority of our face–on disk models had asymmetry ratios ($\frac{\sigma_{asym}}{V_{asym}}$) which were greater than those of the mergers and non-disks (typically > 0.8). We note the caution needed in using this distinction due to the relatively simple nature of our models. As such testing on real objects is necessary to more fully characterise this separation.

15. We use disk models to more accurately constrain the parameters of the disk, primarily the position angle and the inclination of the system. We note that the distributions of PA and inclination are consistent with that expected for a randomly selected sample of disks, which is as expected given our minimal selection criteria.

16. The disk models also allow us to estimate $V_{2.2}$ which should be a more appropriate measure of the rotational velocity than the peak–to–peak velocity. We compare the values of $V_{2.2}$ to measured CO linewidths (Figure 6.7) and see a clear correlation suggesting that the cold molecular gas shares the kinematic structure of the ionised gas (i.e. a rotating disk). This situation is similar to that seen in Hydra-A suggesting that in the majority of BCGs the cold gas forms a rotating disk about the centre of the BCG.

17. For objects which have detections of radio jets and/or X-ray cavities we compare the alignment of the disks axis of rotation with the axis of the radio jets and cavities (Figure 6.8). For most objects with large scale jets or cavities we find that the axis of rotation and the axis along which the AGN is injecting energy into the ICM are aligned to within $< 45^o$. This clearly suggests that most BCGs with ionised gas disks have an alignment similar to the seen in Hydra-A.

We will now use these points to try and answer the questions laid out at the beginning of this chapter. We will begin with the first question, as we discussed in Chapter 3 the results from this study find that the majority of objects have a Hα morphology which suggests the gas is relatively quiescent (Point 2). Similarly while many objects do show gas at high velocities relative to the BCG their velocity structures appear well ordered (points 6 and 7). Interestingly these ordered velocity structures seen in the ionised gas are not shared by the stellar component of the BCG suggesting that the stars and gas are decoupled. Despite this several objects from our sample do show a disturbed morphology and we note that these objects typically show a much greater degree of disorder in the velocity structure of the low surface brightness gas (e.g. Abell 3581, NCG 5044, RXJ 0338+09). While a few of these disturbed systems did show evidence of an interaction with another cluster member (e.g. RXJ 0338+09) it was not a common factor in all disturbed systems. We also identified at least one system (Abell 3880) which showed clear evidence of an interaction with a cluster member but did not have a disturbed morphology. This system however did show a plume of gas which extended from the BCG to the companion suggesting an interaction as the possible cause of the plumes seen in ∼ 10% of the sample. These results clearly indicate that the line emitting systems in the majority of BCGs are not highly disturbed and that the presence of high velocity gas does not require the BCG to be interacting with another cluster member.

In Chapter 4 we address the second question and investigate the role played by the BCG in the cooling of gas from the ICM. By studying a small sub-sample of objects identified as having a BCG which is substantially offset from the bulk of the ionised gas and the peak of the X-ray emission (points 2 and 8) we are able to disentangle the relative effects of the BCG and cluster core. Through the study of these objects we are able to identify the presence of cold molecular gas which is associated with the offset line emission and not the BCG (point 9). While we were not able to identify the reason for these offsets the statistics and kinematics allowed us to determine that they are likely transient (point 10) suggesting the BCG will return to the centre of X-ray cooling in just a few tens to a hundred Myrs. Thus we conclude that BCG is not required for cooling gas to condense from the ICM despite the observation that BCGs have positions which are strongly correlated with that

of the cluster core (Peres et al., 1998; Sanderson et al., 2009b; Hudson et al., 2010).

With the work presented in Chapters 5 and 6 we study the interaction of the cold gas with the feedback from the central AGN, which allows us to answer the third of the questions laid out at the begining of this chapter. For a single object we are able to clearly identify the presence of a disk which contains a substantial mass of cold gas and dust (points 11 and 12). We find that this disk has an axis of rotation which is almost parallel to the axis along which radio jets from the AGN are inflating cavities in the ICM. We note that the mass in the disk is sufficient to fuel a future outburst of comparable magnitude to the one currently seen to be injecting energy into the ICM. To expand this analysis to all objects in the VIMOS sample we use kinemetry (Krajnović et al., 2006; Shapiro et al., 2008) to identify disk systems in our sample and find that $\approx 62\%$ have kinematics consistent with disk rotation (point 13). Using disk models to constrain the peak rotational velocity of the disk systems we compare the disk kinematics to those of the cold molecular gas as measured by the CO linewidths (points 15 and 16) and find that they are consistent. Finally we compare the axis of rotation of these disks to the axis along which the AGN is interacting with the ICM (through the inflation of cavities by radio jets) and find a good alignment for most systems (point 17). This situation bares a remarkable resemblance to the unified model of AGN with the only difference being that the scales involved in these systems is much greater. Despite this the prevalence of these disks and their alignment to the jets and cavities clearly suggests that they play an important part in the feedback process and potentially provides a link between the gas cooling of kpc scales and the fuelling of the central black hole.

While this work has been able to address several important issues in our understanding of the complex relationship between the various gas phases in the cores of clusters of galaxies and their interactions with the BCG it has perhaps raised as many questions as it has answered. In the sections that follow we will describe several follow–up projects that will build on the work presented here through the acquisition of new data and the further analysis of the sample.

7.3   Future Work

7.3.1   Systems with Multiple Velocity Components

The spectral fitting routine described in Chapter 2 was set up to detected the presence of multiple velocity components within the ionised gas of each object. This was primarily included to account for the presence of very broad components in the spectra (from the central AGN) and was able to identify such lines in several objects. However, where broad spectral lines are detected they are typically unresolved given the seeing of our observations. More interestingly however, the fitting routine also identified two objects which had multiple narrow line components in their cores. These objects were Abell 3574 and NGC 5044 and the analysis of NCG 5044 has already begun. Upon closer inspection NCG 5044 also showed evidence of broad line emission from its core regions (Figure 7.1). The identification of multiple lines within the cores of these objects clearly suggests the presence of ionised gas at multiple different velocities.
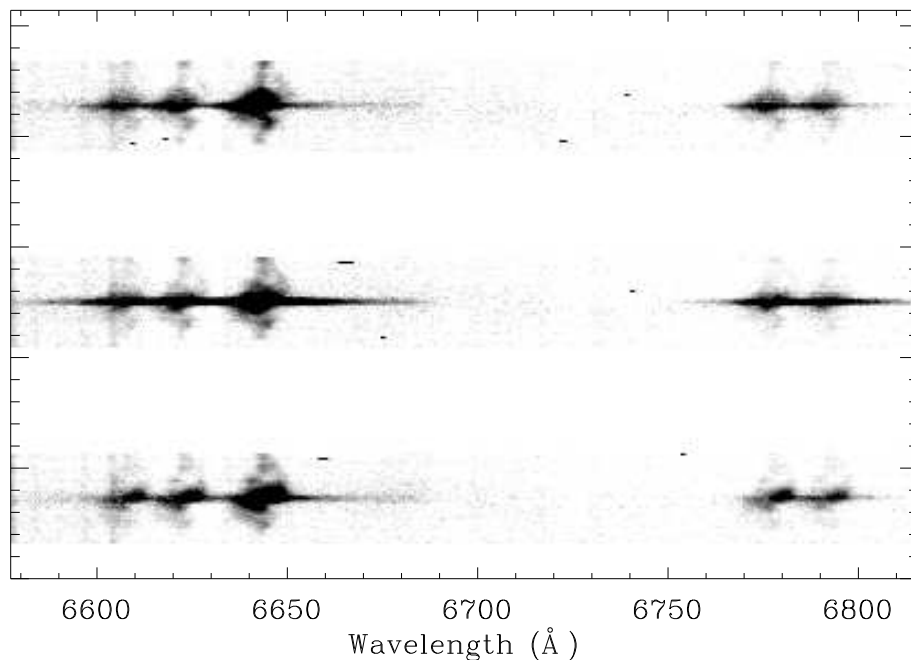

Figure 7.1: Extract of the 2D spectral frame of NGC 5044 showing the Hα, [NII] and [SII] emission lines. The extract covers the central region of the objects and the broad line component can clearly be seen. The complex velocity structure and the multiple velocity components are apparent away form the core regions.

Wilman et al. (2006) identify the presence of gas at different velocities in the core of Abell 1664, so the presence of multiple velocity components is not unprecedented. However, in light of the results presented in this Thesis the origin of these multiple velocity components needs careful consideration. In both Chapters 4 and 5 we identify systems which have multiple peaks in the surface brightness of their ionised gas emission which also have different velocities. In all of these systems we identify an offset between the BCG and the cluster core (spatial for the systems in Chapter 4 and potentially dynamic for Hydra-A in Chapter 5). An implication of the gas cooling from the ICM is that it will retain the velocity of the cluster (see Chapter 4), thus if the BCG is displaced it is possible that two velocity components would be observed. To test for this we fit the integrated spectrum of the two components separately along with that of the sodium D stellar absorption feature (Figure 7.2). What has become apparent from this analysis is that neither velocity component of the line emission is consistent with the velocity of the BCG.

To test if either component is consistent with the velocity of the cluster centre of mass we extracted the known galaxies within ~ 200 kpc from NED and identified 30 potential cluster members whose mean redsift is 0.0082. This is roughly consistent with the velocity of the blue component of the line emission although the number of galaxies used is small so some caution is required. To truly constrain the dynamical separation of the BCG from the cluster core will require good quality spectroscopy of a substantial number of cluster members so that the clusters centre of mass can be well accurately determined. The analysis of NGC 5044 is still ongoing and we have yet to begin a similarly detailed analysis of Abell 3574 however, the initial results suggest that these systems with multiple line components are highly disturbed with the BCG, cluster core and bulk of the line emission all being dynamically separate.

7.3.2 IFU Observations of the Warm Molecular Gas in the Most Rapidly Rotating Systems

In Chapter 5 we use near infrared IFU observations taken with SINFONI to directly constrain the kinematics of the warm molecular gas in Hydra-A, one of the most rapidly rotating objects from our VIMOS sample. What is apparent from these observations is that the disk traced by the Hα emitting gas is shared by the ro-
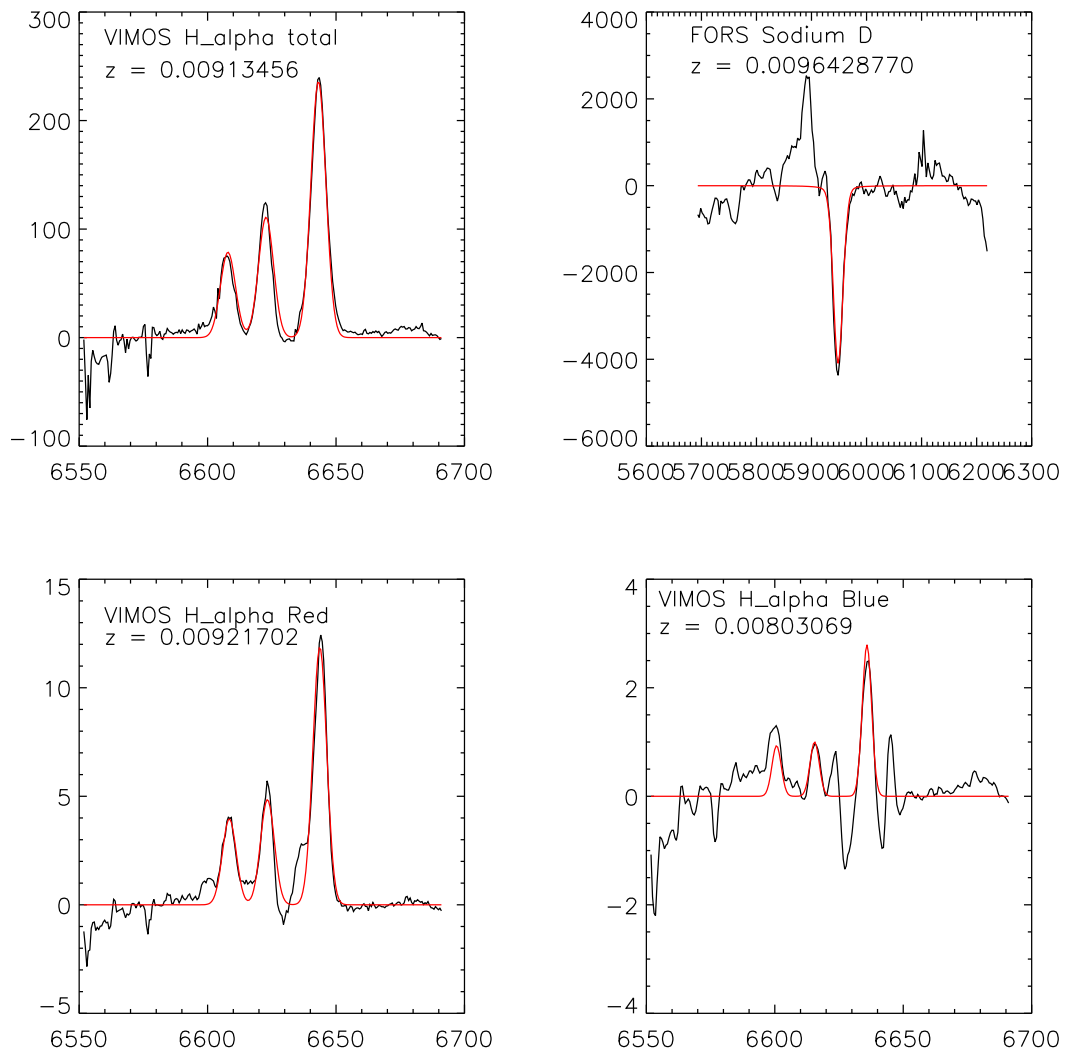
Figure 7.2: *Top Left* - Fit to the integrated spectra of both the velocity components of Hα and [NII] in NGC 5044. *Top Right* - Fit to the integrated spectra of the sodium D stellar absorption feature. *Bottom* - Fits to the integrated spectra of the red and blue components of the Hαand [NII] emission. Interestingly these fits suggest that neither the blue nor the red component of the line emission are kinematicaly consistent with the stellar component of the BCG.

vibrationaly excited molecular emission which clearly established that the disk seen in the ionised emission is related to a much more substantial mass of cold molecular gas. In order to build on these results a sub-sample of seven of the most rapidly rotating systems were selected to be observed with SINFONI (Table 7.1, PI Hamer, Project ID 086.A-0810).

The preliminary analysis of these results has begun and suggest that most of these systems share the consistency between the ionised and warm molecular gas

TABLE. 7.1.
THE TARGETS SELECTED FOR OBSERVATION WITH SINFONI

Object	K_{asym}	$V_{2.2}$ (km s^{-1})
Abell 1348	0.34 ± 0.0027	487 ± 9
Abell 3017	0.12 ± 0.0053	219 ± 8
Abell 3581	0.42 ± 0.011	311 ± 14
Abell 4059	0.12 ± 0.030	343 ± 11
RXCJ0132.6-0804	0.34 ± 0.0050	116 ± 3
RXCJ2014.8-2430	0.47 ± 0.013	352 ± 6
S780	0.28 ± 0.017	205 ± 3
Hydra-A	0.27 ± 0.0082	397 ± 8

Table 7.1: Here we list the targets which were selected for observation with SINFONI to allow for a direct dynamical tracer of the cold molecular gas in these systems. The objects all showed clear evidence of disk rotation and had high rotational velocities comparable to those seen in Hydra-A (Chapter 5). For reference Hydra-A is included in this table though it was not observed as part of these observations.

which is seen in Hyrda-A. Once this analysis of these data is complete it will present a substantial increase the number of systems in which we are able to directly constrain the kinematics of the molecular gas allowing us to test the implications of the analysis of Hydra-A.

7.3.3 The Kinematics of Gas interacting with AGN Feedback

One of the interesting results to come out of the comparison of the structures of the line emitting gas with those seen in the X-rays is the fact the optical lines can be seen in the regions of enhanced X-ray surface brightness which surrounds cavities (McDonald et al., 2011). We were able to identify two such objects in our VIMOS sample, A2052 and NGC5813, which we show in Figure 7.3.

The X-ray cavities are believed to be "bubbles" of non–thermal plasma inflated in the ICM by AGN outbursts. These bubbles are predicted to rise buoyantly (Bîrzan et al., 2004) and can potentially entrain material, pulling it out of the BCG and enriching the ICM. The structural similarities between the two phases of gas prompts the question of whether the line emission and enhanced X-ray emission are related to gas that is uplifted by entrainment, shocked by the expanding bubble or created through enhanced local cooling in the compressed ICM. We have obtained a series of pointed VIMOS IFU observations (PI Hamer, Project ID 089.A-0781) which will substantially increase the signal to noise of the line emitting gas in the
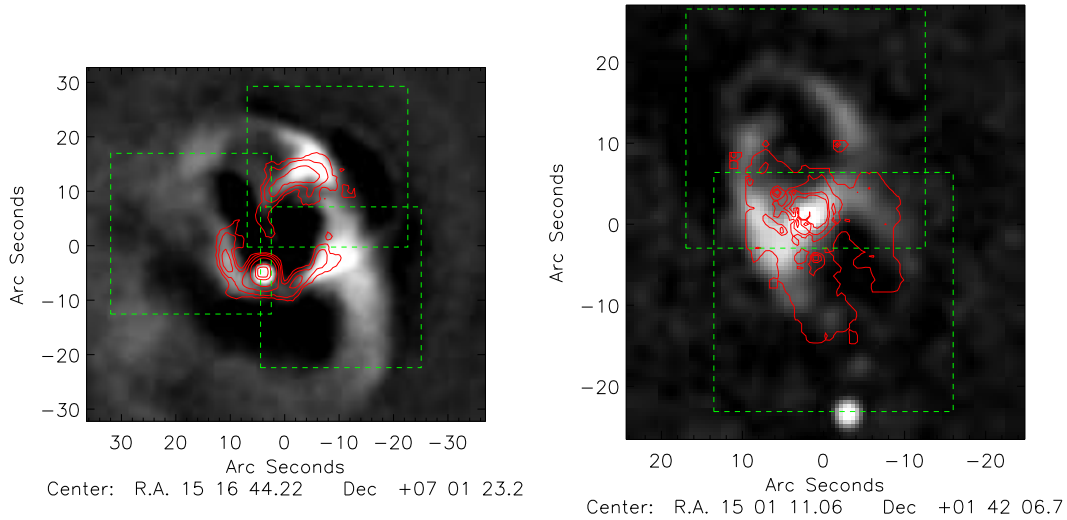
Figure 7.3: The grey scale shows unsharp masked X-ray images from Chandra observations of Abell 2052 (*Left*) and NGC 5813 (*Right*). The red contours show the location of the Hα emission which can be seen to be coincident with locally enhanced X-ray emission at the edges of the cavities. Note that the Hα observation of NGC 5813 did not cover the northern cavity. The dashed boxes show the fields of view of the extra VIMOS observations which will substantially increase the signal to noise of our observations in these two systems.

two systems we identified from our sample. These observations are targeted at the regions depicted in Figure 7.3 which cover the enhanced X-ray emission surrounding the cavities in these two systems. We will use these observations to distinguish between the possible origins of this enhanced emission using the kinematics and excitation state of the ionised gas. If the gas is entrained it will have the outward velocity of the rising bubble. If it is shocked then the line width should be enhanced to close to the local sound speed (300–600 km s^{-1}). However, if it is related to local cooling then it will have the velocity of the surrounding ICM which should match that of the BCG. These observations have recently been taken and show evidence of low surface brightness line emission extended throughout the field of view.

It is the growing consensus within the community that mechanical heating from the AGN hosted in the BCG is responsible for suppressing the cooling of the ICM. However, this consensus requires a much better understanding of how the mechanical feedback couples to the cooling X-ray gas. By combining the data from these observations with deep Chandra imaging (both Abell 2052 and NGC 5813 have observations totalling ~ 650 ks) we will be able to make a direct measurement of how the cavities expand and interact with the surrounding gas having wide implications

for AGN feedback models.

7.4   Conclusions

This work represents a significant step forward in the study of the interplay between the Brightest Cluster Galaxy, the cold gas in the cluster core and the cooling of the hot gas in the ICM. We have shown that despite the high velocity of the ionised gas it is typically quite quiescent and forms simple and ordered spatial and kinematics structures. Such simple structures clearly favour a situation in which the gas has cooled form the surrounding medium and has remained undisturbed by interactions with other cluster members for some time. The detection of line emission and indeed emission from molecular gas at a location offset from the BCG in a handful of systems provides compelling evidence that the Brightest Cluster Galaxy is not an integral part of the cooling and condensing of gas from the ICM. While it clearly will play an important role in the evolution of the cluster core we have shown that even when it is displaced the ICM will continue to cool and deposit cold gas away from the galaxy. Through a detailed analysis of the kinematics of the ionised gas we identify the presence of disks of cold gas in more than 60% of the line emitting systems. The identification of the alignment between the disk rotation and the feedback from the central AGN point at a clear connection between the cooling of gas on kpc scales and the fuelling of the black hole at the centre of the BCG. While the nature of this connection is not fully understood yet it has profound implications for our understanding of the feedback processes in galaxy cluster cores.

Appendix A | *Glossary*

2MASS	2-micron all sky survey
ACS	Advanced camera for surveys
AGN	Active galactic nucleus/nuclei
BCG	Brightest cluster galaxy
BCS	Brightest cluster survey
BPT	Baldwin, Phillips & Terlevich
CMB	Cosmic Microwave Background
CO	Carbon Monoxied
DM	Dark matter
EMIR	Eight mixer receiver
ESO	European Southern Observatory
ESOREX	ESO recipe execution tool
GMOS	Gemini multi-object spectrograph
Hα	Hydrogen recombination line
HIPE	Herschel interactive processing environment
HST	Hubble space telescope
ICM	Intra cluster medium
IFU	Integral field unit
IMF	Initial Mass Function
K$_{asym}$	The total Kinemetric asymmetry of a system
M$_{2.2}$	The Dynamical mass within a radius of R$_{2.2}$
NGS-POSS	National Geographic Society - Palomar observatory sky survey
NVAS	National Radio Astronomy Observatory Very Large Array Archive Survey (NVAS)
OTKP	Open time key project
R$_{2.2}$	2.2 times the galaxy scale radius
RASS	ROSAT All sky survey

RGS	Reflection Grating Spectometer
ROSAT	Rntgensatellit, X-ray satellite observatory
P$alpha$	The Paschen-alpha (n=4 to n=3) transition of the hydrogen atom
R$_{asym}$	Ratio of σ_{asym} over V$_{asym}$
SDSS	Sloan Digital Sky Survey
SF	Star formation
SINFONI	Spectrograph for integral field observations in the near infrared
SMBH	Super Massive Black Hole
UV	Ultra Violet
V$_{2.2}$	The orbital velocity at R$_{2.2}$
V$_{asym}$	A measure of the Asymmetry in the mean velocity field
VIMOS	Visible multiobject Spectrograph
VLT	Very Large Telescope
σ_{asym}	A measure of the Asymmetry in the velocity dispersion field

Bibliography

Abazajian, K. N., Adelman-McCarthy, J. K., Agüeros, M. A., et al. 2009, ApJS, 182, 543

Abell, G. O. 1958, ApJS, 3, 211

—. 1965, ARA&A, 3, 1

Abell, G. O., Corwin, Jr., H. G., & Olowin, R. P. 1989, ApJS, 70, 1

Ascasibar, Y., & Markevitch, M. 2006, ApJ, 650, 102

Baldwin, J. A., Phillips, M. M., & Terlevich, R. 1981, PASP, 93, 5

Bayer-Kim, C. M., Crawford, C. S., Allen, S. W., Edge, A. C., & Fabian, A. C. 2002, MNRAS, 337, 938

Beers, T. C., & Geller, M. J. 1983, ApJ, 274, 491

Bell, E. F., McIntosh, D. H., Katz, N., & Weinberg, M. D. 2003, ApJS, 149, 289

Binney, J., & Tremaine, S. 1987, Galactic dynamics

Bîrzan, L., Rafferty, D. A., McNamara, B. R., Wise, M. W., & Nulsen, P. E. J. 2004, ApJ, 607, 800

Blanton, E. L., Randall, S. W., Clarke, T. E., et al. 2011, ApJ, 737, 99

Böhringer, H., Schuecker, P., Guzzo, L., et al. 2004, A&A, 425, 367

Bondi, H. 1952, MNRAS, 112, 195

Bower, R. G., Benson, A. J., Malbon, R., et al. 2006, MNRAS, 370, 645

Braine, J., & Dupraz, C. 1994, A&A, 283, 407

Canning, R. E. A., Russell, H. R., Hatch, N. A., et al. 2011, MNRAS in press, arXiv:1111.0452

Cappellari, M., & Emsellem, E. 2004, PASP, 116, 138

Carter, M., Lazareff, B., Maier, D., et al. 2012, A&A, 538, A89

Cavagnolo, K. W., Donahue, M., Voit, G. M., & Sun, M. 2008, ApJ, 683, L107

Churazov, E., Sunyaev, R., Forman, W., & Böhringer, H. 2002, MNRAS, 332, 729

Conselice, C. J., Gallagher, III, J. S., & Wyse, R. F. G. 2001, AJ, 122, 2281

Cotton, W. D., Mason, B. S., Dicker, S. R., et al. 2009, ApJ, 701, 1872

Courteau, S. 1997, AJ, 114, 2402

Crawford, C. S., Allen, S. W., Ebeling, H., Edge, A. C., & Fabian, A. C. 1999, MNRAS, 306, 857

Crawford, C. S., Gandhi, P., Fabian, A. C., et al. 2002, MNRAS, 333, 809

Crawford, C. S., Sanders, J. S., & Fabian, A. C. 2005, MNRAS, 361, 17

Croton, D. J., Springel, V., White, S. D. M., et al. 2006, MNRAS, 365, 11

David, L. P., O'Sullivan, E., Jones, C., et al. 2011, ApJ, 728, 162

de Koff, S., Best, P., Baum, S. A., et al. 2000, ApJS, 129, 33

Donahue, M., de Messières, G. E., O'Connell, R. W., et al. 2011, ApJ, 732, 40

Dwarakanath, K. S., Owen, F. N., & van Gorkom, J. H. 1995, ApJ, 442, L1

Dwarakanath, K. S., van Gorkom, J. H., & Owen, F. N. 1994, ApJ, 432, 469

Ebeling, H., Edge, A. C., Bohringer, H., et al. 1998, MNRAS, 301, 881

Edge, A. C. 2001, MNRAS, 328, 762

Edge, A. C., & Frayer, D. T. 2003, ApJ, 594, L13

Edge, A. C., & Stewart, G. C. 1991a, MNRAS, 252, 428

—. 1991b, MNRAS, 252, 414

Edge, A. C., Wilman, R. J., Johnstone, R. M., et al. 2002, MNRAS, 337, 49

Edge, A. C., Oonk, J. B. R., Mittal, R., et al. 2010, A&A, 518, L46

Edwards, L. O. V., Robert, C., Mollá, M., & McGee, S. L. 2009, MNRAS, 396, 1953

Egami, E., Rieke, G. H., Fadda, D., & Hines, D. C. 2006, ApJ, 652, L21

Ekers, R. D., & Simkin, S. M. 1983, ApJ, 265, 85

Ettori, S., Fabian, A. C., Allen, S. W., & Johnstone, R. M. 2002, MNRAS, 331, 635

Fabian, A. C. 1994a, ARA&A, 32, 277

Fabian, A. C. 1994b, in Clusters of Galaxies, ed. F. Durret, A. Mazure, & J. Tran
    Thanh Van, 191

—. 2012, ArXiv e-prints

Fabian, A. C., Hu, E. M., Cowie, L. L., & Grindlay, J. 1981, ApJ, 248, 47

Fabian, A. C., Johnstone, R. M., Sanders, J. S., et al. 2008, Nature, 454, 968

Fabian, A. C., & Nulsen, P. E. J. 1977, MNRAS, 180, 479

Fabian, A. C., Sanders, J. S., Allen, S. W., et al. 2003, MNRAS, 344, L43

Fabian, A. C., Sanders, J. S., Taylor, G. B., et al. 2006, MNRAS, 366, 417

Freeman, K. C. 1970, ApJ, 160, 811

Hamer, S. L., Edge, A. C., Swinbank, A. M., et al. 2012, MNRAS, 2520

Hansen, L., Jorgensen, H. E., & Norgaard-Nielsen, H. U. 1995, A&A, 297, 13

Hatch, N. A., Crawford, C. S., Fabian, A. C., & Johnstone, R. M. 2005, MNRAS,
    358, 765

Hatch, N. A., Crawford, C. S., Johnstone, R. M., & Fabian, A. C. 2006, MNRAS,
    367, 433

Heckman, T. M., Baum, S. A., van Breugel, W. J. M., & McCarthy, P. 1989, ApJ, 338, 48

Herzog, E., Wild, P., & Zwicky, F. 1957, PASP, 69, 409

Hlavacek-Larrondo, J., Fabian, A. C., Edge, A. C., et al. 2012, MNRAS, 421, 1360

Hubble, E. P. 1926, ApJ, 63, 236

Hudson, D. S., Mittal, R., Reiprich, T. H., et al. 2010, A&A, 513, A37+

Jaffe, W., Bremer, M. N., & van der Werf, P. P. 2001, MNRAS, 324, 443

Johnson, R. E., Markevitch, M., Wegner, G. A., Jones, C., & Forman, W. R. 2010, ApJ, 710, 1776

Johnson, R. E., ZuHone, J. A., Jones, C., Forman, W., & Markevitch, M. 2011, ArXiv e-prints

Johnstone, R. M., Fabian, A. C., & Nulsen, P. E. J. 1987, MNRAS, 224, 75

Katz, N., & White, S. D. M. 1993, ApJ, 412, 455

Krajnović, D., Cappellari, M., de Zeeuw, P. T., & Copin, Y. 2006, MNRAS, 366, 787

Lahav, O., Fabian, A. C., Edge, A. C., & Putney, A. 1989, MNRAS, 238, 881

Lewis, G. F., Babul, A., Katz, N., et al. 2000, ApJ, 536, 623

Lim, J., Ao, Y., & Dinh-V-Trung. 2008, ApJ, 672, 252

Lim, J., Leon, S., Combes, F., & Dinh-V-Trung. 2000, ApJ, 545, L93

Lin, Y.-T., Mohr, J. J., & Stanford, S. A. 2003, ApJ, 591, 749

Loewenstein, M. 2004, Origin and Evolution of the Elements, 422

Markevitch, M., & Vikhlinin, A. 2007, Phys. Rep., 443, 1

Markevitch, M., Vikhlinin, A., & Forman, W. R. 2003, in Astronomical Society of the Pacific Conference Series, Vol. 301, Astronomical Society of the Pacific Conference Series, ed. S. Bowyer & C.-Y. Hwang, 37–+

McDonald, M., & Veilleux, S. 2009, ApJ, 703, L172

McDonald, M., Veilleux, S., & Mushotzky, R. 2011, ApJ, 731, 33

McNamara, B. R. 1995, ApJ, 443, 77

McNamara, B. R., & Jaffe, W. 1994, A&A, 281, 673

McNamara, B. R., & Nulsen, P. E. J. 2007, ARA&A, 45, 117

—. 2012, New Journal of Physics, 14, 055023

McNamara, B. R., Nulsen, P. E. J., Wise, M. W., et al. 2005, Nature, 433, 45

McNamara, B. R., & O'Connell, R. W. 1989, AJ, 98, 2018

McNamara, B. R., Wise, M., Nulsen, P. E. J., et al. 2000, ApJ, 534, L135

McNamara, B. R., Wise, M. W., Nulsen, P. E. J., et al. 2001, ApJ, 562, L149

McNamara, B. R., Rafferty, D. A., Bîrzan, L., et al. 2006, ApJ, 648, 164

Mewe, R., Gronenschild, E. H. B. M., & van den Oord, G. H. J. 1985, A&AS, 62,
    197

Mewe, R., Lemen, J. R., & van den Oord, G. H. J. 1986, A&AS, 65, 511

Miller, S. H., Bundy, K., Sullivan, M., Ellis, R. S., & Treu, T. 2011, ApJ, 741, 115

Million, E. T., & Allen, S. W. 2009, MNRAS, 399, 1307

Million, E. T., Allen, S. W., Werner, N., & Taylor, G. B. 2010, MNRAS, 405, 1624

Minkowski, R. L., & Abell, G. O. 1963, The National Geographic Society-Palomar
    Observatory Sky Survey, ed. K. A. Strand (the University of Chicago Press), 481

Mittal, R., Hudson, D. S., Reiprich, T. H., & Clarke, T. 2009, A&A, 501, 835

Mittal, R., O'Dea, C. P., Ferland, G., et al. 2011, MNRAS, 418, 2386

Mittal, R., Oonk, J. B. R., Ferland, G. J., et al. 2012, ArXiv e-prints

Morris, R. G., & Fabian, A. C. 2005, MNRAS, 358, 585

Mushotzky, R. F., Serlemitsos, P. J., Boldt, E. A., Holt, S. S., & Smith, B. W. 1978, ApJ, 225, 21

Nesvadba, N. P. H., Neri, R., De Breuck, C., et al. 2009, MNRAS, 395, L16

Nulsen, P. E. J., McNamara, B. R., David, L. P., & Wise, M. W. 2005, Highlights of Astronomy, 13, 307

Ocaña Flaquer, B., Leon, S., Combes, F., & Lim, J. 2010, A&A, 518, A9

O'Dea, C. P., Baum, S. A., Mack, J., Koekemoer, A. M., & Laor, A. 2004, ApJ, 612, 131

O'Dea, C. P., Baum, S. A., Maloney, P. R., Tacconi, L. J., & Sparks, W. B. 1994, ApJ, 422, 467

O'Dea, C. P., Baum, S. A., Privon, G., et al. 2008a, ApJ, 681, 1035

—. 2008b, ApJ, 681, 1035

O'Dea, K. P., Quillen, A. C., O'Dea, C. P., et al. 2010, ApJ, 719, 1619

Oegerle, W. R., & Hill, J. M. 1994, AJ, 107, 857

Okuda, T., Kohno, K., Iguchi, S., & Nakanishi, K. 2005, ApJ, 620, 673

Oonk, J. B. R., Jaffe, W., Bremer, M. N., & van Weeren, R. J. 2010, MNRAS, 405, 898

Owen, F. N., & Ledlow, M. J. 1997, ApJS, 108, 41

Peres, C. B., Fabian, A. C., Edge, A. C., et al. 1998, MNRAS, 298, 416

Peterson, J. R., & Fabian, A. C. 2006, Phys. Rep., 427, 1

Peterson, J. R., Kahn, S. M., Paerels, F. B. S., et al. 2003, ApJ, 590, 207

Peterson, J. R., Paerels, F. B. S., Kaastra, J. S., et al. 2001, A&A, 365, L104

Pilbratt, G. L., Riedinger, J. R., Passvogel, T., et al. 2010, A&A, 518, L1

Pimbblet, K. A., Roseboom, I. G., & Doyle, M. T. 2006, MNRAS, 368, 651

Rafferty, D. A., McNamara, B. R., & Nulsen, P. E. J. 2008, ApJ, 687, 899

Ramos Almeida, C., Tadhunter, C. N., Inskip, K. J., et al. 2011, MNRAS, 410, 1550

Randall, S. W., Sarazin, C. L., & Ricker, P. M. 2002, ApJ, 577, 579

Russell, H. R., Sanders, J. S., Fabian, A. C., et al. 2010, MNRAS, 406, 1721

Salomé, P., & Combes, F. 2003, A&A, 412, 657

—. 2004, A&A, 415, L1

Salomé, P., Combes, F., Revaz, Y., et al. 2011, A&A, 531, A85+

—. 2008, A&A, 484, 317

Salomé, P., Combes, F., Edge, A. C., et al. 2006, A&A, 454, 437

Sanders, J. S., & Fabian, A. C. 2011, MNRAS, 412, L35

Sanders, J. S., Fabian, A. C., Frank, K. A., Peterson, J. R., & Russell, H. R. 2010, MNRAS, 402, 127

Sanderson, A. J. R., Edge, A. C., & Smith, G. P. 2009a, MNRAS, 398, 1698

Sanderson, A. J. R., O'Sullivan, E., & Ponman, T. J. 2009b, MNRAS, 395, 764

Sarazin, C. L. 1988, X-ray emission from clusters of galaxies

Schombert, J. M. 1987, ApJS, 64, 643

—. 1988, ApJ, 328, 475

Shapiro, K. L., Genzel, R., Förster Schreiber, N. M., et al. 2008, ApJ, 682, 231

Sharma, M., McNamara, B. R., Nulsen, P. E. J., et al. 2004, ApJ, 613, 180

Simkin, S. M. 1979, ApJ, 234, 56

Skrutskie, M. F., Cutri, R. M., Stiening, R., et al. 2006, AJ, 131, 1163

Smith, R. J., Hudson, M. J., Nelan, J. E., et al. 2004, AJ, 128, 1558

Sparks, W. B. 1992, ApJ, 399, 66

Sparks, W. B., Donahue, M., Jordán, A., Ferrarese, L., & Côté, P. 2004, ApJ, 607, 294

Sparks, W. B., Macchetto, F., & Golombek, D. 1989, ApJ, 345, 153

Struble, M. F., & Rood, H. J. 1999, ApJS, 125, 35

Tamura, T., Kaastra, J. S., Peterson, J. R., et al. 2001, A&A, 365, L87

Taylor, G. B. 1996, ApJ, 470, 394

Tremaine, S. 1990, The origin of central cluster galaxies., ed. Wielen, R., 394–405

Tremblay, G. R., Chiaberge, M., Donzelli, C. J., et al. 2007, ApJ, 666, 109

Tremblay, G. R., O'Dea, C. P., Baum, S. A., et al. 2012, MNRAS, 424, 1042

Veilleux, S., Cecil, G., & Bland-Hawthorn, J. 2005, ARA&A, 43, 769

Verdoes Kleijn, G. A., & de Zeeuw, P. T. 2005, A&A, 435, 43

Voges, W., Aschenbach, B., Boller, T., et al. 1999, A&A, 349, 389

Voigt, L. M., & Fabian, A. C. 2004, MNRAS, 347, 1130

Voit, G. M., Cavagnolo, K. W., Donahue, M., et al. 2008, ApJ, 681, L5

White, D. A., Fabian, A. C., Johnstone, R. M., Mushotzky, R. F., & Arnaud, K. A. 1991, MNRAS, 252, 72

Wilman, R. J., Edge, A. C., & Johnstone, R. M. 2005, MNRAS, 359, 755

Wilman, R. J., Edge, A. C., Johnstone, R. M., et al. 2002, MNRAS, 337, 63

Wilman, R. J., Edge, A. C., & Swinbank, A. M. 2006, MNRAS, 371, 93

—. 2009, MNRAS, 395, 1355

Wise, M. W., McNamara, B. R., Nulsen, P. E. J., Houck, J. C., & David, L. P. 2007, ApJ, 659, 1153

Wolfire, M. G., Tielens, A. G. G. M., & Hollenbach, D. 1990, ApJ, 358, 116

Zabludoff, A. I., Geller, M. J., Huchra, J. P., & Vogeley, M. S. 1993, AJ, 106, 1273

Zemcov, M., Borys, C., Halpern, M., Mauskopf, P., & Scott, D. 2007, MNRAS, 376, 1073

ZuHone, J. A., Markevitch, M., & Johnson, R. E. 2010, ApJ, 717, 908

ZuHone, J. A., Markevitch, M., & Lee, D. 2011, ApJ, 743, 16

Zwicky, F. 1938, PASP, 50, 218

Zwicky, F., Herzog, E., & Wild, P. 1963, Catalogue of galaxies and of clusters of galaxies, Vol. 2

—. 1966, Catalogue of galaxies and of clusters of galaxies, Vol. 3

—. 1968, Catalogue of galaxies and of clusters of galaxies

Zwicky, F., Herzog, E., Wild, P., Karpowicz, M., & Kowal, C. T. 1961, Catalogue of galaxies and of clusters of galaxies, Vol. I

Zwicky, F., Karpowicz, M., & Kowal, C. T. 1965, "Catalogue of Galaxies and of Clusters of Galaxies", Vol. V

Zwicky, F., & Kowal, C. T. 1968, "Catalogue of Galaxies and of Clusters of Galaxies", Volume VI